Characterization and Optimization of Multifunctional Automotive Catalysts

by
Sotirios Alexandros Malamis

A dissertation submitted to the

Department of Chemical and Biomolecular Engineering

in partial fulfillment of the requirements for the degree of

DOCTOR OF PHILOSOPHY

in Chemical Engineering

Chair of Committee: Michael P. Harold

Committee Member: William S. Epling

Committee Member: Jeffrey D. Rimer

Committee Member: Praveen P. Bollini

Committee Member: Stanko R. Brankovic

University of Houston
December 2019

Acknowledgements

First and foremost, I dedicate this thesis to my family and friends. They have provided me the deepest and strongest support throughout my PhD career. Their care and support means more than I can express and I will be forever grateful and appreciative of them.

I want to also acknowledge my advisor Michael P. Harold for his guidance and mentorship as well as the research group members for all of their help. As a verdant first-year student I quickly learned that the training and mentorship provided by the seasoned veterans was unequivocally invaluable.

I would like to thank all of my project collaborators throughout the years including Fiat-Chrysler of America for their fruitful discussions during the TWNSC work, and the Grabow group for their meticulous work on passive NO_x adsorbers.

Abstract

Multifunctional automotive catalysts provide new opportunities for gasoline and diesel engines to meet the constantly tightening emissions and fuel economy standards from various regulatory agencies. Meeting these demands is important not only for securing industrial compliance but also for improving human health and air quality. Combining multiple functions into a single catalyst saves design space and reduces material cost. Here we conduct steady state and transient experiments on multifunctional catalysts that span the operational range of gasoline and diesel engines including cold start and high-temperature operations in order to reduce NO_x and hydrocarbon (HC) emissions. We investigate first the Three-Way NO_x Storage Catalyst (TWNSC), a concept that combines three-way and NO_x storage functionalities for optimal performance during high-temperature vehicle operation. A series of experiments identifies operating conditions that maximize conversion and performance for application with a downstream selective catalytic reduction (SCR) catalyst. Second, we characterize new catalysts that address the cold start issue of modern engines, namely the Lean Hydrocarbon NO_x Trap (LHCNT) concept. The LHCNT is a precious group metal (PGM)-zeolite material that combines low temperature NO_x and hydrocarbon storage and catalytic conversion of both species into a single unit. By conducting transient uptake and release experiments we obtain useful insight about competitive adsorption, release temperature, conversion activity, and water impact. We find that hydrocarbon concentration and identity, as well as PGM content and zeolite geometry can affect NO_x/HC uptake and release performance. Findings from single catalyst function experiments are used to evaluate sequential and dual-layered configurations that improve the overall LHCNT performance. The final part of this work investigates the feasibility of modeling such a

catalyst to predict performance and screen new materials. These results provide guidance for improving catalytic systems in the automotive catalysis industry in order to keep up with emission standards.

Table of Contents

List of Tables

List of Figures

Chapter 1: Introduction

In this dissertation the use of multifunctiional catalysts for NO_x and HC emissions control is investigated. Through a combination of systematic experiments and modeling work, catalysts are evaluated for use in their respective applications and optimziation strategies are developed. Two types of systems are described here: the Three-Way NO_x Storage Catalyst (TWNSC) and the Lean Hydrocarbon NO_x Trap (LHCNT). While these catalysts exhibit some form of NO_x storage and release, the mechanisms and operating conditions differ significantly. The TWNSC is designed to trap NO at temperatures above 200°C during a fuel-lean period and release/convert it during a fuel-rich period. In contrast, the LHCNT is designed to trap NO at temperatures *below* 200°C under a constant lean feed, then release/convert it above 200°C. Both of these systems are part of a *multi*-multifunctional catalytic system designed to minimize NO_x and HC emissions for diesel or lean gasoline engines–although the primary focus of this work is for diesel applications. After a brief review of automotive emission control and a summary of monolith catalyst fundamentals, each of the two catalysts is introduced. The main body chapters (2–5) of this dissertation describe the findings of the research. The thesis concludes with a summary of the research and recommendations for future work.

1.1 Automotive emission control

Before any automotive emission control strategies were enacted by governments around the world, densely populated, automobile-dependent cities like Los Angeles, CA, suffered from copious amounts of smog, particularly on hot summer days. The polluted air led to a number of adverse health effects spanning irritated, watery eyes and severe respiratory issues. On their own, engines are unable to fully and effi-

ciently convert hydrocarbons to CO_2 and H_2O, and at the combustion temperatures NO reacts with O_2 to generate NO, a smog precursor. As a result, the Clean Air Act was enacted in 1963 in the United States to regulate air quality, including the regulation of automotive engine exhaust.[1] To comply with the regulations, automotive companies developed the catalytic converter, designed to convert these adverse tailpipe emissions into benign N_2, H_2O, and CO_2, as shown in the following set of simplified reactions:[2]

$$CO + \frac{1}{2}O_2 \rightarrow 2CO_2, \tag{1.1}$$

$$C_yH_x + nO_2 \rightarrow yCO_2 + \frac{x}{2}H_2O, \tag{1.2}$$

and

$$NO_x \rightarrow O_2 + N_2. \tag{1.3}$$

Emissions from the transportation sector still account for up to 67% of total NO_x emissions in the United States, so implementing tighter control strategies and regulations is paramount.[3,4] Fig. 1.1 shows the increasing NO_x emissions regulations for EU standards for both gasoline and diesel vehicles.[5] Clearly, NO_x abatement strategies still need to be developed and refined in order to keep up with these standards.

1.2 Monolith catalysts

Early versions of catalytic converters consisted of Pt pellets that were rudimentary in their ability to catalyze the oxidation of HCs and CO, but they could not catalyze the reduction of NO_x. The pellets unfortunately had low surface area resulting in decreased contact time, and were susceptible to degradation through attrition. To improve long-term stability and oxidation rates, ceramic honeycomb-shaped monoliths were implemented. Monolith catalysts are unique in that they allow for an applied high surface area (100 m^2/g) support to which the active sites are added, and

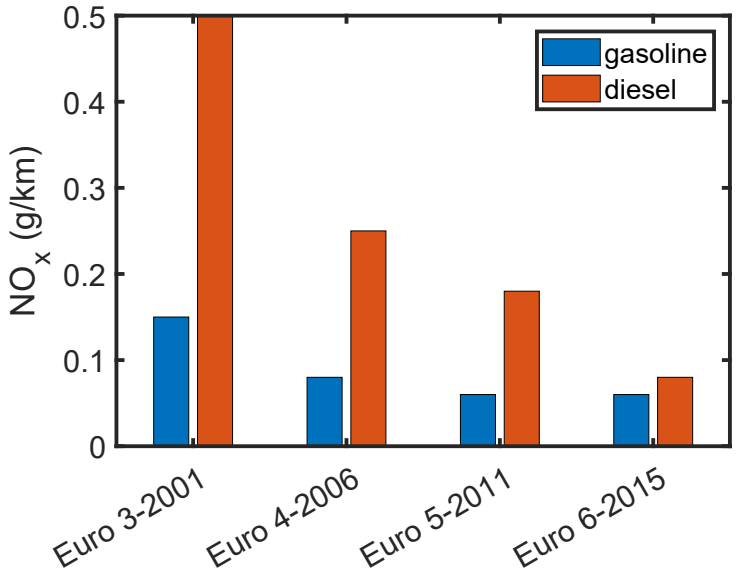

Figure 1.1: EU NO_x emissions regulations for both gasoline and diesel vehicles. Current standards (Euro-6) extend to 2020.

they have lower pressure drop limitations. They are also more economical and practical in an automotive application, in part due to the ever-increasing demand.[6] The washcoat is typically 20–150 μm thick and is applied using a dip-coating method. The monoliths typically used in automotive emission control are made of cordierite, a ceramic material with very high thermal stability resistant to cracking at high operating temperatures. They are typically extruded from mixtures of clays and other materials. Monoliths can also be constructed of metal, in which they are produced by folding thin sheets into specific geometries.[7] These structures can have varying channel densities, with typical values ranging from 400–1000 cells/in^2 (cpsi). Channels typically have a square geometry, although they can be circular, hexagonal or triangular, depending on the application. Other parameters that define the honeycomb include the geometric surface area and the open fraction area, as well as the hydraulic diameter. The wall thickness is also important in that it determines the structural integrity of the monolith.[8]

One of the differences between a monolith catalyst and a powder-loaded packed bed is the significant decrease in pressure drop, allowing for the testing of high flow

rates without performance issues. However, because of the lack of restricted flow, it is important to tune the washcoat thickness, catalyst volume, and flow rate (and resulting space velocity) such that the reactive feed mixture can adequately diffuse into the washcoat without experiencing diffusion limitations. Mass transfer limitations exist in two areas: diffusion limitation in the waschoat and transverse diffusion from the fluid phase to the washcoat surface.[7] Diffusion limitations in the washcoat are important because the overall reaction rate may be lower that the actual rate if the diffusion of reactants into the washcoat is too slow. Such limitations need to be considered for square channel monoliths because most of the washcoat applied to the channel exists in the corners, as shown in Fig. 1.2. Because of these limitations, mass transfer coefficient approximations have been developed to describe the monolith channel environment, depending on the geometry. These are further discussed in the model development section in Chapter 4. Regardless, the use of monolith catalysts brings with it a multitude of operational concerns that need to be considered when designing catalysts for automotive emission control.

1.3 Three way catalysts

The development of three way catalysts (TWC) is instrumental to the history of automotive emission control, as it quickly became the standard for use in gasoline engines. Before the onset of NO_x emission control, basic automotive catalysts focused on oxidizing HC and CO.[2] Copper and nickel were first used, but it was soon discovered that these metals had a very low thermal stability and were susceptible to poisoning from sulfur and fuel additives.[2] Platinum group metals were then studied, and after some experimentation with these metals, manufacturers settled on Pt, Rh, and Pd as automotive catalysts for CO and HC conversion.[10] While was the most stable, it was also highly sensitive to high temperatures, leading to sintering of the Pt particles on the catalysts and rapid deactivation. This effect remains a concern in lean NO_x traps and Pt-based catalysts in use today.[11] In contrast, Pd was found to

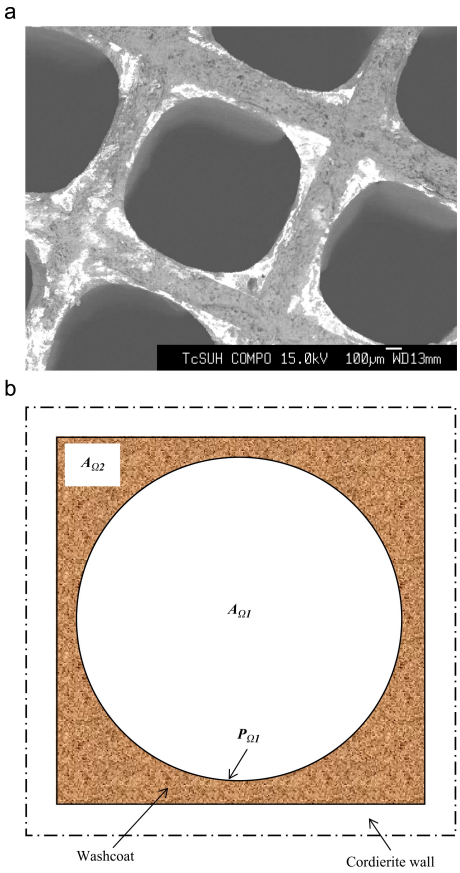

Figure 1.2: SEM image of washcoated monolith channel, figure adapted from Metkar et al.[9]

be more stable at high temperatures, and it was observed that rhodium acts as an ideal NO_x reducing metal in a TWC.[2,10]

Initial systems used a Pt/Rh catalyst to reduce NO_x to N_2 before adding air to the system to oxidize HC and CO using a second catalyst, similar to a modern LNT + SCR system.[2] However, it is rather inefficient and costly to have two catalysts. It was later observed that a Pt/Rh catalyst could convert all three pollutants efficiently because of the fluctuating air-to-fuel ratio (AFR) of the engine. These fluctuations were caused by the inaccuracy and inability of carburetors to maintain a constant AFR.[2] Thus the TWC came to be: a system that uses sensors and feedback control to supply the correct amount of air to maintain stoichiometric operation, and to achieve exceptionally high conversion of NO_x, CO and unreacted hydrocarbons (HC).[10] In the late 1980s, the main formulation for the TWC metals was Pd/Rh, replacing costly

Pt and still allowing for efficient performance.[2] However, it was later found that Pd significantly reduces Rh activity, and the focus shifted to a Pd-only catalyst.[10] Pd is the most abundant and usually the least costly of the precious group metals (PGMs), and has higher resistance to sintering.[12] Its limitations include lower activity for NO_x reduction and sensitivity to sulfur and lead poisoning.[10] A layered catalyst system with Pd and Rh has since been developed to reduce these effects and to improve activity. Moreover, mandated reduction in sulfur levels increase the viability of Pd.[10]

The next step in improving catalyst performance is incorporation of oxygen storage components to enhance catalytic activity. Ceria (CeO_2) was first used for its ability to trap oxygen during lean operation and release it during the rich phase.[2] It is a very important component in automotive catalysis and can be described in terms of the oxygen storage content (OSC), the amount of oxygen that can be stored in the system.[10] CeO_2 also promotes the activity of the water gas shift (WGS) and steam reforming reactions, both of which improve CO and HC conversion.[13,14] It was recently found that zirconia and alumina increase OSC in the catalyst and increase the thermal stability of CeO_2.[10] Three-way catalysts containing CeO_2 are still widely used today in gasoline vehicles.

1.4 LNT + SCR catalysts

While TWCs are practical for gasoline vehicles, they are not appropriate for diesel or lean-burn gasoline engine systems, primarily due to a limited operating window (air/fuel ratio). In addition, a large excess of O_2 in the exhaust prevents a standard TWC from converting NO_x to N_2. Excess O_2, besides that which is stored on CeO_2, is more likely to bind to the metallic surface of the catalyst than NO, hindering adsorption of NO. For these lean systems, it is more appropriate to use either a Lean NO_x Trap (LNT) or a Selective Catalytic Reduction (SCR) catalyst.[2] There has been extensive research on LNT catalysts in the past decade, particularly due to their potential for eliminating the need for urea injection in a downstream SCR.[15–19]

In the LNT, NO_x is trapped during lean operating conditions and reduced to less harmful or more useful species during the rich regeneration period.[20] In an ideal LNT, the system should be able to reach a steady state of lean and rich cycles in which the amount of NO_x stored equals the consumption.[21] Effective NO_x trapping requires Pt and alkaline earth metals such as Ba. The Ba acts as the main storage component for NO_x, while the Pt is necessary for bridging the gap between free NO and trapped NO.[20,21] In order for the NO_x trap to work effectively, NO in the exhaust is first oxidized to NO_2, the main function of Pt during the NO_x trapping phase.[22] This oxidation is most effective between 200 and 350 °C, a window outside of which kinetic and thermodynamic limitations occur.[23] Once the Pt converts NO to NO_2, the NO_2 can more easily be trapped on the catalyst surface, more specifically by binding to the Ba sites in the form of barium nitrates and nitrites. Many previous works have explained the mechanism through which NO_x adsorbs to the catalyst surface, namely the nitrate route and the nitrate route.[23] In the nitrite route, NO stores on BaO_2 to form nitrites, which are then oxidized to nitrates as in the following overall reaction:

$$BaO + 2NO + 1.5O_2 \rightarrow Ba(NO_3)_2. \tag{1.4}$$

With the nitrate route, NO is oxidized to NO_2 on Pt, but then undergoes disproportionation on Ba sites, where one molecule of NO is released for every three molecules of NO_2 consumed, as shown in the following reaction:

$$BaO + 3NO_2 \rightarrow Ba(NO_3)_2 + NO. \tag{1.5}$$

A study by Epling et al. provides evidence for the possibility of two types of NO_x adsorption sites on an LNT, namely sites close to the Pt that undergo the nitrite pathway and sites farther away that proceed with disproportionation.[24]

During the subsequent rich phase, the stored NO_x is released to form N_2, N_2O

and NH_3. This regeneration step also reduces Pt oxide back to Pt metal, sustaining the activity of CO and HC conversion during the lean phase.[20] Various studies detail the interaction between the precious metal and stored nitrates or nitrites on the surface. The nearby nitrates and nitrites decompose in a reverse spillover process that effectively leads to NO bound to the Pt surface before being released in the rich phase.[15,20] In addition to this chemistry, at high temperatures H_2O can react with CO or HC to form additional H_2, which can improve selectivity to NH_3.[13,20,25]

Typical components of an LNT catalyst include precious metals such as Pt and Rh and O_2/NO_x storing materials such as CeO_2 or barium oxide and analogues. Specifically, CeO_2 and Ba have been shown to increase the overall performance of a NO_x storage catalyst. Jacobs et al. reported in a study on low temperature water gas shift that CeO_2 is very good at promoting the formation of H_2 from water gas shift and steam reforming, further promoting the formation of NH_3.[13,26] In an extensive study by Kwak et al., CeO_2 improves NO_x storage when used as a support for a Pt/Ba catalyst and increases resistance to sulfur poisoning compared to alumina.[27] CeO_2 also increases thermal stability of a Pt-based catalyst.[28] Many studies have been performed on the positive effect of Barium and other alkaline earth metals on a NO_x storage catalyst, such as a 2002 study by Nova et al.[29] In this work, it was shown that NO_x is stored on various forms of Ba including, BaO, $BaCO_3$ and $Ba(OH)_2$. In the presence of CO_2, the ubiquitous coombustion product, the main species present is $BaCO_3$, which leads to an increased formation of CO_2 and thus a decrease in NO_x storage.[24,29,30] When available, NO will more readily adsorb on PdO via the pathways previously described above; other studies explain the similar adsorption of NO on $BaCO_3$.[29,31] Such is the current behavior of an LNT, where many studies have been done to fine-tune engine operation for certain applications, including producing NH_3 for a downstream SCR.[17,32]

The Selective Catalyst Reduction (SCR) catalyst is one of the most widely used

systems for diesel NO_x abatement and control. Here we provide a brief overview and describe its use in combination with an upstream LNT or TWC. In addition to LNT characterization and model development, many studies have been done to fine tune engine operation for certain applications, including producing NH_3 for a downstream SCR.[17,32] In an SCR, unreacted NO_x combines with NH_3 and O_2 to form N_2 and H_2O, mainly over zeolite catalysts via three main pathways: standard (NH_3, NO and O_2); slow (NH_3 + O_2); and fast (NH_3 + NO + NO_2).[33] It is important to understand the effect of the reductant on SCR performance, as some amounts of CO, HC or H_2 will make their way into the SCR upon exiting the upstream oxidation catalyst. A recent study by Zgeng et al. concerning the effect of reductant over a Cu-chabazite SCR catalyst shows that all three of CO, H_2 and C_3H_6 promote NO_2 reduction to NO, with C_3H_6 leading to the highest increase in NO_x conversion. It was also found that there is no competition for adsorption between reductants and NH_3, which allows for effective use of an SCR even with reductant slip from the LNT.[34]

1.5 The three way NO_x storage catalyst (TWNSC)

Besides the increasingly stringent NO_x emission standards, fuel economy improvements are also a necessity. The Three Way NO_x Storage catalyst combines the functionality of a TWC (conversion of CO, HC, and NO) with that of the NO_x storage catalyst (cyclic operation to achieve high NO_x reduction). One preliminary study on using a TWC+SCR system determined that all of the NH_3 produced for the SCR is generated during the rich phase, implying the importance of finding the right balance between cycle time and conversion or selectivity.[35] A recent work by DiGiulio et al. looked at a wide range of TWC materials for the possibility of generating NH_3, a system termed passive-ammonia SCR.[36] Four catalyst systems were examined, one of which was an LNT catalyst operating as a TWC. From the results of that study, the LNT behaving as a TWC led to good performance for generating ammonia, and it was determined that adding a NO_x storage component to a TWC can lower the duration

of the rich period and increase fuel economy, akin to the goals of this work. One of the main concerns, however was the decreased conversion of CO at low catalyst temperatures, an effect that must be addressed in future studies.[36] Unlike the TWC+SCR system, the TWNSC has much more operation control in that the cycling frequencies can be tuned to obtain various optimized performance metrics. For example, in order to achieve high N_2 yields in a downstream SCR system, it is important to maximize the ratio of NH_3 in the feed composition to the amount of NO_x produced during a lean-rich cycle (ANR). By tuning the operating conditions we can maximize the ANR and other performance metrics. Through a highly systematic set of experiments, we report these findings in Chapter 3.

1.6 Lean hydrocarbon NO_x trap

The TWNSC is a promising tool for use with a downstream SCR in that it can achieve high conversion of CO, HC, and NO_x, while maintaining an overall lean enivronment in the system (i.e., a net lean feed). However, this catalyst, like the simpler TWC or LNT, is only effective at operating temperatures above 200°C. Advancements in diesel engine technology allow for leaner operation of engines at lower temperatures, which increase fuel economy. However, these conditions lead to increased NO_x emissions. Additionally, below 200°C, the engine emits high levels of unburnt HCs. Therefore we investigate the use of zeolite-based materials to design a catalyst that can trap these harmful species during cold start and release them during warm-up. In addition, this catalyst should be able to aid in oxidizing CO/HC or reducing NO_x at higher temperatures, while also being stable enough to be used over many cold start cycles. In the following subsections we address the various components of the Lean Hydrocarbon NO_x Trap (LHCNT), namely a zeolite support, a hydrocarbon trap, and a NO_x trap.

1.6.1 Introduction to zeolites

The primary support for the LHCNT is a zeolite structure, of which various types have been of interest. Zeolites have been used in many selective catalytic systems due to their well defined pore structures that enable selective adsorption of hydrocarbons, both in the liquid and gas phases.[37–42] Zeolites are nanoporous crystalline materials made of an aluminosilicate backbone. The chemical structure consists of interconnected TO_4 tetrahedra, where T is usually either Si or Al. A zeolite is defined by its three letter code (e.g., BEA, MFI, CHA) and its Si:Al ratio (SAR), which describes the acidity. The higher the SAR, the more siliceous the zeolite is, and therefore more hydrophobic. Zeolites of this type are useful for their selective uptake of molecules through Van der Waals interactions.[43] Zeolites with a lower SAR are more acidic and hydrophilic, and the high number of exchange sites allows for ion-exchange capabilities with various metals (e.g., Ag, Cu, Pd, or Na).[44] Fig. 1.3 shows the generalized aluminosilicate molecular composition of a zeolite. The location of the aluminum atom generates a Bronsted acid site (BAS), which has the ability of being protonated as shown, or exchanged with a metal ion. With the respect to the LHCNT, highly acidic (low SAR) zeolites in the form of BEA, ZSM-5 (MFI), or SSZ-13 (CHA) are of interest. Fig. 1.4 depicts the [100] projection of a 3D structure of each morphology.[45]

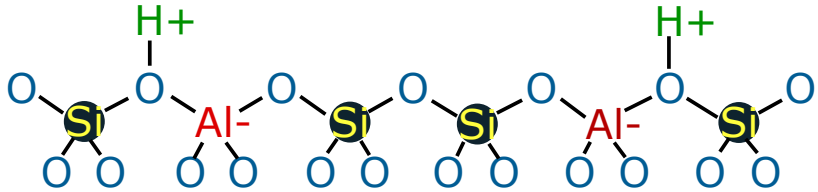

Figure 1.3: Zeolite molecular structure.

BEA zeolite is the largest of the three zeolites, comprising 12-membered rings that can trap molecules as large as tetraethylammonium.[46] The structure also contains smaller 4 and 5-member rings. The large, linear channels have a pore opening

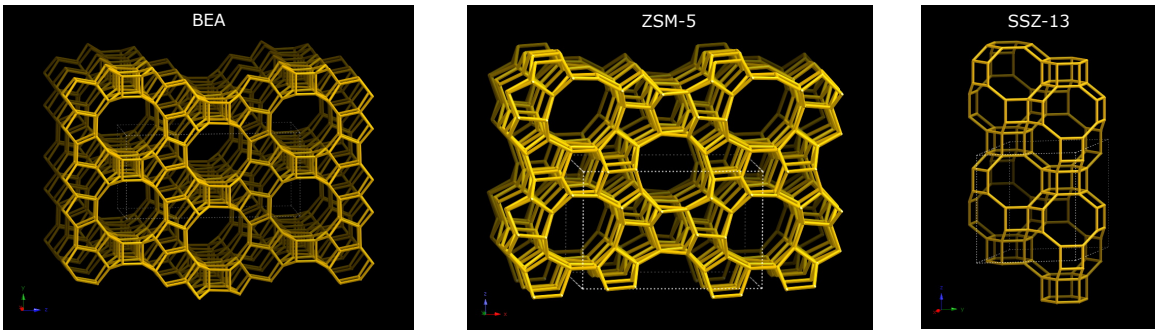

Figure 1.4: Zeolite framework images of the [100] surface for BEA, MFI, and CHA.

that is 5.7 × 7.5 Å.[46] ZSM-5 is a smaller pore zeolite than BEA, consisting of 10-membered rings composed of smaller 5-membered rings, forming a pentasil unit. Each of the vertices consists of either Al or Si, and O is bonded between them to form the rings. A series of these rings forms a straight channel with dimensions of 4.5-4.7 Å.[47] SSZ-13 has the smallest pore size compared to the other two frameworks. It consists of 8-membered rings with a pore size of only 3.8 Å.[48] Its structure can be described as a sinusoidal network of 8-membered rings. SSZ-13 is particularly useful in automotive catalysis due its high hydrothermal stability. It has been extensively studied as a support material for SCR catalysts, namely with Cu or Fe exchanged acid sites.[9,33,49–51]

1.6.2 Hydrocarbons traps

The LHCNT functions are a combination of the hydrocarbon trap (HCT) and the passive NO_x adsorber (PNA). Typical diesel engine exhaust contains small olefins (C_2-C_4), aromatics, and long-chain alkanes (C_{8+}), all of which need to be trapped during cold-start.[52] Investigation of various zeolites has led to many developments of the hydrocarbon trap. Li et al.[53] performed a series of adsorption and desorption experiments on a vareity of zeolites including H-BEA-40, H-ZSM-5, and USY, and found that the acidity of the zeolite is important for trapping small olefins. It was also found that ZSM-5 and BEA zeolites had higher desorption temperatures than the Y zeolites tested, which is beneficial in the context of cold start emissions.

In the work by Lopez et al., a number of zeolite-type materials including silicoaluminuphosphates such as SAPO-5 and SAPO-41 were investigated for their ability to trap propylene for cold start emissions.[54] It was found that BEA is ideal for trapping propylene over the other catalysts, likely because of its larger pore size. A study by Migliardini found that because of its smaller pore size compared to BEA, ZSM-5 is able to trap small olefins like ethylene, whereas large zeolites could not. The study also found a maximum in the adsorption temperature of certain hydrocarbons. For example, isobutene experiences a maximum adsorption at 413 K on HZSM-5. This is an interesting result when discussing the use of zeolites for low temperate uptake, as some materials may be better than others at various temperatures.[55]

The presence of water in the exhaust feed is unavoidable, and its effects on HCTs needs to be addressed. In a study by Otto et al., it was found that even by using a hydrophilic material such as silicalite, adsorption of hydrocarbons in the presence of water is inhibited.[56] They argue that the concentration of water in the exhaust feed is much greater than the concentration of hydrocarbons, so even if the nature of the material preferentially adsorbs the hydrocarbons, a large fraction of the total adsorption capacity will consist of water. The amount of catalyst required to adsorb enough hydrocarbon in the presence of water is therefore too large to be practical. A similar study by Burke et al. found an inhibiting effect of water on the uptake of propylene and toluene on various forms of BEA.[57] However, a recent study by Zelinsky determined that the presence of water does not impact the adsorption of larger hydrocarbons on BEA, such n-$C_{12}H_{26}$, suggesting that the size of the hydrocarbon and the mechansim of adsorption also plays a role in determining the extent of inhibition by water.[58] In the work reported in later chapters we examine the effect of water on propylene and dodecane uptake on various LHCNT materials, which leads to some promising results.

1.6.3 NO_x adsorbers

The second component of the LHCNT is the Passive NO_x Adsorber, or PNA. Like the HCT, it is designed to trap NO at low temperature and release it above 200°C to a downstream oxidation catalyst or SCR. The reactivity of NO has led to a number of findings regarding the efficacy of zeolites to adsorb NO. Recent work by Ambast et al. found that unexchanged zeolites in the absence of water adsorb very high amounts of NO (more detail in Chapters 3 and 5).[59] However in the presence of water it was found that practically all of the NO uptake was reduced to zero, suggesting complete inhibition of NO adsorption on the BAS.

In a pioneering study by Chen et al., it was found that Pd-exchanged zeolites such as BEA, MFI, and CHA adsorb NO even in the presence of water.[60] This development led to considerable interest in the automotive catalysis community, with many groups seeking to further investigate the use of these materials and to understand the uptake mechanism.[60,61] Chen et al. suggested that the main reason for NO adsorption is that highly dispersed Pd cations exchanged with the protonated acid sites of the zeolites can strongly adsorb one molecule of NO.[60] A number of studies since then suggest that the mechanism is highly complex, although it is clear that isolated Pd cations certainly improve NO uptake.[62] More details of the potential adsorption mechanistic pathways are described in Chapter 3. In contrast, agglomeration of Pd cations into PdO nanoparticles leads to a loss of NO uptake.[63] This deactivation mechanism occurs in the presence of prolonged CO exposure and in possibly more rapidly in larger pore zeolites. While CO does ultimately deactivte the catalyst, it can serve as a protective barrier towards H_2O inhibition, which can not only block adsorption on the acid sites but also on the Pd cations.[64] Some studies suggest that CO, and potentially other small reductants such as ethylene, can form a complex with NO on Pd that blocks H_2O.[65] The oxidation state of Pd is highly dependent on the zeolite framework, acidity, and pretreatment conditions, and each form of Pd can

store NO at varying bind strengths. For example, Pd in a 2+ oxidation state may exist as isolated $[Pd\text{-}OH]^+Z^-$ or as "naked" Pd in the form of Z^-PdZ^-, where Z^- represents the $[Si\text{-}O\text{-}Al]^-$ exchange site.[62] The probability of Pd occurring as the single isolated form versus the "naked" form depends on the number of available exchange sites and their proximity. In BEA for example, it is believed that isolated Pd is the primary form due to the large pores that limit the existence of nearby exchange sites. In contrast, smaller pore zeolites like SSZ-13 will form more "naked" sites due to the close proximity of the exchange sites in the small pores.[66]

The catalyst preparation method also plays a role in achieving high adsorption of NO. A recent report by Khivantsev et al. describes a new synthesis method that can achieve nearly 100% dispersion of Pd cations of up to 2 wt.% on SSZ-13.[67] In contrast, older work suggests that less than 1wt% is ideal for maximizing NO uptake and preventing deactivation.[63,68] As such, there is a significant amount of research being conducted on NO adsorption on these materials, including experimental and theoretical (DFT) work. However, the focus of this portion of the dissertation is not to investigate the details of a newly proposed reaction mechanism. Rather the aim is to characterize the performance of various LHCNT materials. In other words, materials that can not only trap NO but also HCs, and potentially oxidize them at higher temperatures. This significantly complicates the fundamental nature of the mechanism, introducing a number of coupling effects between the HCs and NO. Through a combination of experiments and modeling work in Chapters 3–5, we report the performance of both single and mixed catalsyt architectures as LHCNT materials under practical conditions.

1.7 Research objectives and outline

The overall objective of this work is to study the performance of multi-functional catalysts that can trap and convert adverse emission components including NO, CO, and HCs. First, the Three-Way NO_x Storage Catalyst is investigated with the aim

of improving fuel economy and reducing NO_x emissions while maintaining high oxidation activity of CO and HCs. Second, the use of the Lean Hydrocarbon NO_x Trap was investigated, a multi-functional material that can trap NO and HCs at low temperature and release or convert them at higher temperatures. Together, these two catalysts span a range of operating conditions of an after-treatment system, with both of the catalysts potentially serving to work in tandem with a downstream catalyst such as an SCR. Through a combination of systematic experiments and modeling work, we aim to achieve the following objectives:

1. Conduct steady state and cycling experiments on a commercially supplied TWNSC to characterize the performance in a variety of operating conditions

2. Understand details of the reaction network of the TWNSC based on experimental observations

3. Design and implement an optimization strategy of the TWNSC reactor system in order to achieve optimal conversion and yield for a specified set of operating conditions, with emphasis on NH_3 generation for use with a downstream SCR, as well as maintaining as net-lean an environment as possible

4. Investigate the use of Pd/BEA as a model LHCNT catalyst through a number of systematic adsorption and desorption experiments

5. Conduct DRIFTS measurements to identify surface species during combined exposure of NO and C_3H_6 that may elucidate part of the complex LHCNT mechanism

6. Develop a deeper understanding of the LHCNT and implement design strategies to improve performance

7. Expand on the findings of the LHCNT research by building a nonisothermal model to predict and explain the behavior of the Pd/BEA LHCNT

8. Investigate the use of potential LHCNT materials for use in a multi-component system that can further improve NO and HC uptake in the presence of H_2O

9. Determine optimal operating strategies for both dual-layered and sequential configurations of the LHCNT for use with a downstream SCR or other oxidation catalyst

Chapter 2: Steady state and lean-rich cycling of a three-way NO_x storage catalyst: experiments

The following chapter was published as Malamis, S. A.; Li, M.; Epling, W. S.; Harold, M. P. Steady state and lean-rich cycling study of a three-way NO_x storage catalyst: experiments. *Applied Catalysis B: Environmental* **2018**, *237*, 588-602.

2.1 Introduction

Consumer demand for gasoline-powered vehicles spanning passenger cars to light-duty trucks and SUVs has generally increased over the past 6 years.[69] At the same time, vehicle manufacturers must respond proactively to the increasingly stringent emission and fuel economy standards through the development of more efficient and cleaner emitting vehicles.[3] This requirement has led to increased interest in lean-burn engines, which are typically more fuel efficient than their more conventional stoichiometric counterparts. Dual mode engine operation affords a combination of lean-burn and stoichiometric combustion with transitions between each depending on driving conditions and power needs.[70] Stoichiometric gasoline vehicles are equipped with three-way catalysts (TWCs) to simultaneously eliminate CO, HCs, and NO_x. Fig. 2.1 shows the narrow air-to-fuel ratio window wherein TWCs are efficient in removing CO/hydrocarbons as well as NO_x. Outside of this window, conversion of reductants (CO, HCs) is difficult under rich conditions and conversion of NO_x is a challenge under lean conditions.[10] Fuel-lean operation results in excess (unreacted) O_2 in the exhaust gas. As a result, whereas the net oxidizing exhaust enables the straightforward oxidation of partial combustion exhaust species CO and hyd$_r$ocarbons (HCs), the catalytic reduction of NO_x (NO + NO_2) is more difficult.[71,72] Overall, TWCs are ineffective for the reduction of NO_x in diesel or lean-burn gasoline

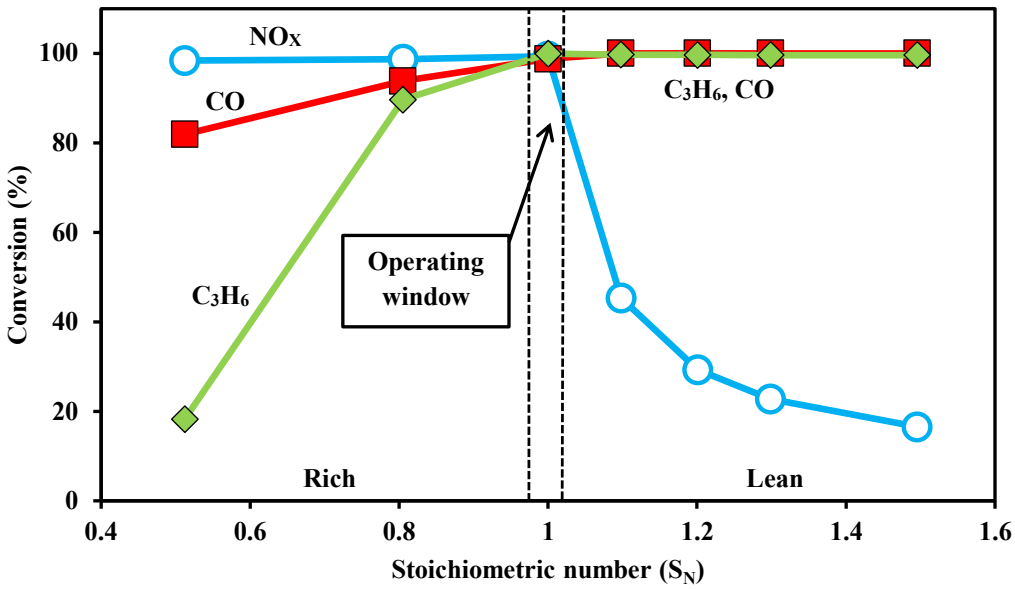

Figure 2.1: Operating a TWC to the left or right of the operating window leads to significant performance loss.

vehicle exhaust.

Considerable progress in reducing NO_x from diesel and lean burn gasoline vehicles has been made in recent years. NO_x storage and reduction (NSR) and selective catalytic reduction (SCR) catalysts have been developed and commercialized.[2] NSR is a cyclic process wherein NO_x is trapped during fuel-lean operating conditions and reduced to benign (N_2), less harmful (CO_2, N_2O), or more useful species (NH_3; see below) during a fuel-rich regeneration period.[20] Lean NO_x trap catalysts require a combination of oxidation, reduction, and NO_x storage functionalities. Precious metals provide the first two functions, while oxides of alkaline earth metals provide the latter.[21] The basic LNT material contains BaO and Pt, with the former serving as the NO_x storage material, and the latter providing catalytic sites for NO oxidation and NO_x reduction.[20,21] Many previous studies have explored the NSR mechanism through which NO_x is stored on the catalyst surface, i.e., the nitrite and nitrate routes.[23] Epling et al. provided evidence for two types of sites for NO_x adsorption, namely sites close to Pt that undergo the nitrite pathway, with subsequent oxidation

to nitrates, and sites farther away where nitrates form via disproportionation.[24] Kumar et al. showed that the two populations of sites are a manifestation of stored NO_x diffusion limitations.[18]

During the subsequent rich phase or regeneration step, the stored NO_x is released and reduced leading to the mixture of the aforementioned N-containing products N_2, N_2O and NH_3. Various studies detail the interaction between the precious metal and stored nitrates or nitrites on the surface, namely the reverse spillover process, in which "proximal" nitrates and nitrites decompose, leading to NO that is catalytically converted to N_2 on the Pt.[15,21] In addition to this chemistry, at high temperatures H_2O can react with CO or HC to form H_2, which results in higher selectivity to NH_3.[13,21,25] Furthermore, the presence of H_2 on the Pt surface during this phase leads to H_2 dissociation that can reduce nearby NO species through a "forward spillover" process.[73]

In contrast to NSR, selective catalytic reduction (SCR) requires the deliberate injection of NH_3 into or formation of NH_3 in the exhaust system; the latter is typically accomplished by the thermal conversion of aqueous urea.[74] Exhaust NO_x combines with NH_3 and O_2 to form N_2 and H_2O, mainly over zeolite catalysts via three main pathways: standard SCR (NH_3 + NO + O_2); NO_2 SCR (NH_3 + NO_2); and fast SCR (NH_3 + NO + NO_2).

In recent years there has been increased interest in combining NSR and SCR technologies.[32,75] One such application involves designing the NSR catalyst to generate NH_3 for a downstream SCR catalyst.[32] The main advantage of this approach is that an external source of NH_3 is not needed, while the main disadvantage is that periodic operation is required. One of the key metrics used to understand and optimize SCR behavior is the ratio of NH_3 produced to NO_x slipped from the upstream NSR catalyst (Ammonia-to-NO_x ratio, ANR).[19,32,74,76]

To remove NO_x from the exhaust gas and still operate the engine with a higher

air to fuel ratio than the TWC, the concept of combining the TWC with NO_x storage functionality was first proposed by Ikeda et al. as the three-way NO_x storage and reduction catalyst (TWNSC).[77] While the TWNSC is generally applied to lean gasoline engine emission control, it serves a similar role as that of the sequence of the diesel oxidation catalyst (DOC) + LNT encountered in diesel emission control. Unlike the DOC + LNT, which operates with sustained lean-rich cycling, the TWNSC serves to trap NO_x during the lean acceleration modes and to regenerate during coast/deceleration modes of engine operation. The challenge is to achieve a balance between the two catalyst functionalities while saving space and cost. As one might expect, there are many parameters involved in achieving or even optimizing this balance, such as the total cycle time, the fraction of the cycle that the engine is in regeneration mode, etc.[21] Performance metrics would certainly include conversion of NO_x, CO, and HC, and the selectivity to N_2, N_2O, and NH_3.

Recent experimental studies provide important insight about the modified TWC. The study by Theis et al. of a TWC+SCR system showed that all of the NH_3 was produced during the rich phase, implying the importance of finding the right balance between cycle time and conversion or selectivity.[35] DiGiulio et al. characterized different TWCs and their comparative abilities in generating NH_3 for use in a downstream SCR, a system referred to as passive-ammonia SCR.[36] In their work, four catalyst systems were examined, one of which was an NSR catalyst operating as a TWC. The study showed that the periodic operation expectedly generates NH_3 and the addition of a NO_x storage component to a TWC lowers the required duration of the rich period while increasing the fuel economy. One of the main drawbacks is the decreased CO conversion at low catalyst temperatures; an effect that must be addressed in future studies.[36]

The objective of this study is to systematically evaluate the performance of a commercial TWNSC under a range of cycling protocols. Specific attention is placed

on the impacts of operating parameters on conversion and product distribution. The data are interpreted in terms of the anticipated application, be it a standalone unit intended to maximize the NO_x conversion and N_2 selectivity or a TWNSC + SCR tandem unit in which the intent is to shift up to half of the NO_x conversion to the downstream SCR. Conditions are identified that lead to the best performance for each application. Where possible, the performance trends are interpreted from the standpoint of known TWC and NSR features. The TWNSC is meant to operate once the vehicle has warmed up to allow sufficient activity of the emission catalyst. In principle, the TWNSC could be modified to enable low temperature HC and NO_x trapping. While not a focus of the current study, similar catalytic objectives are discussed in later chapters.

2.2 Experimental

2.2.1 TWNSC experimental setup

Both steady state and cycling experiments for the TWNSC work were conducted in a horizontal quartz tube reactor equipped with MKS mass flow controllers capable of flowing Ar, CO_2, Kr, CO, NO, C_3H_6, H_2, and NO. The feed streams to the reactor tube consist of a main stream, used for CO_2 and Ar, and two additional streams, one rich and one lean. The lean stream represents the oxygenated feed and contains lean species such as NO and O_2, while the rich stream contains all of the reductants including CO, C_3H_6 and H_2. The flow between the lean and rich streams is controlled by an electromagnetic 4-way actuator valve connected to the LabView software. A fourth stream containing carrier Ar and H_2O, vaporized through heated lines and pumped into the system using an ISCO pump, is located near the inlet of the reactor. All of the lines were subsequently wrapped with heating tape and maintained at 180°C throughout operation to prevent condensation.

Data analysis was conducted using a Fisher-Scientific (Thermo-Nicolet) FT-IR

that analyzed the concentration of the effluent. Three type K thermocouples were used to monitor the temperatures within the system. One was placed 0.5 cm upstream of the catalyst (T_{inlet}); one was placed in the radial and axial center of the catalyst (T_{cat}); and one was placed 0.5 cm downstream (T_{out}). Before starting any experiments, all mass flow controllers were calibrated for accurate flow rate agreement between the LabView software and the MFCs. FT-IR data was processed using OMNIC software. All of the potential species to be analyzed by the FT-IR were calibrated and correction factors where obtained for a practical range of concentrations for use in data handling, which was practiced using a combination of Microsoft Excel® and MATLAB. This reactor is also equipped with a Hiden Spaci MS for obtaining spatio-temporal analyses of the monolith catalyst, some experiments of which were conducted by Li et al.[76] The reactor system was also equipped with a mass spectrometer (Hiden Analytic Ltd., HPR-20), which was used to measure effluent N_2 and H_2 concentrations for some LHCNT experiments. Figure 2.2 provides a more detailed view of the reactor system.

2.2.2 Catalyst characterization

The commercial TWNSC used in this work was received from Fiat Chrysler Automobiles LLC. (FCA). The commercially supplied catalyst is a mixed catalyst containing precious group metals (PGM) comprising a mixture of TWC and LNT components such as barium oxide (for NO_x storage), ceria (for O_2 storage), and alumina (binder, support). Table 2.1 provides the ICP-measured mass percentages of the oxide components (Ba, Ce, Al, La, and Zr). The precious group metal mass percentage was 1.2 wt.% in a Pd:Pt:Rh ratio of 73:26:1. Samples were cut from a monolith "brick" to 1 cm in diameter and 1.8 cm long. CO chemisorption using a Micromeritics apparatus gave a PGM metal dispersion of 40% for a fresh sample, before degreening. Because the ratio of Pd:Pt:Rh in the sample is known, an average value for the stoichiometry factor was determined in order to calculate the dispersion, which in this case is one.

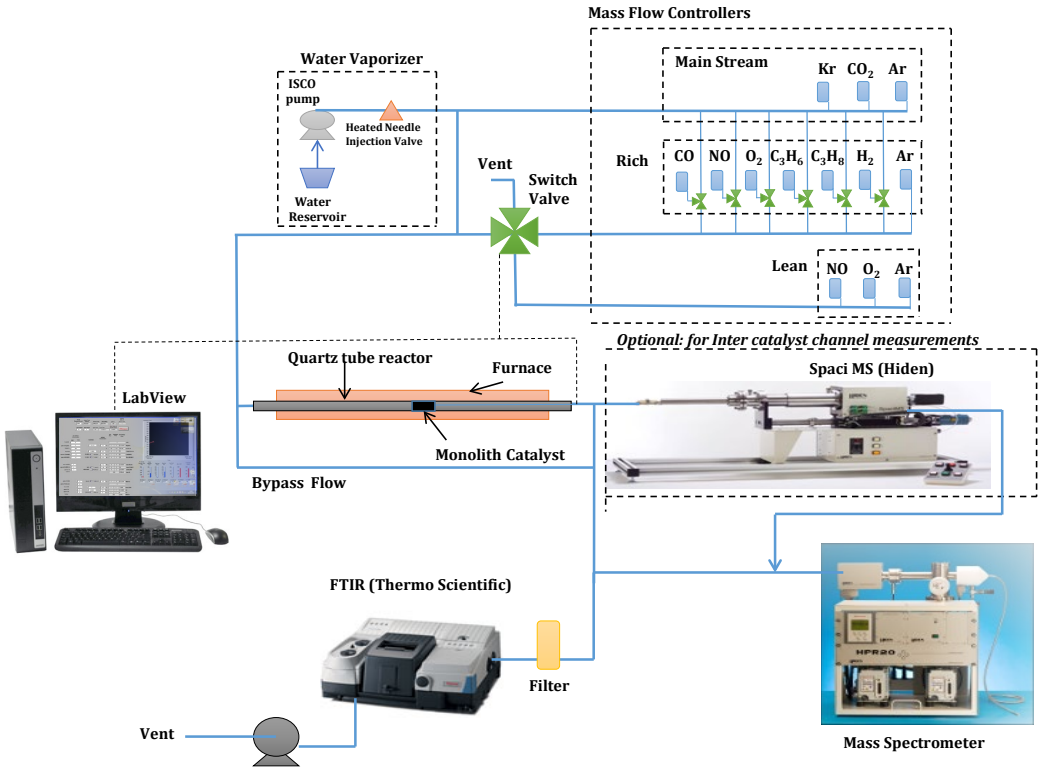

Figure 2.2: TWNSC reactor setup.

Table 2.1: Mass percentages of the washcoat oxide components measured by ICP.

Element	Al	Ba	Ce	La	Pt+ Pd + Rh	Zr
wt.%	19.3%	4.7%	9.96%	1.22%	1.16%	8.92%

2.2.3 Operating conditions

One sample was used for all experiments conducted in this work. The sample was degreened at 700°C for 4h in 10% H_2O and 10% CO_2 with a balance of Ar. The sample was then wrapped in ceramic paper and placed in the horizontal-flow quartz tube reactor described above. The total flow rate and space velocity for the system were kept constant at 3000 sccm (standard cm^3/min), which corresponds to a gas hourly space velocity at standard conditions of 99,000 h^{-1}. Inlet and outlet lines were maintained at 180°C to prevent condensation. T_{feed} and T_{cat} were primarily used as the reference temperatures for the experiments in this work.

2.2.4 Steady state experiments

For the steady state experiments, the catalyst was first pretreated with 5% O_2, 10% CO_2, and 7% H_2O at 500°C for 20 min. After the pretreatment, the reactor was purged for 10 min with Ar and cooled to the desired feed temperature, during which time a steady flow of feed gases was established through the bypass. Once the reactor temperature was stable, the flow was switched from the bypass to the reactor and the effluent concentrations were monitored until steady concentrations (± 2%) were obtained over a 10 min period. The desired feed temperature was achieved by adjustment of the furnace temperature.

2.2.5 NO_x storage experiments

NO_x storage experiments were conducted in the same quartz tube reactor. First, the catalyst was pretreated in a feed of 2% H_2 at the feed temperature for 30 min, after which the catalyst was purged under Ar for 10 min. During adsorption, a feed containing 500ppm NO and 5% O_2 was introduced to the catalyst until the output concentration reached steady state (i.e., site saturation). The NO/O_2 mixture was then turned off and the catalyst was held at the adsorption temperature until the outlet concentration of NO_x reached zero, eliminating any weakly adsorbed NO_x from the surface. Then the catalyst underwent a temperature-programmed desorption under Ar at a rate of 10°C/min up to 600°C. This procedure was repeated for a variety of feed temperatures ranging from 130 to 415 °C.

2.2.6 Lean-rich cycling experiments

In this work, the stoichiometric number is used to characterize the feed composition, defined by

$$S_N = \frac{2C_{O_2} + C_{NO}}{C_{CO} + C_{H_2} + 9C_{C_3H_6}}. \tag{2.1}$$

S_N measures the deviation of the catalyst environment from a stoichiometric neutral feed (S_N =1). Unless otherwise specified, the feed composition consisted of 1% CO,

3300 ppm H_2, 500 ppm NO, 10% CO_2, 7% H_2O, and a variable concentration of O_2 to achieve a prescribed S_N. When C_3H_6 was used its concentration was 1000 ppm. The balance of all mixtures was Ar in order to maintain a constant total feed flowrate or space velocity.

For the cycling experiments, the same pretreatment was used, followed by a 10 min Ar purge. Instead of establishing a steady flow through the bypass, a steady cycling rate through the bypass was obtained. A pseudo steady state was defined by an unchanging effluent temporal profile for at least 5 cycles. Once the feed was established and the reactor temperature stabilized, the flow was switched to the reactor tube and effluent concentrations were measured until 10 repeatable cycles were obtained. The feed system enables precise control of the rich and lean feeds to as short as a 1s duration. In this study, typical total cycle times τ_T, were in the range of 20 to 60 s with rich duty fractions, d_r, between 0.05 and 0.7, defined by

$$\tau_{\mathrm{T}} = \tau_r + \tau_\ell \tag{2.2}$$

and

$$\mathrm{d_i} = \frac{\tau_{\mathrm{i}}}{\tau_{\mathrm{T}}} \quad \mathrm{i} = \mathrm{r}, \ell. \tag{2.3}$$

Details of more complex cycling experiments are described later in the Results and Discussion section.

2.2.7 Performance metrics

Several performance metrics were defined and calculated, including reactant conversion, selectivity, and yield. The cyclic values were time integrated over at least 5 cycles, yielding a cycle-averaged value. The cycle-averaged NO_x conversion is defined as

$$X_{NO_x} = \frac{\int C_{NO_{x_{in}}} - \int C_{NO_{x_{out}}}}{\int C_{NO_{x_{in}}}}, \tag{2.4}$$

with the NO_x concentration equal to the sum of NO and NO_2. The cycle-averaged CO conversion is similarly defined as

$$X_{CO} = \frac{\int C_{CO_{in}} - \int C_{CO_{out}}}{\int C_{CO_{in}}}. \tag{2.5}$$

A similar equation was used to calculate the conversion of C_3H_6. The corresponding steady state quantities were obtained using standard definitions. The cycle-averaged selectivity of the N-containing product is given by

$$S_{N_{\text{species}}} = \frac{\alpha \int C_{Nspecies,out}}{\int C_{NO_x,reacted}}, \tag{2.6}$$

where α represents the molar coefficient of the species (α = 1 for NO, NO_2 and NH_3; α = 2 for N_2O). The N_2 selectivity was calculated by difference of the other species selectivities. The NH_3 yield is defined by

$$Y_{NH_3} = \frac{\int C_{NH_{3_{out}}}}{\int C_{NO_{x_{in}}}}. \tag{2.7}$$

In addition to conversion and selectivity, the cycle-averaged temperature was determined using a similar time-integrated method. Finally, the ratio of ammonia produced to NO_x slip (ANR) is defined by

$$ANR = \frac{\int C_{NH_{3_{out}}}}{\int C_{NO_{x_{out}}}}. \tag{2.8}$$

Finally, the lean NO_x storage efficiency, η_ℓ, is the fraction of NO_x stored during the lean phase of duration τ_ℓ, calculated as

$$\eta_\ell = \frac{C_{NOin} * \tau_\ell - \int C_{NOx_{out}} d\tau_\ell}{C_{NO_{in}} * \tau_\ell} * 100. \tag{2.9}$$

2.3 Results and discussion

2.3.1 Steady state catalyst performance

A series of steady state experiments was used to characterize the TWNSC activity and performance over a range of feed temperatures and compositions spanning lean to rich as described above in the Experimental section.

The steady state NH_3, CO, NO_x, and N_2O effluent concentrations under various lean or rich feed conditions at a fixed feed temperature of 270°C are shown in Fig. 2.3. The figure also reports the mid-core temperature rise, measured as the difference between mid-catalyst temperature and feed temperature, $T_{cat} - T_{feed}$. The inset shows an expanded view of the $0.85 < S_N < 1.15$ range, and also includes concentrations of individual NO_x components NO and NO_2. The stoichiometric condition ($S_N = 1$) is the demarcation between the lean and rich feeds. At $S_N = 1$ the reacting species concentrations approach zero, as expected.

To the left of the neutral feed is the rich regime ($S_N < 1$). As S_N decreases from unity, the NH_3 concentration increases, the CO and C_3H_6 concentrations increase (conversions decrease), and the NO_x concentration approaches zero (complete NO_x conversion). In an O_2 deficient condition the NO_x is reduced to either N_2 or NH_3 with negligible production of N_2O. The increasing levels of CO and C_3H_6 with decreasing S_N result in a shift to NH_3 as the main N-containing product. Global chemical reactions that occur under rich conditions include NO reduction by the reductants, as shown in the following:

$$NO + H_2 \rightarrow 0.5N_2 + H_2O, \tag{2.10}$$

$$NO + 2.5H_2 \rightarrow NH_3 + H_2O, \tag{2.11}$$

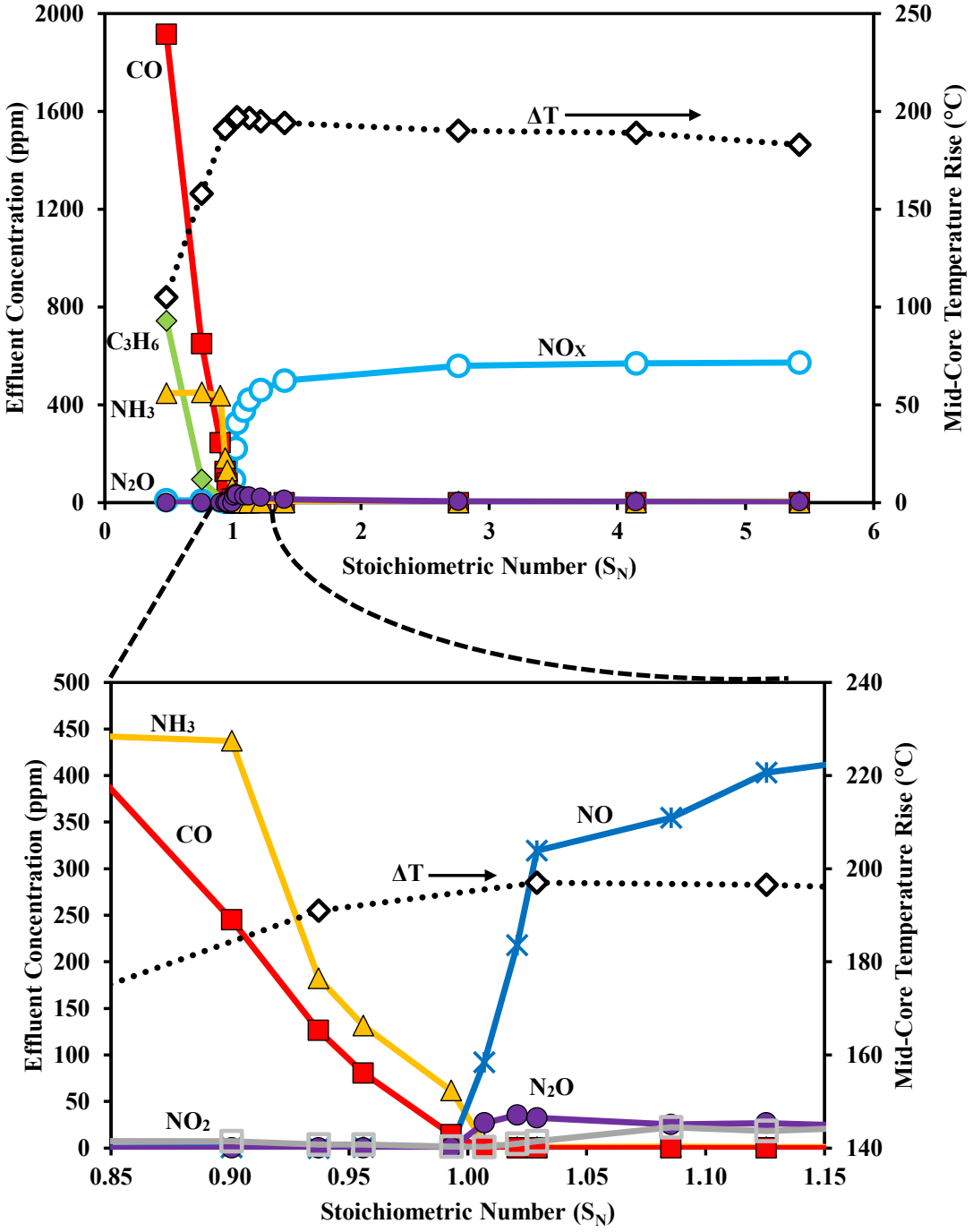

Figure 2.3: Effluent concentrations of NH_3, CO, C_3H_6, NO_x (NO + NO_2), and N_2O and catalyst temperature rise (°C) vs. S_N. T_{feed}=270°C. 1% CO, 500ppm NO, 1000ppm C_3H_6, 3300ppm H_2, 7% H_2O, 10% CO_2, varied O_2.

and

$$NO + CO \rightarrow 0.5N_2 + CO_2. \tag{2.12}$$

Under rich conditions both complete and partial oxidation reactions may occur, as shown in the following set of reactions:

$$CO + 0.5O_2 \rightarrow CO_2, \tag{2.13}$$

$$H_2 + 0.5O_2 \rightarrow H_2O, \tag{2.14}$$

$$NH_3 + 0.75O_2 \rightarrow 0.5N_2 + 1.5H_2O, \tag{2.15}$$

$$C_3H_6 + 4.5O_2 \rightarrow 3CO_2 + 3H_2O, \tag{2.16}$$

and

$$C_3H_6 + 3O_2 \rightarrow 3CO + 3H_2O. \tag{2.17}$$

Additionally, reactions involving H_2O as a reactant include water gas shift,

$$CO + H_2O \leftrightarrow CO_2 + H_2, \tag{2.18}$$

and steam reforming,

$$C_3H_6 + 6H_2O \leftrightarrow 3CO_2 + 9H_2. \tag{2.19}$$

To the right of the stoichiometric condition is the lean regime ($S_N > 1$). The global reactions occurring under the stoichiometric excess are expectedly oxidation of the various species, including the previously identified total oxidation reactions (eqs. 2.13–2.16). Other oxidation reactions that can occur include NH_3 oxidation to N_2O,

$$NH_3 + O_2 \rightarrow 0.5N_2O + 1.5H_2O \tag{2.20}$$

and to NO,

$$NH_3 + 1.25O_2 \rightarrow NO + 1.5H_2O, \tag{2.21}$$

plus oxidation of NO to NO_2, expressed as

$$NO + 0.5O_2 \leftrightarrow NO_2. \tag{2.22}$$

The distribution of nitrogen oxides depends on the temperature and O_2 concentration, among other factors.[19] For this set of conditions, NO oxidation to NO_2 in the range of $1.0 < S_N < 1.5$ is minimal. The low NO_2 concentration is in part a result of its high reactivity as an oxidant. Reaction may also occur between NH_3 and NO especially near the stoichiometric point. As S_N increases from unity, very little NH_3, CO, and C_3H_6 are detected due to their respective oxidations, while a low but nonzero N_2O concentration is observed, as well as a shallow N_2O maximum at S_N ~1.02, before decreasing towards zero for $S_N > 1.5$. NO_x concentrations increase sharply with increasing S_N, approaching the feed value of 500 ppm by S_N ~2. The inset reveals that in a slight excess of O_2 (S_N ~1.01) all of the reductants are oxidized, as expected. The negligible but non-zero N_2O level for higher S_N is attributed to the presence of NO and O_2 in the gas phase.[78] Under these slightly lean steady state conditions, the precious metal sites are occupied by an admixture of O, NO and N species. N_2O can form through the reaction[79]

$$N - Pt + NO - Pt \rightarrow N_2O + 2Pt. \tag{2.23}$$

The N_2O maximum reflects adsorbed O_2 inhibition of NO sorption and reaction. At sufficiently large S_N the inhibition is sufficient so as to prevent N_2O formation.

The catalyst temperature rise reaches a maximum of ~200°C near $S_N = 1$. The maximum is attributed to the complete conversion of the reductants which results

in the highest exotherm. With the temperature rise as a measure of the aggregate conversions of the reactants, it follows that full conversion of all species leads to the highest temperature rise. The slight decrease with increasing S_N beyond 1 is due to the non-adiabatic nature of the reactor. With increasing S_N, the oxidation reactions occur at higher rates, and thus became more localized toward the upstream portion of the catalyst. As the reactions occur more in the upstream portion, some heat loss can occur downstream.

Fig. 2.4 shows the conversions and selectivities of the reacting and product species over a range of feed temperatures for a slightly lean, almost stoichiometric feed (S_N = 1.01). The NO_x, C_3H_6, and CO conversions are shown in Fig. 2.4a, while the selectivities to N_2O, NH_3, and N_2 (by difference) are shown in Fig. 2.4b. As the feed temperature increases from ~150 to 200 °C, the CO and C_3H_6 conversions sharply increase to 100%. In contrast, the NO_x conversion reaches a 60% maximum at 275°C before decreasing to 35% at 500°C. The NO_x conversion maximum is attributed to the competing effects of adsorption, desorption, and reaction. At low temperature, CO and NO are not converted due to self-inhibition.[80] As the temperature increases, surface reactions commence, including CO and C_3H_6 oxidation, as well as NO_x conversion to N_2O and N_2. The abrupt increase in conversion of CO and C_3H_6 is indicative of a reduction in CO coverage due to CO desorption, freeing up sites for oxidation. At sufficiently high temperature an increased rate of NO desorption leads to a decline in NO_x conversion. The decreasing N_2O selectivity (Fig. 2.4b) is due in part to a declining availability of NO due to the increasing NO desorption rate. That N_2O is highest at low temperature is a result of the lower rate of N-O bond scission, making NO available to react through N-NO (rxn. 2.23) or NO-NO coupling[81] as

$$NO - Pt + NO - Pt \rightarrow N_2O + Pt - O + Pt. \tag{2.24}$$

N_2O formation sharply decreases at higher temperatures due to the increased selectivity to N_2, a result of an increased rate of N-O bond scission at higher temperatures, minimizing the presence of NO available for N-NO coupling, and yielding N-N coupling instead.

Finally, NH_3 formation is favored under rich conditions, which for S_N = 1.01 (slightly lean) is negligible.[82] The observed small but nonzero NH_3 selectivity at 150°C is attributed to low temperature formation of NH_3 via H_2, even though the feed is slightly lean. It was previously shown that H_2 reacts readily with NO to form a mixture of N_2O, N_2, and NH_3 on Pt at low temperature and anaerobic conditions.[83] In the presence of a slight excess of O_2 there is competition between O_2 and NO to oxidize H_2, leading to the negligible but nonzero formation of NH_3. That is, H_2 oxidation by O_2 is slower than by NO at low temperatures.

2.3.2 NO_x storage evaluation

In order to evaluate the ability for the TWNSC to store NO_x during the lean phase, a series of experiments was conducted at a variety of feed temperatures in which 500ppm NO and 2% O_2 were fed over the catalyst. The results of this experiment are shown in Fig. 2.5, which plots the average amount of total NO_x adsorbed and desorbed vs. feed temperature. Because the adsorption experiment was conducted until the catalyst reached saturation of NO_x, the values in Fig. 2.5 represent the total NO_x storage capacity of the TWNSC at a given feed temperature. The error between the calculated amount of adsorbed and desorbed NO_x is less than 10% in most cases, closing the mass balance between the two measurements. Note that the adsorption capacity of the TWNSC is bimodal in that there are two local adsorption maxima, consistent with earlier studies of lean NO_x trap adsorption behavior.[17] This type of behavior suggests storage on two types of sites, namely BaO and alumina. Note also that H_2O is not present in these experiments, which leads to a significant increase in NO_x storage performance when compared to cycling data that contains

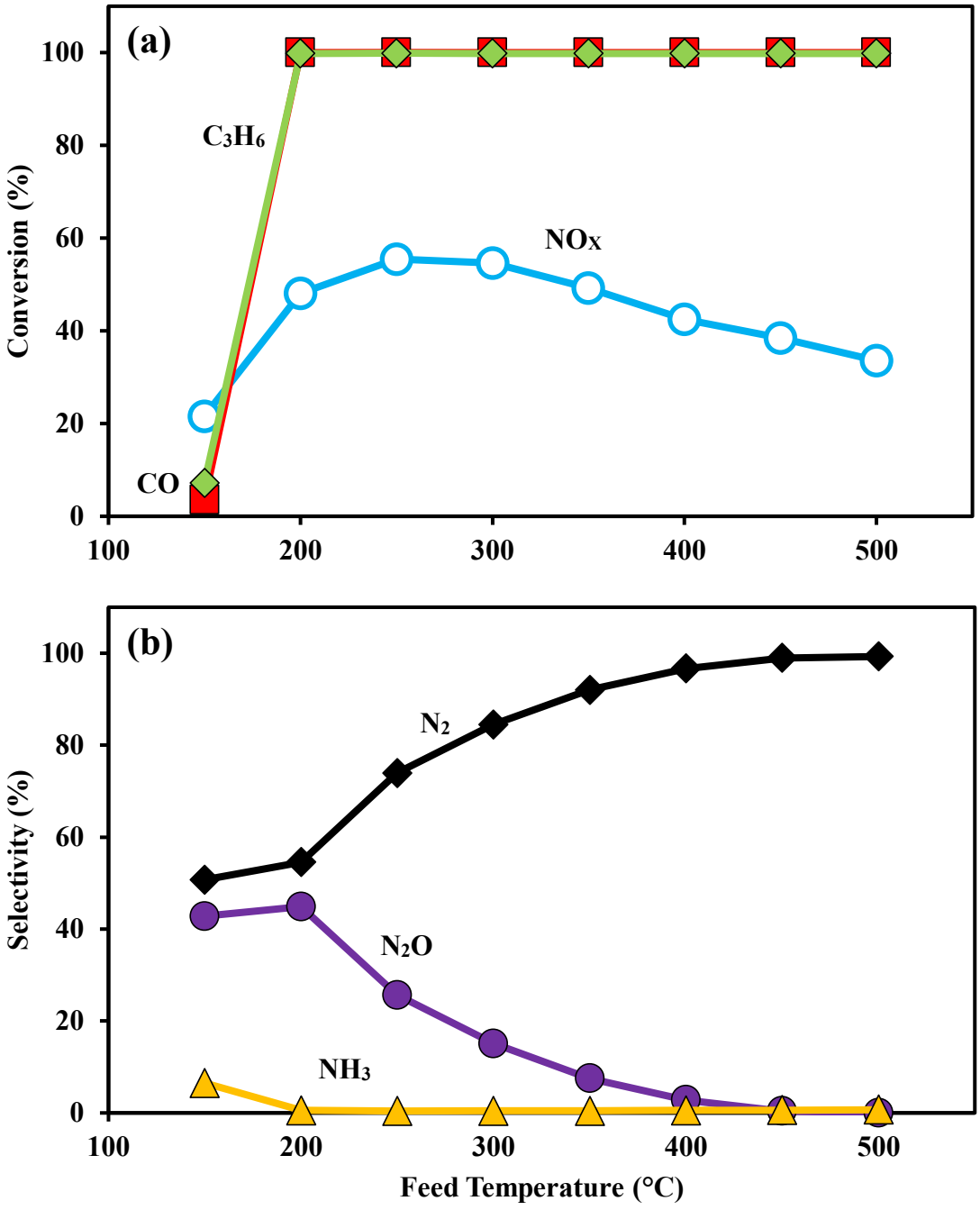

Figure 2.4: Steady state (a) CO, NO_x, and C_3H_6 conversion and (b) N_2, N_2O and NH_3 selectivity vs. feed temperature. S_N=1.01. Feed: 1% CO, 500ppm NO, 1000ppm C_3H_6, 3300ppm H_2, 7% H_2O, 10% CO_2, 1.08% O_2.

the full simulated exhaust feed.

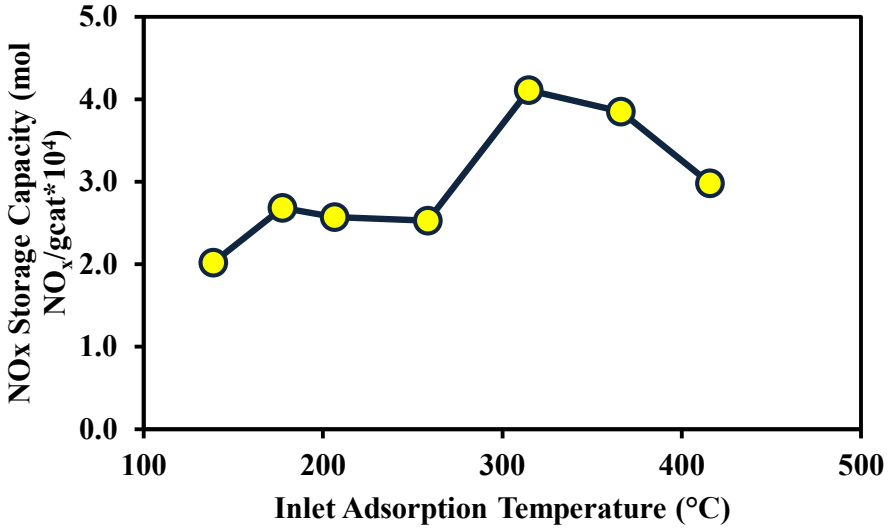

Figure 2.5: Total storage capacity of TWNSC. Catalyst was pre-reduced at the inlet temperature using 2% H_2/Ar. During adsorption, feed consisted of 500ppm NO in 5% O_2, and during desorption the feed contained only Ar.

2.3.3 Lean-rich cycling experiments overview

For application in lean combustion exhaust, the transient and cyclic performance of the TWNSC is critical since NO_x trapping during lean periods and reduction during rich periods must be effective. With cyclic operation, several additional operating parameters present both a challenge and opportunity for optimizing TWNSC performance. In the next several sections the impacts of these parameters on catalyst performance are evaluated. The operating parameters that are varied include the rich time (τ_r), lean time (τ_ℓ), and total cycle time (eqns. 2.2 and 2.3). It is convenient to define lean and rich stoichiometric numbers ($S_{N,\ell}$; $S_{N,r}$), thereby defining a cycle-averaged stoichiometric number ($S_{N,avg} = (1–d_r)S_{N,\ell} + d_r S_{N,r}$), which will influence performance. To achieve a prescribed $S_{N,r}$ the rich phase composition is adjusted through the reductant and O_2 concentrations. Finally, there are additional parameters including the feed temperature (T_{feed}) and total flowrate, which are discussed as well.

2.3.4 Baseline cyclic performance

Typical transient cycling data are shown in Fig. 2.6 for a feed when the temperature (T_{feed}) is fixed at 270°C and lean and rich times are fixed at 25s [τ_T = 50 s, d_r = τ_r/τ_T = 0.5]. The feed gas contains 500 ppm NO, 1% CO, 3300 ppm H_2, 7% H_2O, and 10% CO_2 with O_2 switched between 5% during the lean and 0.3% during the rich. These concentrations give $S_{N,\ell}$ = 7.55 and $S_{N,r}$ = 0.45 and a cycle-averaged value of $S_{N,avg}$ = 4.03, which is a net-lean feed.

During the lean phase of the cycle, 80% of the feed NO is trapped on the catalyst based on an analysis of the transient NO_x data shown in Fig. 2.6a. There is a short period of duration of ~3 s during which no NO_x is observed. This is followed by breakthrough and a monotonic increase in NO_x concentration up to the start of the rich phase, indicating storage of NO_x throughout the lean cycle. These trends are similar to those reported for the typical storage phase of a lean NO_x trap.[20] During the lean phase, NH_3 and CO concentrations drop to zero with the NH_3 concentration tail more protracted than CO. The NH_3 tail is due in part to the propensity of NH_3 to adhere to surfaces, delaying its decrease to zero.[84] This effect was confirmed with a blank tube experiment (data not shown here). It is also noted that with the large excess of O_2 during the lean phase, NO storage generally occurs through its oxidation to NO_2 which stores on trapping sites. The presence of NO_2 and lack of N_2O during the lean cycle affirms this. Fig. 2.6b shows the transient profile of the NO_x components, NO and NO_2. At the start of the lean phase, there is a slight decrease in NO_2 concentration, due to lean storage of some residual NO_2 present at the end of the rich phase, followed by a minimum before its breakthrough. The NO_2 breakthrough is delayed relative to that of NO. We attribute this to the balance between the rates of NO oxidation to NO_2, the rate of adsorption, and the sustained feed of NO.[84,85]

NO_2 is more readily adsorbed than NO, as has also been shown for lean NO_x traps.[21] Once NO breakthrough is observed, NO_2, formed through NO oxidation,

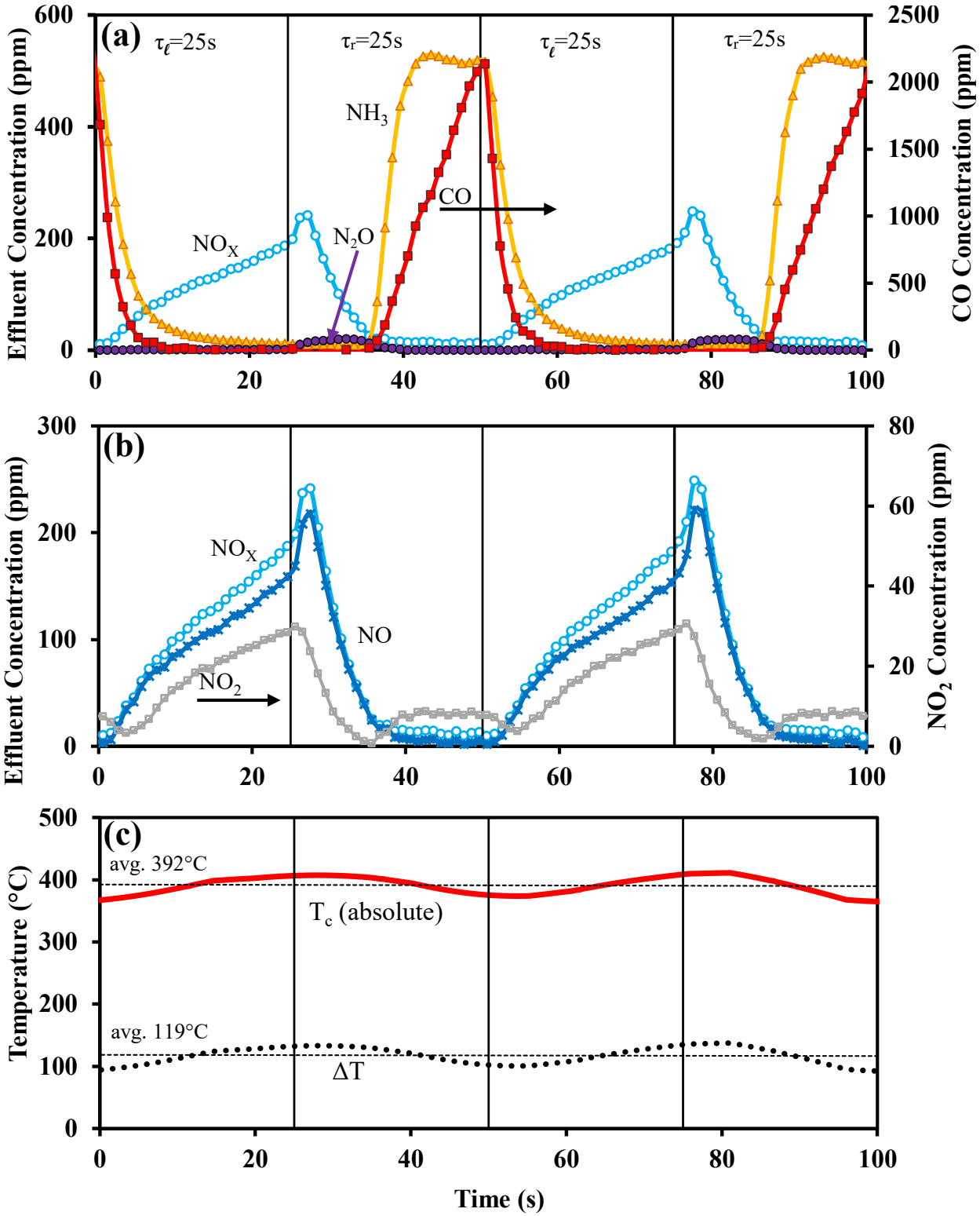

Figure 2.6: (a) Effluent concentration of NO_x, NH_3, CO, N_2O. (b) NO_x profile (NO + NO_2). (c) T_{cat} and ΔT. T_{feed}=270°C. Lean feed ($S_{N,\ell}$ =7.55): 500ppm NO, 1% CO, 3300ppm H_2, 7% H_2O, 10% CO_2, 5% O_2. Rich feed ($S_{N,r}$ =0.45): 500ppm NO, 1% CO, 3300ppm H_2, 7% H_2O, 10% CO_2, 0.3% O_2.

continues to adsorb. As the storage sites become saturated, NO oxidation continues and NO_2 breakthrough occurs throughout the remainder of the lean cycle. During this period O_2 is also stored on the catalyst, both on the precious metal crystallites and on/in the ceria phase.

During the rich phase of the cycle the formation of NH_3, N_2O, and N_2 involves complex chemistry that depends on many variables including the local catalyst temperature, the relative supply of the various reacting species, and the O_2 coverage on the precious metal crystallites, among other factors.[17] The transient data have three notable features.

First, just after the switch to the rich phase there is a brief increase in the NO_x concentration, akin to the "NO_x puff" encountered during regeneration of stored NO_x on the LNT catalyst.[31] In NSR studies the NO_x puff is attributed to the difference between the rate of stored nitrite/nitrate decomposition leading to NO_x release and the rate of NO_x reduction.[23,31] As regeneration proceeds, less NO_x is released, allowing the reduction rate to exceed the release rate leading to the eventual decrease in NO_x concentration. A vanishing NO_x concentration means that its reduction rate is high relative to the release rate. In some NSR studies the NO_x concentration during the puff may exceed the feed NO_x concentration value as the accumulated stored NO_x desorbs rapidly and with its sustained feed leads to this short-lived additive effect.[31]

Second, at about the same time that the NO_x concentration approaches zero, both NH_3 and CO breakthrough are observed. The NH_3 originates from the reduction of both feed NO and NO_x stored during the previous lean phase. NH_3 formation behaves as expected during the rich phase, consistent with the steady state and other experiments.[86] The delay in the breakthrough of NH_3 and CO is attributed to their reactions with O_2 and NO_x stored downstream on the ceria and barium components.[17] While there is O_2 in the rich phase inlet gas (0.3%), it is mostly consumed in the net rich environment ($S_{N,r}$ = 0.45). O_2 is stored on the catalyst, most notably

on the ceria phase, and is consumed by the feed reductant and the formed NH_3. Production of NH_3 via H_2 or CO takes place once the Pt surface is fully reduced and less O and NO is available.[17,87] Eventually the surface O is consumed through oxidation of the incoming reductants, and at that point reductant breakthrough is observed. During this period there is a small increase in NO_2, indicating equilibrium between NO on the surface being reduced or decomposing to form N and O adatoms that could partially form NO_2. This process evolves spatially; consumption of stored O_2 occurs upstream and moves through the monolith. NH_3 is generated in the O_2-deficient zone and moves closely behind the CO and H_2 reductant front, and, like H_2, will readily react with stored O_2 (on the ceria phase) and stored NO_x (on the barium and ceria phases).[17]

The third feature is the small but detectable formation of N_2O evident early in the rich phase, followed by its decrease to zero. N_2O is formed due to NO bond scission, generating N adatoms which react with the NO released at the commencement of the regeneration (rxns. 2.23 and 2.24). Another route is from the reaction between NH_3 formed upstream and NO_x stored downstream.[17] These data do not show evidence for a second peak which has been reported during NSR studies.[87]

The temperature profile for the previously discussed lean and rich cycles is shown in Fig. 2.6c. As expected, during the lean phase in which combustion of hydrocarbons occurs, there is an increase in the catalyst temperature, peaking at 130°C relative to the feed temperature. This value corresponds to a peak absolute catalyst temperature of 405°C. After transitioning to the rich phase, the temperature starts to $d_r$op since the large exotherms from combustion are not present. Using this data, a cycle-averaged feed temperature and temperature rise can be calculated.

2.3.5 Impact of rich injection intensity

A series of experiments was conducted in which the total amount (volume) of reductant was fixed, while the time over which the reductant was injected was varied.

Of interest is whether the reductant injection strategy provides an opportunity to optimize the NO_x conversion in the case of the standalone TWNSC or the NO_x conversion and NH_3 selectivity for the TWNSC + SCR system. In a previous LNT study, Kabin et al.[16] varied the rich phase intensity using C_3H_6 as reductant. More recently Shakya et al. examined the effect of H_2 reductant intensity during NO_x storage and reduction on a Pt/BaO NSR monolith catalyst.[88]

Fig. 2.7 shows the cycle-averaged results in which the rich duty percentage (100*d_r) varies over a 5 to 70 % range for five different feeds during a cycle having a fixed lean duration of τ_ℓ = 40s. The rich time (τ_r) and rich reductant feed volume fraction (C_r, %vol.) was adjusted to maintain a fixed volume of reductant ($V_r = V_{CO} + H_2$ = constant; CO/H_2 = 3) according to

$$C_r = \frac{100 V_r}{d_r \tau_T Q_T}, \tag{2.25}$$

where V_r is the volume of reductant (CO + H_2 in standard cm^3, or scc), d_r is the duty fraction of the rich phase, τ_T is the total cycle time (s), and Q_T is the standard volumetric flow rate of the feed (scc/s); V_r and Q_T are evaluated at standard conditions. Table 2.2 summarizes the feed parameters for each of the five feeds. For four of the Feeds (I, II, III, IV) the fixed reductant amount is 20 scc while for Feed V the fixed amount is 10 scc. The fixed amount (10 or 20 scc) was varied to access a wider range of rich duty fraction values (for fixed C_r). The volumetric concentration of O_2 in the rich feed was fixed at three different levels, 0, 0.27, and 0.53 %. Feeds IV and V represent the case in which the O_2 is varied tightly around the stoichiometric point; i.e., 0.8% O_2 during the lean phase ($S_{N,\ell}$ = 1.24) and 0.53% during the rich phase. The feed temperature was fixed at 270°C for four of the five Feeds (I, II, IV, V) and at 470°C for Feed III.

Figs. 2.7a and 2.7b show the rich phase stoichiometric number ($S_{N,r}$) and cycle-averaged NO_x conversion as a function of rich duty percentage, $100 \times d_r = 100 \times \tau_r / \tau_T$.

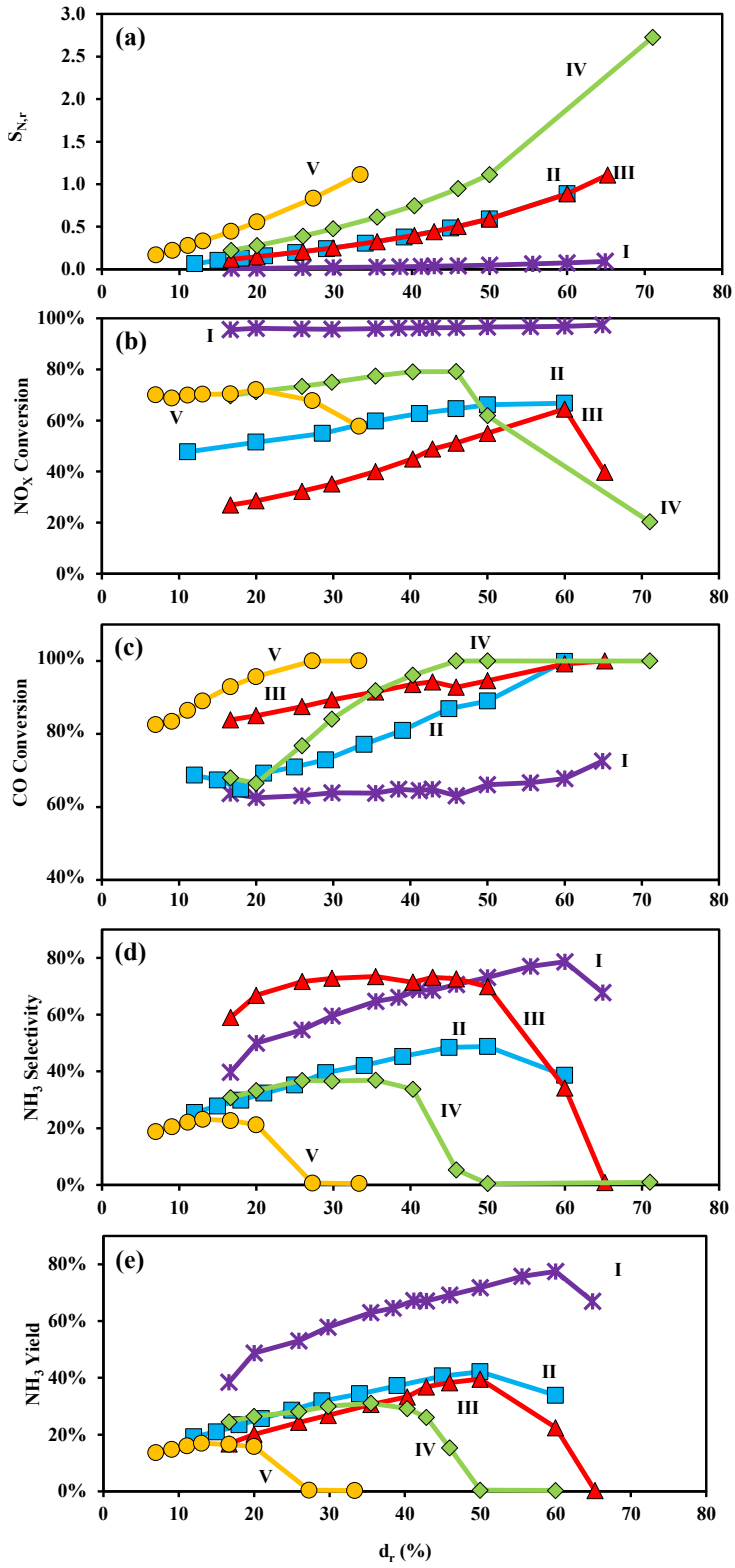

Figure 2.7: (τ_ℓ)=40s, (τ_r) varied based on d_r value. Lean feed (S_N=1.24): 500 ppm NO, 1% CO, 3300 ppm H_2, 0.8% O_2. Rich feed: 500 ppm NO, var. O_2, var. CO/H_2 concentration (10 or 20 cc, V_{CO}/V_{H_2}=3).

Table 2.2: Rich feed details for d_r experiments. Varied CO/H_2 in a 3:1 ratio.

Feed	$\%O_2$	T_{feed}(°C)	V_{CO+H_2} (cc)	$d_r(S_{N,r}=1)\%$
I	0	270	20	–
II	0.27	270	20	63
III	0.27	470	20	63
IV	0.53	270	20	47
V	0.53	270	10	30

Figs. 2.7c and 2.7d show the effect of the rich duty percentage on the cycle-averaged CO conversion and NH_3 selectivity, respectively. Each point in the figures represents one cycling experiment.

Examination of Fig. 2.7 reveals several notable trends. First, the NO_x conversion (Fig. 2.7b) for each case generally increases with d_r up to a value in which a neutral stoichiometric mixture is achieved, i.e., $d_r(S_{N,r} = 1)$. Those values are provided in Table 2.2 for each feed. For $d_r > d_r(S_{N,r} = 1)$ the NO_x conversion decreases as the gas phase becomes net lean. This trend reflects that a rich phase that is both more prolonged and of a lower reductant concentration is more effective than a shorter, more intense pulse, as long as the feed does not become lean. For example, for Feed II, X_{NO_x} (d_r = 0.20, τ_T=50s, $y_{r,CO} + y_{r,H_2}$= 0.063) is 51%, while X_{NO_x} (d_r = 0.60, τ_T=100s, $y_{r,CO} + y_{r,H_2}$= 0.00637) is 67%.

Fig. 2.7b shows that for fixed d_r, the NO_x conversion decreases with increasing rich phase O_2 concentration (increasing $S_{N,r}$) and increasing feed temperature (T_{feed} = 270 to 470 °C). The former trend underscores that increased reductant enhances NO_x conversion. The latter trend reflects the detrimental impact on NO_x storage capacity at high temperature. In contrast to NO_x conversion, the CO conversion is an increasing function of d_r and T_{feed} (Fig. 2.7c). The X_{CO} dependence on d_r reflects that a leaner rich phase benefits the oxidation of CO by gas phase O_2 or stored O_2, as expected. The dependence on T_{feed} simply indicates that an increased temperature increases the rate of oxidation. Fig. 2.7d shows that NH_3 selectivity is a non-monotonic function of d_r. This trend reflects the similar trend for NO_x conver-

sion versus d_r, although the maximum S_{NH_3} occurs at a lower d_r value than the d_r value resulting in a maximum NO_x conversion.

The trends in the NH_3 production reflect the balance between NH_3 generation and consumption. A shorter and more intense rich phase is less effective in generating NH_3 as is a rich phase that is not sufficiently rich. At first glance, it may seem counterintuitive that NH_3 selectivity decreases as S_N decreases, as it was shown for steady state conditions that a rich environment leads to a higher NH_3 production (Fig. 2.3). However, the pulses for lower d_r are very short and concentrated which likely leads to a transient poisoning effect of CO on the Pt sites, which inhibits NO reduction to NH_3. As the rich phase becomes leaner (d_r and $S_{N,r}$ increasing) the selectivity and conversion increase to a maximum value before starting to decrease when the S_N,r value approaches unity. The prolonged rich phase is insufficiently rich, which decreases the NH_3 generation rate and increases its oxidation rate. It is interesting to note that Feeds II—V follow the same locus of S_{NH_3} versus d_r for decreasing d_r. This trend suggests a limit on the NH_3 production when the rich phase is sufficiently rich. Indeed, the Feed I results clearly show that a critical variable is the O_2 concentration. A rich phase devoid of O_2 gives the highest NH_3 yield over a wide range of rich duty fractions.

2.3.6 Impact of feed temperature

The data in Fig. 2.7 include two sets at identical conditions but two different feed temperatures of 270 and 470 °C, Feeds II and III, respectively. Similar qualitative trends for conversion and selectivity are evident up to a 60% rich duty ($S_{N,r}$ < 1), but the magnitudes are different. At 470°C the NO_x conversion is lower than it is at 270°C while the NH_3 selectivity is considerably higher, or equivalently, the N_2 selectivity is much lower (given the relatively negligible N_2O selectivity). Note however that that NH_3 yield (Fig. 2.7e) is nearly identical regardless of temperature, indicating the amount of NH_3 produced is not affected by temperature under these

conditions. By definition, the variation in selectivity is due to the variation in NO conversion. The NO conversion trend is due in part to the decreased NO_x storage at higher temperatures with a larger fraction coming from direct catalytic conversion during the lean and rich phases. Recall that the steady state data show the NO conversion decreasing over this temperature range for a near-stoichiometric feed (Fig. 2.4a). On the other hand, the steady-state N_2 selectivity increases with temperature (Fig. 2.7b). This would appear to contradict the observed opposite trend during cyclic operation (Fig. 2.7d). Under steady-state conditions the increased N_2 selectivity is a result of the increased rates of NO bond scission and N adatom recombination. The high NH_3 selectivity achieved under cyclic conditions at 470°C occurs at lower NO_x conversion and during the rich phase.

To better understand the effect of feed temperature on catalyst performance, Fig. 2.8 shows the NO_x, N_2O, NH_3, and CO effluent concentrations for feed temperatures of 270 and 470 °C and a 50% rich duty (lean and rich durations of 40s). The NO_x transient data demonstrate that at lower temperatures there is a higher storage of NO_x, consistent with the NO_x storage data reported in Fig. 2.5. This observation explains why there is a higher NO_x conversion at the lower temperature. Upon comparing the two profiles, both breakthroughs occur at the same time, although the lower temperature NO_x profile has a slower approach to saturation than at 470°C. At higher temperatures the stored NO_x is not as stable and will undergo desorption and reduction. As shown in Fig. 2.5, the storage exhibits two maxima, one around 175°C and one around 300°C, suggesting that the lean NO_x storage performance of the catalyst is sensitive the inlet temperature. At 470°C, the TWNSC is less effective at storing NO_x under the conditions presented in this paper, but a higher frequency of lean-rich switching (i.e., shorter τ_ℓ) would improve the performance. The individual NO and NO_2 profiles are shown in Fig. 2.8b. For these conditions, the extent of NO oxidation to NO_2 is dependent on the feed temperature, consistent with the

lean NO_x conversion trends shown in Fig. 2.4. This behavior suggests that as the operating temperature changes, the cycling protocol can be adjusted to improve both NO_x conversion and storage efficiency. Additionally, at both feed temperatures the rich phase NO_x conversion is complete within 20s of the rich phase feed, suggesting this portion of the cycle is independent of the temperatures used in this study.

The N_2O transient data show a moderate N_2O selectivity at 270°C but a negligible level at 470°C, consistent with typical N_2O behavior at low vs. high temperatures for NO_x storage catalysts. Unlike the results shown earlier for which a wider range of lean/rich switching ($S_{N,\ell}$ of 7.4 to $S_{N,r}$ of 0.49) was employed and negligible N_2O was generated (Fig. 2.5), at 270°C the narrow lean/rich switching of $S_{N,\ell}$ = 1.24 to $S_{N,r}$ = 0.60 results in an N_2O concentration as high as 50 ppm during the rich phase. The formation of N_2O during the rich phase only occurs during the first 20s of the cycle, during which time stored O_2 is available. Once the O_2 storage is depleted, NO_x is fully reduced to N_2/NH_3.

The NH_3 transient data are nearly identical at the two feed temperatures. NH_3 breakthrough occurs about 10s after the start of the rich phase, indicating the consumption of stored O_2 and NO_x occurring at similar rates in both cases. After breakthrough, the NH_3 concentration approaches 500 ppm, which indicates that NH_3 is the major product in this rich environment, independent of the temperature. NH_3 is not detected during the lean phase. The high selectivity at 270°C is due to the increased storage of NO_x in the lean phase, and the yield is the same at both temperatures because the reactor environment is sufficiently rich to fully reduce NO_x to NH_3 instead of N_2, likely due to the high concentration of H_2 in the feed. While NH_3 decomposition is expected at higher temperatures, previous studies on similar catalyst compositions have shown that the presence of H_2 during regeneration can prevent this phenomenon.[17] Additionally, there is a notable difference in the breakthrough profile depending on the temperature. At 270°C, the NH_3 spikes much faster

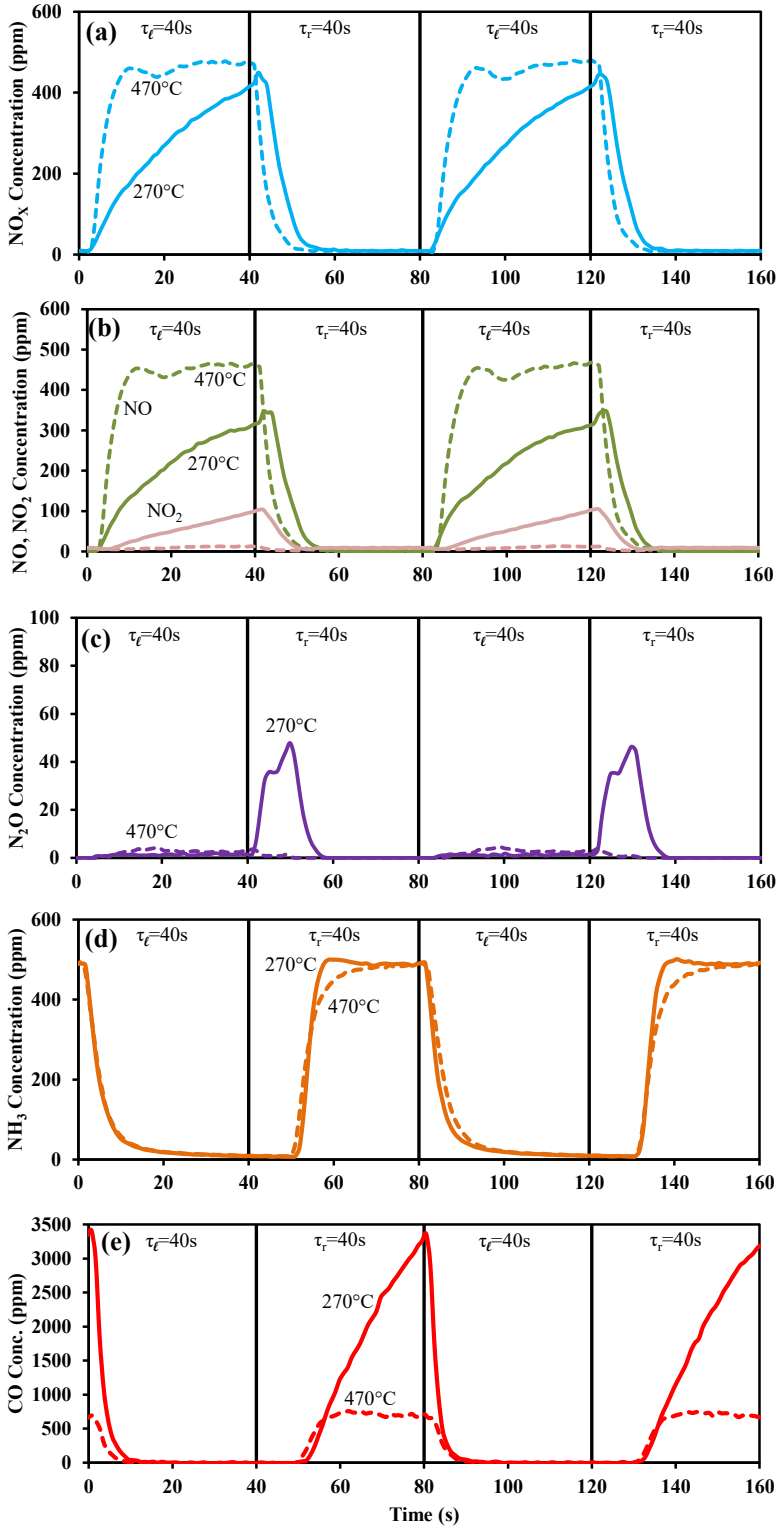

Figure 2.8: (a) NO_x, (b) NO, NO_2, (c) N_2O, (d) NH_3, and (e) CO (ppm). Lean feed ($S_{N,\ell}$ =1.24): 1% CO, 3300ppm H_2, 0.8% O_2. Rich feed ($S_{N,r}$ = 0.60): 0.27% O_2, 0.75% CO, 0.25% H_2. Both had 500ppm NO, 7% H_2O, 10% CO_2.

than at 470°C, overshooting the feed value of 500ppm NO, possibly due to the low concentration of CO present during this time as it is still oxidized using stored O_2. As the CO effluent concentration increases, the NH_3 production rate decreases due to the poisoning effect of CO on the reactive sites. However, at 470°C, because the CO undergoes water gas shift, there is less poisoning and the NH_3 formation occurs more gradually, approaching 500ppm as more H_2 is formed.

Finally, the CO transient data reveal breakthrough at the same point as NH_3 upon O_2 depletion. While the 470°C profile shows CO leveling off at about 700 ppm, the 270°C profile shows a progressively increasing concentration during the rich phase. The differences can be attributed to a lower extent of CO conversion by reaction with H_2O at 270 than at 470 °C; i.e., the exothermic water gas shift reaction.

2.3.7 Impact of total cycle time

The total cycle time, τ_T, is another important operating parameter which must be tuned in conjunction with the rich duty fraction. We report in this section the impact of τ_T for several different cases corresponding to feeds of varying stoichiometric numbers, feed temperatures, and reductant types.

Fig. 2.9 shows the impact of τ_T on catalyst performance for two different feed temperatures: 270°C (Fig. 2.9a) and 470°C (Fig. 2.9b) with a rich duty of 50%. This d_r value provides a relatively high NO_x conversion over this temperature range. The lean and rich O_2 concentrations are 5% and 0.37%, respectively, resulting in $S_{N,l}$ and $S_{N,r}$ = 7.4 and 0.6, respectively. The ANR calculated using eqn. 2.8 is shown on the secondary vertical axis.

With the wide disparity in lean and rich compositions a distinct NO_x conversion maximum is obtained for the 270°C feed temperature (Fig. 2.9a). The maximum X_{NO_x} is 87% for a τ_T = 18s. At shorter cycle times the conversion falls off sharply, approaching 47% for τ_T = 4s. For longer cycle times the conversion decreases gradually, approaching 67% at τ_T = 200s. A NO_x conversion maximum at an intermediate

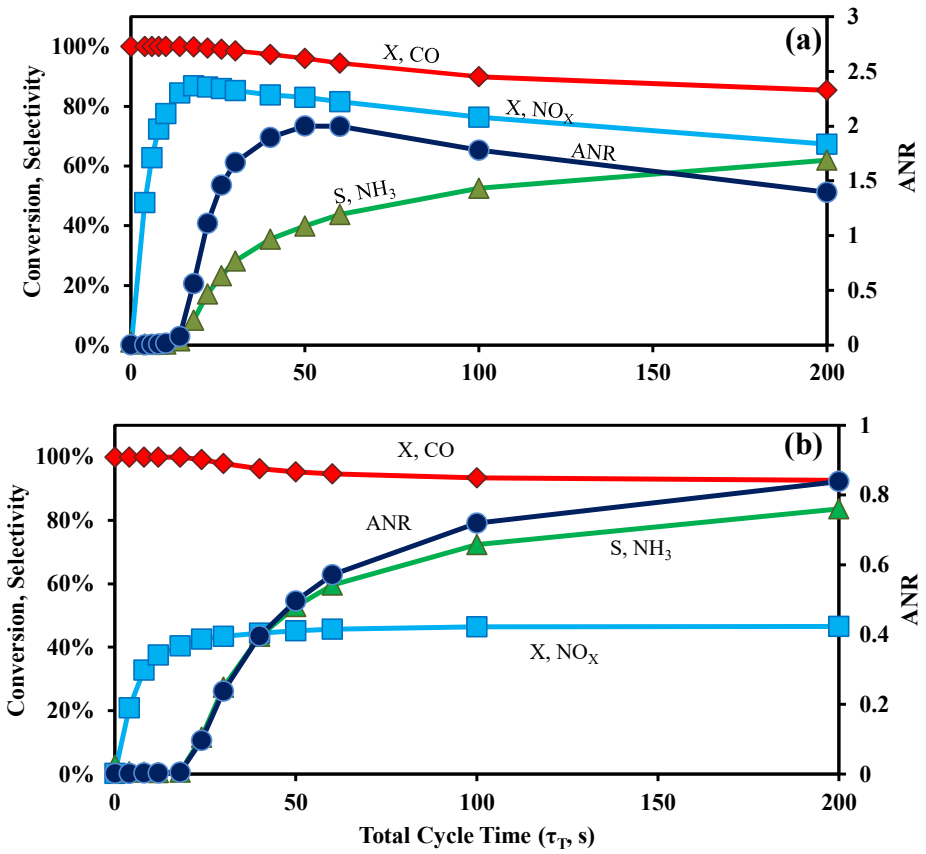

Figure 2.9: T_{feed} = (a) 270°C (b) 470°C. d_r=50%. Lean feed ($S_{N,\ell}$ =7.4): 500ppm NO, 1% CO, 3300ppm H_2, 7% H_2O, 10% CO_2, 5% O_2. Rich feed ($S_{N,r}$ =0.6): 500ppm NO, 1% CO, 3300ppm H_2, 7% H_2O, 10% CO_2, 0.37% O_2.

cycle time was first reported by Kabin et al.,[16] who examined a lean NO_x trap catalyst using C_3H_6 as the reductant. They showed that as the cycle time gets shorter, upstream mixing of the lean and rich feeds results in a feed approaching that of a "mixed feed" at steady state. For the current study, with rich and lean duties both 50%, the mixed feed would correspond to a simple arithmetic average of the two; i.e., O_2 feed concentration = (5 + 0.37)% / 2 = 2.69% O_2. Referring to earlier steady state results in Fig. 2.3, such a lean feed would result in a negligible NO_x conversion. Indeed, an extrapolation of X_{NO_x} to zero cycle time in Fig. 2.9a confirms this analysis. In contrast to the NO_x conversion, the CO conversion decreases monotonically with cycle time (Fig. 2.9a) from its maximum value of 100% for τ_T = 0, while the

NH_3 selectivity monotonically increases from 0 starting at τ_T = 14s. The CO conversion decline merely reflects that with a more protracted rich phase, more reductant breaks through. In fact, the appearance of NH_3 at τ_T ~14 s occurs at about the same point as the onset of the decrease in CO conversion, referring back to the transient profiles in Fig. 2.6a that show the coincident breakthrough of CO and NH_3. The declining NO conversion combined with the increase in S_{NH_3} result in an ANR having a maximum at an intermediate cycle time; i.e., ANR ~2.0 at τ_T = 50 s. As we expand on later, the existence of the NO_x conversion maximum and ANR maximum at two different cycle times poses an interesting operational question.

At 470°C neither the NO_x conversion nor the ANR exhibit maxima (Fig. 2.9b). Under these conditions the extent of NO_x storage is much lower. As a result the catalyst performance is effectively a combination of lean and rich operations. The NO_x conversion increases sharply from the short cycle mixed-feed limit to 47% at long cycle times. This value approaches the weighted average conversion of the lean feed (100%, $S_{N,r}$ = 0.6) and rich feed (0%, $S_{N,\ell}$ = 7.4) both operated at steady state. The NH_3 selectivity also increases monotonically from 0 to 0.8 at τ_T = 200s. The magnitude of the ANR is much lower at this rather high feed temperature.

For comparison, another cycle time sweep was carried out with a feed temperature of 270°C but a shorter rich duty of 14%. Fig. 2.10 shows the same performance metrics when the lean-rich switching is confined to an S_N range between 1.18 (lean) and 0.83 (rich) and a feed temperature of 270°C. The NO_x conversion has two extremes over the τ_T range of 0 to 200 s; a maximum of 77% for τ_T = 0s (obtained with a mixed feed and S_N =1.005), and a minimum of 52% at τ_T = 18s. For the longest cycle time of τ_T = 200 s, X_{NO_x} is 61%. That the highest conversion is encountered with the continuously-fed mixed feed indicates that cycling is actually detrimental for this near-stoichiometric feed. The CO conversion exceeds 99% over the entire range of cycle times. NH_3 generation under these conditions is quite low with a max-

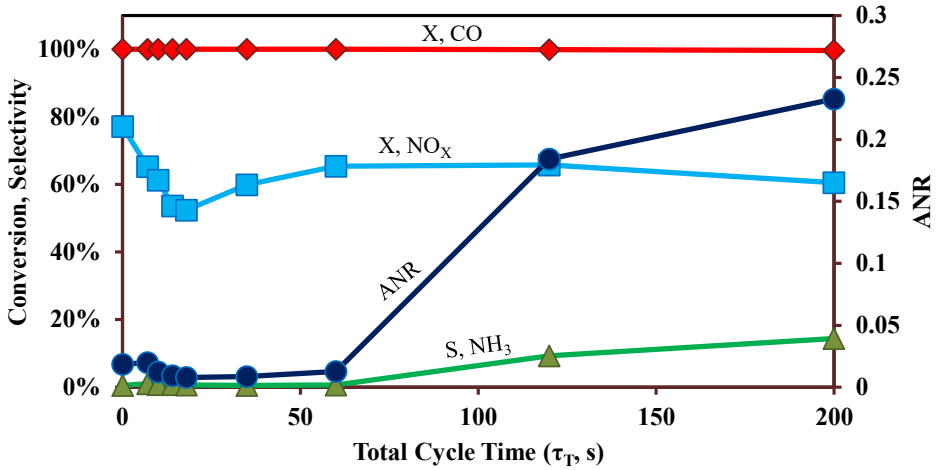

Figure 2.10: T_{feed}=270°C. d_r= 14%. Lean feed ($S_{N,\ell}$ =1.18): 500ppm NO, 1% CO, 3300ppm H_2, 7% H_2O, 10% CO_2, 0.8% O_2. Rich feed ($S_{N,r}$ =0.83): 500ppm NO, 1% CO, 3300ppm H_2, 7% H_2O, 10% CO_2, 0.53% O_2.

imum selectivity of only 14% achieved at a cycle time of 200 s while the net NH_3 generation is negligible for cycle times less than 60s.

2.3.8 Impact of reductant type

Most of the experiments presented up to this point have involved a reductant feed containing CO and H_2. In practice, the feed also contains hyd$_r$ocarbons, so it is useful to assess the TWNSC performance when each of the three reductant types is present. Fig. 2.11 shows the results for a three-reductant feed (Fig. 2.11a) and a feed containing C_3H_6 as the sole reductant (Fig. 2.11b). Both experiments were conducted at the same feed temperature of 270°C while the rich duty was fixed at 50%. The C_3H_6 concentration in the lean and rich phases for each experiment was fixed at 1000 ppm while the CO and H_2 concentrations were 1% and 3300 ppm, respectively, for the three-reductant feed. The O_2 concentrations in the rich and lean phases were adjusted to ensure that the S_N,r and $S_{N,l}$ were fixed at 7.4 and 0.8, respectively. Table 2.3 reports the feed concentrations. Note that the exothermic heat effects (Fig. 2.10c) are larger for the three-reductant feed.

For the three-reductant feed results (Fig. 2.11a) there is a distinct maximum in

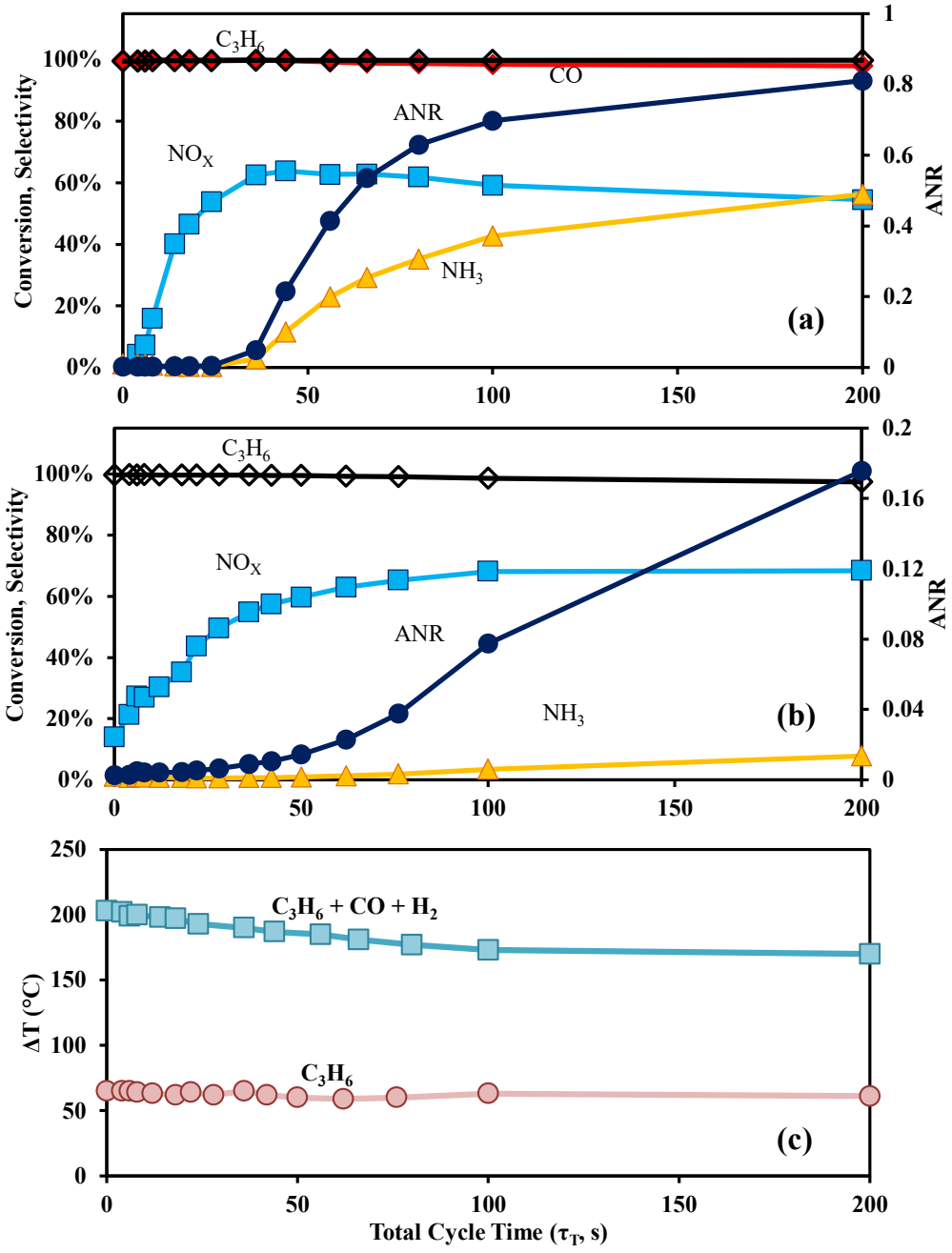

Figure 2.11: (a,b) Conversion, selectivity and ANR (c) ΔT comparing feeds (a) CO + H_2 + C_3H_6 and (b) C_3H_6.

Table 2.3: Concentration of reductants and O_2 during the lean and rich phase used in the reductant analysis cycling experiments explained in Fig. 2.12

	Set	CO	H_2	C_3H_6	CO + H_2	CO + H_2 + C_3H_6
O_2 (%)	Lean	5	5	5	5	8.4
	Rich	0.53	0.53	0.53	0.53	0.9
CO (%)	Lean/Rich	1.33	–	–	1	1
H_2 (%)	Lean/Rich	–	1.33	–	0.33	0.33
C_3H_6 (%)	Lean/Rich	–	–	0.147	–	0.1

the NO_x conversion (64%) at τ_T = 44 s. At the cycle time limits of 4s (mixed feed) and 200 s, NO_x conversion is 0.2 and 56 %, respectively. In contrast, for the C_3H_6 only feed (Fig. 2.11b) the NO_x conversion increases monotonically from 12% at τ_T = 4s to 68% at τ_T = 200s. The comparison shows that C_3H_6 is more effective in reducing NO_x than the three-component mixture for shorter cycle times (τ_T < 10s) and nearly as effective for longer cycle times. The short cycle time difference may be due to CO inhibition as was discussed earlier (Figs. 2.3 and 2.4). Each case shows nearly complete conversion of the reductant over the entire range of cycle times. This is the result of the overall lean conditions (S_N = (7.4 + 0.8)/2 = 4.1). On the other hand, a large difference is evident in NH_3 generation under these conditions. Clearly CO and H_2 are much more effective in generating NH_3. Corresponding to these trends is a much higher ANR for the three-reductant feed than the C_3H_6-only feed. This is not surprising given that NO conversion by H_2 to NH_3 is very effective under these conditions.

Fig. 2.12 shows the effect of using various combinations of reductants on the cycle-averaged NO_x conversion and NH_3 selectivity. To enable a meaningful comparison, the cycle time and rich duty (τ_T = 80s; d_r = 0.5), feed temperature (270°C) and stoichiometric numbers for both the lean ($S_{N,l}$ = 7.6) and rich phases ($S_{N,r}$ = 0.83) were fixed. Species concentrations were adjusted to maintain the fixed $S_{N,l}$ and $S_{N,r}$ values. Overall, the conversion of NO_x varies less with the type of reductant in the feed than does the NH_3 selectivity. X_{NO_x} varies between 62% (mixture of three reduc-

tants) and 77% (H_2 only) while S_{NH_3} varies between 45% (H_2 only) and 5% (C_3H_6). In maximizing both NO_x conversion and NH_3 selectivity, H_2 is the most effective reductant.[79,83] Any feed that contains H_2 increased the NH_3 selectivity, consistent with the discussion in previous sections regarding the enhancement of H_2 on NH_3 selectivity.

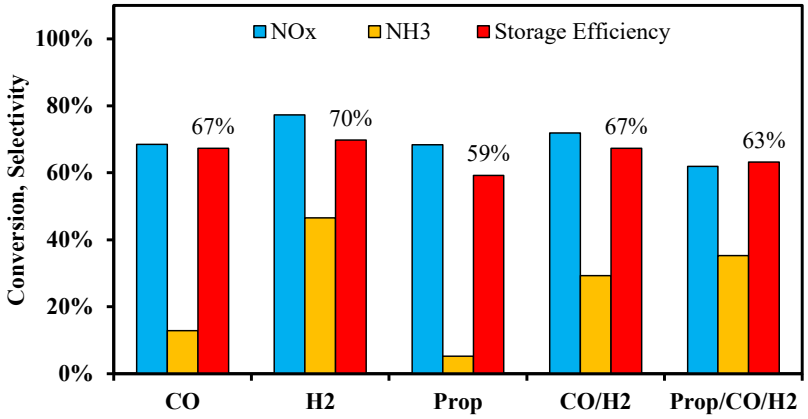

Figure 2.12: NO_x conversion and NH_3 selectivity for various combinations of reductant in the feed. T_{feed} = 270°C. τ_T = 80s, τ_ℓ=40s, τ_r =40s. See Table 2.2 for feed concentrations.

To better understand these trends, Fig. 2.13a shows the transient effluent NO_x concentration for one lean-rich cycle using each of the reductant feeds. Each of the NO_x profiles are qualitatively similar. During the lean phase there is a brief period of complete NO_x trapping followed by NO_x breakthrough with a gradual increase; during the rich phase there is a NO_x spike followed by a sharp decrease. Overall the data show that H_2 is the most effective reductant, followed by CO/H_2. The NO_x conversion is primarily affected by two factors, the lean storage and the intensity of the NO_x spike that occurs during the lean-rich transition. An estimate of the lean NO_x storage efficiency η_ℓ, determined using eqn. 2.9, is highest for H_2 (70%) and lowest for C_3H_6 (59%). The C_3H_6 data shows the steepest NO_x breakthrough during the first half of the lean phase while all of the other feeds have nearly identical NO_x breakthroughs during this period. Interestingly, the C_3H_6-only NO_x breakthrough

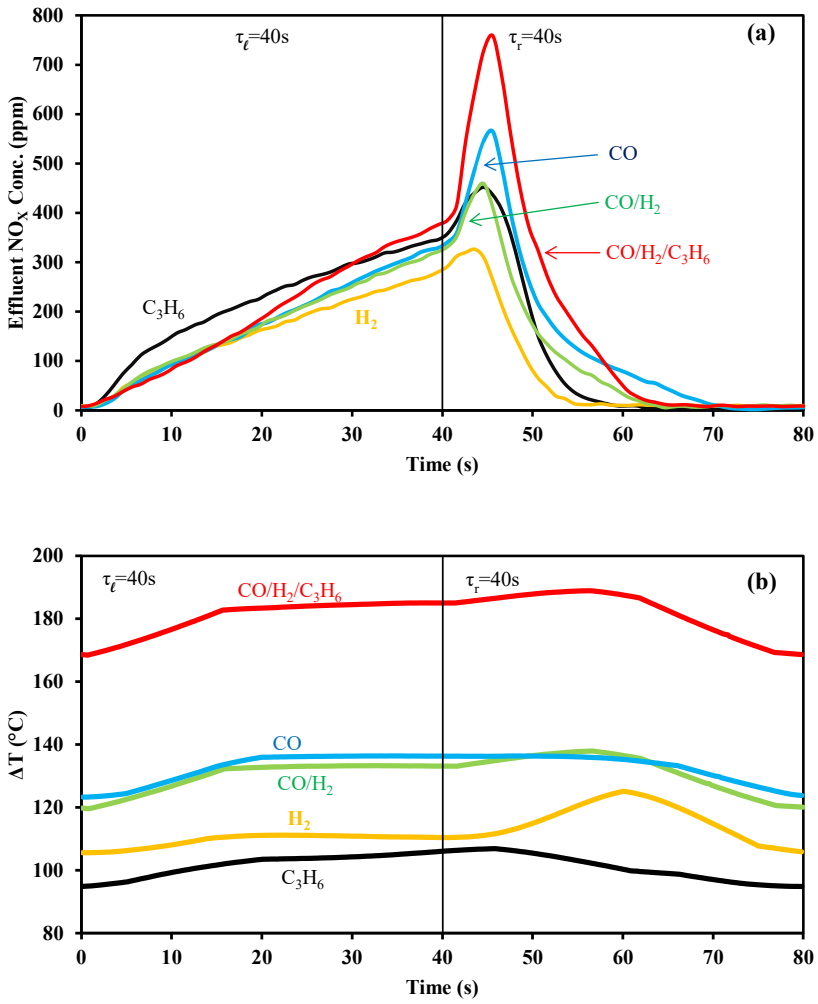

Figure 2.13: (a) NO_x concentration profile for one cycle. (b) Temperature rise of one cycle for each of the five feeds described in Fig. 2.11. $S_{N,\ell}$ =7.6, $S_{N,r}$ = 0.83 (see Table 2.2 for concetrations).

intersects the three-component feed near the end of the lean period. The NO_x concentration during the rich phase shows greater disparity in the several cases. For feeds containing CO, the NO_x spike is most pronounced. This would appear to indicate that CO inhibits the regeneration. The comparison of the CO-only and H_2-only or the C_3H_6-only and the three component feeds underscore this point.

Fig. 2.13b shows the corresponding transient mid-point catalyst temperature. For all feeds, there is a gradual increase during the lean phase (oxidation), followed by a decrease during the rich phase (reduction). The lowest temperature rise is encoun-

tered with the C_3H_6-only case, followed by the H_2 case, and then the CO containing cases. The highest temperature rise is seen with the three-reductant feed. Fig. 2.14 shows the measured, cycle-averaged temperature rise for each case compared to an estimate for the theoretical steady-state value using the following expression for the adiabatic temperature rise,

$$\Delta T = \frac{-\Delta H_{rxn} X C_r}{C_p}, \tag{2.26}$$

where $-\Delta H_{rxn}$ is the heat of combustion of the reductant, X is the conversion, C_r is the concentration (% vol.), and C_p is the heat capacity of the feed gas. As shown in the figure, there is agreement in the trend between the temperature rise of individual species and the reductant mixtures. However, there is an overall difference in magnitude between the measured and theoretical values, most attributed to reactor heat losses. The observed conversion of each reductant mixture in this set of experiments is more than 98%. As such, the temperature rise values are attributed to variations in reductant concentration and the heat of combustion of each species.

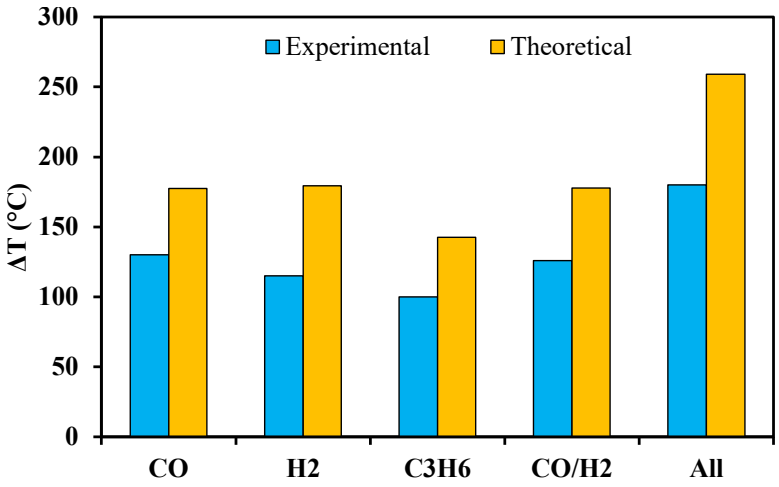

Figure 2.14: Comparison of cycle-averaged catalyst temperature rise to theoretical values calculated according to eqn. 2.26.

2.3.9 Optimal operation

The TWNSC performance results suggest that system optimization is nontrivial. The manipulated operating parameters include the cycle time, rich duty fraction, rich phase O_2 concentration, and feed temperature. The choice of which performance metric is the most critical depends on intended application of the TWNSC. For the standalone TWNSC, operating conditions should be selected that maximize the NO_x conversion, reductant conversion, and N_2 selectivity while minimizing the reductant usage. In contrast, for the TWNSC followed by a SCR, the NO_x conversion should be balanced across both reactors to take advantage of the lower cost SCR. In that case the rich phase operating conditions should be selected that give a NO_x conversion approaching 50% and a NH_3 selectivity as high as possible to affect downstream SCR,[19,76] i.e., ANR ~1. Identifying the precise operating conditions would require a detailed multi-variable optimization.

To illustrate the optimization strategy, it is instructive to evaluate the case when cycling is done with widely different feed compositions. Fig. 2.9a shows such a case using CO + H_2 as the reductant mixture that might represent a lean gasoline application. In those experiments the data reveal the existence of two maxima obtained at different cycle time values. The first maximum is of the NO_x conversion while the second is of the ANR. Selecting the NO_x conversion maximum (87%) as the operating point for the standalone TWNSC would require a total cycle time of 18 s at the duty rich fraction of 50%. Under these conditions the NH_3 selectivity is rather low (20%) and the CO conversion is very high (99.9%). On the other hand, for the TWNSC + SCR configuration, there are two potential operating points at which ANR ~1. If a downstream SCR catalyst is available, as mentioned earlier the optimal ANR value is unity. The first is to the left of the ANR maximum, while the second is well to the right of the ANR maximum (e.g., at τ_T = 20 s and at τ_T = 200 s, respectively). The latter would appear to be the better choice as X_{NO_x} = 67% and S_{NH_3} = 62% which are

closer to the desired optimal values of 50% and 100%, respectively. However, the CO conversion at this cycle time is 85%, an issue that still needs to be addressed for a TWNSC system. Another potential operating point might be at the ANR maximum which occurs for τ_T = 50s. In this case the NO_x conversion is 83% and the NH_3 selectivity is 44%. Moreover, the CO conversion is 96%. Obviously, this illustration over-simplifies the optimization but it does provide insight into the main issues.

The catalyst performance is qualitatively different at a higher feed temperature (Fig. 2.9b). Because the lean NO_x storage is poor at 470°C, the cycle-averaged conversion stabilizes after only 40s instead of exhibiting a maximum, indicating that even with longer lean periods, the NO_x breaks through and increases to its feed concentration within 40s. Another key difference at the higher feed temperature is that the NH_3 selectivity and ANR steadily increase. The ANR value does not approach 1.0 in these conditions, mostly due to the decrease in NO_x conversion at higher feed temperature. Since the NO_x conversion stabilizes, we would expect NH_3 selectivity to increase because a longer rich period generates more NH_3. To optimize this system, a total cycle time of 40s would be a good choice leading to 45% NO_x conversion and a reasonable NH_3 selectivity (ANR of 0.4, and a CO conversion of 96%). A higher cycle time would lead to better NH_3 yield, but long cycle times are much less practical for engine operation, and the additional loss of CO conversion is problematic.

2.3.10 Parallel modeling study

A follow-up study was conducted in which a global kinetic model was developed to predict and further analyze the experimental data described above. The model was developed by Mengmeng Li and was published as Li,M.; Malamis, S. A.; Epling, W.; Harold, M. P. Steady state and lean-rich cycling study of a three-way NO_x storage catalyst: Modeling. *Applied Catalysis B: Environmental* **2019**, *242*, 469-484.

The model captures most of the experimental trends of a model TWNSC reported here. A systematic method was used to develop the main underlying catalytic reac-

tions, NO_x storage, and O_2 storage processes. The process involved a combination of specific steady-state and transient experiments designed to estimate kinetic parameters. According to the model prediction under the steady-state condition, the TWNSC model is capable of capturing the effluent trend spanning a range of S_N values. The cyclic model could capture the cycle-averaged NO_x and CO conversions, NH_3 generation and ANR through a wide range of TCT and the transient species profiles at TCT = 50 s. Model-predicted spatio-temporal profiles of NO_x storage sites coverage and solid and fluid temperature profiles significantly enhance the understanding of dynamic NO_x storage profiles and nonisothermal features within the TWNSC monolith, which provides information for catalyst design and optimization. This type of modeling work serves as the basis for the work described in Chapter 4.

2.4 Conclusions

A systematic study of the performance of a commercial three-way NO_x storage catalyst (TWNSC) was conducted. The study provides insights regarding potential use in lean-burn gasoline vehicles as a standalone unit or in tandem with a downstream SCR. The steady-state performance expectedly shows the demarcation between rich and lean such that within a narrow window around the stoichiometric neutral point high conversion of CO, hydocarbon (C_3H_6), and NO can be achieved. In general, CO and C_3H_6 conversions increase with temperature and stoichiometric number S_N, while NO_x conversion and NH_3 production decrease with increasing temperature and S_N.

The performance features under lean/rich cycling are amenable for either standalone TWNSC or the tandem TWNSC + SCR configuration. The cycling protocol may be designed to achieve a high NO_x conversion and N_2 selectivity, but this will generally require reductant exceeding a threshold value that leads to difficulty in avoiding NH_3 and CO slip whereas insufficient reductant will lead to an inadequate NO_x conversion. The concentrations of reductant and O_2, duration of the rich pulse

(duty fraction), and cycle time may be tuned to achieve a desired NO_x conversion and/or NH_3 selectivity. If there is a large disparity in the lean/rich ratio over the cycle, the NO_x conversion exhibits a maximum value at an intermediate cycle time, as does the ANR. Optimization should be possible for a particular application that maximizes the NO_x conversion and reductant utilization. A follow-up modeling study enables enhanced understanding of the TWNSC including providing details for spatiotemporal behavior of the monolith.

Chapter 3: Coupled NO and C_3H_6 trapping, release and conversion on Pd-BEA: evaluation of the lean hydrocarbon NO_x trap (LHCNT)

The following chapter was accepted as Malamis, S. A.; Harold, M.P.; Epling, W. S.; Coupled NO and C_3H_6 trapping, release, and conversion on Pd/BEA: Evaluation of the lean hydrocarbon NO_x trap. *Industrial and Engineering Chemistry Research* **2019**.

3.1 Introduction

The combination of higher fuel economy and tightening emission regulations motivates the development of more efficient engines and effective emission control systems. Advanced compression-ignition engines and enhanced efficiency diesel engines are being developed to meet the fuel economy challenge.[21,89] Vehicles with these engines operate at a lower combustion temperature and emit relatively higher amounts of hydrocarbons (HC) and CO. Moreover, these systems operate lean, resulting in increased NO_x emissions. It is well known that conventional emission control systems including the Three-Way Catalytic converter (TWC), Lean NO_x Trap (LNT), and the combination of Diesel Oxidation Catalyst (DOC) + Selective Catalytic Reduction catalyst (SCR) are ineffective at temperatures below 200°C.[60] Thus, because engines undergo a cold-start duration of 1–3 minutes, it is imperative to address the slip of pollutants that occurs before the catalyst reaches its threshold operating temperature.

While the challenge of cold-start emissions is well documented, increasingly stringent emission standards have led to renewed interest in developing an effective so-

lution. The Passive NO_x Adsorber, or PNA, has been proposed to specifically address the low temperature emission of NO_x. Researchers from Johnson Matthey described in the first open literature report the main features of the PNA; i.e., the trapping of NO and NO_2 at low temperature and their release at a temperature high enough for downstream conversion by SCR.[60] The most commonly-studied PNA materials include Pd-exchanged zeolites including BEA, ZSM-5, or SSZ-13, due to their high thermal stability and resistance to sulfur poisoning.[60,62,64] Although these materials have expressed a high affinity for NO_x storage at low temperature, the NO adsorption mechanism on these materials is still under debate. One interpretation is that highly dispersed isolated Pd cations leads to considerable storage, but the nature of Pd in these catalysts is highly variable and not fully understood.[62,64,67,90]

Key literature studies have investigated NO adsorption and the nature of Pd in/on Pd-containing zeolite materials. The Pd exists in a variety of states, which can impact NO uptake. Several of these states include PdO, as either isolated molecular moieties or nanoparticle clusters; Pd^{2+} exchanged in the zeolite framework at a single $(Al–O–Si)^-$ site (abbreviated Z^-) in the form of $Z^-[Pd–OH]^+$, or at a dual-site in the form of $Z^-[Pd]^{2+}Z^-$; and monovalent Pd^+Z^-.[62,63,68,91–93] Zheng et al.[62] proposed that sufficiently small PdO_x (x > 1) clusters located on the external surface of the zeolite may contribute to NO uptake through their reduction by NO (to NO_2) and subsequent NO adsorption. The distribution of Pd states and their collective response to transient system conditions is practically important because agglomerated PdO particles are not effective in adsorbing NO or reducing NO_2.[63,92–94] Several studies conclude that the distribution is a function of the pretreatment conditions, gas composition such as the presence of O_2, NO, or reductants, as well as the zeolite framework type and its acidity. Adelman and Sachtler[91] found that the Brønsted acid sites (BAS) of ZSM-5 disperse exchanged Pd ions and prevent PdO agglomeration if the ratio of Pd/Al is low enough (~0.1). Aylor et al.[68] found that PdO clusters

can be redispersed upon exposure to a feed of NO + O_2 for low loadings of Pd on the zeolite (0.44 wt%). Although the exact mechanism through which NO adsorbs on Pd is still being investigated, it is well-understood that NO can bind to each Pd site type at various adsorption energies, which leads to desorption at different temperatures during warm up.[62,68,90]

In addition to the complex storage mechanism involving Pd, NO can also store on BAS but in the presence of H_2O these sites are largely blocked.[63,94] To increase adsorption in the presence of H_2O, various pretreatment strategies have been reported, including thermal or hydrothermal oxidative treatments, depending on the zeolite. These methods have been shown to redisperse PdO and to facilitate Pd ion exchange in the zeolite framework, increasing NO uptake.[95,96] Thus, extensive literature exists regarding NO adsorption on these materials and many new studies are underway to determine an energetically favorable mechanism.

Although a large amount of research is being conducted for NO adsorption to address the cold-start problem, the co-existence of other undesirable exhaust species including CO and unreacted HCs must also be addressed. Typical diesel engine exhaust contains small olefins (C_2-C_4), aromatics, and long-chain alkanes (C_{8+}), all of which need to be trapped during cold-start.[52] The PNA concept follows from the much earlier developed hydrocarbon trap (HCT), which stores HC on selective zeolite materials.[97] Zeolites are effective sorbents of HCs through a combination of the pore structure and acidity of the exchange sites.[57,63,65,93,98,99] Large pore zeolites such as BEA (12-member rings) are effective in trapping linear, higher molecular weight HCs (C_{10+}) that can access the pores and bind on the pore walls. Medium pore zeolites such as H-ZSM-5 (10-member ring) are effective in trapping olefins and aromatics on BAS, the extent of which depends on the silicon to aluminum ratio (SAR).[53,57,100] Although there is extensive research on the development of HCTs, incorporation with low-temperature NO_x storage capability has not been extensively studied. A recent

publication by Theis et al.[65] reported on the effect of ethylene on NO adsorption on ceria zirconia and found that NO adsorption increases due to the formation of alkyl nitrites and nitrates. In the pioneering study of Pd-zeolites as PNA materials by Chen et al.,[60] experiments involving n-$C_{10}H_{22}$ were reported, but extensive discussion of its effect on NO uptake or the use of smaller HCs was lacking.

To better understand the combined NO_x and HC storage on Pd-zeolite materials, we investigated the use of Pd-BEA as a model material for the aptly-named Lean Hydrocarbon NO_x Trap (LHCNT), a multifunctional material that traps and releases both NO_x and HCs and partially eliminates HCs (through oxidation) and NO (through reduction) during normal operation. Through a combination of transient adsorption/desorption experiments and in situ DRIFTS, we propose a phenomenological mechanism to explain the observed performance features of the Pd-BEA LHCNT. Specifically, we report performance metrics for a variety of conditions including the effect of H_2O and adsorption temperature for single adsorbate feeds and the combined NO and C_3H_6 feed. The results enhance our understanding of the properties and performance of Pd-BEA for subsequent model development, simulation, and LHCNT material/device optimization.

3.2 Experimental

3.2.1 LHCNT reactor setup

The LHCNT reactor setup was built over the course of three months using an existing furnace installed in a vertical position. Note this is a completely separate system from the TWNSC reactor. The setup comprised a vertical quartz tube reactor equipped with an MKS 2030D FT-IR for effluent gas composition measurement (Fig. 3.1). MG2000 software was used to analyze and process FT-IR spectra obtained during experiments. Feed gas flows were controlled both manually and electronically using a combination of Omega Engineering rotameters, calibrated for air at 1 atm

and 20°C, and MKS mass flow controllers (GM50A) connected to a control box with a digital interface (946 Controller). To conduct adsorption and desorption experiments, four feed streams were utilized: a main stream containing Ar and O_2 (MFCs); an adsorbate stream capable of flowing NO, NO_2, C_3H_6, and carrier Ar (MFCs); a makeup Ar stream to balance the adsorbate stream (rotameter); and a water injection system located downstream. The latter comprised a 60mL syringe pump (Cole-Parmer, IL), a house-made metal vaporizer unit set to 225°C, and a carrier Ar rotameter. For experiments requiring dodecane (see Chapter 5), a similar vaporizer unit was installed, but only a 10mL syringe pump was used due to the lower required flow rate. Figure 3.1 depicts the reactor system in more detail.

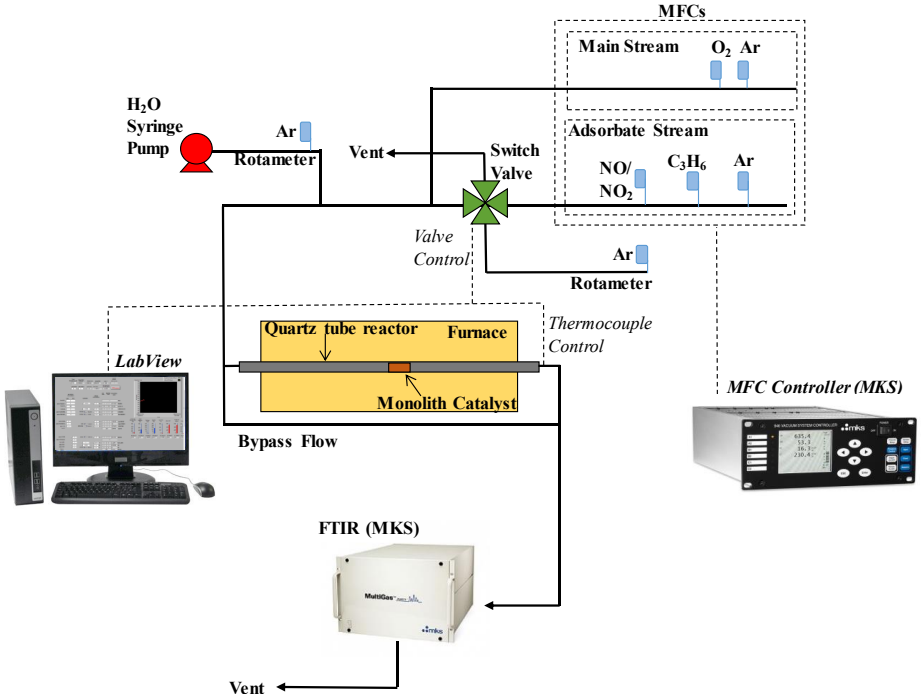

Figure 3.1: Quartz tube monolith reactor diagram (note that the furnace is actually oriented vertically).

3.2.2 Catalyst preparation and property evaluation

A catalyst composed of 2wt.% Pd-BEA zeolite was prepared using incipient wetness impregnation. BEA zeolite (Si/Al = 19, surface area = 710m^2/g) was obtained from Zeolyst International. A slurry was first prepared using $Pd(NO_3)_2 \cdot 2H_2O$ pre-

cursor dissolved in H_2O equal to the pore volume of BEA (35mL/g), which was then added dropwise to the zeolite, dried at 120°C for 18h, and calcined at 550°C for 4h. The resulting powder mixture was then combined with 10wt.% alumina binder, diluted in H_2O, and ball-milled for 36h. Cordierite monolith cores (cell density of 400 cpsi) were dipped into the resulting slurry mixture until the desired loading was reached. For all experiments in this study, a 2wt.% Pd-BEA monolith with a loading of 1.3g/in^3 was used. The monolith sample was 52mm long and had a cross section of 80mm^2, giving a total catalyst loading of 0.31g. Assuming complete incorporation of Pd into the zeolite, the estimated concentration of exchanged Pd and BAS were 187 and 633 μmol/g-cat, respectively, giving an Pd/Al value of 0.29 and a total site concentration of 820 μmol/g-cat. Pd dispersion was measured using a Micromeritics (3Flex Chemisorption) apparatus for both a fresh sample and a used sample that underwent many storage and release cycles. The catalyst samples were pre-reduced in 1% H_2 at 400°C for 30 min followed by CO pulse chemisorption. Using a 1:1 stoichiometry for CO adsorption on Pd, the resulting dispersion for each sample was 20% and 16%, respectively.

3.2.3 Adsorption and desorption protocols

Adsorption experiments were conducted in the vertical quartz tube reactor described above using a total flow rate of 2500sccm, corresponding to a gas hourly space velocity (GHSV at STP) of 32k h^{-1}. All gas feed compositions mentioned in this work are balanced with Ar unless noted otherwise. The catalyst sample was first degreened in 5% O_2 at 600°C for 4h. Before each experiment, a sample pretreatment was conducted in 5% O_2 at 500°C for 30 min, followed by sample cooling under a flow of Ar to the desired adsorption temperature of 50, 80, or 150 °C. To begin the adsorption, the adsorbate feed was injected into the reactor using an electronically actuated 4-way switching valve (Fig. 3.1). In this study both dry and wet feeds were used (Table 3.1). Any other feed compositions that deviated from those in Table 3.1

are described in the Results section. The monolith was exposed to the feed mixture for 300s, after which the adsorbate feed was switched off and the effluent concentrations were monitored until the NO and/or C_3H_6 concentration reached zero, purging the catalyst of weakly adsorbed gases. Next, the desorption was initiated by ramping the temperature at a rate of 20°C/min to 500°C in a flow of 2% O_2. For the wet feeds, the adsorption phase of the experiment was varied slightly due to reactor design limitations. To ensure simultaneous exposure of NO/C_3H_6 and H_2O on the catalyst, the entire feed mixture was established in the bypass, followed by a switch to the reactor. Because the protocol between wet and dry experiments differed, a blank monolith experiment was conducted for each feed composition, ensuring proper subtraction of dead time and weak adsorption in the system (Fig. A.1). Most experiments were repeated three times to ensure reproducibility, and the results did not vary by more than 10%.

Table 3.1: Experimental feed temperature and composition

T_{ads} (°C)	C_{NO} (ppm)	C_{NO_2} (ppm)	$C_{C_3H_6}$ (ppm)	C_{O_2} (%)	C_{H_2O} (%)
50	400	–	–	2	–
50	–	–	800	2	–
50	400	–	800	2	–
80	400	–	–	2	–
80	–	400	–	2	–
80	–	–	800	2	–
80	400	–	800	2	–
80	400	–	400	2	–
80	–	400	800	2	–
80	400	–	–	2	3
80	–	–	800	2	3
80	400	–	800	2	3
150	400	–	–	2	–
150	–	–	800	2	–
150	–	400	800	2	–

3.2.4 DRIFTS experiments

Samples for *in situ* DRIFTS (diffuse reflectance infrared Fourier transform spectroscopy) were pressed and sieved to a particle size of 60-80 mesh. Approximately

50mg of each sample were loaded into a high temperature reaction chamber (Harrick Praying Mantis^{TM}) equipped with KBr windows. For spectral measurements a Nicolet 6700 FTIR spectrometer equipped with a liquid N_2 cooled MCT detector was used, and a type-K thermocouple under the sample stage was used to monitor the cell temperature. DRIFTS spectra were collected at a range of 4000-650cm^{-1} with a resolution of 4cm^{-1}, using Kubelka-Munk units for intensity. For each experiment, the sample was first pretreated at 500°C with 5% O_2 in He for 1h before cooling to 80°C. Once the reactor temperature was steady, a background spectrum was collected and then subtracted out for each spectrum collected during adsorption. Adsorption experiments were initiated using a feed of 400 ppm NO and/or 800 ppm C_3H_6 with 2% O_2 in a balance of He at a total flowrate of 50sccm. The adsorption feed mixture was held for 1h and a 64-scan spectrum was collected continuously for the duration of the experiment.

3.3 Results and Discussion

3.3.1 Performance evaluation metrics

To evaluate the Pd-BEA catalyst, we measured several performance metrics using uptake and release data. Here we report NO_x and C_3H_6 uptake as μmole adsorbate/g-cat (total washcoat). Note that there is a small fraction (10 wt.%) of colloidal alumina binder in the washcoat, but we expect only a minor contribution to the catalyst performance. Since NO uptake on Pd is desired, and although uptake may also occur on unexchanged BAS, it is useful to report the moles NO_x adsorbed per mole Pd (NO/Pd). For a highly adsorbent catalyst, a value of NO/Pd at or exceeding unity is desired; this means that on average one or more NO molecules adsorbs on each well dispersed Pd cation moiety. A value less than unity implies that a fraction of the Pd is agglomerated and/or ineffective in adsorbing NO. The coverage θ_i of NO_x and C_3H_6 is defined as the moles of adsorbate i adsorbed per mole of storage

site including both Pd and H^+, given by

$$\theta_i = \frac{\int_0^t C_{i,in}dt - \int_0^t C_i dt}{C_{Pd} + C_{H^+}}, \tag{3.1}$$

where C_i ($C_{i,in}$) is the effluent (feed) concentration of species i in ppm while C_{Pd} and C_{H^+} are the concentrations of Pd-exchanged and unexchanged BAS in the zeolite framework. The cumulative trapping efficiency η_T is the percentage of NO_x or C_3H_6 fed that is trapped at temperature T during uptake time τ as

$$\eta_T(\tau) = 100 \times \left[1 - \frac{\int_0^\tau C_{NO_x}dt}{\int_0^\tau C_{NO_x,in}dt}\right]. \tag{3.2}$$

The effectiveness of an LHCNT material is also assessed by the percentage of trapped NO_x that is released above a prescribed temperature T(^{o}C) during the temperature ramp, given by

$$d_T = 100 \times \left[\frac{\int_T^{T_{final}} C_{NO_x}dT}{\int_{T_{ads}}^{T_{final}} C_{NO_x}dT}\right]. \tag{3.3}$$

In this study we report d_{200} values as 200°C is the nominal threshold temperature above which a downstream SCR is active. In addition to quantifying the overall desorption that occurs above 200°C, we also report the selectivity S_i of the desorbing species,

$$S_i = 100 * \left[\frac{\int_{Tads}^{T_{final}} C_i dT}{\int_{T_{ads}}^{T_{final}} C_T dT}\right], \tag{3.4}$$

where C_i is the concentration of the desorbing species i and C_T is the total concentration of all desorbing species on the same basis (N-1 or C-1). These metrics are useful in defining a standard for catalyst evaluation in this work and are used throughout the rest of the chapter.

3.3.2 NO adsorption with O_2

To assess the performance of Pd-BEA with respect to the first LHCNT function, NO_x adsorption, several baseline experiments were carried out using a simple feed of 400 ppm NO and 2% O_2 at three adsorption temperatures (50, 80, and 150 °C). Each uptake profile (Figs. 3.2a, A.2a, A.2b) exhibits a short period where no NO_x is detected, followed by a longer period of monotonically increasing NO_x effluent concentration that eventually approaches the feed concentration. The period of complete NO_x storage is 10, 2, and 0 s, respectively, for 50, 80, and 150 °C. The protracted approach to the 400 ppm feed concentration indicates a gradual saturation of storage sites. For these experiments, site saturation was only reached during the 300s storage period for the 150°C case (Fig. A.2b), suggesting that the uptake has an even longer saturation time at lower adsorption temperatures. Accordingly, storage efficiency η_{300} (27%, 21%, and 7%) and total storage (184, 160, and 36 μmol NO_x/g-cat) decrease with increasing temperature. Table 3.2 provides the detailed quantified uptake and release values for all experiments (μmol/g-cat, NO/Pd, θ_{NO_x}, η_{300}, and d_{200}).

Table 3.2: NO adsorption and desorption metrics (NO only)

T_{ads} (°C)	Details	NO Ads. (μmol/g-cat)	NO Ads. (mol NO_x/mol Pd)	NO_x Des. (μmol/g-cat)	θ_{NO_x}	$\eta_{NO_{x(300)}}$	d_{200}
50	–	184	0.981	179	0.225	27%	48%
80	–	160	0.853	183	0.195	21%	52%
80	3% H_2O	31	0.167	34	0.038	5%	75%
80	400ppm NO_2	223	1.185	228	0.271	32%	77%
150	–	36	0.192	40	0.044	7%	96%

During uptake most of the effluent NO_x was composed of NO, but between 10 and 18 ppm NO_2 was detected. The NO_2 was higher than the 4 ppm detected in the bypass (~1% impurity of the feed NO_x concentration). While the measured NO_2 effluent concentration is relatively small compared to NO, the apparent concentration is a manifestation of its generation and uptake rates. In other words, the total NO_2 generated during the NO uptake may be higher due to low-temperature NO_2

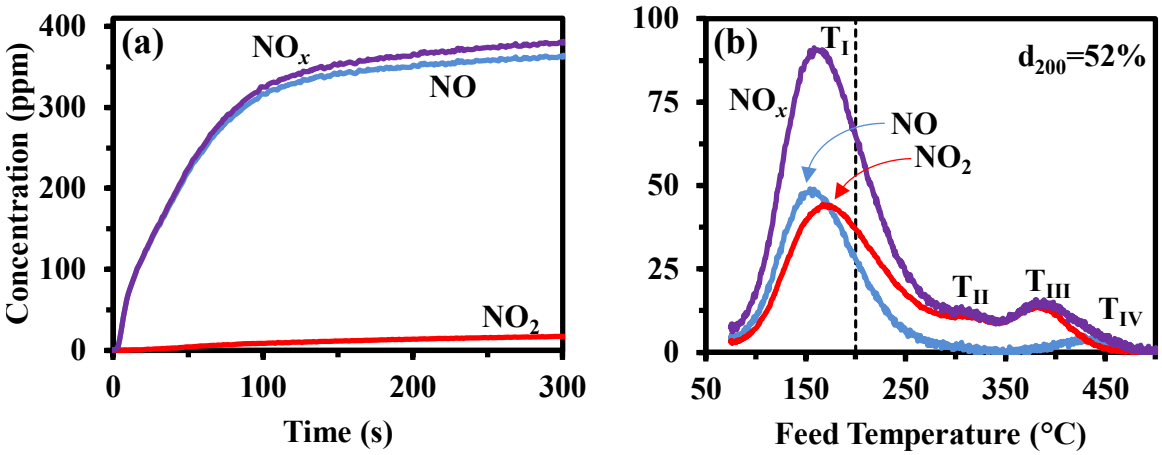

Figure 3.2: (a) Effluent NO_x, NO, and NO_2 during adsorption for 300s at 80°C for a feed of 400ppm NO, 2% O_2. (b) Corresponding desorption curves vs. feed temperature during TPD at 20°C/min following adsorption of (a).

adsorption. The formation of NO_2 is most likely caused by NO oxidation via several potential mechanisms. Earlier literature studies, albeit using Pd-ZSM-5, suggest that NO uptake involves the reduction of two Pd^{2+} to two Pd^{+}, generating NO_2 according to[63,93]

$$2[PdOH]^{+}Z^{-} + NO \leftrightarrow 2Pd^{+}Z^{-} + NO_2 + H_2O. \tag{3.5}$$

Additionally, a recent DFT study on Pd-BEA by Mei et al.[66] suggests that NO oxidizes to NO_2 through the reduction of $Z^{-}H^{+}[PdO]H^{+}Z^{-}$ (isolated PdO) to Pd^{0}, or of $Z^{-}[Pd\text{-}O\text{-}Pd]^{2+}Z^{-}$ (exchanged Pd cation) to form two Pd^{+} sites, one of which adsorbs NO_2. This result is consistent with our analysis that NO_2 binds to the surface, leading to less NO_2 elution. As mentioned in the Experimental section, we performed CO-chemisorption on the Pd-BEA catalyst, which likely reduced PdO to Pd during H_2 pretreatment, and obtained a dispersion value of 20%. These PdO particles may also oxidize NO. Additionally, the homogeneous oxidation of NO to NO_2 may occur within the nanopores of the zeolite framework, even in the absence of Pd, given by

$$2NO + O_2 \leftrightarrow 2NO_2. \tag{3.6}$$

Lobo and coworkers reported such low temperature homogeneous NO oxidation in various zeolites.[101,102] We have confirmed comparable oxidation rates with H-ZSM-5 (Si/Al = 15) in work to be reported elsewhere. Once generated, NO_2 may undergo a series of coupling and disproportionation reactions that lead to the adsorption of NO_2 on the BAS in the form of nitrates as follows:[94,101,102]

$$2NO_2 \leftrightarrow N_2O_4, \tag{3.7}$$

$$N_2O_4 \leftrightarrow NO^+ + NO_3^-, \tag{3.8}$$

and

$$H^+Z^- + NO^+ + NO_3^- \leftrightarrow NO^+Z^- + HNO_3. \tag{3.9}$$

To probe the affinity for NO_2 to adsorb on Pd-BEA, we performed a similar experiment using 400 ppm NO_2 rather than NO (Fig. 3.3). Comparing the results for 80°C adsorption of NO, the uptake of NO_2 was found to be 223 μmol NO_x/g-cat, a 40% increase from the NO feed. This increase is likely due to the increased affinity of NO_2 to form stable surface complexes in the zeolite pores.[94] Unlike for the NO feed, for which NO_2 production steadily increases during the uptake duration, Fig. 3.3a shows a maximum NO formation, suggesting that NO_2 is reduced to NO through rxn. 3.9, the rate of which is dependent on the available fraction of BAS.

To further understand the NO adsorption features, we looked at the desorption profiles for each experiment, plotted as a function of feed temperature (Figs. 3.2b, A.2c, A.2d). Each profile has multiple peaks, indicating several adsorption sites with different binding strengths. The 50°C (Fig. A.2c) and 80°C (Fig. 3.2b) desorption profiles have four peaks while the 150°C (Fig. A.2d) desorption profile has two. These peak temperatures occur over various finite ranges, including T_I (150°C–250°C), T_{II} (275–350°C), T_{III} (350–400°C), and T_{IV} (400–450°C). Comparison of the fraction of stronger held NO_x as measured by the d_{200} (Table 3.2) for the NO feed shows an

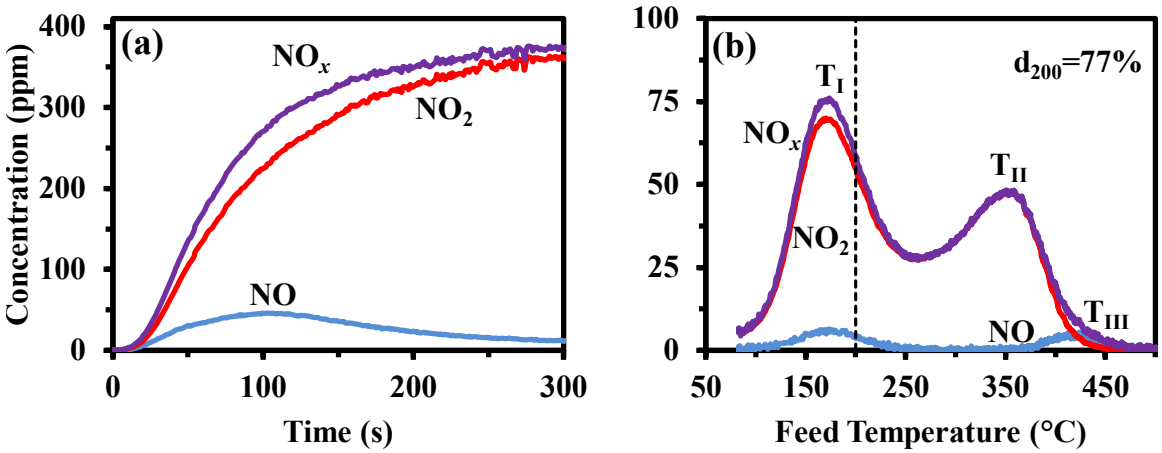

Figure 3.3: (a) Effluent NO_x, NO, NO_2, and N_2O during 80°C adsorption with 400ppm NO_2, 2% O_2. (b) Corresponding desorption profiles vs. feed temperature during TPD at 20°C/min following adsorption of (a).

increase from 48% for the 50°C uptake experiment, to 52% for the 80°C uptake, to 95% for the 150°C uptake. The d_{200} value at 150°C is higher than at lower uptake temperatures because of the lower equilibrium coverage (during uptake) of weakly bound NO. This is an important parameter to identify when interpreting the LHCNT performance because it represents the effectiveness of the PNA function in practice.

To provide a more accurate identification of the surface species leading to these desorption peaks, we performed DRIFTS experiments using H-BEA and 2wt% Pd-BEA (Fig. 3.4). Separate one-hour exposures of each sample were conducted at 80°C using a feed composed of 400 ppm NO, 2% O_2, bal. He. After one hour the spectra did not indicate any notable temporal changes to the peak frequencies. Based on previous literature results, we assign the broad peak at ~2100cm^{-1} to NO^+ on the BAS[103] with possible contribution of a cationic NO^+ complex with NO_2 as shown in the following reaction:[63,67,94,104]

$$NO^+Z^- + NO_2 \leftrightarrow \left(NO^+NO_2\right)Z^-. \tag{3.10}$$

The adsorbed complex is formed through interactions of NO with the BAS and NO_2 that is formed during low temperature NO oxidation. The smaller, narrower peaks

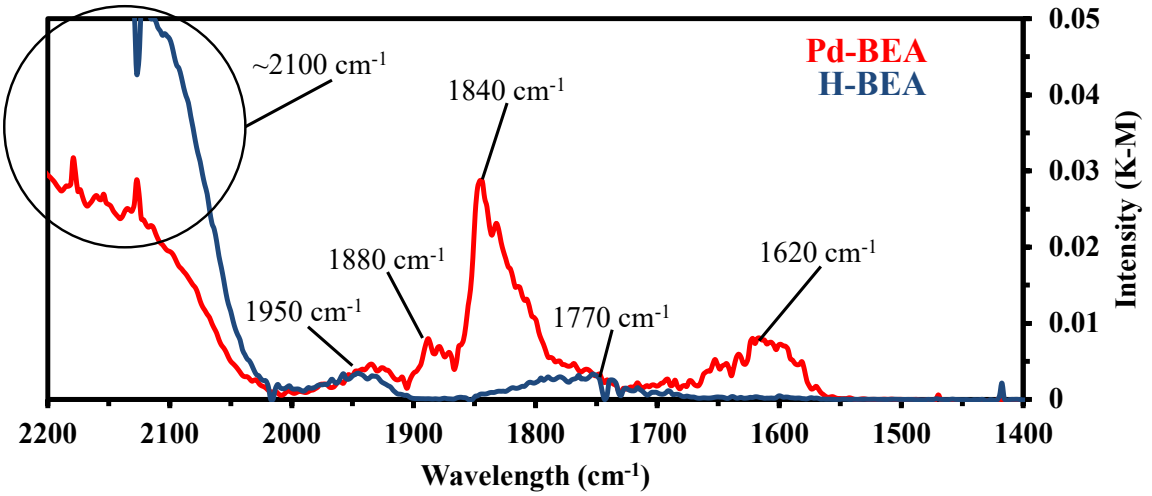

Figure 3.4: DRIFTS spectra for H-BEA and 2wt% Pd-BEA exposed to 400ppm NO, 2% O_2, bal. He at 80°C.

are evidence for adsorption and reaction on protonated and Pd-exchanged sites. The peak at 1950cm^{-1}, which is present for both the H-BEA and Pd-BEA samples, is evidence for the formation of gas phase N_2O_3 that is produced through coupling of NO and NO_2 within the zeolite given by[67,103]

$$NO + NO_2 \leftrightarrow N_2O_3. \tag{3.11}$$

The impregnated Pd-BEA sample exhibits two additional sharp peaks at 1880 and 1840 cm^{-1}, which we assign to NO bound to Pd cations as nitrosyl complexes.[63] The peak assignment at 1620cm^{-1} is less clear. It has been attributed to NO adsorbed on Pd^0 crystallites,[105] but this is not likely given the presence of 2% O_2 in the feed that would oxidize Pd^0 to PdO, which does not adsorb NO very strongly.[60,62] It has also been attributed to NO_2 bound to Pd,[106] or to bidentate nitrate formation stabilized by Pd,[103] given by

$$NO_3^- + Pd^+Z^- \leftrightarrow (O_2NO)^- Pd^{2+}Z^-. \tag{3.12}$$

These assignments are made to sites involving Pd since the 1620 cm^{-1} stretch is not

seen during NO uptake on H-BEA zeolite. On the other hand, the peak at 1770 cm^{-1} appears for both Pd/BEA and H-BEA, and is attributed to N_2O_4 adsorbed on the BAS.[105] These peak identifications support our earlier conclusions that a number of stable surface species are formed as NO adsorbs on the Pd and BAS.

Based on the DRIFTS spectral analysis, the gas phase NO and NO_2 peaks that emerge during temperature-programmed desorption are more easily identified (Fig. 3.2b). The first peak encountered during TPD after the 50 and 80 °C uptakes (T_I ~ 150–170 °C) are assigned to NO and NO_2 desorbing from the BAS. This is supported by the nearly 1:1 ratio of NO_2 to NO of the first peak, indicating the decomposition of N_2O_3, rxn. 3.11.[103] In experiments with H_2O in the feed the NO and NO_2 peaks (or overall peak T_I) are more than 75% suppressed. That is, adsorption of H_2O onto BAS inhibits NO_2 formation and sorption of NO and NO_2. The effects of H_2O are discussed in more detail below.

The second peak (T_{II} ~ 275–350°C) only consists of NO_2, suggesting nitrate decomposition from the BAS or Pd. We have conducted concurrent experiments (not reported here) that establish the existence of two desorption peaks on the protonated zeolite H-ZSM-5, the second of which occurs around 300°C and is composed of only NO_2. The sample devoid of Pd provides strong evidence for formation of NO_2 by the BAS.

The third and fourth peaks (Fig. 3.2b), T_{III} (350–400°C) and T_{IV} (400–450°C), are attributed to the desorption of NO from Pd^+ or Pd^{2+}, i.e.,

$$NO + Pd^+Z \leftrightarrow NO - Pd^+Z^- \tag{3.13}$$

and

$$NO + Z^-Pd^{2+}Z^- \leftrightarrow Z^-\left(NO - Pd^{2+}\right)Z^-. \tag{3.14}$$

The NO_x peak is mostly NO_2 at lower temperature (T_{III}) but shifts to NO at higher

temperature (T_{IV}). This selectivity shift could be due to Pd-catalyzed NO oxidation, which is favorable at lower temperatures, and NO_2 decomposition at elevated temperatures. The desorption peaks for the 150°C uptake experiment (Fig. A.2d) are more difficult to identify due to the decreased adsorption capacity at this higher temperature. Nevertheless, it is expected that while adsorption on the BAS is reduced, adsorption on Pd is comparable to that at lower temperatures due to the higher stability of the sorbed NO.

If we compare the desorption profiles for the NO feed (Fig. 3.2b) to the NO_2 feed (Fig. 3.3b), we note three peaks for the latter: 160, 350, and 430 °C. In this case, most of the desorbing NO_x consists of NO_2, suggesting that NO formation under these conditions is not favored, except for the nitrosonium ion formed by disproportionation in rxn. 3.9. The first peak is therefore desorption of NO_2 from the NO^+NO_2 complex formed in rxn. 3.10.[104] The second peak is likely due to the subsequent desorption of NO^+Z^- reacting with the more stable HNO_3 in the pores to give NO_2 (rxns. 3.7–3.9). Above 350°C, there is a small peak of NO that forms, likely due to decomposition of NO_2 on the Pd. Because there is more NO_2 present in this feed, there is an increased formation of nitrates (T_{II}), leading to 77% NO_x desorption above 200°C. In contrast, the NO-feed experiment has a d_{200} of 52%. From these experiments we conclude that NO uptake on Pd-BEA adsorbs on both BAS and Pd, although the exact oxidation states of Pd cannot be ascertained.

3.3.3 C_3H_6 adsorption

To understand the HC uptake and release performance of Pd-BEA, experiments were conducted with 800 ppm C_3H_6, 2% O_2 for three different uptake temperatures (50, 80, and 150 °C, Fig. 3.5). Table 3.3 provides the measured uptake metrics for each case, including 3% water at 80°C. The data show that the C_3H_6 breakthrough times decrease with temperature, as would be expected for a conventional adsorption process. However, the adsorption profiles show two extrema. For example, after

breakthrough in the 150°C profile there is a sharp increase in the effluent concentration to a local maximum (~610 ppm). The concentration then decreases to a local minimum (~410 ppm) before increasing again as the storage sites become saturated. For the dry experiments the effluent C_3H_6 concentration approaches ~75% of the 800 ppm feed value after 300s. Longer uptake experiments (not shown here) indicate that up to one hour of C_3H_6 exposure is required to achieve complete saturation of the storage sites.

The local minimum suggests additional C_3H_6 uptake occurs via the coupling of adsorbed C_3H_6 upon adsorption onto the BAS. Previous studies have explained the oligomerization of C_3H_6 on acidic zeolites to form higher alkane chains.[107–110] The following set of reactions are representative although far from inclusive:

$$H^+Z^- + H_3C(CH) = CH_2 \leftrightarrow \left[H_3C^+(CH)CH_3\right]^+ Z^-, \tag{3.15}$$

$$\begin{aligned} H_3C(CH) = CH_2 + \left[H_3C^+(CH)CH_3\right]^+ Z^- \leftrightarrow \\ \left[H_3C(CH_2)(CH_2)(H_2C)(CH)^+(CH_3)\right]^+ Z^-, \end{aligned} \tag{3.16}$$

and

$$2\left[H_3C^+(CH)CH_3\right]^+ Z^- \leftrightarrow \left[H_3C(CH_2)(CH_2)(H_2C)(CH)^+(CH_3)\right]^+ Z^- + H^+Z^-. \tag{3.17}$$

Table 3.3: C_3H_6 adsorption and desorption metrics

T_{ads} (°C)	Details	C_3H_6 Ads. (μmol/g-cat)	$\theta_{C_3H_6}$	$\eta_{C_3H_6(300)}$	$S_{C_3H_6}$	S_{CO}	S_{CO_2}	S_{HC}
50	–	857	1.05	58%	1.5%	0.5%	41%	57%
80	–	826	1.01	59%	1.4%	0.6%	49%	49%
80	3% H_2O	155	0.19	20%	5.3%	0.6%	71%	23%
150	–	271	0.33	30%	0%	0%	100%	0%

Reaction 3.15 describes the adsorption of C_3H_6 onto a single BAS forming a C_3 carbocation. In rxn. 3.16 C_3H_6 adds to an existing C_3 carbocation to form a C_6 carbocation.

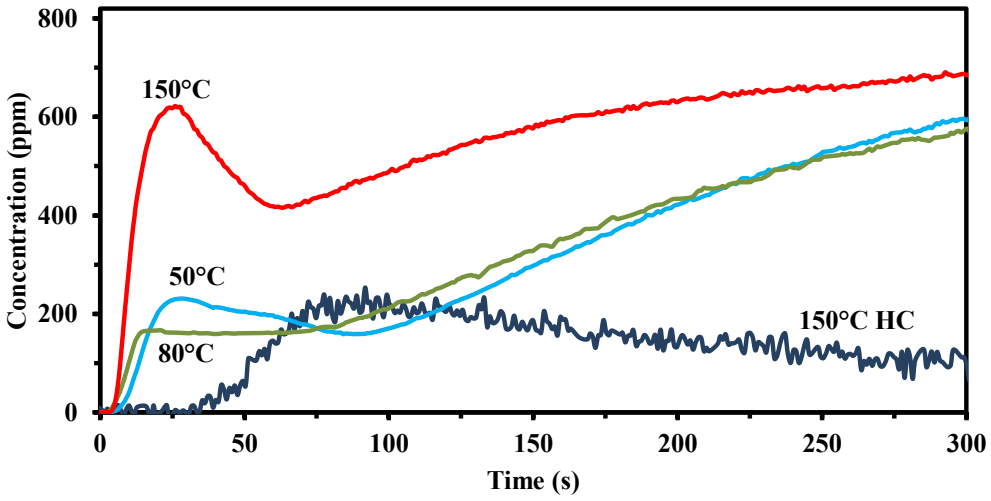

Figure 3.5: Transient adsorption profiles of C_3H_6 during 300s adsorption at 50, 80, and 150 °C for a feed of 800 ppm C_3H_6, 2% O_2. For the 150°C adsorption experiment, effluent HC signal (C_1 basis) is also shown.

Reaction 3.17 describes an alternative path to a C_6 carbocation from the combination of two neighboring carbocations, which frees up an acid site for additional adsorption or reaction. The latter two paths can repeat, leading to a longer surface carbocation, with the extent constrained by the size of the zeolite pores and the number of available BAS. In fact, the estimated fractional coverage $\theta_{C_3H_6}$ for lower temperature (50, 80°C) C_3H_6 uptake (Table 3.3) exceeds unity even though the effluent does not exhibit saturation. For a longer saturation time of 2000s, the fractional coverage is 1.62. This suggests that either sorption sites other than BAS (rxns. 3.16 and 3.17) participate in the uptake or that multilayer adsorption occurs. The adsorption of C_3H_6 onto the Pd cations is certainly expected.

To further demonstrate the existence of these reactions during uptake, the 150°C profile (Fig. 3.5) reveals that HCs other than C_3H_6 are detected in the effluent as indicated by the curve labeled "150°C HC". The "HC" signal is a combined signal on a C_1 basis and includes C_3-C_8 alkanes formed during uptake. [Note: Due to the complexity of the oligomer distribution formed during adsorption, the HC signal accounts for overlap of the spectral regions of each hydrocarbon with some error

(Fig. A.3).] The relative maximum in the C_3H_6 profile occurs at about the same time (~30s) as the appearance of the HC species, and the relative minimum in the C_3H_6 profile is concurrent with the maximum in the HC curve. These data indicate that 150°C is high enough for both oligomerization and desorption to occur, leading to an increase in the C_3H_6 uptake as adsorption sites are freed up. Eventually the desorption of HC species reaches a maximum and then subsides, which is consistent with an increasing concentration of C_3H_6.

DRIFTS measurements provide further support for the oligomerization pathways described above. Steady state DRIFTS spectra were acquired for H-BEA and 2wt% Pd-BEA samples using a one-hour exposure of C_3H_6 and O_2 at 80°C (Fig. 3.6). The set of larger peaks at 2950, 2910, and 2850 cm^{-1} are associated with C-H stretches of the CH_2 group of adsorbed HC species, which are likely present as long-chain alkanes formed during C_3H_6 coupling.[111] The smaller peaks between 1100 and 1300 cm^{-1} are associated with bending of the CH_2 and CH_3 groups of these hydrocarbons (Fig. 3.6b). Additionally, these peaks are evident in both Pd-BEA and H-BEA spectra, as well as in the presence of NO in the feed.

The corresponding desorption profiles for each adsorption experiment provide a more detailed distribution of the oligomerization products. In addition to the adsorption metrics for each experiment, Table 3.3 includes the selectivity of HC, CO_2, CO, and C_3H_6 during desorption, calculated by converting each to a C_1 basis. From 80°C up to 225°C, C_3H_6 and coupling products including C_3H_8, C_5H_{12}, and longer HC chains are released (Fig. 3.7). As the temperature surpasses 200°C, partial oxidation of these species leads to CO formation, as well as a large peak of CO_2 that is 97% depleted by 400°C. Only 1.4% of the desorbing products consists of C_3H_6, indicating the extensive oligomerization that occurs on the acidic zeolite surface. While the 50°C uptake TPD profile (Fig. A.4a) exhibits a similar release of coupled products, the 150°C uptake TPD (Fig. A.4b) shows no evidence for coupling beyond that formed

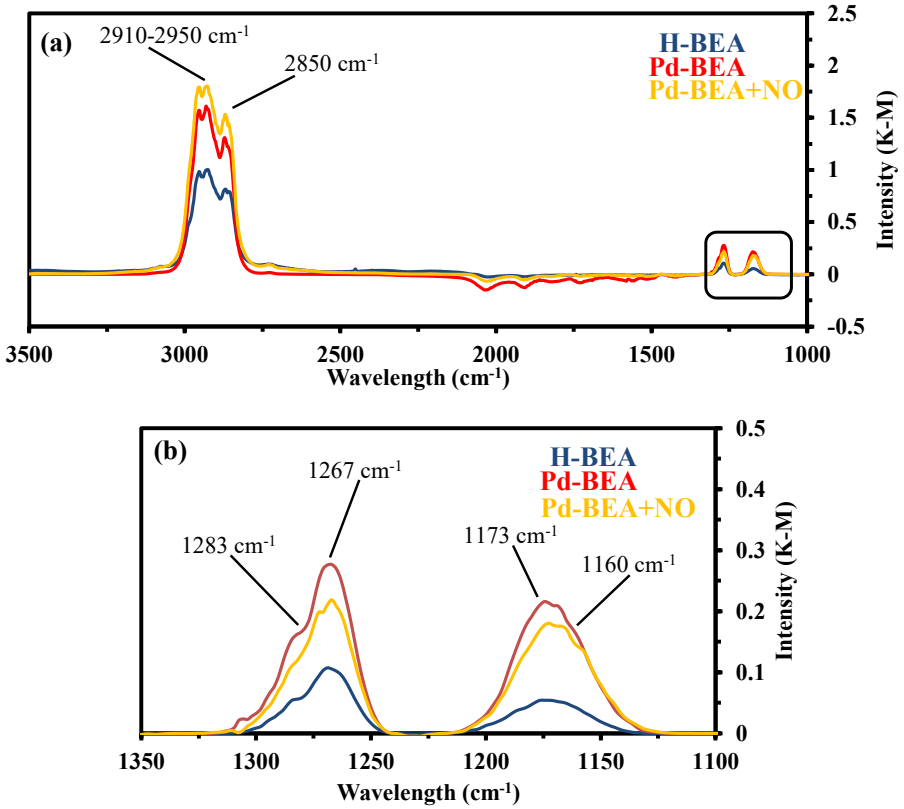

Figure 3.6: (a) DRIFTS spectra for H-BEA and 2wt% Pd-BEA exposed to 800 ppm C_3H_6, 2% O_2, bal. He at 80°C and a spectrum for a feed of 400 ppm NO, 800 ppm C_3H_6, 2% O_2, bal. He on 2wt% Pd-BEA. (b) inset figure for (a).

during adsorption. The only observed product species is CO_2. Because all coupled products (and unreacted C_3H_6) desorb at temperatures below 250°C, it is important to consider this feature when assessing LHCNT performance. Long chain hydrocarbons account for up to 60% of all desorbing species, further highlighting the need to address their formation when considering LHCNT performance and design.

As an additional probe towards understanding the desorption and coupling behavior of C_3H_6, we conducted variable adsorption duration experiments. We add that such an experiment is practically relevant. The same feed was used in each experiment (800 ppm C_3H_6 + 2% O_2 at 80°C), but the storage time was varied between 18 and 300s. For each experiment, the amount of C_3H_6 adsorbed and CO_2 and HC desorbed were calculated and plotted relative to a 300s transient C_3H_6 adsorption profile (Fig. 3.8). While the amounts of trapped C_3H_6 and generated CO_2 increase

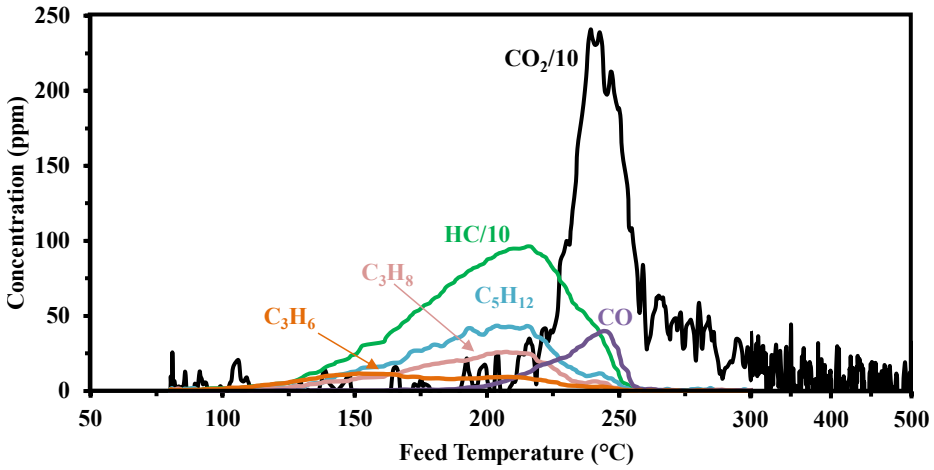

Figure 3.7: Corresponding desorption profiles vs. feed temperature following 80°C adsorption of 800 ppm C_3H_6, 2% O_2. TPD rate was 20°C/min with 2% O_2, bal. Ar. CO_2 and HC are scaled down by a factor of 10.

monotonically with storage time, HCs were not detected until the 98s uptake experiment (Fig. A.5b). Note that at 37s (the local maximum), there is no HC formation because the C_3H_6 coverage is too low for measurable oligomerization (Fig. A.5a). In other words, the initial adsorption mechanism probably follows rxn. 3.15, while additional uptake drives rxns. 3.16 and 3.17. This observation is consistent with the desorption profiles in which very little C_3H_6 desorbs. Therefore, in order to curtail the formation of HCs, the storage time should be shortened.

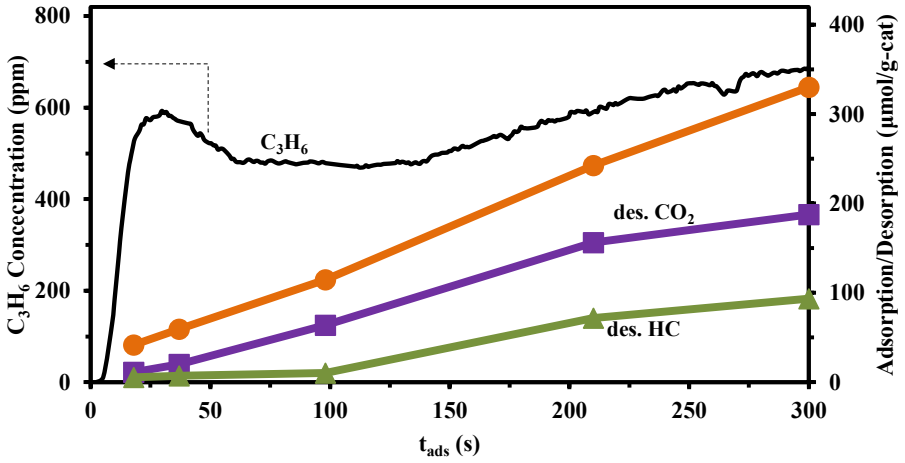

Figure 3.8: Variable storage time experiments for a feed of 800 ppm C_3H_6, 2% O_2. C_3H_6 adsorption profile for 300s storage is overlapped with values of adsorbed C_3H_6, desorbed CO_2 and HC.

3.3.4 Combined adsorption of NO and C_3H_6

To assess the ability of the LHCNT to adsorb multiple species and to understand how the individual uptake and release features are impacted by the presence of the other species, experiments were conducted for a feed containing both NO and C_3H_6. Uptake performance metrics are reported in Tables 3.4 and 3.5 for NO and C_3H_6 uptake/release, respectively, for a variety of conditions. These values are useful in comparing the behavior of Pd-BEA across the various feeds.

Table 3.4: NO adsorption and desorption metrics (NO+C_3H_6)

T_{ads} (°C)	Details	NO Ads. (μmol/g-cat)	NO Ads. (mol NO_x/mol Pd)	NO_x Des. (μmol/g-cat)	θ_{NO_x}	$\eta_{NO_{x(300)}}$	d_{200}
50	–	83	0.44	59	0.10	13%	83%
80	–	61	0.32	37	0.07	9.8%	86%
80	3% H_2O	23	0.13	25	0.03	7%	93%
80	400ppm C_3H_6	88	0.47	63	0.11	13%	74%
80	NO_2	287	1.53	206	0.35	40%	88%
150	–	26	0.14	17	0.03	5%	95%

Table 3.5: C_3H_6 adsorption and desorption metrics (NO + C_3H_6)

T_{ads} (°C)	Details	C_3H_6 Ads. (μmol/g-cat)	$\theta_{C_3H_6}$	$\eta_{C_3H_6(300)}$	$S_{C_3H_6}$	S_{CO}	S_{CO_2}	S_{HC}
50	–	768	0.94	53%	2.8%	0.95%	38%	58%
80	–	832	1.02	57%	2.1%	0.8%	36%	61%
80	3% H_2O	63	0.05	14%	35%	0.9%	64%	0%
80	400ppm C_3H_6	494	0.60	42%	1.5%	0.9%	56%	42%
80	NO_2	442	0.54	30%	2.2%	2.1%	86%	9%
150	–	321	0.392	30%	0%	0%	100%	0%

Data for the combined uptake and release experiment featuring the baseline condition of 80°C adsorption with 400 ppm NO and 800 ppm C_3H_6 in 2% O_2 are illustrated in Fig. 3.9. In addition to the concentration of various species, the feed and catalyst temperatures are also plotted. Like the profiles without C_3H_6 (Fig. 3.2), NO breakthrough is followed by a monotonic increase in the NO concentration (Fig. 3.9b). However, there is a notable decrease in NO_x storage efficiency from 21% to 10%, indicating inhibition of NO_x adsorption. There is also a negligible level of NO_2 during the uptake and a small but measurable formation of N_2O. The adsorption

efficiency of C_3H_6 exhibits a 2% decrease to 57% and maintains a high adsorption capacity with continued evidence for coupling. Below 200°C, the primary desorbing species include NO (Fig. 3.9c) and HC, after which small amounts of CO and C_3H_6 are released (Fig. 3.9c). Just above 250°C, a large peak of CO_2 is formed, concurrent with a small N_2O peak and a 25°C exotherm in the catalyst temperature. As the feed temperature surpasses 275°C, NO steadily desorbs and the CO_2 concentration tapers to zero.

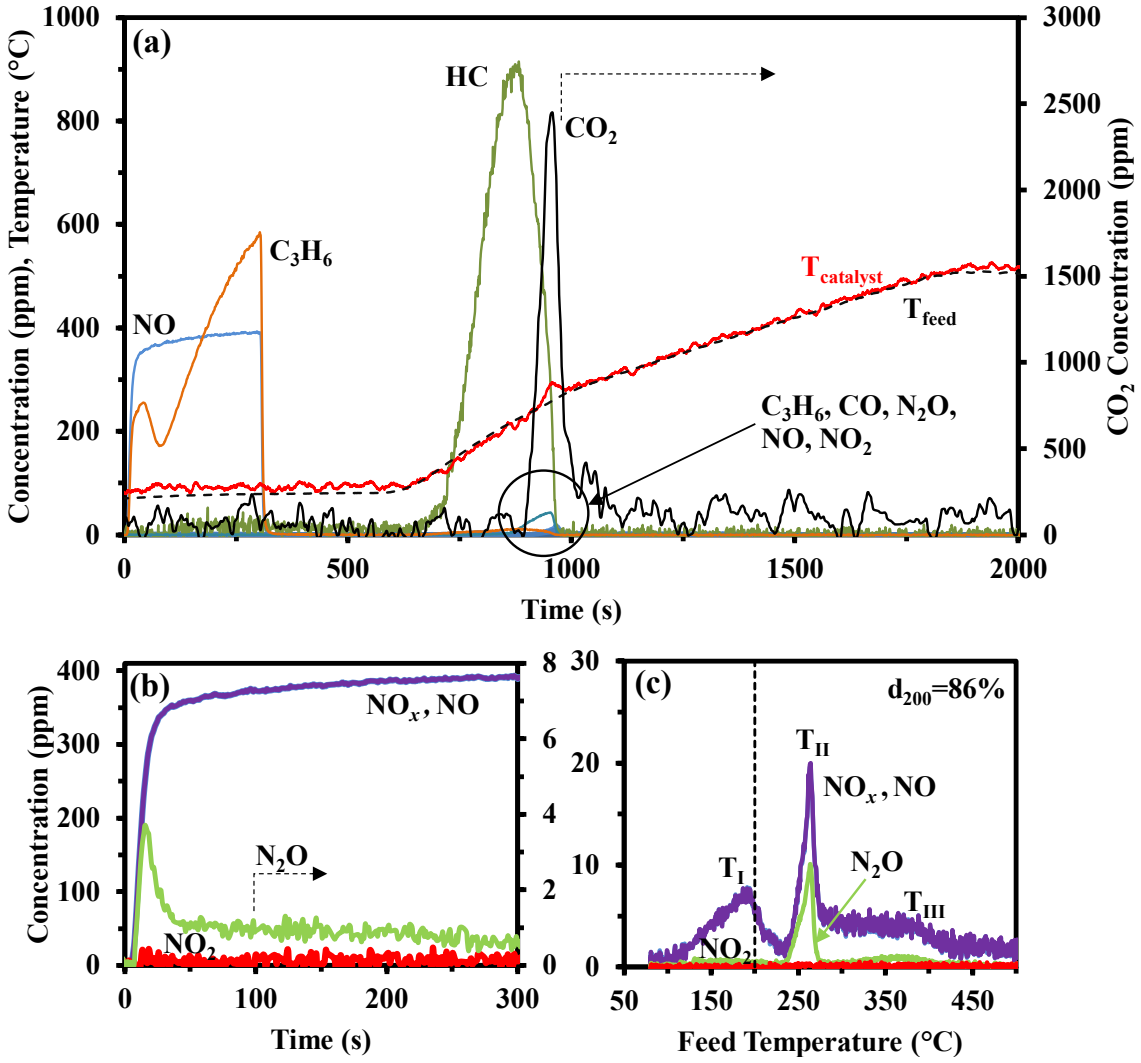

Figure 3.9: (a) Transient profiles for 400 ppm NO, 800 ppm C_3H_6, 2% O_2 at 2500sccm. (b) Effluent concentrations of NO_x and N_2O during adsorption. (c) Corresponding TPD profile.

To better understand the lack of NO_2 formed during uptake in the presence of

C_3H_6, experiments were conducted using NO_2 in place of NO in the feed at 80°C (Fig. 3.10). The presence of C_3H_6 leads to a 29% increase in NO_x uptake when compared to the NO_2-only feed (Fig. 3.3a), and a significant, 473% increase compared to the NO + C_3H_6 feed (Fig. 3.9b). There is strong evidence for low-temperature reduction of NO_2 to NO indicated by the large amount of NO formed at the start of the uptake along with some N_2O. Li et al.[112] showed that the acidity of NaY zeolite, which has the same pore limiting diameter as BEA (6.7Å), is capable of NO_2 reduction by C_3H_6 at room temperature; our results show a similar trend. During adsorption with C_3H_6, NO_2 disproportionation proceeds as in reactions R3—R5 to form nitrosonium and nitrate ions. The nitrosonium ions react with C_3H_6 in the BEA pores through an electron transfer mechanism to produce neutral NO and a propylene radical cation via the following reaction:

$$NO^+ + C_3H_6 \rightarrow [C_3H_6]^{\bullet +} + NO. \tag{3.18}$$

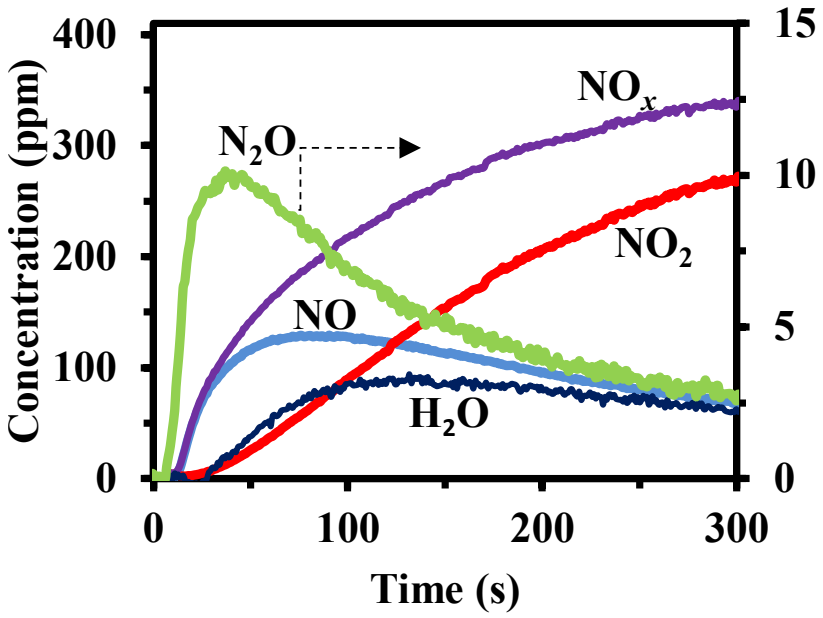

Figure 3.10: Effluent concentrations of NO_x and N_2O during adsorption for 300s at 80°C for a feed of 400 ppm NO_2, 800 ppm C_3H_6, 2% O_2 at 2500sccm.

Based on the large NO elution during uptake (Fig. 3.10), the NO formed by reaction

R14 likely does not adsorb on BAS, but does adsorb on Pd. The nitrate ions then react with the radical and BAS to from organic nitro complexes and H_2O according to the reaction

$$NO_3^- + [C_3H_6]^{\bullet +} + H^+Z^- \rightarrow C_3H_5NO_2 + H_2O + Z^-. \tag{3.19}$$

In fact, there is a sustained release of H_2O during co-adsorption of NO_2 and C_3H_6, supporting the chemistry described here. We rule out C_3H_6 oxidation because there is no detection of CO or CO_2 during uptake. Simultaneously, the C_3H_6 radicals can react with empty acid sites produced by rxn. 3.19 according to

$$[C_3H_6]^{\bullet +} + Z^- \rightarrow C_3H_6^+Z^-. \tag{3.20}$$

Because the NO_2 + C_3H_6 reactions are faster than the coupling rxns. 3.16 and 3.17, a 47% decrease in C_3H_6 uptake from 832 to 442 μmol/g-cat is observed. In other words, C_3H_6 coupling competes with NO_2 uptake on BAS. We conclude that any NO_2 that forms in the case of NO + C_3H_6 is either co-adsorbed with C_3H_6 through stable surface complexes or is reduced to NO or N_2O.

Additionally, residual NO_2 reduction to NO can occur on Pd via C_3H_6 oxidation and may explain the minor amount of N_2O formed during uptake. There is also a minor amount of N_2O formation at each of the three uptake temperatures for the NO + C_3H_6 feed (Fig. 3.9c, A.6a, A.6b). This is likely a byproduct of NO_x reduction, which has been reported to occur on Pt even in the presence of O_2.[72,113] N_2O formation is commonly encountered during lean NO_x reduction by hydrocarbons at higher temperatures, so this residual amount is expected.[17,114]

The corresponding desorption profiles for the combined feed of C_3H_6 and NO introduce several new features (Figs. 3.9c, A.6c, A.6d). Because of the lower NO_x uptake in the presence of the inhibiting C_3H_6, the total amount of desorbing NO_x

is lower (61 vs. 160 μmol NO_x/g-cat), but 86% of the NO that is trapped is released above 200°C. Two rather sharp NO peaks are encountered for the 50 and 80 °C cases. These contrast with the smoother NO_x desorption profile comprising a large, low temperature peak and a broad, higher temperature peak for the simpler feed (Fig. 3.2a). The first peak commences near the uptake temperature and has a maximum at ~190°C, and is smaller than the second peak at ~260°C. The second peak is unique to the co-adsorption experiment, and it occurs concurrently with the generation of N_2O and the localized temperature excursion (Fig. 3.9a). This increase in temperature is caused by the oxidation of HCs and leads to a rapid increase in the desorption rate and a sharp desorption peak. A third broad peak starting at ~300°C monotonically decreases out to 500°C. Comparing Fig. 3.9c to 3.2b, the lower temperature peak (T_I) is suppressed, which supports our earlier assignment of the lower temperature NO_x peak to a zeolitic acid site; with a stronger affinity for the BAS, C_3H_6 inhibits NO adsorption. While suppressing NO uptake at lower temperature, the presence of C_3H_6 leads to a moderate shift in the NO_x desorption temperature of T_I from 150 to 190 °C. Adsorbed C_3H_6 may inhibit the transport of desorbing NO or may block adsorption at lower temperature sites, causing the NO to reside at more thermally stable binding sites. The intensity of the broad third NO_x peak is much less impacted by the C_3H_6 because NO strongly adsorbs on Pd, which is not as inhibited by C_3H_6.

The appearance of N_2O and lack of NO_2 during desorption are manifestations of C_3H_6 oxidation. The notable N_2O peak that occurs at ~250°C is consistent with the aforementioned lean NO_x reduction on precious metal catalysts, which exhibits a maximum rate of formation at intermediate temperatures (200–300 °C).[33] The desorption profile for the 150°C uptake experiment (Fig. A.6d) has no low temperature peak, and there is less N_2O formation, likely due to the decreased adsorption capacity. As shown in Table 3.4, there is up to 30% discrepancy between the calculated adsorbed NO_x and desorbed NO_x + N_2O (N basis), suggesting that the remaining

nitrogen is accounted for by N_2 formation.

A comparison of the C_3H_6 uptake with NO (Fig. A.7) to without NO (Fig. 3.5) reveals a much smaller inhibition of C_3H_6 uptake by NO, which is also evidenced by the adsorption metrics in Tables 3.3 and 3.5. Only minor differences are seen in the nonmonotonic features associated with coupled C_3H_6 uptake and oligomerization. However, in the presence of NO_2, the C_3H_6 profile consists of 9% HC and 86% CO_2 (Table 3.5), indicating that the NO_2 does indeed inhibit the rate of C_3H_6 coupling. In the presence of NO the coupling is unaffected, resulting in up to 60% HC formation. Additionally, the desorption profiles with NO (Fig. A.7) compared to without NO (Fig. 3.7, A.4) show minimal impact on the HC distribution based on high HC and CO_2 yields. While C_3H_6 largely impacts NO uptake, there is little effect of NO on C_3H_6 uptake on Pd-BEA.

To further probe the effect of C_3H_6 on NO uptake, the concentration of C_3H_6 was reduced from 800 to 400 ppm (Fig. 3.11). This resulted in increased NO_x storage efficiency from 9.8% to 13.3%, which is undoubtedly a result of the reduced concentration of the inhibiting C_3H_6. The intensity of the first desorption peak is much larger, confirming that the first peak is affected by the presence of C_3H_6 (Fig. 3.11b). This observation further supports the assignment of the first peak to NO storing on the BAS. Regarding the other NO_x desorption peaks, the temperature of the sharp peak (250°C) and the shoulder (390°C) do not change between the two cases, but the magnitudes slightly increase in the reduced concentration case. This would indicate that C_3H_6 can also impact NO adsorption on Pd, either due diffusional limitations created by the coupling products or because of adsorption of C_3H_6 on Pd. We therefore conclude that the lesser the concentration of inhibiting HCs in the feed, the higher the uptake of NO.

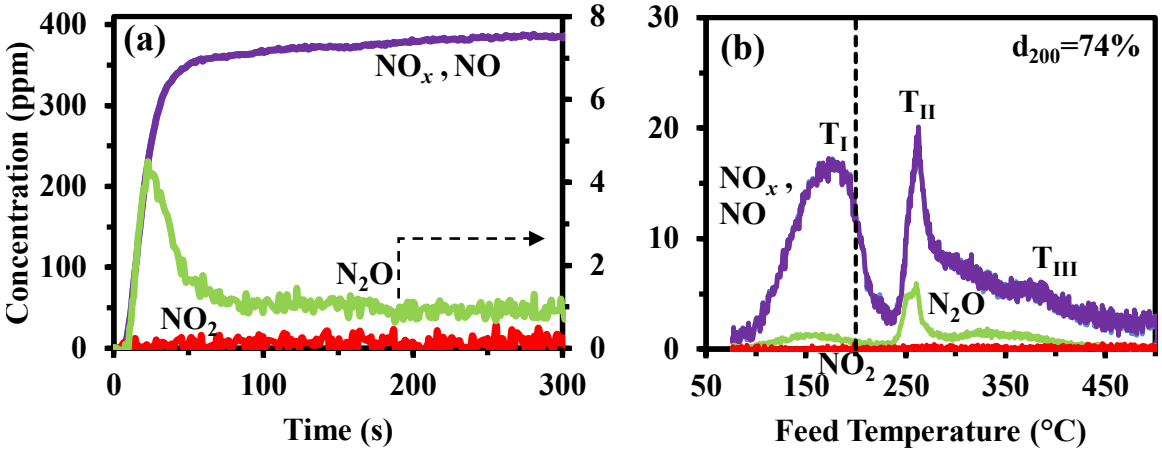

Figure 3.11: (a) Effluent NO_x and N_2O during 80°C adsorption for a feed of 400 ppm NO, 400 ppm C_3H_6, 2% O_2 at 2500sccm and (b) corresponding TPD profile.

3.3.5 Adsorption of NO and C_3H_6 with H_2O

Vehicle exhaust contains high levels of H_2O, making it imperative to assess its impact. The addition of 3% H_2O is significantly detrimental for both NO_x and C_3H_6 uptake at 80°C. The NO_x trapping efficiency decreases from 21.1% in the absence of H_2O to 4.8% in its presence (Table 3.2, Fig. 3.12a), while the C_3H_6 trapping efficiency decreases from 59% to 20% (Table 3.3, Fig. 3.12b). Zeolites with sufficiently low SAR are known to be effective in adsorbing water in the form of H_3O^+ on protonated sites according to

$$H_2O + H^+Z^- \leftrightarrow [H_3O]^+ Z^-, \tag{3.21}$$

so these findings are expected.[115]

The inhibition of NO is mainly due to the competitive adsorption on the BAS, but the H_2O uptake may also hinder access to Pd ion exchange sites.[67] Further evidence of the H_2O inhibition is apparent in the NO_2 profile (Fig. 3.12a), which exhibits its highest concentration just as NO breakthrough occurs. This indicates that the H_2O has a higher affinity for the BAS than does NO_2, preventing NO_2 adsorption. Because the H_2O blocks the BAS, any NO_2 that forms during this uptake experiment is likely caused by reduction of Pd, and not by the BAS. While the amount of adsorbed

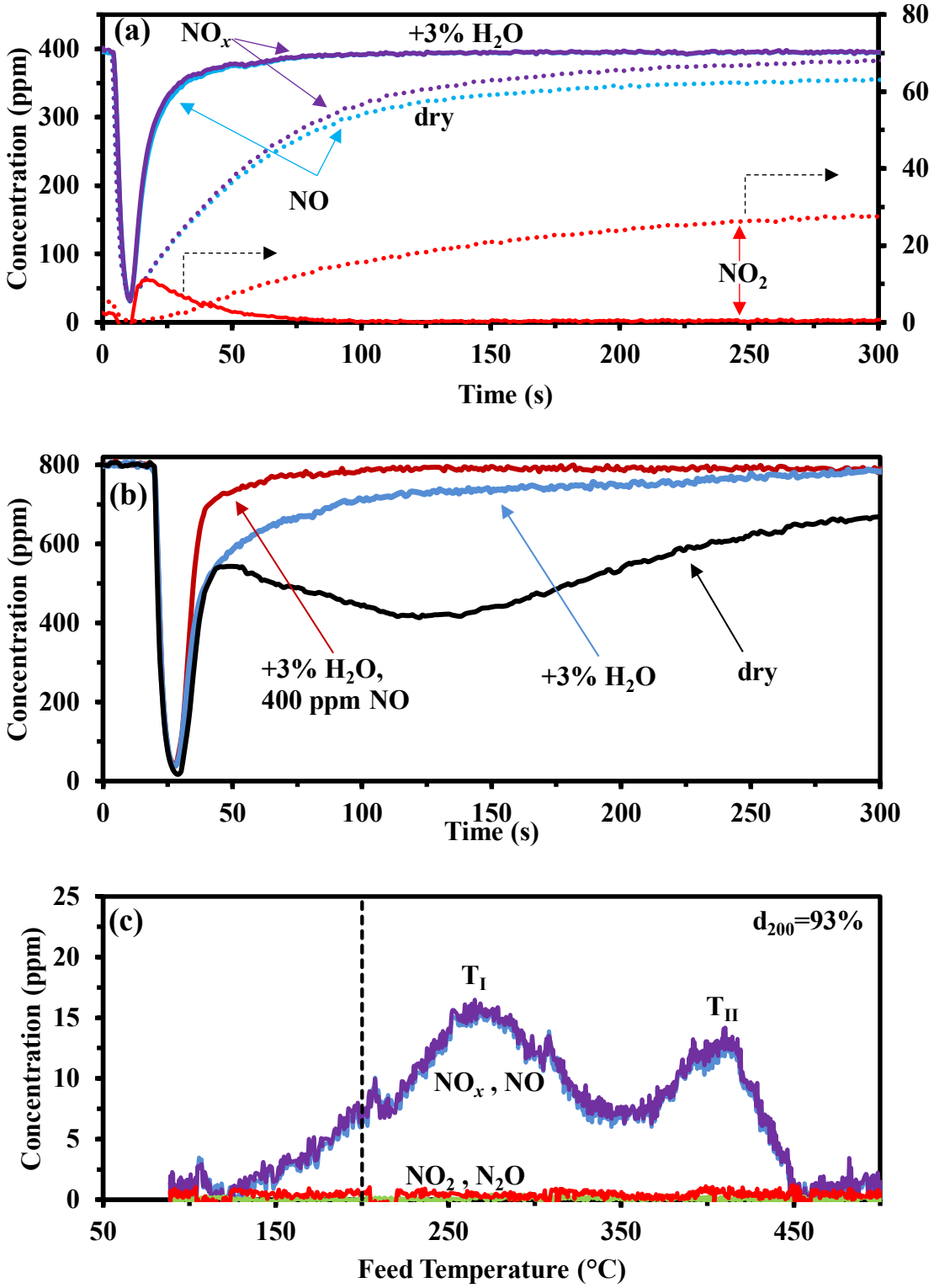

Figure 3.12: (a) NO_x adsorption profiles with (solid line) and without (dotted lines) 3% H_2O at 80°C (2% O_2, 400 ppm NO). (b) C_3H_6 adsorption profiles with and without H_2O. (c) NO_x TPD (400 ppm NO, 800 ppm C_3H_6, 3% H_2O).

NO_x on the BAS is limited in the presence of water, desorption is delayed, with 75% desorbing above 200°C (Table 3.2).

A similar inhibitive effect of H_2O is seen on C_3H_6 adsorption (Fig. 3.12b). Again, strong inhibition by H_2O is apparent, which results in an 81% decrease in storage efficiency of propylene. The desorption profile contains 5% C_3H_6, 71% CO_2, and 23% HC, indicating that the presence of H_2O reduces the coupling rate by blocking a large fraction of BAS. This phenomenon is also observed in the transient adsorption profile in which the profile for the wet experiment does not show the concentration decrease after the initial uptake. In fact, we see that the initial uptake regime for each case is identical, suggesting that a fraction of C_3H_6 adsorption sites is not inhibited by H_2O.

In a co-adsorption experiment of NO, C_3H_6, and H_2O, the adsorption of both NO and C_3H_6 is further suppressed, leading to a 27% and 59% decrease in storage efficiency, respectively (Table 3.4 and 3.5). The reduction of NO uptake is expectedly due to increased inhibition by C_3H_6. The decrease in C_3H_6 uptake is likely due to a combination of H_2O preventing HC coupling reactions and the inhibiting effect of NO_2 that is released during initial uptake (Fig. 3.12a). During uptake of C_3H_6 and NO in the presence of H_2O, the NO_2 peak is not present, suggesting its reaction with C_3H_6 as in reactions R14 and R15. This is further evidenced by the lack of coupled products desorbing from the wet (0%) or NO_2 (~9%) feeds (Table 5). During desorption, the first NO desorption peak that occurs around 200°C without H_2O is non-existent, and two peaks instead occur at 268 and 412 °C (Fig. 3.12c). The lack of the first peak, which we suggest is due to the dissociation of N_2O_3, indicates that H_2O prevents the disproportionation of NO_2, and instead forms HNO_3 according to[104,116]

$$3NO_2 + H_2O \leftrightarrow 2HNO_3 + NO, \tag{3.22}$$

which most likely adsorbs on Pd in the presence of H_2O. The desorbing NO at T_I would therefore be attributed to HNO_3 decomposition, and T_{II} is likely NO nitrosyl

stored on Pd. The d_{200} in the presence of water increased from 86 to 93 %, indicating that while inhibition of adsorption on the BAS is detrimental to the storage capacity of the catalyst, it is advantageous in delaying desorption to higher temperatures.

3.3.6 Discussion of coupling effects

We have thus far presented a detailed analysis of the combined NO and C_3H_6 uptake and release on Pd-BEA for both dry conditions and in the presence of H_2O. The multi-functional effectiveness of the Pd-BEA requires evaluation of coupling effects of each of the three adsorbing species (NO_x, C_3H_6, and H_2O). The data show that Pd-BEA is limited in its ability to trap NO in the presence of either C_3H_6 or H_2O. This is mainly due to C_3H_6 and H_2O uptake on the BAS and Pd, inhibiting NO uptake. However, the NO that does adsorb has a d_{200} value of >80% in the presence of the inhibiting species, indicating that NO adsorption on Pd is more stable than on the BAS. Studies have shown that certain species such as C_2H_4 and CO can enhance NO uptake on Pd-zeolite materials in the presence of H_2O. One potential mechanism is an enhanced reduction of Pd(II) to Pd(I) by the reductant, leading to a larger fraction of the latter that may bind NO more strongly. Another explanation is attributed to the formation of an NO-R complex on the Pd sites that prevents H_2O adsorption.[65,67,117]

While the exact details of this phenomenon is a part of an active ongoing debate, the predominant mechanism may depend on a number of factors including the Pd loading and the zeolite structure (i.e., BEA vs. SSZ-13). Concurrent PNA studies in our research group with Pd-exchanged SSZ-13, a small pore zeolite, show much higher NO uptake with NO:Pd ~1 in the presence of H_2O, CO, and C_2H_4, which will be reported in a later work. In the present work, however, we do not observe enhancement of NO uptake using C_3H_6. We believe that C_3H_6 molecules may be too large to allow for the co-adsorption of NO on Pd, and instead may lead to diffusional limitations. We do however note the increased adsorption of NO_2 in the presence of

C_3H_6, although this benefit is primarily due to BAS interactions and not Pd. As a C_3H_6 trap, Pd-BEA is extremely effective in the absence of water, as indicated by the high storage amount relative to the total number of active sites. This is due to the coupling effect of C_3H_6 that effectively increases the number of storage sites. The presence of water, however, inhibits C_3H_6 adsorption by blocking BAS and limiting oligomerization. Regarding its ability to oxidize C_3H_6 and reduce NO, the Pd-BEA catalyst is somewhat effective. We have shown strong evidence for hydrocarbon reduction of NO and NO_2 during the TPD and found that above 225°C all desorbing hydrocarbons are oxidized to CO_2 regardless of the presence of NO in the feed.

Finally, regarding the stability of Pd-BEA, recent work by Gu et al. suggests that certain reductants including H_2 and CO can have a detrimental irreversible effect on the state of Pd.[118] While this type of investigation is beyond the scope of this work, it is certainly important to address the long-term the stability of Pd on these materials for practical use.

3.4 Conclusions

The effectiveness of a 2wt% Pd-BEA monolith sample as an LHCNT material was examined through adsorption and desorption experiments in a flow reactor. The data were evaluated in terms of the large number of adsorption steps and reactions on the multiple site types comprising the Pd-BEA. The desorption profiles indicate that there are at least three types of NO_x desorption peaks, and DRIFTS results were used to confirm the existence of various moieties bound to the surface during adsorption. We show the existence of competitive adsorption between NO and C_3H_6 on BAS, and a strong inhibitive effect of both species in the presence of H_2O. However, it was found that C_3H_6 can delay NO desorption to higher temperatures due to diffusional blockage and BAS adsorption inhibition. Compelling evidence was found that C_3H_6 oligomerizes on the surface during adsorption, which leads to increased adsorption on the BAS. In summary, Pd-BEA was found to exhibit a variety of interesting chem-

ical interactions, enabling a deeper understanding of the co-uptake and assessment of the integration of NO and HC trapping. This data could be used in conjunction with a predictive model for coupled NO and hydrocarbon trapping to optimize the design and operating strategies of the LHCNT.

Chapter 4: NO + C_3H_6 adsorption, release, and conversion: LHCNT reactor model

This chapter describes a global kinetic model developed to predict various features of the Pd-BEA LHCNT including NO and C_3H_6 adsorption, desorption, and conversion. The model aims to capture as much detail as possible while reducing computation time using a low dimensional formulation of a single monolith channel.

4.1 Introduction

Because low temperature NO_x and HC trap materials are quickly gaining popularity in both the research and commercial communities for addressing NO_x emissions, it is important to fundamentally understand how these materials function. Developing a predictive model for catalysts is useful for better understanding the reaction mechanism, screening performance of new/improved materials, and for optimizing a catalytic system, thereby reducing experimental efforts. In the current literature there has been no modeling work performed on PNA materials in combination with HCs. Ambast et al. recently developed a model for NO adsorption on Pd/ZSM-5 with and without H_2O in the feed.[59] As mentioned in Chapter 3, the exact NO uptake mechanism is under debate. The general consensus is that NO uptake proceeds through adsorption on the Bronsted acid sites (BAS) and highly dispersed Pd cations, the distribution and oxidation state of which depend on the zeolite framework and acidity. Given the mechanistic uncertainty in the exact model, multiple kinetic models must be considered. The work by Ambast et al. describes a microkinetic model for NO adsorption through two reaction schemes. Scheme I involves the reduction of isolated Pd^{2+} to Pd^{+}, which bind NO (refer to Chapter 5, eqns. 5.1 and 5.2). In contrast, Scheme II involves the reduction of PdO_x particles to generate NO_2

and adsorb NO through the formation of nitrates. The study was able to successfully predict the NO uptake and release behavior for both schemes, underscoring the challenge of settling on a single mechanism.

In this chapter we investigate the use a model to predict the behavior of the Pd/BEA LHCNT using experimental data from Chapter 3. In that work, through a combination of transient adsorption/desorption experiments and in situ DRIFTS, a series of reactions was determined that can explain the observed performance features of the catalyst. The primary objective is to use the experimental data to develop a kinetic model that predicts the behavior of the PdBEA for a variety of feed conditions. The model serves as a foundation for building a more detailed and robust model that can predict the performance of other LHCNT architectures and materials.

4.2 Experimental

A 2wt.% Pd/BEA coated monolith was used to generate data for model fitting and parameter estimation. Chapter 3 outlines the preparation and details of the monolith sample. Steady state and transient experiments were conducted in the vertical quartz tube reactor. Experiments were conducted using a total flow rate of 2500sccm, corresponding to a gas hourly space velocity (GHSV at STP) of 32k h^{-1}. The catalyst sample was degreened in 5% O_2 at 600°C for 4h. Before each experiment, a sample pretreatment was conducted in 5% O_2 at 500°C for 30 min, followed by sample cooling under a flow of Ar to the desired adsorption temperature of 50, 80, or 150 °C. To begin the adsorption, the adsorbate feed was injected into the reactor using an electronically actuated 4-way switching valve. The monolith was exposed to the feed mixture for 300s, after which the adsorbate feed was switched off and the effluent concentrations were monitored until the NO and/or C_3H_6 concentration reached zero, purging the catalyst of weakly adsorbed gases. Next, the desorption was initiated by ramping the temperature at a rate of 20 °C/min to 500°C in a flow of 2% O_2.

Temperature programmed oxidation experiments were conducted using a feed of 800 ppm C_3H_6, 400 ppm NO or both with and without 3% H_2O in the presence of 2% O_2. The feed was first established in the bypass, then followed by a switch to the reactor and held under a constant flow until the catalyst was saturated and the outlet concentration of NO or C_3H_6 reached the feed value. The furnace temperature was then increased from 50 to 500 °C at a rate of 5 °C/min. Steady state experiments were conducted in a similar fashion. While the concentration of the feed was stabilized in the bypass, the furnace was set and maintained at a constant temperature for the duration of the experiment. Once the reactor conditions were stable, the feed was switched to the reactor and held constant until the measured outlet concentration was steady.

4.3 Model development

A one-dimensional model was developed following that of Joshi et al. for the LHCNT model.[119–121] This type of model is useful for describing a single monolith channel with uniform catalyst distribution where a number of mass and energy balances are solved, each incorporating convection, diffusion, and reaction effects. The equations to be solved comprise a system of partial differential equations as follows. The fluid phase concentration of each species is represented by

$$\frac{\partial X_{j,f}}{\partial \mathrm{t}} = -\overline{u}\frac{\partial X_{j,f}}{\partial z} - \frac{k_{m,o}(T)}{R_{\Omega_1}}(X_{j,f} - X_{j,s}), \tag{4.1}$$

the washcoat concentration of each species as

$$\varepsilon_s \frac{\partial X_{j,s}}{\partial \mathrm{t}} = \frac{k_{m,o}(T)}{\delta}\left(X_{j,f} - X_{j,s}\right) + \frac{1}{C_T}\left[\sum_{i=1}^{rxn}\left(\vartheta_{ij}R_i(\theta, X_s, T)\right) - R_{ads,j} + R_{des,j}\right], \tag{4.2}$$

the energy balance of the system, including the temperature of the fluid as

$$\frac{\partial T_f}{\partial t} = -\overline{u}\frac{\partial T_f}{\partial z} - \frac{h}{R_{\Omega_1}\rho_f c_{p,f}}(T_f - T_s), \tag{4.3}$$

and of the washcoat as

$$\delta\rho_s c_{p,s}\frac{\partial T_s}{\partial t} = \delta k_s \frac{\partial^2 T_s}{\partial z^2} + h\left(T_f - T_s\right) + R_{\Omega_2}\sum_{i=1}^{rxn}\left(-\Delta H_{rxn,i}R_i(\theta, X_s)\right), \tag{4.4}$$

and the site balance on the surface of the washcoat as

$$\frac{\partial\theta_k}{\partial t} = \frac{\sum_{i=1}^{rxn}\left(\vartheta_{ik}R_i\left(\theta, X_{j,s}\right)\right)}{C_{T,k}}. \tag{4.5}$$

For this model the following three types of active sites ($C_{T,k}$) are defined: C_Z, the concentration of available BAS in the form Z^+H^-; C_{ZPdOH}, the Pd-exchanged sites on a single BAS in the form $[Pd\text{-}OH]^+Z^-$; and C_{ZPdZ}, the concentration of bridged Pd sites in the form Z^-PdZ^-. In order to estimate the amount of each type of Pd site, the nature of the zeolite framework was considered in combination with the ratio of the NO_x peaks in the TPD representing Pd sites. Because the BEA zeolite has larger pores and more open cages, we expect most of the Pd to be exchanged on a single BAS. However, we cannot rule out the existence of bridged Pd as the distribution of aluminum sites may be more concentrated in some instances.[122] To estimate the ratio of C_{PdOH} versus C_{ZPdZ} in the catalyst, we estimate the positional probability of two aluminum atoms in the 12-member ring of the BEA pore. We assume based on Loewenstein's rule[123] that no aluminum atoms will be located directly next to each other (i.e., zero T sites away). As illustrated in Fig. 4.1a, the fraction of C_{ZPdZ} sites is thus related to the probability of two aluminum atoms existing one T site away from each other (n=12), and the fraction of C_{ZPdOH} is based on two aluminum atoms being more than two sites apart (n=42), where n is the number of possible configurations

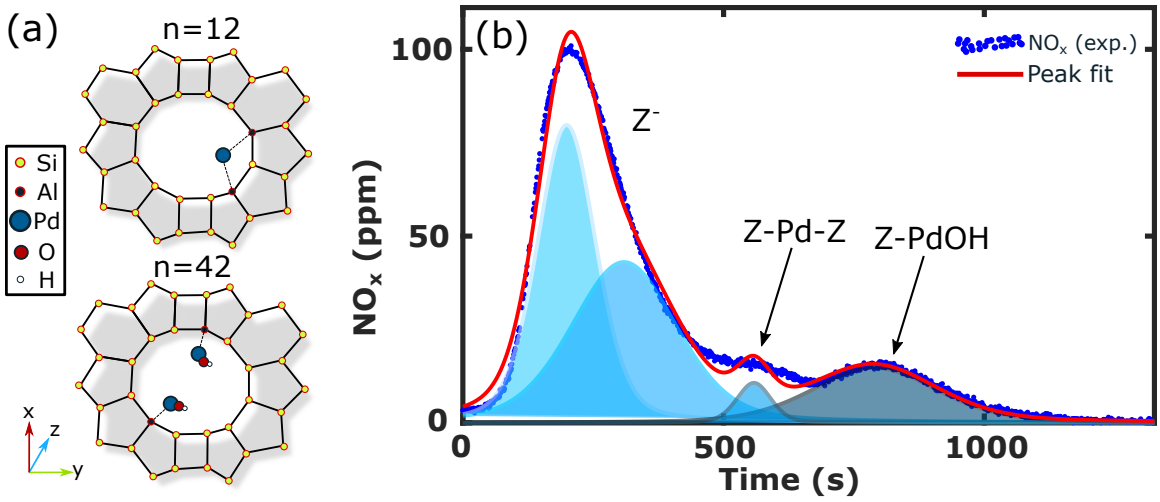

Figure 4.1: (a) Illustration of (top) $Z^{-}PdZ^{-}$ sites and (bottom) $[Pd\text{-}OH]^{+}Z^{-}$ distributed within the 12-member ring of BEA. (b) Peak deconvolution of NO_x TPD profile at 50°C .

within the ring. We thus estimate the fraction of C_{ZPdOH} to be ~78%. This is a simplified estimate as it does not account for bond energies between atoms nor the neighboring T sites in the three-dimensional structure of the pore (i.e., bridging of Pd between two proximal T sites in the z-direction.)

To confirm the site distribution using TPD data (400 ppm NO adsorbed at 50°C), a peak deconvolution was computed using a hybrid Gaussian/Lorentzian peak distribution fitting the NO_x profile to four peaks. Assuming peaks III and IV (500 and 750 s) represent the Pd sites, the relative fraction of C_{ZPdOH} based on the area of each peak is ~83%, which is in agreement with the statistical analysis of the Pd sites. Based on these two calculations, we use a value of 80% for the fraction of C_{ZPdOH} and 20% for C_{ZPdZ}. By estimating the total number of exchange sites in the zeolite based on the SAR, we obtain a value of 820 μmol/g-cat. Based on the mole fraction of Pd in the catalyst, 45% of these sites are exchanged with Pd. Combining this value with an estimate for the total cite concentration in mol/m^3 washcoat and accounting for the fact that each $Z^{-}PdZ^{-}$ site occupies two BAS, we obtain the following site concentrations: C_{Total} = 410 mol/m^3; C_{Pd}=0.45×C_T = 185 mol/m^3; C_{ZPdOH} = 0.8×C_{Pd} = 148 mol/m^3; C_{ZPdZ} = 0.2×C_{Pd} = 37 mol/m^3; and C_Z = C_T –2 C_{ZPdZ} – C_{ZPdOH} = 188

mol/m^3.

For the site balances in this model we include 12 coverages (θ_k), which are listed in Table 4.1. These are used in the rate expressions described in the reaction schemes below.

Table 4.1: Site balance for coverages θ_k

Site	Balance
θ_Z	$1-\theta_{Z-NO}+\theta_{Z-NO_2}+\theta_{Z-NONO_2}+\theta_{Z-C_3H_6}+\theta_{HC-Z}$
θ_{ZPdOH}	$1-\theta_{ZPd}+\theta_{ZPd-NO}+\theta_{ZPd-NO_2}$
θ_{ZPdZ}	$1-\theta_{ZPdZ-NO}$

The following set of equations represents the inlet conditions for the system:

$$X_{j,f}(x,t=0)=X_{j,f0}, \tag{4.6}$$

$$X_{j,s}(x,t=0)=X_{j,s0}, \tag{4.7}$$

$$T_f(x,t=0)=T_{f0}, \tag{4.8}$$

$$\theta_k(x,t=0)=1 \text{ (adsorption)}, \tag{4.9}$$

and

$$\theta_k(x,t=0)=0 \; or \; \theta_k(x,t_{ads}) \text{ (desorption)}. \tag{4.10}$$

The boundary conditions are represented by

$$z=0,\; X_{j,f}=X_{j,f,in}(t), \tag{4.11}$$

$$y=0,\; -D_{e,j}\frac{\partial X_{j,s}}{\partial y}=k_{m,o}\left(X_{j,f}-X_{j,s}\right), \tag{4.12}$$

$$y=\delta,\; \frac{\partial X_{j,s}}{\partial y}=0 \text{ (no flux)}, \tag{4.13}$$

$$z=0,\; T_f=T_{f,in}(t), \tag{4.14}$$

and

$$z = 0 = L :, \frac{\partial T_s}{\partial z} = 0 \text{ (no flux)}. \tag{4.15}$$

Table 4.2 defines the variables used in eqns. 4.1–4.15.

Table 4.2: Table of nomenclature for low-dimensional model equations

$c_{p,f}$	Fluid phase heat capacity	$\overline{u}$	Average fluid velocity
$c_{p,s}$	Heat capacity of washcoat	$X_{j,f}$	Concentration of species j in fluid phase
C_T	Total gas phase concentration	$X_{j,s}$	Concentration of species j in washcoat
$C_{T,k}$	Total site concentration of species k	δ	Effective wall thickness
h	Heat transfer coefficient	$\Delta H_{rxn,i}$	Heat of reaction
$k_{m,o}$	Overall mass transfer coefficient	ε_s	Washcoat porosity
k_s	Thermal conductivity of washcoat	ϑ_{ij}	Stoichiometric coefficient of species j for reaction i
$R_{ads,j}$	Rate of adsorption of species j	θ_k	Fraction site coverage of species k
$R_{des,j}$	Rate of desorption of species j	ρ_f	Fluid density
R_i	Reaction rate i	ρ_s	Washcoat density
T_f	Fluid phase temperature	$R_{\Omega 1}$	Transverse diffusion length for flow area
T_s	Washcoat temperature	$R_{\Omega 2}$	Transverse diffusion length for washcoat

The model formulation is based on the following assumptions: laminar, fully developed flow entering the channel; a channel length that is much greater than the hydraulic diameter (this allows for negligible axial diffusion in the fluid and washcoat phases); and physical properties are constant.[119] The Method of Lines with discretization in the axial-direction is used to solve the resulting system with respect to time. A first-order upwind scheme is used for the first derivative approximations and a second order central difference formula was used for the second derivative approximations. For this work, the axial direction is divided into n=30 segments, and the resulting discretized equations (with boundary and inlet conditions) are solved. Evaluation of the boundary conditions in the discretized model using the method of false boundaries yields the solid phase temperature equations at z=0 and z=L. The IVP system solver ODE15s from the MATLAB function library is used to solve the system equations. ODE15s is an implicit, adaptive time step, stiff ODE solver that uses finite difference methods of order 4/5 (Runge-Kutta) to solve the equations with respect to time. It evaluates the Jacobian numerically and monitors the rate of convergence to adjust the step size accordingly.

One of the main characteristics that makes this model computationally efficient

is the use of overall mass transfer coefficients that describe the diffusion of species in the fluid phase into the washcoat while neglecting washcoat diffusional limitations. The overall mass transfer coefficient is calculated by

$$\frac{1}{k_{m,o}} = \frac{1}{k_{m,e}} + \frac{1}{k_{m,i}}, \tag{4.16}$$

where $k_{m,e}$ and $k_{m,i}$ are the external and internal mass transfer coefficients for a given species. These values are calculated using the external and internal Sherwood numbers, which relate the convective and diffusive rates of a species between the bulk fluid phase/fluid-washcoat interface and between the washcoat/fluid-washcoat interface, respectively. The following equations relate the Sherwood numbers to the mass transfer coefficients:

$$k_{m,e} = \frac{D_f Sh_e}{4R_{\omega 1}}, \tag{4.17}$$

and

$$k_{m,i} = \frac{D_s Sh_i}{4R_{\omega 2}}, \tag{4.18}$$

where D_f and D_s are species diffusivities in the fluid and solid phases of the channel, respectively. $R_{\omega 1}$ and $R_{\omega 2}$ represent the characteristic length scales for the fluid phase and the washcoat. The external Sherwood number (Sh_e) is typically calculated as a position-dependent value represented by[124]

$$Sh_e = Sh_{e,\infty} + \frac{0.272\frac{P}{z'}}{1 + 0.083\left(\frac{P}{z'}\right)^{2/3}}, \tag{4.19}$$

where $Sh_{e,\infty}$ is 3.608 for a round square channel, $z' = z/L$, the dimensionless length down the channel, and P is the transverse Peclet number defined for each gaseous species in the system as

$$P_i = \frac{\tau_D}{\tau_C} \triangleq \frac{R_{\Omega_1}^2/D_{f,i}}{L/\bar{u}} \triangleq \frac{R_{\Omega_1}^2 \bar{u}}{L D_{f,i}}. \tag{4.20}$$

The transverse Peclet number P represents that ratio of transverse diffusion (τ_D) to convection (τ_C) times. Smaller values of P indicate faster diffusion to the monolith walls. Fig. 4.2 shows the Peclet number as a function of temperature from 50 to 500 °C for each of the species used in the model. The diffusivities were calculated using correlations of the Lennard-Jones potential of each species according to Fuller[125] (Table 4.3). Based on these calculations, C_3H_6 has the largest value for P (0.25) at 50°C, indicating slower diffusion to the wall than axial convection compared to the other species. However, the diffusion time is still four times shorter than the convection time. Balakotaiah and West calculated the exit conversion of various channel geometries as a function of P and found that in a circular channel for P < 0.1 conversion exceeds 99%.[126] For the model described here, the values for P quickly approach 0.1 by 200°C, and drop to an asymptotic value between 0.02 and 0.05, so we do not expect any mass transfer limitations that would limit reactivity at higher temperatures.

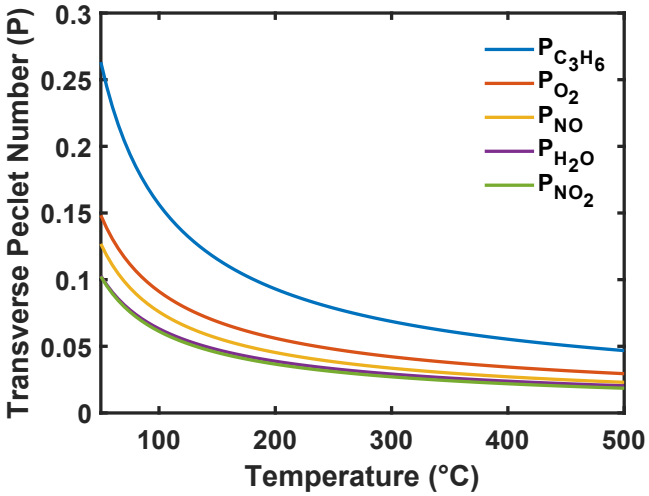

Figure 4.2: Calculated transverse Peclet number vs. temperature for reacting species C_3H_6, O_2, NO, H_2O, and NO_2.

To calculate the internal Sherwood number (Sh_i), a correlation involving the Thiele modulus is used. The correlation was reported by Joshi et al. and is calculated

by[119,121]

$$Sh_i = Sh_{i,\infty} + \frac{\Lambda\Phi_i^2}{1+\Lambda\Phi_i}. \tag{4.21}$$

In this model the channel is represented as rounded square, so the values for $\mathrm{Sh}_{i,\infty}$ and Λ are 3.65 and 0.39, respectively.[124] The Thiele modulus was calculated using the following expression:

$$\Phi_i^2 = \frac{R_{\Omega 2}^2}{D_{s,i}} \times \sum_j \left(-\frac{R_{i,j}(X_{j,s},\theta)}{C_0} \right). \tag{4.22}$$

There are certain exceptions to using variable Sherwood numbers. For the case of a very long channel, a constant Sherwood number may be adequate, and for a slow reaction (Thiele modulus <<1), a constant value may be used for the Sh_i. It is important to consider these approximations when developing the LHCNT model. In our model we use a variable Sh_i to account for variations in the Thiele modulus given the large number of reactions in the system.

Table 4.3: Temperature-dependent parameters

Parameter	Expression	Parameter	Expression
$\bar{u}$	$0.5525\times\mathrm{T}$ m/s	D_{f,CO_2}	$0.825\times10^{-9}\times\mathrm{T}^{1.7148}$ m^2/s
$D_{f,NO}$	$1.13\times10^{-9}\times\mathrm{T}^{1.7418}$ m^2/s	$D_{f,HC}$	$3.42\times10^{-10}\times\mathrm{T}^{1.75}$ m^2/s
D_{f,NO_2}	$1.4\times10^{-9}\times\mathrm{T}^{1.7418}$ m^2/s	D_{f,N_2O}	$0.93\times10^{-9}\times\mathrm{T}^{1.7148}$ m^2/s
D_{f,O_2}	$1.13\times10^{-9}\times\mathrm{T}^{1.7019}$ m^2/s	D_{f,N_2}	$1.158\times10^{-9}\times\mathrm{T}^{1.75}$ m^2/s
D_{f,C_3H_6}	$5.275\times10^{-10}\times\mathrm{T}^{1.75}$ m^2/s	$D_{f,CO}$	$1.13\times10^{-9}\times\mathrm{T}^{1.7148}$ m^2/s
D_{f,H_2O}	$1.62\times10^{-9}\times\mathrm{T}^{1.7033}$ m^2/s		

Table 4.4 describes the fixed parameters that were used in the model. The values for $R_{\Omega 1}$, $R_{\Omega 2}$, and δ were estimated from measurable properties of a single channel taken from a 400 cpsi monolith. $R_{\Omega 1}$ is equal to $0.25\times d_h$, the hydraulic diameter of the channel, which is estimated to be 1.08 mm. $R_{\Omega 2}$, the effective washcoat thickness of the channel, and δ, the effective wall thickness, were estimated using the loading of the washcoat (1.3 g/in^3), the washcoat density (ρ_s), and the thickness of the monolith wall (165μm).[119,127] The value for λ, which represents the ratio of the

Table 4.4: Fixed parameters

Parameter	Value
$R_{\Omega 1}$	270 μm
$R_{\Omega 2}$	10 μm
δ	92.5 μm
L	0.05 m
$\mathrm{Sh}_{e,\infty}$	3.608
$\mathrm{Sh}_{i,\infty}$	3.65
ϵ_{wc}	0.42
λ	100
Λ	0.39
C_{pf}	520.3 J/kg/K
C_{pw}	947 J/gk/K
ρ_f	1.78 kg/m^3
ρ_s	2715 kg/m^3
k_s	2.6 W/mK
h	43 W/m^{2}K

fluid phase diffusivty to the effect washcoat diffusivity, is estimated to be ~100, based on adsorption measurements of isobutane on various BEA morpholiges reported by Batalha et al.[128] The porosity of the washcoat was estimated from values reported in literature for BEA zeolite with a similar SAR (12.5).[129]

4.3.1 Model tuning and parameter estimation

In order to build a robust and realistic model, various strategies were employed to estimate kinetic parameters including pre-exponential factors and activation energies. Where applicable, activation energies were fixed based on previous literature values (experimental estimations or DFT calculations), and were set to zero for all adsorption reactions. Pre-exponential factors were mostly estimated using a Levenberg-Marquardt algorithm (*lsqcurvefit* in MATLAB). The algorithm is an efficient tool for least squares curve fitting when many parameters need to be fitted, although due to time constraints no more than two parameters were fitted at a given time. These parameters were fitted to the experimental data reported in Chapter 3, and were then used to validate data at different conditions.

Steady state and transient experiments were conducted on the 2wt% Pd/BEA

sample including C_3H_6 and NO oxidation experiments with and without water in the feed. Fig. 4.3 shows an Arrhenius plot for apparent activation energy resulting from steady state experiments with a feed of 800 ppm C_3H_6 and 2% O_2. From this experiment, the activation energy is estimated to be 88.6 kJ/mol, consistent with recent literature data on other Pd catalysts.[130] The prexponential factor was then fit to experimental data obtained from temperature-programmed oxidation experiments using 800 ppm C_3H_6, 2% O_2, resulting in the simulated light off curve shown in Fig. 4.7. All of the above techniques were thus combined to efficiently estimate the kinetic parameters of the reactions in the reaction network, which is described in the following section. Refer to Table 4.5 for fitted and estimated preexponential factors, activation energies and heats of reaction for the reactions described below.

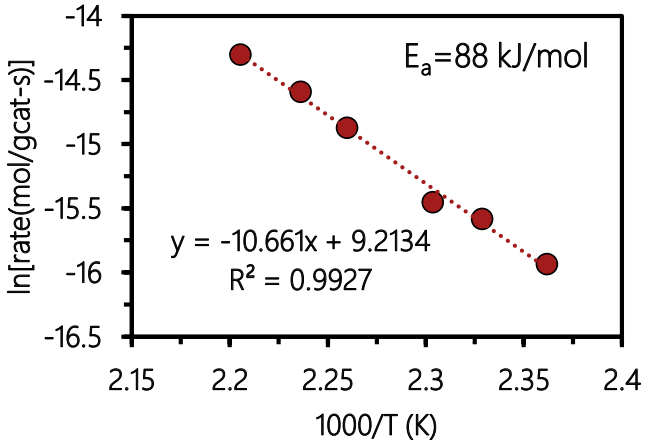

Figure 4.3: C_3H_6 oxidation Arrhenius plot.

4.4 Reaction network

In determining an adequate level of detail for the reaction network, the main objective of this work was not to develop a fully detailed microkinetic model. Rather the aim was to build an 'engineering' model that can accurately (within a threshold error) predict the general behavior of the PdBEA as an LHCNT including NO and C_3H_6 adsorption on BAS or Pd sites and reaction in the absence of H_2O. We used as few reactions as possible to describe the system, but added more detailed steps

Table 4.5: Fitted values for A_i, E_a, and ΔH

Rxn.	A_i (1/s)	E_a (kJ/mol)	ΔH
1	106.49	-35.9	-114.1
2	78.5	0	50.53
3	195	0	
4	200	35	
5	8.59e9	39	
6	5e6	93	
7	1.798e3	0	
8	8.76e12	180	
9	2.47e3	8.5	
10	7.8e7	100	
11	5e8	83	
12	140	0	
13	3.8661e3	19	
14	8.6e3	0	-3.4
15	1e10	155	
16	400	20	
17	100	30	
18	47.2	0	
19	4.6e3	0	
20	4.0135e4	88	-2058
21	1.76e14	80	-283
22	9.366e5	38	-121
23	7.999e8	21	
24	5.3619e8	34	
25	7.999e8	19	

when data trends could not be captured. The reaction network established in this work uses reactions mainly from the results and discussion of Chapter 3, resulting from DRIFTS data and literature comparison in combination with selected reactions adapted from Scheme I from the work by Ambast et al.[59]

4.4.1 NO_x adsorption

The reaction scheme used for adsorption, desorption, and conversion of NO is described in Table 4.6. For simplicity, Z (or Z^-) represents a single BAS in the pore structure of zeolite. Reaction R1 describes the homogeneous low temperature oxidation of NO to NO_2 due to confinement effects in the zeolite pores, as described by the works of Loiland and Lobo.[101,102] This reaction has an overall negative activation

energy, which is -35.9 kJ/mol in this model. Here we represent the NO oxidation as a single step reaction, although it is known to involve a series of intermediate steps. We model the simultaneous uptake of NO and NO_2 on acid sites due to interactions that occur between NO_2 and BAS, leading to the formation of complexes including [$NONO_2$]–Z (R6). Based on the TPD data (Fig. 3.2), we explain in our previous work that the first peak is likely NO and NO_2 desorbing from the BAS. The ratio of NO:NO_2 is ~1, indicating that the two species desorb from the same sites at the same temperature, which we represent by the decomposition of $NONO_2$ (R7). Therefore the adsorption of NO proceeds as follows: NO oxidizes to NO_2 at low temperature in the acidic pores of the zeolite, which then adsorbs on the BAS together with NO cations that form in the pores. The rxn. R1 rate law includes an NO_2 inhibition term that predicts a decrease in the rate of NO oxidation as the concentration of NO_2 increaases. According to rxns. 3.7–3.9 from Chapter 3, the NO_2 that forms from rxn. R1 can dimerize and undergo disproportionation, resulting in the adsorption of NO and NO_2 on the BAS. We capture this chemistry through rxns. R2 and R4 (and corresponding desorption rxns. R3 and R5).

Reaction R8 describes the Pd reduction mechanism that forms NO_2 adsorbed on the reduced Pd-Z. NO can then adsorb on the Pd-Z as in rxn. R10. Additionally, since Pd can exist in a multiplicity of oxidation states within the zeolite framework, we include the adsorption of NO on bridged species Z-Pd-Z (R12,13). Finally, we include the catalytic oxidation of NO on Pd through a global reaction using a rate law with inihbition terms defined in the modeling work of Li et al.[131] In that work, NO oxidation was modeled to occur on Pt, so the parameters are adjusted to fit the NO oxidation data obtained here.

4.4.2 C_3H_6 adsorption

The reaction scheme used for adsorption, desorption and conversion of C_3H_6 is described in Table 4.7. The inclusion of C_3H_6 coupling effects adds some complexity to

Table 4.6: NO reactions on Pd/BEA

Reaction no.	**Reaction**	**Rate *r***
R1	2NO+ $O_2 \rightarrow 2NO_2$	$\frac{k_1 X_{NO}^2 X_{S,O_2}}{1+X_{s,NO_2}}$
R2	$NO^+ + Z^- \rightarrow$ NO–Z	$k_2 C_Z X_{s,NO} \theta_Z$
R3	NO-$Z^- \rightarrow$ NO + Z^-	$k_3 C_Z \theta_{Z-NO}$
R4	$NO_2 + Z^- \rightarrow$ NO_2-Z	$k_4 C_Z X_{s,NO_2} \theta_Z$
R5	NO_2-$Z^- \rightarrow$ NO_2 + Z^-	$k_5 C_Z \theta_{Z-NO_2}$
R6	NO-Z + $NO_2 \rightarrow$ Z-$NONO_2$	$k_6 C_Z X_{s,NO_2} \theta_Z$
R7	Z-$NONO_2 \rightarrow$ NO + NO_2 + Z^-	$k_7 C_Z \theta_{Z-NONO_2}$
R8	2[PdOH]$^+Z^-$+NO $\rightarrow$ PdZ-NO_2 + PdZ +H_2O	$k_8 C_{ZPdOH} X_{s,NO} \theta_{ZPdOH}^2$
R9	PdZ-$NO_2 \rightarrow$ Pd-Z +NO_2	$k_9 C_{ZPdOH} \theta_{PdZ-NO_2}$
R10	PdZ+NO$\rightarrow$ NO-PdZ	$k_{10} C_{ZPdOH} X_{s,NO} \theta_{ZPd}$
R11	ZPd-NO $\rightarrow$ PdZ + NO	$k_{11} C_{ZPdOH} \theta_{ZPd-NO}$
R12	ZPdZ+NO $\rightarrow$ NO-ZPdZ	$k_{12} C_{ZPdZ} X_{s,NO} \theta_{ZPdZ}$
R13	ZPdZ-NO $\rightarrow$ ZPdZ + NO	$k_{13} C_{ZPdZ} \theta_{ZPdZ-NO}$
R14	2NO + $O_2 \rightarrow$ $2NO_2$	$\frac{k_{13} X_{s,O_2} \left[1-\left(\frac{X_{s,NO_2}}{K_{eq}\sqrt{X_{s,O_2} X_{s,NO}}}\right)^2\right]}{K_1 X_{s,NO} + \frac{K_4 X_{s,NO_2}}{K_3 K_1 X_{s,NO}}}$

the model, so global reactions are incorporated where applicable. Simple adsorption of one C_3H_6 molecule on a BAS is depicted in R15 and R16, while R17–19 describe the coupling of C_3H_6 molecules to form higher hydrocarbons (HC). For estimation of heats of reaction and oxidation of these desorbing HCs, the HC carbon chain length was expressed as $n \times C_3H_6$, where n represents the extent of coupling. For example, a value of two suggests two C_3H_6 molecules couple to form C_6H_{12} through the carbocation formation described in rxns. 3.16 and 3.17. The extent of coupling is limited by the number of available sites and the volume of the pore. As a preliminary assumption, we use n=3 in the modeling results presented here. The remaining rxns. R20–25 represent global kinetic reactions involving C_3H_6 that desorbs from the BAS including oxidation to CO_2, partial oxidation to CO, and reduction of NO_x to N_2 and N_2O. In Chapter 3 we discuss the complex chemistry that occurs between C_3H_6 and

NO_2 during adsorption. For simplicity we model this as rxn. R25, although it is a simplification of the chemistry.

Table 4.7: C_3H_6 reactions on Pd/BEA

Reaction no.	Reaction	Rate r
R15	Z + C_3H_6 → Z-C_3H_6	$k_{15}C_Z X_{s,C_3H_6}\theta_Z$
R16	Z-C_3H_6 → Z + C_3H_6	$k_{16}C_Z\theta_{Z-C_3H_6}$
R17	Z-C_3H_6 + C_3H_6 → HC-Z	$k_{17}C_Z X_{s,C_3H_6}\theta_{Z-C_3H_6}$
R18	HC-Z → HC + Z^-	$k_{18}C_Z\theta_{HC-Z}$
R19	2[C_3H_6-Z] → HC-Z + Z^-	$k_{19}C_Z\theta^2_{Z-C_3H_6}$
R20	C_3H_6 + 4.5O_2 → 3CO_2 + 3H_2O	$\frac{k_{20}X_{s,O_2}X_{s,C_3H_6}}{\left(1+K_{C_3H_6}X_{s,C_3H_6}+K_8X_{s,NO}\right)^2}$
R21	C_3H_6 + 3O_2 → 3CO + 3H_2O	$\frac{k_{21}X_{s,O_2}X_{s,C_3H_6}}{\left(1+K_{C_3H_6}X_{s,C_3H_6}\right)^2}$
R22	2CO + O_2 → 2CO_2	$\frac{k_{22}X_{s,O_2}X_{s,CO}}{\left(1+K_{C_3H_6}X_{s,C_3H_6}+K_{CO}X_{s,CO}\right)^2}$
R23	C_3H_6 + 2NO + 3.5O_2 → N_2 + 3H_2O + 3CO_2	$r21\times\frac{k_{23}X_{s,NO}}{\left(1+K_9X_{s,O_2}\right)(1+K_{12}X_{s,NO})\left(1+K_{13}X_{s,C_3H_6}\right)}$
R24	C_3H_6 + 2NO + 4O_2 → N_2O + 3H_2O + 3CO_2	$r21\times\frac{k_{24}X_{s,NO}}{\left(1+K_9X_{s,O_2}\right)(1+K_{12}X_{s,NO})\left(1+K_{13}X_{s,C_3H_6}\right)}$
R25	C_3H_6 + NO_2 +4O_2 → NO + 3H_2O + 3CO_2	$r21\times\frac{k_{25}X_{s,NO_2}}{\left(1+K_9X_{s,O_2}\right)(1+K_{12}X_{s,NO})\left(1+K_{13}X_{s,C_3H_6}\right)}$

4.5 Results and discussion

The following section discusses the modeling results of the following cases: NO adsorption and desorption on Pd-BEA, oxidation of NO and C_3H_6, and co-adsorption of NO + C_3H_6. Each section outlines the relevant chemical reactions occurring during both adsorption and desorption, as well an any global reactions. A discussion is then made relating the experimental observations to the model equations and their predictions.

4.5.1 NO adsorption on Pd/BEA

In order to estimate kinetic parameters for this model, a series of baseline experiments was used, namely the 50°C adsorption and corresponding desorption profiles for a feed of 400ppm NO + 2% O_2 (Figs. A.1a and c). Fig 4.4 shows the uptake of NO_x, NO and NO_2 during the 300s adsorption and the fitted model results. This

result includes all of the NO adsorption reactions, resulting in good fit of the overall NO_x profile as well as the individual NO and NO_2 components. Based on the pre-exponential factors from the parameter fitting, the adsorption consists of a fast and slow adsorption regime. The fast adsorption relates to NO on available Pd after it is reduced to Pd^+, resulting in the steep breakthrough of the NO_x profile. The slow adsorption occurs near the end of the adsorption profile and is related to adsorption on the BAS. This results in unoccupied BAS by the end of the 300s adsorption. The model successfully captures the oxidation of NO to NO_2, the adsorption of NO_2 on Z and NO-Z, and the reduction of $[PdOH]^{2+}$ to PdZ, indicated by the early formation of H_2O.

If we increase the adsorption temperature to 80 and 150 °C, we see a decrease in the formation of NO_2 as well as an overall decrease in NO adsorption. Fig 4.5 shows the experimental NO_x adsorption in terms of the average of the measured adsorption and desorption quantities in μmol/g-cat for each of the three temperatures compared to the estimated results from the model. For the 50°C case, which was used to fit the model, the NO_x adsorption agrees within 7% of the experimental value. at 80°C, the values are even closer, to with 2%, but there is a large discrepancy at 150°C between the model values and the experimental values. However, the trend of generally decreasing adsorption with increasing temperatures is clearly displayed.

4.5.2 NO desorption on Pd/BEA

Figure 4.6 shows the corresponding TPD profile for both the experimental and modeling results for the adsorption experiment described above. Consistent with the experiments, desorption occurs as a series of overlapping peaks, with most of the desorbing NO_x composed of NO_2. We note here that the feed temperature profile used in the model (and all other desorption experiments) was not linear. Rather, it is represented by fitting a polynomial function to the experimental feed temperature profile. While this profile should be linear, due to inconsistencies with the temper-

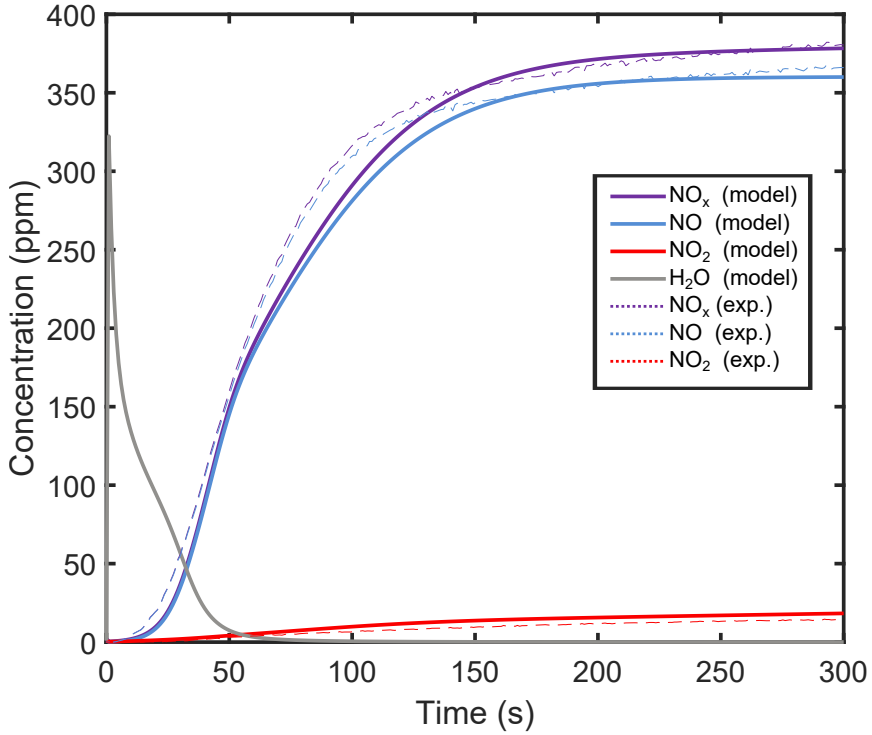

Figure 4.4: Experimental (dashed line) and model (solid line) fit data for NO adsorption at 50°C.

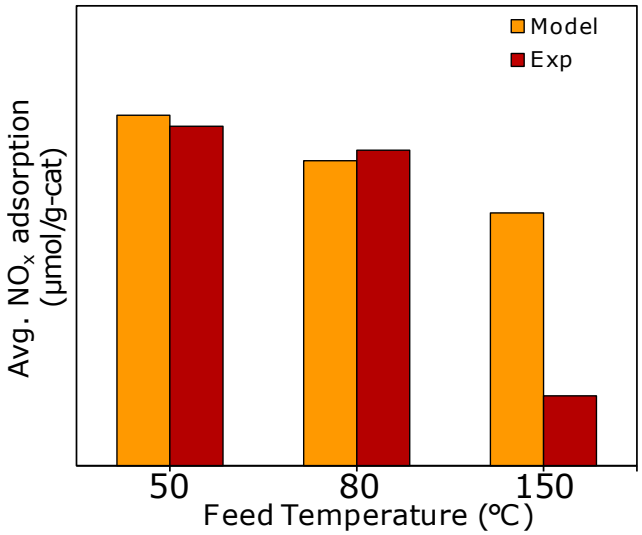

Figure 4.5: Model predicted NO_x adsorption vs. experimental values.

ature controller and heat losses in the furnace, the temperature experiences some overshoot. We correct this in the model, which allows us to obtain a more accurate representation of the TPD profile.

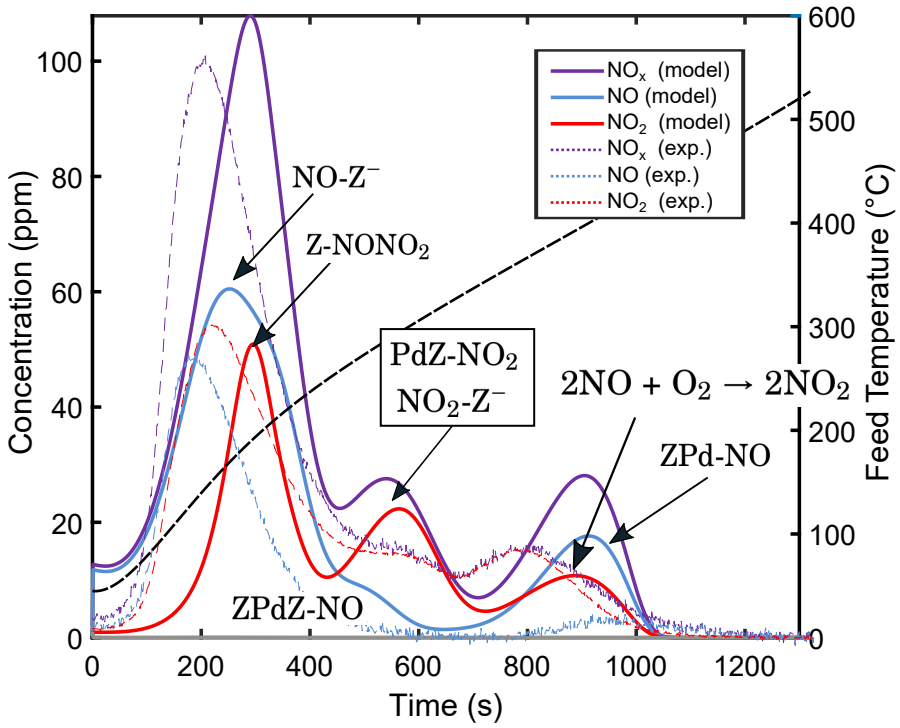

Figure 4.6: NO_x TPD model results vs. experimental data.

Based on the reaction scheme used in the model, the first peak is attributed to the desorption of NO from the BAS (R3), as well as the decomposition of the $NONO_2$ complex that results in equal (1:1) desorption of NO and NO_2 (R7). The second peak consists of NO_2, the desorption of NO_2 from the BAS that were stored in the form of nitrates (R5), and some NO, the desorption from the ZPdZ sites (R13). The fourth peak represents NO desorbing from PdZ (R11), which has a higher binding energy than the nitrates or the NO adsorbed on ZPdZ. As shown in Table 4.5 the binding energies for each of the species increase from 30 to 180 kJ/mol, values that are adapted from the work by Ambast et al.[59] and Mei et al.[66]

There are admittedly some differences between the model TPD profile and the experimental data that result in an imperfect fit. First, there is more NO desorbing from the BAS (first peak) than NO_2 in the model. This is caused by increased adsorption of NO on the acid sites due to the simplification of the reaction scheme. The increased NO_x desorbing from the high temperature peak is due to differences in

the estimation of exposed Pd in the sample. CO chemisoprtion measurements were conducted on a PdBEA sample, and dispersion was measured to be 20%. However, this value was presumed to represent agglomerated Pd as PdO, with the remaining (80%) Pd accessible for NO uptake. Based on these results, the CO chemisorption experiments could suggest that only 20% of the total Pd is accessible for any of the reactions to occur. It is difficult, however, to accurately identify the nature of Pd in this catalyst, so the actual value may lie between these values. Additionally, the TPD peaks are much sharper in the model than in the data, where they are more protracted. This is likely a result of ignoring the washcoat diffusion effects in the model. By ignoring these effects, the species can desorb more freely and solely based on the temperature, resulting in the sharper peaks seen here.

4.5.3 C_3H_6 oxidation

Because C_3H_6 oxidation on Pd is easily modeled and useful for predicting the carbon balance of the system, the model was fitted to experimental TPO data using rxn. R20. The TPO data was obtained using a feed of 2% O_2, 800 ppm C_3H_6, and a ramp rate of 5 °C/min. Note that this rate expression is adapted from the work of Raj et al. and includes C_3H_6 self-inhibition and NO inhibition terms. The C_3H_6 inhibition term is expressed as

$$K_{C_3H_6} = A_{C_3H_6} exp\left(\frac{\Delta H_{C_3H_6}}{RT}\right), \tag{4.23}$$

where $\Delta H_{C_3H_6}$ is the estimated heat of adsorption of C_3H_6, which results in a value of 3 kJ/mol.[132] The activation energy for the oxidation was kept constant at 88 kJ/mol, obtained from our steady state experiments as explained above. Fig. 4.7 shows the agreement between the TPO data and the model fit using this rate expression. Using these estimated parameters as a guideline, we can fit more complex reactions with mixed feeds, as described below.

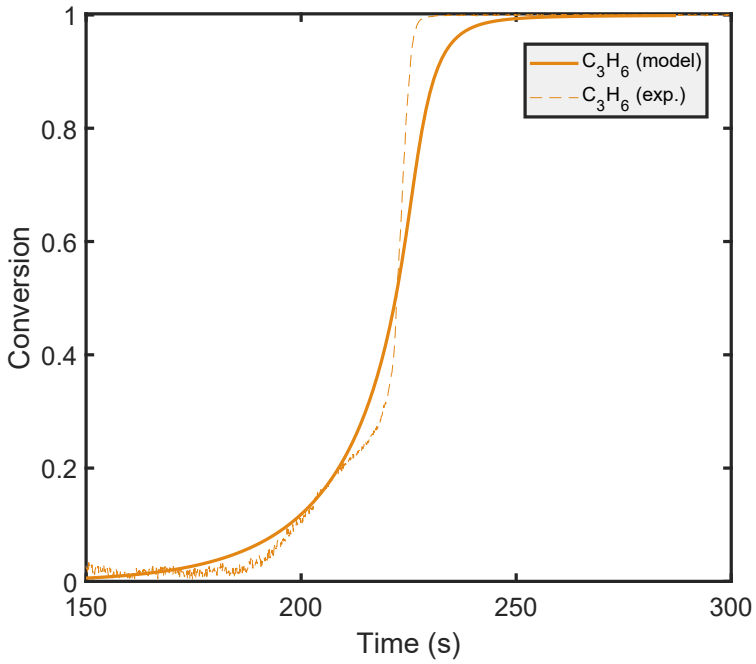

Figure 4.7: C_3H_6 Light-off profile vs. model prediction.

4.5.4 Co-uptake of NO and C_3H_6 on Pd/BEA

Modeling the behavior of NO + C_3H_6 on PdBEA presents a significant challenge. Fig. 4.8 shows experimental data for a TPO experiment using a feed of 400ppm NO, 800ppm C_3H_6, and 2% O_2. The complexities of this system are evident in the NO consumption profiles as well as the C_3H_6 profile. Once the concentrations of both NO and C_3H_6 are stable, the temperature ramp is initiated. Initially, there is a release peak of C_3H_6, proportional to the amount adsorbed. Then there is a large HC peak resulting from the desorption of coupled species that formed during uptake. Around 200°C, NO and C_3H_6 are consumed, resulting in the formation of CO and N_2O. These are the products of the partial oxidation of C_3H_6 at intermediate temperatures.

As the temperature increases, oxidation shifts towards CO_2 formation, and because the temperature is high enough to fully oxidize C_3H_6, NO oxidation is less inhibited, oxidizing instead to NO_2. The exotherm in this case (Fig. 4.8c) is caused by the oxidation of C_3H_6, and is approximately 61°C. This value is slightly lower

than the theoretical value for the adiabatic temperature rise (76°C, rxn. 2.26), but this difference is likely due to heat loss in the reactor.

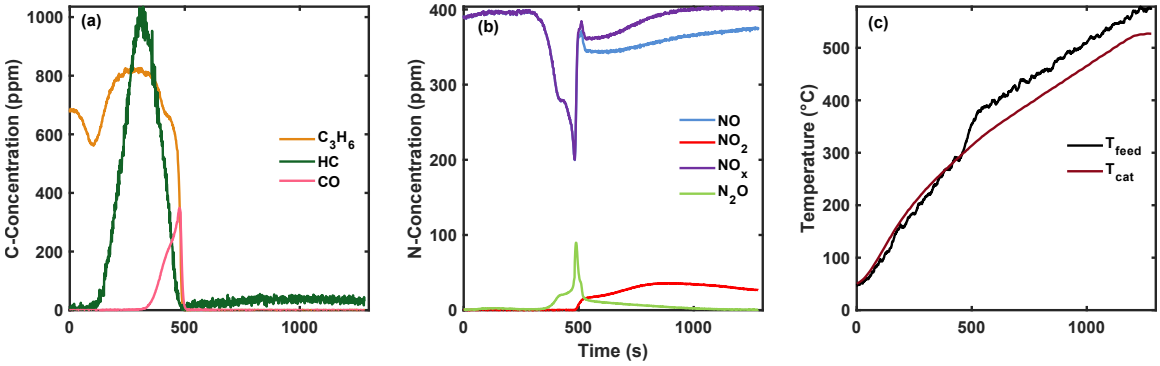

Figure 4.8: NO and C_3H_6 TPO on PdBEA using 400ppm NO, 800pm C_3H_6, 2% O_2 from 50°C to 500°C at a rate of 20° C/min. (a) C based species (b) N species (c) temperature profiles.

To model the system with both NO and C_3H_6 in the feed, the global reactions R21–25 were fitted using combined-feed temperature ramp data from Fig. 4.8. The rate laws and fitting parameters for the inhibition terms for each reaction are based on the work by Khosravi et al., who developed a global steady state kinetic model for the SCR of NO by C_3H_6 on Pt and mixed Pt:Pd oxidation catalysts.[114] For this model, the parameters were adjusted accordingly. After fitting the data, we obtain the resulting transient temperature ramp profiles shown in Fig. 4.9. While the fit is not perfect, it is indeed able to capture a number of the complex coupling effects during the co-feed of NO + C_3H_6 over Pd/BEA, which is useful as a starting point for developing a more accurate model. For example, Fig. 4.9 is able to predict the partial oxidation of C_3H_6 to CO (Fig. 4.8), as well as the increased light-off temperature due to inhibition by NO in the feed (300 versus 255 °C, Fig. 4.7).

Co-adsorption of NO and C_3H_6 model prediction vs. experimental data is plotted in Fig. 4.10. As expected, the uptake of NO decreases in the presence of C_3H_6, and the model successfully captures the reduction of NO_2. However, the mechanism used for NO_2 reduction in this case was obtained from the global reaction scheme, resulting in the excess formation of H_2O as a result of C_3H_6 oxidation. In Chapter 3,

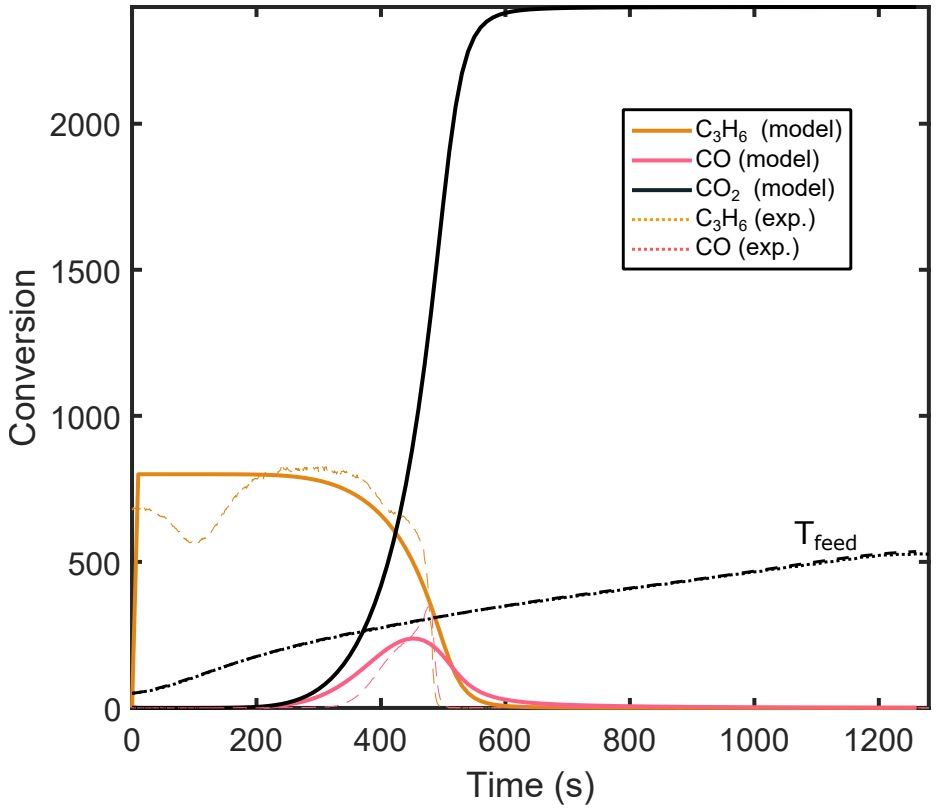

Figure 4.9: Model predicted C_3H_6 total and partial oxidation during temperature ramp. Data was fitted using estimated activation energy of 88 kJ/mol.

we describe the complex surface chemistry that occurs between C_3H_6 and NO_2, which results in adsorption of one or both species on the BAS. During the temperature ramp, the nitro-complex desorbs and is reduced by C_3H_6 to NO or N_2O. Because water is known to impact uptake on acidic zeolites, it may be more practical to update the reaction scheme so that it captures the reduction of NO_2 without oxidizing the C_3H_6. Additionally, the model is not able to accurately predict the uptake of C_3H_6 due to the complexity of modeling the oligomerization. The uptake profile plotted in Fig. 4.10 therefore represents uptake of C_3H_6 without the coupling reactions. Because the coupling reactions are not inlcuded in this fit, the inhibtion of NO uptake is not as severe as shown in the experimental data, resulting instead in more uptake on BAS.

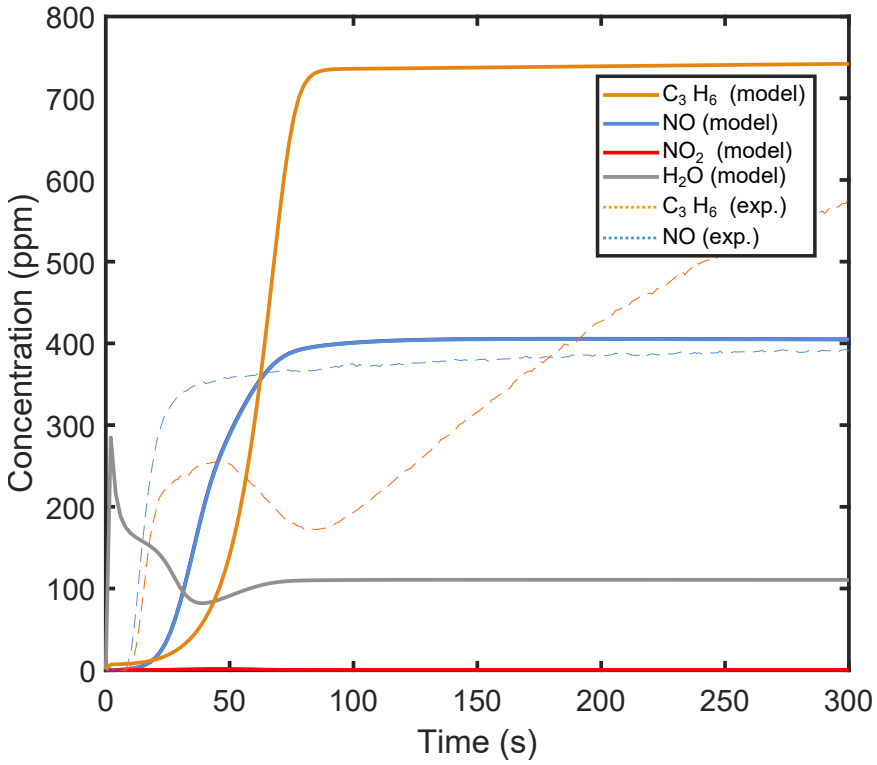

Figure 4.10: Model predicted vs. experimental data for NO + C_3H_6 adsorption on Pd/BEA at 50°C.

4.6 Conclusions

In this work we establish a well-defined model that solves the convection, diffusion, and reaction equations in a single washcoated monolith channel. The model predicts the low temperature uptake of NO and NO_2 on various types of sites, and can determine desorption behavior that closely matches the experimental data. We successfully determine the oxidation behavior of propylene on the catalyst, predicting the partial oxidation to CO as well as the oxidation to CO_2 at higher temperatures. The model was then partially validated against data from a co-adsorption experiment (NO + C_3H_6) with some good agreement of certain aspects. While the model is not yet fully functional in terms of predicting all behavior observed in the data in Chapter 3, it acts as a stepping stone for future work. Regardless of the difficulty in obtaining fitting parameters, the model itself is very robust and can be used to predict the behavior of the catalyst under a variety of conditions including temperature,

flow rate, monolith length, Pd loading and zeolite type and acidity. Next steps after obtaining a more complete model would certainly be to develop the model for use in a multifunctional environment such as a dual-layer or sequential configuration.

Chapter 5: Optimizing the lean hydrocarbon NO_x trap: sequential and dual-layer configurations

A portion of the work in this chapter was presented at the North American Catalysis Society biennal meeting on June 24th, 2019. The contents of this chapter were submitted to the Catalysis Today NAM special issue and is currently under review.

5.1 Introduction

In this chapter the extension of the Lean Hydrocarbon NO_x Trap to multifunctional systems is discussed. As mentioned in Chapter 3.1, cold start emissions are a key concern for lowering overall NO_x and HC tailpipe emissions. In this study we investigate the use architectural design strategies to improve upon the single-catalyst LHCNT, a multi-functional device that traps, releases, and converts NO_x, CO, and HCs.

The Passive NO_x Adsorber, or PNA, has been proposed to specifically address low temperature NO_x emissions. The PNA is designed to trap NO at low temperature and release both NO and NO_2 at temperatures high enough for downstream conversion by SCR.[60] The most effective PNA materials developed to date are Pd-exchanged zeolites, the latter of which include BEA, ZSM-5, or SSZ-13. The zeolite pore size, framework structure, and silicon to aluminum ratio (SAR) provide varying NO trapping capabilities in terms of the NO_x storage capacity and NO_x release temperature. The performance results of these PNA materials hold promise, and the consensus is that highly dispersed Pd cations are responsible for the NO storage. However, the NO uptake mechanism details including the identity of the Pd cations responsible for NO binding are highly variable and not fully understood.[62,64,67,90] The state of the Pd within the zeolite depends on the pretreatment conditions, feed gas composition, and

zeolite framework type and acidity.[63,68,93,95,133] Studies show that the Pd-based zeolites readily trap NO under dry or simpler feeds (i.e., NO + O_2 + H_2O). For more complex feeds containing reductants like CO, studies report that Pd/SSZ-13 in particular is effective in trapping NO.[62,67] Zheng et al.[62] performed NO uptake experiments on Pd/BEA, Pd/SSZ-13, and Pd/ZSM-5 and found that in the presence of H_2O and CO, Pd/SSZ-13 has the highest NO adsorption capacity as well as a higher NO and NO_2 desorption temperature, with nearly all of the desorption occurring above 200°C. Additionally, it was found that CO not only increases the NO_x desorption temperature, but also leads to an increase in NO adsorption capacity.[117,134] Progress towards understanding the PNA trapping mechanism may be inhibiting further advances such as the discovery of new materials, particularly those that are intended to trap HCs as well as NO, for example.

A typical diesel engine exhaust contains low molecular weight olefins (C_2—C_4), aromatics, and long-chain alkanes (C_{8+}), all of which should be trapped during cold-start in order to meet emission targets.[52,97] Zeolites are effective HC traps (HCTs) because of a combination of the pore structure and acidity of the exchange sites.[57,63,65,93,98,99] Large pore zeolites such as BEA (12-member ring) are effective in trapping linear, higher molecular weight HCs (C_{10+}) that can access the pores and bind on the pore walls through van der Waals interactions.[135] Medium pore zeolites such as ZSM-5 (10-member ring) are effective in trapping olefins and aromatics on Bronsted acid sites (BAS), the extent of which depends on the SAR and H_2O concentration.[53,57,100] On the other hand, small-pore zeolites, like SSZ-13, have a pore diameter less than 0.4 nm, limiting their ability to trap HCs. This calls into question the utility of SSZ-13 as a material to trap both NO_x and HCs.

The PNA concept itself follows from the HCT concept. Despite that fact, most of the PNA studies to date have focused on the mechanistic aspects of NO uptake, using feeds containing O_2, H_2O, CO_2, and the model reductant CO. There have been very

few studies on the effect of HCs on the performance of PNA materials, and definitely not their mixtures. Chen et al.[60] used decane to test the NO uptake on BEA, SSZ-13, and ZSM-5, but there was little emphasis on this aspect of the experiments in the discussion. Other work, such as that done by Theis et al.,[65] used smaller hydrocarbons in the feed such as ethylene, where it was found that ethylene, like CO, delays NO_x desorption due to a possible complex formation between ethylene and NO.

The maturity of HCT technology and the recent advances in PNAs notwithstanding, there have been comparatively few studies about combined low temperature NO_x and HC trapping. An exception is our recent study in which we used a multifunctional Pd/BEA washcoated monolith to conduct coupled trapping of NO and C_3H_6.[136] We showed synergy through coupled HC and NO trapping and release, such as delayed NO desorption and lean NO_x reduction with C_3H_6. However, the selection of Pd/BEA as a single trapping and catalytic material constrained the performance gains, particularly in the presence of H_2O.

The combination of materials with different trapping and catalytic functions may lead to performance improvements in a more compact device. Materials identification, development, and optimization of the multiple functions becomes a practical if not necessary goal to meet emission targets. Developing a catalyst with multiple functions requires implementation of multiple designs and configurations. For example, the combined lean NO_x trap LNT and SCR system can have a sequential or dual-layer configuration.[137] Both are effective, and while the sequential configuration is simpler, the dual-layer is more compact (but more complicated). However, the dual-layer configuration may impose diffusional limitations due to the top layer. This is particularly true at high space velocity. Zheng et al. found that by using partially coated zones in the dual layer system, some of these limitations can be lessened.[75]

In the current study, we investigate the use of Pd-exchanged BEA, with and without Pt, along with Pd-exchanged SSZ-13 to carry out coupled NO_x and hydrocarbon

trapping and conversion. Based on the previous work on these materials, Pd/BEA is examined for its effectiveness of high molecular weight HC (such as dodecane) trapping and Pd/SSZ-13 for NO trapping. Because of its relevance to simulated diesel exhaust, this study incorporates *n*-dodecane (C_{12}) as the model large hydrocarbon for trapping on BEA. We additionally incorporate Pt into the Pd/BEA catalyst to improve the oxidation activity while lowering the overall PGM loading of the catalyst. Our main objective is to investigate the effectiveness of combining multiple PGM-zeolite components into a single functioning unit; i.e., the LHCNT. Through a combination of transient adsorption/desorption experiments with the individual components, we converge on a pair of materials for use in both sequential and dual-layered monolith configurations. We evaluate the performance of these configurations with the goal of maximizing uptake of both NO_x and HC (C_{12}). The study enhances the understanding of LHCNT materials with particular consideration of coupling effects and provides guidance towards improving uptake of multiple species over a range of operating conditions.

5.2 Experimental

5.2.1 Catalyst preparation and properties

A series of catalysts was prepared using a combination of vendor-supplied monoliths and in-house synthesized catalysts. The catalysts included 2 wt.% Pd/BEA (abbreviated "PdBEA"), 1 wt.% Pt-Pd/BEA ("PtPdBEA"), and 1 wt.% Pd/SSZ-13 ("PdSSZ"). Note that the LHCNT requires oxidation activity in addition to NO_x and HC trapping. For this reason, Pt was added to the Pd/BEA. The Pt-Pd/BEA component functions as a combined HC trap and oxidation catalyst. An added benefit of the Pt + Pd mixture is the potential inhibition of PGM sintering due to cooperative effects of the Pt and Pd.[138]

Table 5.1 provides information about each of the six catalyst systems as well

as their abbreviations in the text and some measured properties. The 1 wt.% Pd/SSZ-13 (Si/Al = 15) monolith with a loading of 1.5g/in^3 was obtained from Johnson Matthey, Inc.. For the BEA zeolite monoliths, BEA (SAR 19, surface area = 710m^2/g) was obtained from Zeolyst International. Both 2 wt.% Pd/BEA and 1 wt.% Pt-Pd/BEA catalysts were prepared using incipient wetness impregnation. The 2 wt.% Pd/BEA slurry was prepared using $Pd(NO_3)_2{\cdot}2H_2O$ precursor dissolved in H_2O equal to the pore volume of BEA (35mL/g), which was added dropwise to the zeolite, dried at 120°C for 18h, and calcined at 550°C for 4h. For the Pt-Pd/BEA sample, $Pt(NH_2)_4(OH)_2{\bullet}xH_2O$ precursor was used and co-impregnated with Pd into the BEA zeolite, resulting a 1:1 molar ratio of Pt:Pd. The resulting powder mixtures were then combined with 10 wt.% alumina binder, diluted in H_2O, and ball-milled for 36h to reduce the particle size and improve adhesion to the cordierite support.[139] Each of the monoliths had a length of 1 in and 1 cm square cross-section. For the single-layer catalysts, cordierite cores (cell density of 400 cpsi) were dipped into the resulting slurry mixtures and dried at 80°C. These steps were repeated until the desired loading was reached. The dual-layer catalyst consisted of the Johnson Matthey Inc. supplied Pd/SSZ-13 monolith, which was coated with a top layer of Pt-Pd/BEA with the same loading as the base layer.

Table 5.1: Catalysts and their properties

Catalyst ID	Description	Washcoat Loading (g/in^3)	Washcoat Mass (g)	Length (in)
PdBEA	2 wt.% **Pd/BEA**	1.3	0.17	1
PtPdBEA	(0.64 wt.% **Pt**-0.36 wt.% **Pd**)/**BEA**	1.5	0.22	1
PdSSZ	1 wt.% **Pd/SSZ**-13	1.5	0.22	1
Seq-BS	**Seq**uential PtPd**B**EA → Pd**S**SZ	1.5	0.22+0.22	2
Seq-SB	**Seq**uential Pd**S**SZ→PtPd**B**EA	1.5	0.22+0.22	2
DL	**D**ual-**L**ayer PtPdBEA on Pd/SSZ	1.5/layer	0.21/0.20	1

5.2.2 Reactor setup and experimental protocol

Adsorption experiments were conducted in the vertical quartz tube reactor described in Chapter 3 using a total flow rate of 2500 sccm. The reactor system was modified to enable the feed of *n*-dodecane (C_{12}) using a custom vaporizer unit and a Cole-Parmer syringe pump. Unless noted otherwise, the primary feed components in this work comprised 400 ppm NO, 200 ppm C_{12}, and 2% O_2, balanced with Ar. Table 5.2 describes the feed conditions of each of the experiments.

Table 5.2: Experimental feed conditions for single and mixed catalysts

Catalyst	Type(s)	C_{NO}(ppm)	$C_{C_{12}}$ (ppm)	Notes
PdBEA	1 + 2	400	–	
PdBEA	1 + 2	400	200	
PtPdBEA	1 + 2	400	–	
PtPdBEA	1 + 2	400	200	
Seq-BS	1 + 2	400	–	
Seq-BS	1 + 2	400	200	
Seq-SB	1 + 2	400	–	
Seq-SB	1 + 2	400	200	
DL	1 + 2	400	–	
DL	1 + 2	400	200	
DL	1 +2	400	–	+800ppm C_3H_6
DL	1 + 2	400	200	+800ppm C_3H_6

Prior to the uptake experiments, the catalyst samples were de-greened in 5% O_2 at 600°C for 4 h. Before each experiment, a sample pretreatment was conducted in 5% O_2 at 500°C for 30 min, followed by sample cooling under a flow of Ar to the desired uptake temperature of 100°C.

We describe two experimental protocols, Type I and Type II, that were carried out to evaluate the monolith samples. For both, the feed mixture was first established in the bypass for at least 5 min, followed by a switch of the feed to the reactor. During adsorption, the monoliths were exposed to the feed mixture for 300 s at 100°C. In the Type I experiment, the adsorbate feed was turned off after this time and the reactor was purged of any weakly adsorbed or residual gases (including H_2O). The

temperature programmed desorption (TPD) was then initiated by ramping the temperature at a rate of 20 °C/min to 500°C in 2% O_2. For the Type II experiments, the feed composition was not altered after the adsorption period, which was the same as in Type I (5 min at 100°C). Instead, the same feed flowed over the catalyst during the temperature ramp. Performing each of the protocols allowed for determining unique performance metrics. The Type I experiments allowed for a more accurate analysis of the desorbing species by eliminating background interference, while the Type II experiments represented a more practical feed and enabled bulk oxidation and reduction metrics such as the light-off temperature of C_{12}.

Several point temperatures were monitored using three Type K thermocouples. The thermocouple measuring the inlet temperature (T_{feed}) was located 1 cm upstream of the front face of the monolith. The thermocouple measuring the catalyst temperature (T_{cat}) was located in the center of the monolith (radially and axially). For sequential monoliths the mid-core catalyst temperature of the downstream monolith was monitored. Finally, a third thermocouple was placed 1 cm downstream, providing the effluent temperature (T_{out}). A blank monolith experiment was conducted for each Type of experiment, ensuring proper subtraction of dead times and weak adsorption. Most experiments were repeated three times to ensure reproducibility, and error bars are given where applicable.

5.3 Results and discussion

5.3.1 Single catalyst evaluations

Single component catalysts were first evaluated to quantify their individual trapping and catalyst performance. These data are needed to interpret the performance of the more complex multi-component formulations. We tested each of the three catalysts using the feed conditions provided in Table 5.2. Assessment of performance included uptake of NO and C_{12} in μmol i /g-cat (washcoat) (i= NO, C_{12}), conversion

of NO to NO_2, and HC oxidation light-off temperature. We performed a series of preliminary experiments with C_{12} on PdBEA and found consistently good adsorption (~247 μmol C_{12}/g-cat) under both dry and wet conditions, and with and without NO (Fig. B.1). Similar experiments were conducted with C_{12} on PdBEA in the recent literature; our results are consistent with these observations.[58]

To establish baseline performance metrics, each catalyst was evaluated in a Type I experiment, which involved a simple feed of 400 ppm NO and 2% O_2 at 100°C; i.e., constant temperature with no subsequent temperature ramp. Fig. 5.1 includes the NO_x uptake (μmolNO_x/g-cat) on each individual sample and three multi-component samples with and without C_{12} in the feed. [For the time being, ignore the additional uptake represented by the unshaded area. We address that later.] As summarized in Table 5.3, the overall NO_x uptake is highest for PdSSZ (73.4 μmol/g-cat), followed by PdBEA (28.1), and PtPdBEA (15.8). With the Pd loading higher for PdBEA (2 wt.%) than PtPdBEA (0.64 wt.%), the NO_x uptake is expectedly higher on the former than the latter.

Table 5.3: NO adsorption with and without C_{12}, maximum NO_x conversion

	Ads μmol NO_x/g-cat	Ads NO_x w/ C_{12}	X_{NO} (%, NO only)
PdBEA	28.1	22.0	35
PtPdBEA	15.8	10.1	7
PdSSZ	73.4	75.2	4
Seq-BS	72.3	73.2	34
Seq-SB	74.7	73.0	30
DL	86.1	77.2	36

Each of the adsorption profiles shown in Fig. 5.2a exhibit similar qualitative features, although the uptake magnitudes vary, consistent with the measured uptake. Figs. 5.2b and 5.2c show details of the uptake including NO and the generation of NO_2, respectively. In the bypass a background NO_2 level of 5 ppm was detected. At the onset of admission of the feed to the catalyst, there is a dip in both NO and NO_2, signifying uptake of both species on the catalyst. A peak of NO_2 concentra-

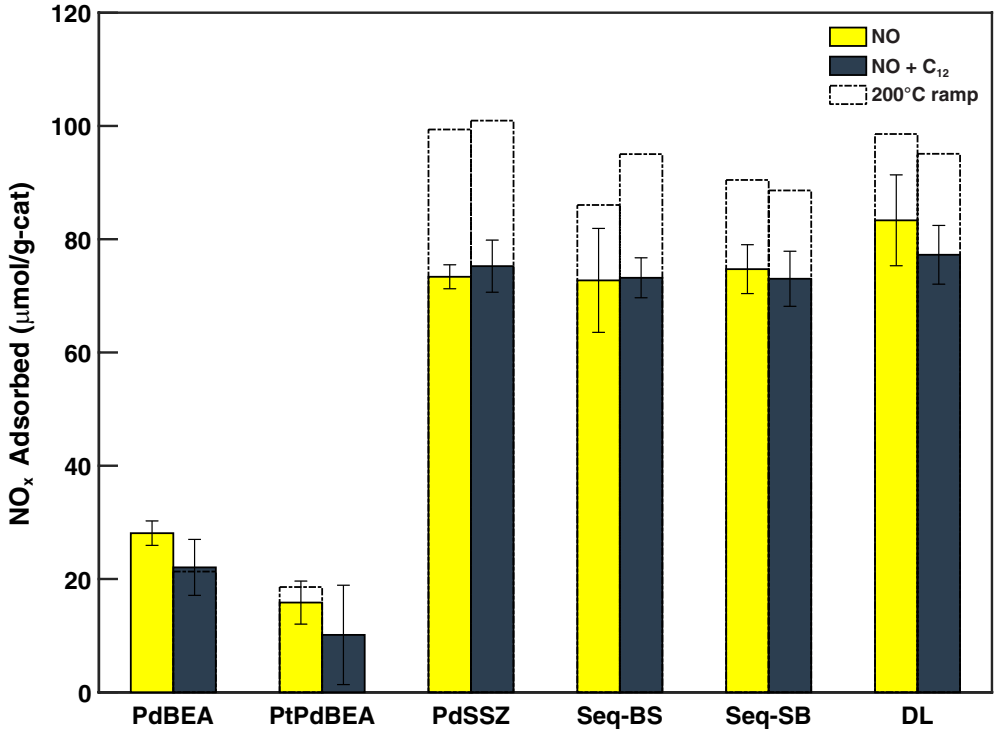

Figure 5.1: Measured NO_x adsorption for each catalyst for (i) NO only and (ii) NO + C_{12}. The dotted bar extensions represent additional uptake that occurred during the TPD for Type II experiments from 100 to 200 °C.

tion is noted shortly after the minimum in the NO concentration, which is highest for PdSSZ and lowest for PdBEA. After its peak, the NO_2 returns to its background level for the BEA catalysts. There is a clear link between the amount of NO_2 generated and the amount of NO adsorbed. For example, it is noted that PdSSZ has the highest NO_2 peak and adsorbs the most NO. For PdSSZ, the NO_2 does not return to its background concentration. These measurements warrant some discussion.

There is currently an active debate regarding the formation of NO_2 during uptake. One proposed mechanism involves the reduction of Pd cations in the form of $[PdOH]^+$ that are bound to the negatively-charged $[Al\text{-}O\text{-}Si]^-$ of the zeolite. A two-step sequence is proposed as follows:[63,93]

$$2[PdOH]^+Z^- + NO \leftrightarrow 2Pd^+Z^- + NO_2 + H_2O \tag{5.1}$$

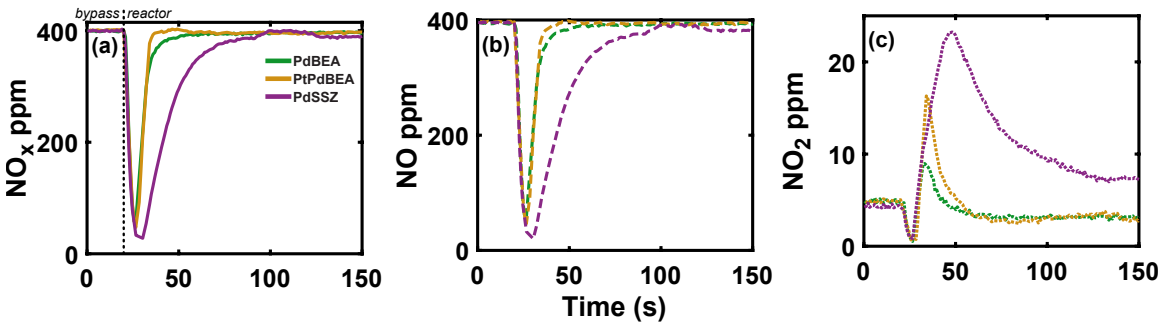

Figure 5.2: (a) NO_x, (b) NO, and (c) NO_2 adsorption profiles for PdBEA, PtPdBEA, and PdSSZ (400ppm NO, 2% O2 and 3% H_2O).

and

$$NO + Pd^{+}Z^{-} \leftrightarrow NOPd^{+}Z^{-}. \tag{5.2}$$

According to rxns. 5.1 and 5.2 , each generated NO_2 involves the reduction of two Pd cations from the +2 to +1 valence states. Another interpretation of these data is the reduction of bulk PdO_2 to PdO that oxidizes NO to NO_2, which stores as nitrates on PdO, as in the following reaction:[59,62]

$$3NO + PdO_2 + 1.5O_2 \leftrightarrow Pd(NO_3)_2 + NO_2. \tag{5.3}$$

Because the distribution of Pd species is dependent on characteristics of the zeolite framework including the pore size and SAR, the mechanism for NO uptake and NO_2 formation may vary. That point aside, while PdBEA adsorbs more NO than does PtPdBEA, PtPdBEA produces more NO_2 during uptake (Fig. 5.2c). This result contradicts the aforementioned link between NO uptake and NO_2 generation. The inconsistency is attributed to the Pt in the PtPdBEA sample. We expand on the NO_2 generation below.

The TPD profiles reveal two desorption regimes, one between 100 and 300 °C, and the other between 300 and 500 °C (Figs. 5.3a–c). The existence of multiple desorption peaks from Pd-exchanged zeolites and the sites associated with the desorbing species have been proposed in the recent literature. The low temperature NO_x peak that

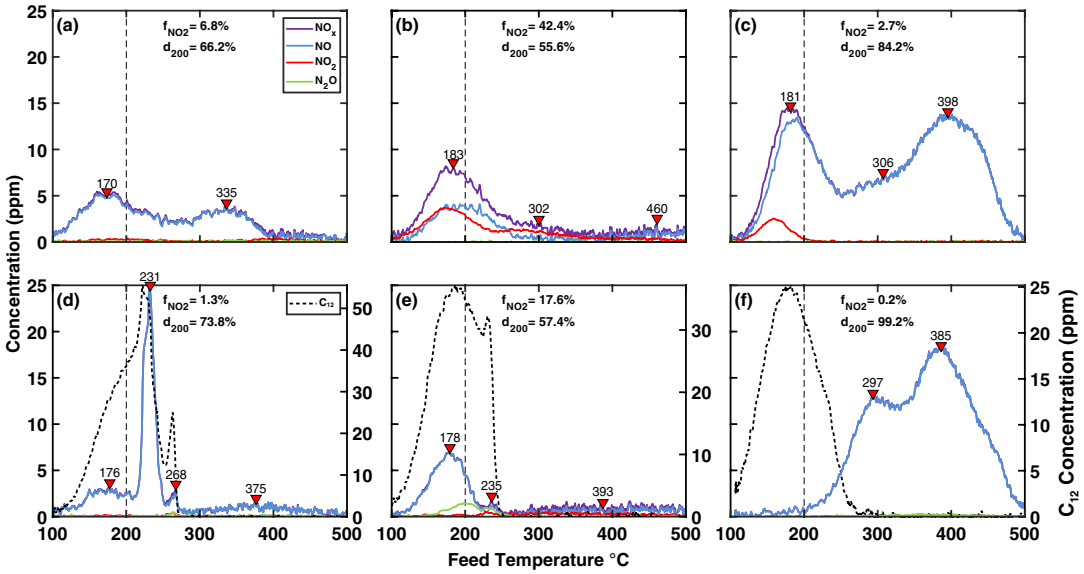

Figure 5.3: Impact of C_{12} on NO TPD profiles for (a,d) PdBEA, (b,e) PtPdBEA and (c,f) PdSSZ. Feed conditions include (Top Row) 400ppm NO or (Bottom Row) 400ppm NO and 200ppm C_{12}.

occurs between 170-185°C is mostly as NO for PdBEA (Fig. 5.3a) but includes some NO_2 for PtPdBEA (Fig. 5.3b) and PdSSZ (Fig. 5.3c). This peak is attributed to the formation of nitrates, through the interaction of NO_2 that forms during uptake and H_2O, which adsorbs on Pd in the form of $Z^-Pd^{2+}Z^-$ or $Z^-[Pd(OH)]^+$.[62,104,116] The higher temperature peak is likely due to more stable NO species adsorbed on isolated Pd cations such as the nitrosyl, $NOPd^+Z^-$, or to surface nitrates bound to Pd cations; e.g., $NO_3^-Pd^+Z^-$.[64,103]

In addition to the TPD peak temperatures and magnitudes, it is instructive to measure the percentage of desorbing NO_2, given by

$$f_{NO_2} = 100 \times \left[\frac{\int_{Tads}^{T_{final}} C_{NO_2} dT}{\int_{Tads}^{T_{final}} C_{NO_x} dT} \right], \tag{5.4}$$

where T is the feed temperature and C_i is the concentration of i (i = NO, NO_2, NO_x)

in ppm. We also report the percentage of NO_x that desorbs above 200°C, given by

$$d_T = 100 \times \left[\frac{\int_T^{T_{final}} C_{NO_x} dT}{\int_{T_{ads}}^{T_{final}} C_{NO_x} dT} \right]. \tag{5.5}$$

The f_{NO2} value is ~7, 42, and 3 % for PdBEA, PtPdBEA, and PdSSZ, respectively. Table 5.4 provides these values in more detail. PdBEA generates little NO_2 during the NO uptake and therefore releases very little during the TPD; PtPdBEA releases NO_2 throughout the TPD; and PdSSZ releases NO_2 both during the low temperature peak and at lower levels throughout the uptake period. These differences in the NO_2 are attributed to a combination of two factors; (i) the catalytic NO to NO_2 oxidation activity, and (ii) the low temperature NO adsorption mechanism. Factor (i) concerns the direct oxidation of NO to NO_2. Pt is a much more effective NO oxidation catalyst than is Pd.[140,141] Factor (ii) concerns the generation of NO_2 during NO uptake by the aforementioned Pd reduction mechanism (i.e., rxn. 5.1).

Table 5.4: NO desorption metrics

	d_{200} (%, NO only)	d_{200} (%, NO + C_{12})	f_{NO_2} (%, NO only)	f_{NO_2} (%, NO + C_{12})
PdBEA	66.2	73.8	7.8	1.3
PtPdBEA	55.6	57.4	42.4	17.6
PdSSZ	84.2	99.2	2.7	0.2
Seq-BS	78.8	99.6	7.4	41.6
Seq-SB	85.6	96.4	0.7	27.7
DL	86.0	95.4	58.3	23.2

Besides the extent of NO_2 formation, the TPD peak magnitudes and desorption temperatures vary for each catalyst. PdBEA has two peaks, one at 170°C and the other at 335°C. PtPdBEA has a larger low temperature peak than PdBEA but a much smaller peak at 302°C. PdSSZ has a clear bimodal, and possibly trimodal, TPD peak distribution. The differences in the TPD profiles are attributed to the framework type and to the PGM loadings. Since the PdBEA catalyst has a higher Pd loading than PtPdBEA, it stores more NO at the higher temperature binding site represented by

the peak at 335°C. PtPdBEA has a lower PGM (and Pd) loading, so its overall NO uptake is lower. The addition of Pt catalyzes more NO oxidation to NO_2, resulting in a higher low temperature peak. PdSSZ has both a large desorption peak that occurs at 180°C and one at 400°C, resulting in an increase in the d_{200} value from 55% and 65% for PdBEA and PtPdBEA, respectively, to 84% (Table 5.4).

A comparison of the NO uptake and release data show that PdSSZ is the superior NO trap. Even with half the Pd loading of the PdBEA sample, significantly more NO is adsorbed. The findings suggest that Pd is not as well dispersed in the BEA zeolite as it is in SSZ-13 zeolite. This may mean that Pd exists in the form of PdO clusters on BEA, which not only have a lower dispersion than atomically dispersed Pd cations but also have a lower affinity for NO. Clearly, in the presence of H_2O, the 1wt.% Pd/SSZ-13 sample is the best choice, consistent with previous experimental findings.[62]

The NO trapping features of the catalyst samples were further evaluated by adding 200 ppm C_{12} to the feed. Fig. B.2 shows the transient C_{12} uptake profiles for the samples. These data demonstrate the dramatic contrast between the BEA-containing materials and the SSZ-only catalyst. The C_{12} uptake on the BEA catalysts is the highest (204 and 142 μmol/g-cat) but is much lower (66 μmol/g-cat) on PdSSZ. This decrease is a result of the difference in pore size of the zeolites; small-pore SSZ-13 has a pore size of 0.37 nm compared to 0.65 nm for BEA. Thus C_{12} experiences a higher diffusional resistance in the SSZ-13. Most of the C_{12} uptake on PdSSZ is likely on the external surface of the SSZ-13 crystallites resulting in little or no inhibition of NO uptake by C_{12}. In contrast, NO uptake is inhibited by C_{12} on the larger pore BEA (Table 3.3, Fig. 5.1). The adsorption profiles show no consumption of NO_2 (non-zero concentration) nor any formation of N_2O, indicating negligible reactivity between the co-adsorbing NO and C_{12} (Fig. B.3). In our previous work we described the formation of N_2O (and lack of NO_2) during co-adsorption of NO and C_3H_6, which

signified reduction of NO_2.[136] The difference is likely due to the more reactive nature of C_3H_6 at low temperatures and interaction with the BAS, while C_{12} is less reactive at these temperatures.

The TPD profiles of each catalyst with C_{12} added to the feed reveal significant changes in the desorption behavior (Figs. 5.1d—f). For PdBEA there is a small NO peak below 180°C, which is followed by a very sharp doublet with peaks at 231 and 268 °C, and finally a smaller broad peak at 375°C (Fig. 5.1d). The sharp peaks are concurrent with the C_{12} desorption peaks and appear to be associated with the exotherm associated with C_{12} oxidation. The NO_x profile, which consists only of NO, has an increased fraction of strongly held NO with the d_{200} increasing from 66% without C_{12} to 74%. For PtPdBEA the peak distribution is like the NO-only feed but includes a new small but sharp peak at 235°C (Fig. 5.1e). In the presence of C_{12} there is a decrease in the magnitude of the first peak, as well as an absence of NO_2 and a peak of N_2O. The slight decrease in NO_x desorption indicates inhibition of NO uptake by C_{12}, while N_2O formation is likely due to NO_x reduction by the C_{12} or its partially oxidized products. N_2O formation is commonly observed during lean NO_x reduction by hydrocarbons on precious metal catalysts.[142] The difference in the peak distribution for the PdBEA and PtPdBEA catalysts is likely due to the presence of Pt in the latter, which is a more active NO reduction catalyst.[113] Once the C_{12} is consumed, some NO_2 formation ensues, resulting in ~18% NO_2 formation during the TPD. In the PdBEA catalyst, however, the absence of Pt leads to desorption of NO only, resulting in ~1% of NO_2 formation.

While most of the NO desorbs during the period of C_{12} desorption and oxidation for PdBEA and PtPdBEA, there is a noted shift in NO desorption to higher temperatures for PdSSZ. In the absence of C_{12} there is a low temperature peak at 180°C, while in the presence of C_{12} a dual NO peak at 297 and 385°C (Fig. 5.1f) is observed. The shift results in a very high fraction (99%) of trapped NO desorbing above

200°C. Since the desorbing amount of NO is nearly the same for both feeds (73 vs. 75 μmol/g-cat), this feature indicates that C_{12} inhibits NO release. This outcome was not expected given the rather low uptake of C_{12} on the small-pore SSZ-13 sample. This may suggest that C_{12} residing on the external surface or in the mouths of the pores of the PdSSZ crystallites restricts NO desorption. Not until C_{12} is completely desorbed/oxidized is NO released, suggesting that the C_{12} blocks the NO from leaving the crystallite. In contrast, for the PdBEA sample, the larger pores enable the intracrystalline transport of C_{12} and NO. This is evident from the simultaneous release of the two species during the TPD. This temperature shift in the NO desorption is yet another reason why PdSSZ is a better choice as a PNA material.

The C_{12} desorption behavior is related to the adsorption capacity and PGM loading of each catalyst. A large fraction of C_{12} is trapped on PdBEA, which leads to a large desorption peak during TPD followed by the formation of CO_2 at 260°C (Fig. B.4a). The C_{12} peak consists of two sharp features, the second of which probably results from the oxidation exotherm. In addition, the PdBEA exhibits some activity for C_{12} cracking during the TPD, the products of which desorb during the low temperature C_{12} peak (Fig. B.5). These cracking products include hexane, pentane, octane, propylene, and acetaldehyde, which together comprise 57% of the total carbon released during desorption. The remaining carbon is in the form of CO_2 (18%) and C_{12} (25%, Table 5.5). For PtPdBEA, which stores slightly less C_{12} than PdBEA, similar features are evident during the TPD, including a primary release peak followed by a sharp CO and CO_2 peak (Fig. B.4b). However, C_{12} cracking was not observed. This is likely due to the increased activity of Pt that enables a more efficient catalytic oxidation, resulting in 77% of the C desorbing in the form of CO_2. Finally, PdSSZ stores less C_{12} than the BEA catalysts because of its smaller pores. It also exhibits lower oxidation activity and generates more CO and less CO_2. These appear as more protracted peaks compared to the BEA catalysts (Fig. B.4c). Because of the resistance

to oxidation (and lack of sharp exotherm) the C_{12} peak desorbs without an additional sharp peak. While the low temperature release of C_{12} seems detrimental to the overall performance of the LHCNT system, the PtPdBEA and PdSSZ catalysts mitigate some of this effect by generating more CO_2 than unoxidized C_{12}.

Table 5.5: C_{12} adsorption, light-off, and TPD selectivity

	Ads C_{12} (μmol C_{12}/g-cat)	Light Off (°C)	$S_{C_{12}}$	S_{CO_2}	S_{CO}	$S_{C_3-C_8}$
PdBEA	204±38	280	25%	18%	<1%	57%
PtPdBEA	142±20	300	26%	73	<1%	0%
PdSSZ	66	340	23%	77%	<1%	0%
Seq-BS	203±23	280	24%	75%	<1%	0%
Seq-SB	219±26	293	27%	73%	<1%	0%
DL	163±43	278	25%	74%	<1%	0%

In order to evaluate the performance of these catalysts under more realistic conditions, Type II experiments were conducted using feeds of NO and NO + C_{12}. From these data, the light-off temperature of C_{12} and maximum conversion of NO were determined (Tables 5.3 and 5.5). The resulting C_{12} light-off temperatures are 340°C, 300°C, and 280°C for PdSSZ, PdBEA, and PtPdBEA, respectively (Fig. 5.4). Some improvement in light-off is evident by the addition of Pt to the PdBEA. More notable is the difference in the ability of the PtPdBEA to fully oxidize C_{12} by 380°C, while PdBEA exhibits a more gradual approach to 100% conversion beyond 400°C. While the PdSSZ catalyst is able to light-off C_{12}, it does not achieve complete conversion and instead approaches 95%. The variations in oxidation activity are a result of Pt/Pd accessibility and zeolite pore size. In the BEA catalysts, which probably contain PdO/PtO nanoparticles (as indicated by the lower NO uptake), C_{12} can easily access the active sites. For PdSSZ however, the Pd is mostly distributed in the pores of the zeolite crystallites, so oxidation is diffusion limited and the C_{12} cannot easily access the Pd.

The findings from the single catalyst experiments provide guidance for selecting materials and designing the multi-functional LHCNT catalyst, which we consider in

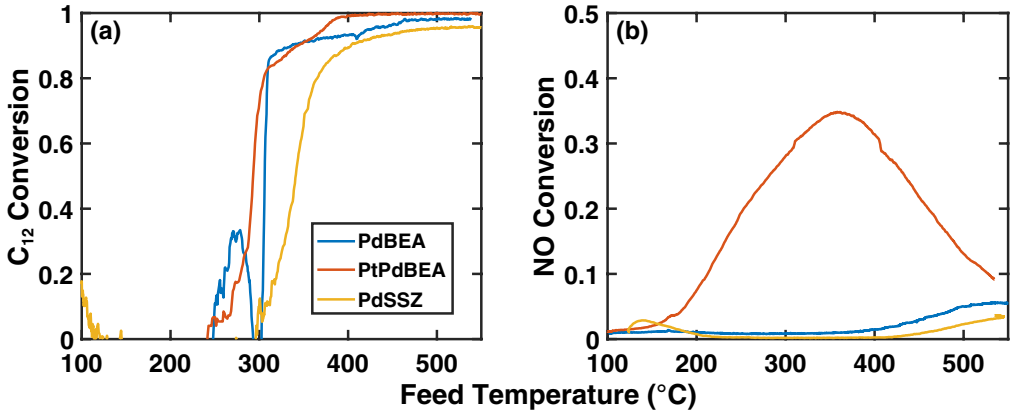

Figure 5.4: Conversion vs. feed temperature for PdBEA, PtPdBEA and PdSSZ. (a) C_{12} conversion using 200ppm C_{12}, 400ppm NO, 2% O_2 and 3% H_2O. (b) NO conversion using 400ppm NO and 2% O2 and 3% H_2O.

the next section. As mentioned previously, PdSSZ is the clear choice for NO uptake. For C_{12} adsorption, both PtPdBEA and PdBEA are equally effective. However, PtPdBEA shows higher oxidation activity for C_{12} and has an overall lower loading of PGM. Furthermore, enhanced NO conversion (to NO_2) is achieved with the PtPdBEA catalyst, indicated by a maximum NO conversion of 35% at 350°C (Fig. 5.4b). In contrast, the NO conversion does not exceed 5% with the PdBEA and PdSSZ catalysts. The NO oxidation activity of Pt is well-known, but demonstrating its activity with BEA is reaffirming.[140] If the LHCNT is to be used in tandem with a downstream SCR, high NO oxidation rates contribute to the "fast SCR" reaction, which involves NO and NO_2 , as shown in the following reaction:[9]

$$2NH_3 + NO + NO_2 \rightarrow 2N_2 + 3H_2O. \tag{5.6}$$

This "fast SCR" reaction is desirable in that it promotes the reduction of NO_x to N_2 compared to either standard SCR (NH_3 + NO + O_2) or NO_2 SCR (NH_3 + NO_2) [40,41].[9,33] Further, due to diffusional limitations of the small pore zeolite, Pt needs to be incorporated into the top (PtPdBEA) layer of a dual-layer catalyst. Therefore, we combined PtPdBEA and PdSSZ into a series of multi-component configurations

that comprise the remaining results of this work.

5.3.2 Sequential systems

Based on the findings from the individual catalyst evaluations, PdSSZ and Pt-PdBEA are good candidates to be used in a sequential catalyst system. In this section we analyze two sequential configurations; the first has the PtPdBEA catalyst placed upstream of the PdSSZ while the second has the PdSSZ positioned upstream of the PtPdBEA. We compare the two configurations with the focus on identifying both desirable and undesirable coupling effects.

Pt-Pd/BEA → Pd/SSZ-13 (Seq-BS)

The first sequential configuration consists of PtPdBEA upstream of PdSSZ ("Seq-BS"). For a feed containing NO, the uptake profile is very similar to that of PdSSZ only, as noted by a large peak of NO_2 at the onset of adsorption, followed by a sustained generation of NO_2 (Fig. B.3d). Seq-BS gives an NO uptake of 72.3 μmol/g-cat, which is within 2 % of the NO uptake of 73.4 μmol/g-cat obtained with PdSSZ alone (Table 5.3, Fig. 5.1). In the presence of C_{12}, as with the PdSSZ sample, the NO uptake changes negligibly (72.3 vs. 73.2) and the uptake profile exhibits similar characteristics (Fig. B.3j). Adsorption of C_{12} increases from 142 μmol/g-cat for PtPdBEA (and 66 in the PdSSZ sample) to 203 μmol/g-cat, which is close to the sum of the individual catalyst adsorption capacities. Thus, neither the NO nor C_{12} uptakes obtained with the Seq-BS catalyst configuration show any loss in performance during the uptake part of the experiment.

Further evaluation of the sequential design considers the TPD portion of the experiment with the data for Seq-BS shown in Fig. 5.5a (NO only) and 5c (NO + C_{12}). For the NO-only feed, NO desorbs as 3 peaks at ~190, 290, and 400 °C, with NO_2 formation occurring only in the first peak (Fig. 5.5a), and results in 83 μmol NO_x /g-cat desorbed. Addition of C_{12} to the feed decreases the NO_x release to 76 μmol/g-

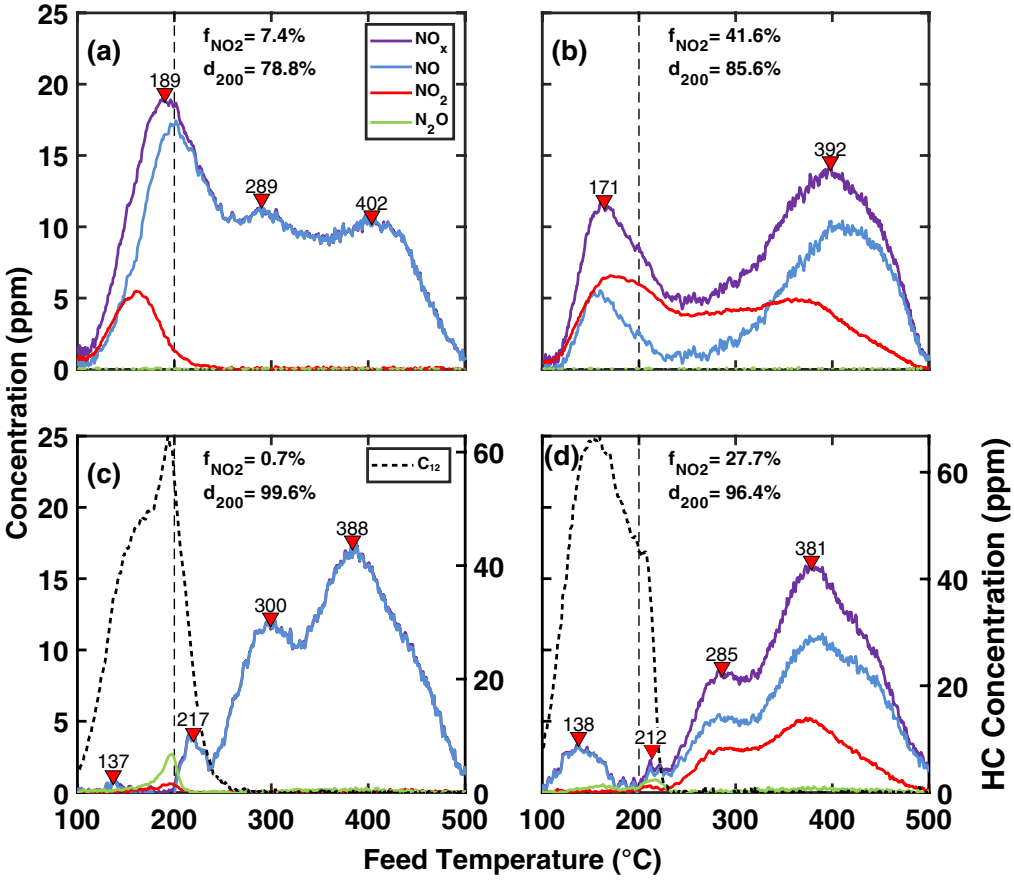

Figure 5.5: TPD Profiles using a feed of 400ppm NO (top row) or 400ppm NO and 200ppm C_{12} (bottom row), 2% O_2, 3% H_2O, using a ramp rate of 20°C/min for (a,c) Seq-BS and (b,d) Seq-SB catalysts.

cat. There is an appreciable delay in the NO desorption, shifting the temperature of the first large peak from 189°C (Fig. 5.5a) to 300°C (Fig. 5.5c). The overall outcome is two primary peaks at 300 and 388°C, the latter of which is larger. There is a very small NO peak at ~140°C, which is likely a product of desorption from the Pt-PdBEA layer (more discussion on this point to follow). There is also the appearance of minor peaks of N_2O and NO_2 at the same temperature as maximum C_{12} desorption (~200°C). The delay in NO desorption with C_{12} in the feed, as discussed for the individual PdSSZ earlier, is attributed to adsorbed C_{12} blocking the release of NO.

The C_{12} desorption profile for Seq-BS consists of a large peak between 100 and 200 °C, concurrent with a sharp peak of CO_2 and some CO formation in two different

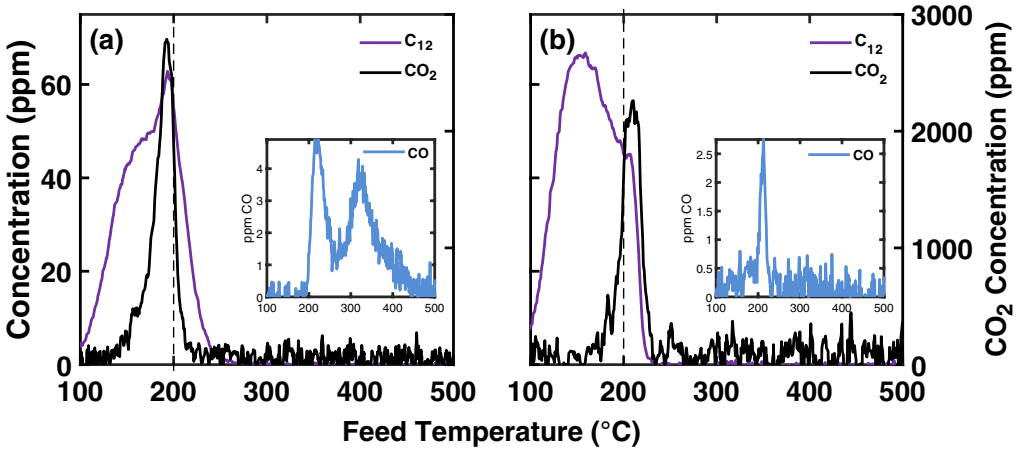

Figure 5.6: Corresponding C_{12}, CO_2, and CO (inset) TPD profiles for (a) Seq-BS and (b) Seq-SB for a feed of 400ppm NO, 200 ppm C_{12}, 2% O_2 and 3% H_2O.

regions of the TPD profile (Fig. 5.6a). CO is observed at the onset of CO_2 formation, and then again at 330°C. Because there is no C_{12} desorbing (or CO_2 forming) at the higher temperature, that CO may be a result of CO released earlier that re-adsorbs downstream on the Pd sites of the PdSSZ. Previous studies involving CO adsorption on Pd/SSZ-13 and Pd/BEA indicate that CO not only adsorbs on these materials, but can also delay NO desorption to higher temperature [15,16].[117,134] Thus, CO desorbing from the upstream PtPdBEA may adsorb on the favorable PdSSZ sites. This is a beneficial effect because the total amount of low-temperature CO slip is reduced. In addition to these features, an exotherm is generated at the peak desorption of C_{12} (Fig. B.6). The temperature increase propagates downstream to the PdSSZ catalyst which has the effect of increasing desorption rates, resulting in the sharp peak in the temperature range of 200-220°C (Fig. 5.5c). This peak initially consists of N_2O as C_{12} continues to oxidize and reduce NO_x, but then shifts back to NO as the temperature rise subsides.

Pd/SSZ-13 → Pt-Pd/BEA (Seq-SB)

To determine if there is a significant performance impact of sequence order on NO or C_{12} uptake, a series of experiments were conducted on the sequential configu-

ration in which PdSSZ is placed upstream of the PdBEA ("Seq-SB"). In the absence of C_{12}, NO uptake remains high at 75 μmol/g-cat, which is very close to that obtained with Seq-BS (Table 5.3). One of the key differences encountered with Seq-SB is the increased formation of NO_2 during the TPD, resulting in an f_{NO2} of 41.6%, compared to only 7.4% with Seq-BS (Fig. 5.5a, 5.5b). The PtPdBEA component is much more active for NO oxidation, as shown earlier (Fig. 5.4b). This feature is clear evidence of NO desorbing from the upstream PdSSZ and traveling downstream where it is oxidized to NO_2 on the PtPdBEA. As the temperature increases, reaction equilibrium increases the rate of NO_2 decomposition. As a result, less oxidation occurs during the second peak at ~392°C.

The Seq-SB configuration with a co-feed of NO + C_{12} shows a large delay in the NO and NO_2 desorption (compare Fig. 5.5d to 5.5b). A similar feature was encountered for NO with the Seq-BS configuration (compare Fig. 5.5c to 5.5a). The d_{200} for Seq-SB is 96.4%, and the NO uptake is 73 μmol/g-cat, a minor deviation from the NO-only case. The corresponding TPD profiles for C_{12}, CO and CO_2 show only one peak for each of the three species (Fig. 5.6b). This is a clear difference from the Seq-BS configuration, which has multiple CO desorption peaks (Fig. 5.6a). The single peak for Seq-SB indicates no additional downstream adsorption of CO. This is because the downstream PtPdBEA catalyst is active enough to oxidize any CO that forms during partial oxidation upstream. As with Seq-BS, once C_{12} is fully desorbed or oxidized, NO_x desorption commences. One of the main differences between Seq-SB and Seq-BS is a somewhat larger low temperature NO desorption peak (138°C) for the former (compare Figs. 5.5d and 5.5c). This NO desorption occurs simultaneously with the C_{12} desorption and N_2O formation. A similar feature was observed during the TPD with PtPdBEA (Fig. 5.3b). This low temperature NO peak is likely caused by simultaneous desorption of NO and C_{12} from the downstream PtPdBEA catalyst, whereas in Seq-BS the desorbing species may be re-adsorbed downstream

on the PdSSZ catalyst, similar to CO discussed earlier. While the early release of NO hinders the performance of the LHCNT, the amount only leads to a 3% decrease in the d_{200} from 99.6% in Seq-BS to 96.5%. As with the NO_x TPD for Seq-BS, most of the NO_x desorbs from two primary peaks, one at 285°C and one at 381°C. The magnitude and temperature of these peaks is similar for both sequential configurations, showing that NO adsorption on the primary sites (i.e., Pd on SSZ) is negligibly affected by the order of the catalysts.

5.3.3 Dual layer catalyst performance

The two sequential configurations show some distinct features and performance advantages for coupled NO and C_{12} trapping and conversion. However, these come at the expense of increased catalyst volume. It is therefore of interest to determine if comparable performance improvements can be achieved with a dual-layer (DL) configuration. To this end, we conducted the same set of experiments with a DL catalyst that contains the same total amount of washcoat in each layer as the two catalysts from the sequential configurations. Specifically, the bottom layer consists of the PdSSZ, and the top layer PtPdBEA (1.5 g/in^3/layer, Table 5.1). Thus, whereas the two sequential systems have two thinner washcoats in series, each with loadings of 1.5g/in^3, the DL sample has a single thicker washcoat with twice the loading (3g/in^3) but half as long.

Performance results for the NO-only feed and NO + C_{12} feed are shown in Figs. 5.7a and 5.7b, respectively. The NO uptake was measured to be 86 μmolNO_x/g-cat for the former and 77 μmolNO_x/g-cat for the latter. These values are consistent with the performance of the sequential configurations, if not slightly higher (Fig. 5.1, Table 5.3). The adsorption profile for the DL catalyst is similar to the sequential systems, with a slight decrease in the NO_2 peak formation (Figs. B.3f, B.3*l*). In the absence of C_{12}, the TPD profile consists of 58% NO_2 (Fig. 5.7a) and decreases to 23% in the presence of C_{12} (Fig. 5.7b).

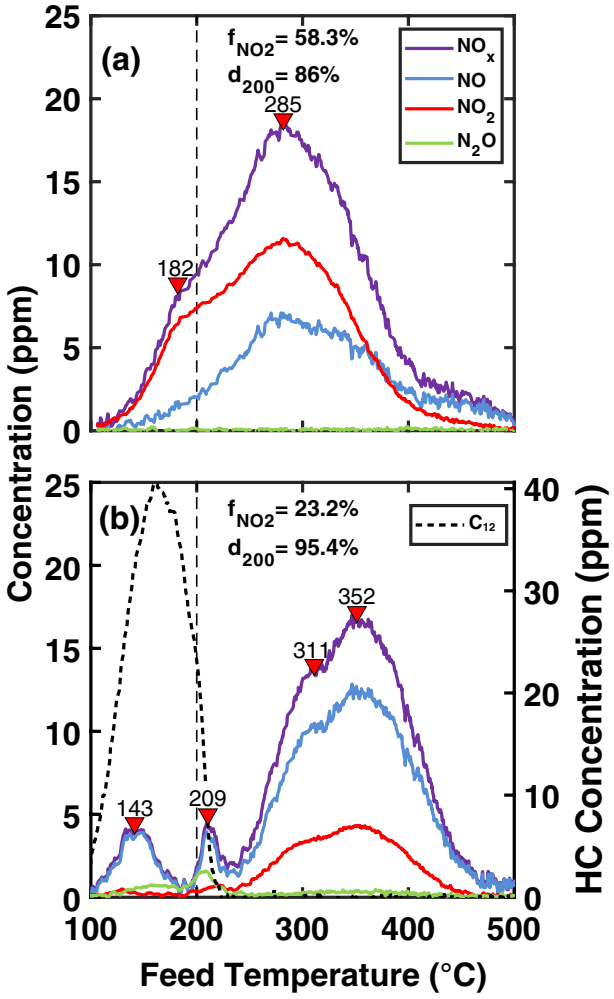

Figure 5.7: TPD Profiles for DL catalyst. Feed: (a) 400ppm NO or (b) 400ppm NO + 200ppm C_{12} and 2% O_2, 3% H_2O, using a ramp rate of 20°C/min.

The TPD for the NO-only feed to the DL catalyst consists of two overlapping regions comprising a shoulder at 182°C and a peak at 285°C (Fig. 5.7a). Beyond the maximum is a long tail extending out to 450°C. This contrasts to the sequential systems that have two or more clearly-defined NO_x (and NO) peaks (Figs. 5.5a,b). More specifically, there is a smaller amount of low temperature NO released for the DL sample compared to the Seq-BS sample, and an earlier release of the ~400°C peak. The single NO_x peak with the shoulder results in more efficient NO oxidation in the PtPdBEA top layer. The NO_2 profile in Fig. 5.7a shows a distinct maximum in NO_2 concentration of ~11 ppm at 285°C. This is higher than either of the sequential

configurations (Figs. 5.5a, 5.5b), and results in 58% of NO_x desorbing as NO_2. The increase may be due to the fact that all of the NO that is trapped in the bottom PdSSZ layer must diffuse through the top layer, so there is more contact with the Pt sites. In contrast, in the Seq-SB experiment, the desorbing NO from the PdSSZ catalyst flows down the channels of the PtPdBEA. If the flow rate is too high NO_x slip may occur, lowering the extent of NO oxidation. Since the NO oxidation to NO_2 typically exhibits a temperature maximum, the tail above 400°C represents NO_2 decomposition to NO. The difference in the peak profiles between the DL and Seq configurations could also be a result of shorter length and thicker coating of the DL catalyst, making it susceptible to washcoat diffusional effects.

In contrast, for the NO + C_{12} co-feed the TPD results are similar to the Seq-SB sample, consisting of a small NO peak at 143°C, a sharp peak at 209°C concurrent with C_{12} oxidation and N_2O formation, and a delayed desorption of NO_x above 300°C containing the characteristic NO_x double peak (Fig. 5.7b). This would indicate that the placement of the PdSSZ layer does not impact performance. The inhibition of NO desorption by C_{12} is a bigger factor than the low temperature desorption effects created by the top layer. The low-temperature NO peak at 143°C represents NO desorbing concurrently with C_{12} from the PtPdBEA top layer. Unlike the Seq-BS case, where that low temperature peak did not exist due to its adsorption downstream on the PdSSZ catalyst, the NO peak in the DL catalyst suggests NO from the top layer does not re-adsorb downstream into the PdSSZ layer. This is likely due to diffusion limitations and the shorter length of the catalyst. In other words, the diffusivity of NO from the top layer into the bottom layer is less than the diffusivity into the bulk phase.

The distribution of NO and NO_2 is similar to the Seq-SB sample (23% NO_2), as is the formation of N_2O near 200°C. One of the notable differences is the increased magnitude of the intermediate NO_x peak at 311°C. For Seq-SB this peak is smaller

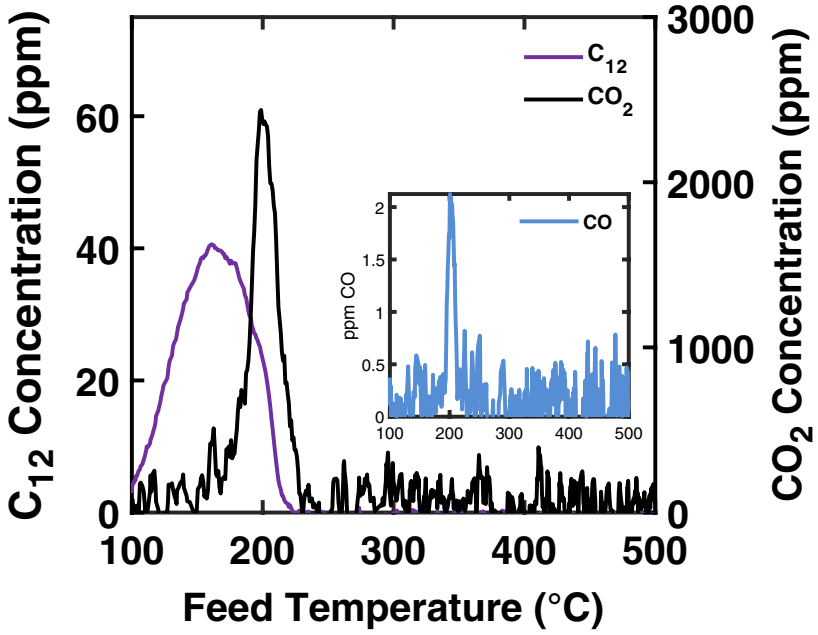

Figure 5.8: Corresponding C_{12}, CO_2, and CO TPD profiles for DL catalyst for a feed of 400ppm NO, 200 ppm C_{12}, 2% O_2 and 3% H_2O.

and occurs at a lower temperature (285°C). Both the Seq-SB and DL catalysts with C_{12} in the feed exhibit lower NO_2 formation compared to the NO-only feed, but since most of the C_{12} desorbs before NO_2 is formed (Fig. 5.7b), this is not caused by reduction but by decreased NO oxidation rates at the higher NO desorption temperature. Thus, in order to maximize NO_2 formation and desorption above 200°C, the NO desorption temperature needs to be tuned so as not to occur too late (or early).

The C_{12} TPD for the DL catalyst resembles that of the sequential configurations, indicating that the PtPdBEA top layer is still active for HC uptake (Fig. 5.8). The total adsorbed C_{12} is lower for DL than for either of the sequential catalysts. This may be due to the diffusional resistance of the PtPdBEA top layer limiting uptake on the bottom PdSSZ layer. Following the desorption of C_{12} there is a sharp CO_2 peak and a small (2ppm) CO peak just above 200°C, indicating complete oxidation and desorption. The selectivity of CO_2 during the TPD is ~75%, indicating sustained oxidation activity for the multicomponent systems (Table 5.5).

5.3.4 Type II experiments

In order to better understand the effect of combining the two catalyst functions, Type II experiments were conducted for Seq-BS, Seq-SB, and DL catalysts with and without C_{12}. As a reminder, in these experiments the feed to the catalyst is sustained throughout while the temperature is ramped from 100 to 500 °C after a 5 min exposure at 100°C.

Fig. 5.9 shows the results for Seq-BS, Seq-SB, and the DL catalysts for the NO-only feed (top row, Figs. 5.9a–c) and NO + C_{12} co-feed (bottom row, Figs. 5.9d–f). [Note that the time scale has been readjusted relative to the start of each temperature ramp for uniformity.] A common feature for each of the samples is the uptake of NO and generation of NO_2 that occur at the start of the temperature ramp. This feature was found to be unique to the Pd/SSZ-13 catalyst which is present in each of the configurations. As described by Gupta and Harold,[143] the uptake of NO and concurrent generation of NO_2 is a result of competitive adsorption between NO and H_2O along with the reduction of Pd. That feature is not observed with Pd/BEA (Fig. B.7). This additional NO uptake generated by the temperature ramp is added to the bars in Fig. 5.1 as a dotted line section for each of the catalysts and feeds (i.e., with or without C_{12}). The increase in NO uptake is attributed to the desorption of H_2O from the Pd cations at higher temperature, which is replaced by NO on the same sites. Finally, each of the three configurations shows comparable NO oxidation, with the DL catalyst exhibiting the highest peak conversion of 36% at ~350°C (Figs. 5.9a–c).

The addition of C_{12} to the feed leads to significant changes in the behavior of each of the configurations. For each, following the additional NO uptake below 200°C, there is a large dip in the NO_x concentration at 225°C, concurrent with the non-negligible generation of N_2O at a concentration of ~90ppm. Fig. 5.10 shows the corresponding C_{12} conversion for the co-feed Type II experiments. The decrease in NO_x occurs as C_{12} is oxidized, resulting in lean NO_x reduction. In the temperature range

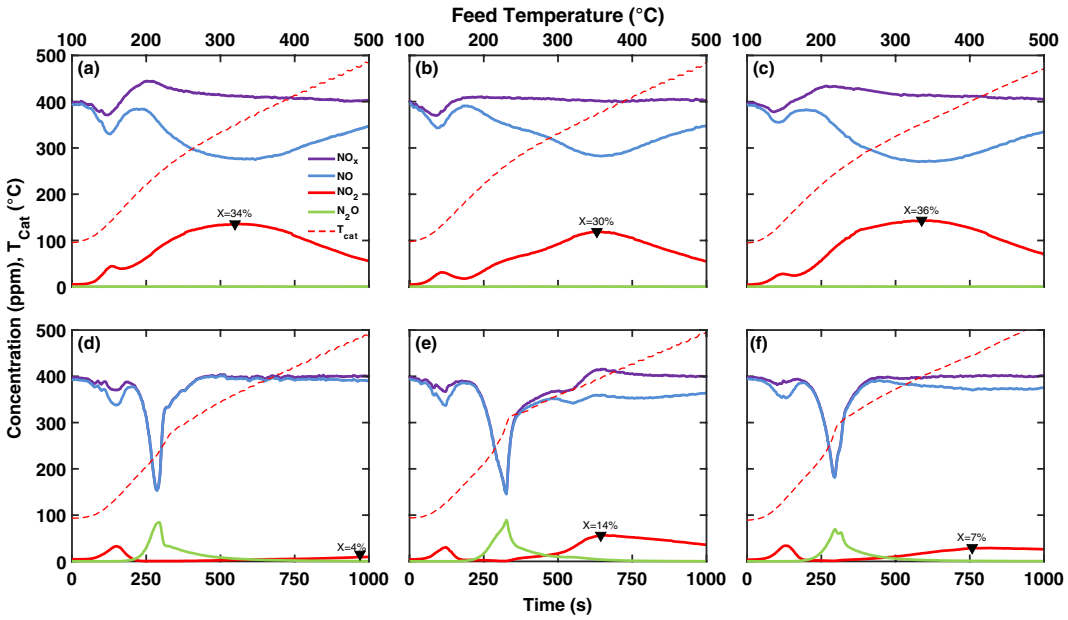

Figure 5.9: NO_x, NO, NO_2, N_2O, and Tcat profiles during Type II experiment temperature ramp. Top Row: NO only for (a) Seq-BS, (b) Seq-SB and (c) DL. Bottom Row: NO + C_{12} for (d) Seq-BS, (e) Seq-SB, and (f) DL.

of C_{12} oxidation light-off (270°C-300°C), very little NO_2 is detected, indicating that it is being consumed through reaction with C_{12} or partial oxidation products. Once the conversion of C_{12} exceeds 90%, N_2O formation subsides and NO_2 formation begins. The configuration type affects the amount and temperature of NO_2 formation. For Seq-BS, there is very little NO_2 formation, never exceeding 4% NO conversion beyond 500°C. For Seq-SB, there is a notable peak of NO_2 above 300°C which is probably due to the oxidation of desorbing NO that occurs in this temperature range. Because the oxidation catalyst is upstream in Seq-BS, it is likely that the exotherm leads to an increase in NO desorption at lower temperature that is consumed during reduction to N_2O. In contrast, for Seq-SB the exotherm effect is downstream so NO desorption proceeds at the conventional temperature and is then oxidized to NO_2.

Consistent with conclusions drawn from the Type I experiments, Seq-SB is the best configuration for generating NO_2 and desorbing NO_x at higher temperatures. For the DL catalyst, there is a slight decrease in NO oxidation in the presence of C_{12} compared to the Seq-SB catalyst, resulting in an NO conversion of only 7%. This is

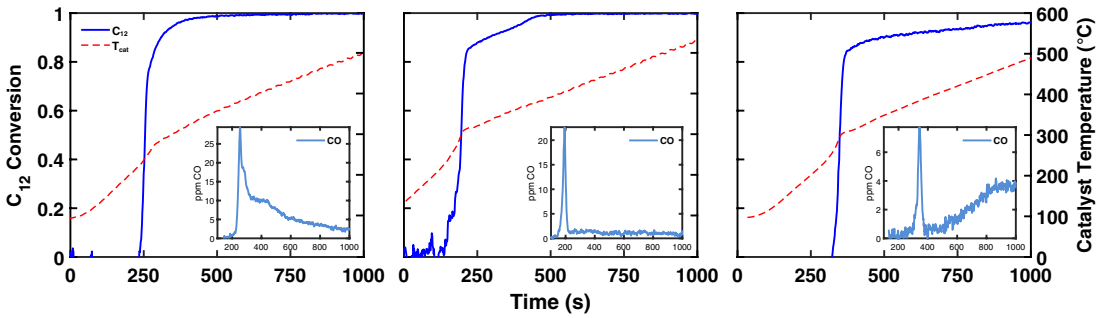

Figure 5.10: Conversion of C_{12} and T_{cat} profile during Type II temperature ramp. 400ppm NO, 200ppm C_{12}, 2% O_2, 3% H_2O for (a) Seq-BS, (b) Seq-SB and (c) DL. Ramp rate was 20°C/min. Inset: CO concentration profile.

due to the decreased conversion of C_{12} during the ramp (Fig. 5.10c), which we discuss below.

The C_{12} oxidation for the sequential systems is similar to the DL catalyst, with a light-off temperature of 280°C for Seq-BS and 293°C for Seq 2 (Figs. 5.10a, 5.10b). There are some differences in the CO formation profiles for all three cases, with the Seq-BS giving a sharp peak of CO followed by a slow decline, and the Seq-SB only having a sharp peak during light off. The presence of CO could be due to partial oxidation of C_{12} on the downstream PdSSZ catalyst, resulting in CO slip. This may also lead to reduced NO oxidation at higher temperatures due to CO inhibition, whereas the Seq-SB catalyst generates more NO_2 and less CO. Unlike the sequential systems, which achieve 100% conversion during the TPD, the DL catalyst does not achieve complete oxidation (Fig. 5.10c). This undesirable feature is similar to the PdSSZ only case (Fig. 5.4a), which also exhibited a maximum conversion of 95%. This would indicate that the light-off behavior is controlled by the PtPdBEA layer, but at higher temperatures the oxidation activity is controlled by the PdSSZ layer and therefore exhibits diffusional limitations. This is further evidenced by the gradual increase in CO formation, indicating partial oxidation of C_{12} interacting with the PdSSZ layer. The persistence of C_{12} therefore inhibits NO oxidation.

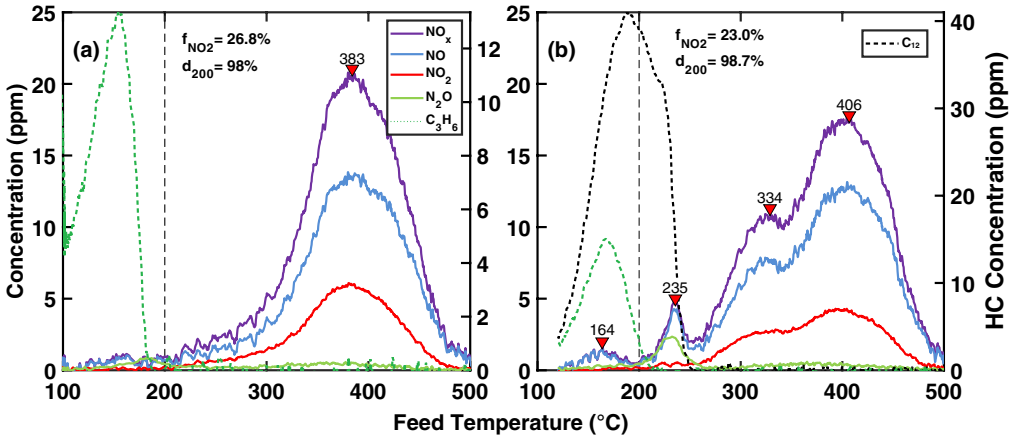

Figure 5.11: NO_x TPD profiles comparing feeds on DL catalyst. (a) 400ppm NO and 800 ppm C_3H_6, (b) 400ppm NO, 800ppm C_3H_6, and 200ppm C_{12}.

5.3.5 Effect of C_3H_6 on NO and C_{12} uptake

To determine the effect of smaller hydrocarbons on the NO TPD profile of the DL catalyst, selected Type I experiments with 800 ppm of C_3H_6 in the feed were conducted (Table 5.2). The TPD profiles shown in Fig. 5.11 for NO + C_3H_6 and NO + C_{12} + C_3H_6 indicate that the mechanism for C_3H_6 adsorption is unsurprisingly different than that for C_{12} adsorption. For the feed containing NO and C_3H_6, there is a desorption peak of C_3H_6 between 100 and 200 °C followed by a large single release peak of NO_x at 383°C, composed of 27% NO_2. Because there is only one peak, the d_{200} in the presence of C_3H_6 is 98%. In the presence of both C_3H_6 and C_{12}, the TPD profiles of NO_x and C_{12} are identical to those without C_3H_6 (Fig. 5.7b), with a d_{200} of 98.7%. The total amount of NO_x desorbing during these two experiments is similar (73.2 and 72.5 μmol/g-cat), indicating that the presence of these HCs does not affect the extent of NO uptake.

The HCs do have an impact on the NO_x desorption behavior, however (Fig. 5.11). In comparing the TPD profiles for C_{12} only (Fig. 5.7b) and for C_{12} + C_3H_6 (Fig. 5.11b), the low temperature NO peak at 164°C is not as pronounced when there is C_3H_6 in the feed. This suggests that C_3H_6 inhibits NO uptake in the PtPdBEA

layer. In addition, since the NO profiles for the C_{12}-containing feeds with and without C_3H_6 are similar, it is likely that C_{12} limits C_3H_6 adsorption on the PtPdBEA layer. Further, because NO desorbs as a single peak in the presence of C_3H_6 only, C_3H_6 affects NO adsorption on PdSSZ sites, thereby preventing the 334°C NO peak from occurring (Fig. 5.11b) and shifting the desorption instead to a single peak.

In the presence of both hydrocarbons, C_3H_6 fully desorbs by 200°C, but C_{12} continues to desorb until 236°C. In the corresponding C_3H_6 and C_{12} TPD profiles (Fig. 5.12), the CO_2 formation peak for C_3H_6 is much smaller than in the presence of C_3H_6 + C_{12}. This is likely a result of decreased uptake of C_3H_6. Here the CO_2 profile exhibits a second peak that occurs at the same temperature range as the NO_x desorption, indicating that indeed there is additional C_3H_6 uptake occurring on PdSSZ that desorbs as the oxidation product CO_2 (Fig. 5.12a). This may indicate the formation of stable surface species between adsorbing C_3H_6 and NO that results in the delayed desorption of NO_x. In the presence of C_{12}, this secondary CO_2 peak is not measurable, with CO_2 desorbing instead as one large peak at 250°C (Fig 5.12b). This single peak formation is similar to all C_{12}-containing experiments, indicating that C_{12} adsorption controls the overall system behavior.

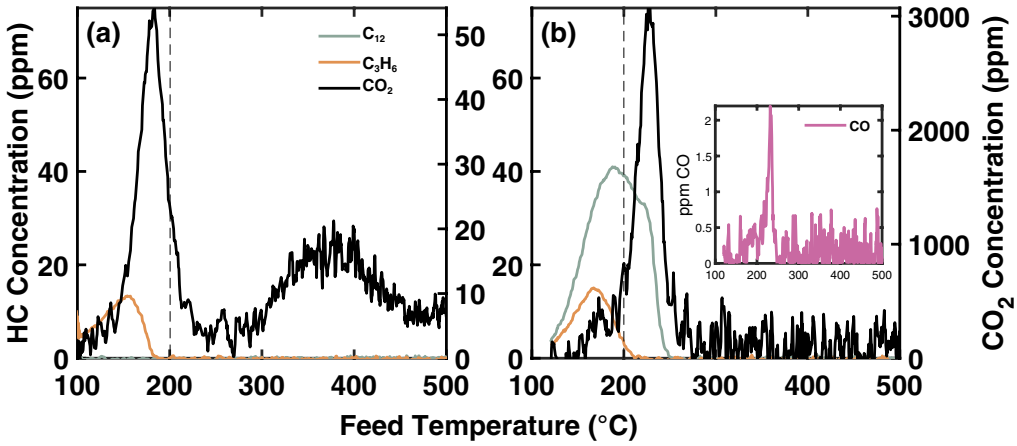

Figure 5.12: HC TPD profiles comparing feeds on DL catalyst. (a) 400ppm NO and 800ppm C_3H_6, (b) 400ppm NO, 800ppm C_3H_6, and 200ppm C_{12}.

To assess the performance of the DL catalyst under more practical feed condi-

tions, Type II experiments were conducted using a feed of NO + C_3H_6 (+ C_{12}). Because of the smaller size and higher reactivity of C_3H_6 within the zeolite pores, several notable interactions are observed (Fig 5.13). During uptake, NO_2 forms only in the absence of C_3H_6 (Fig. 5.13a,b). This is likely due to reaction with C_3H_6 leading to stable surface intermediates or adsorption inhibition, not reduction of NO_2. This is evidenced by the lack of N_2O, CO and CO_2 formation during uptake (Fig. B.8). As the temperature increases, there is no additional uptake of NO nor formation of NO_2, further suggesting that the C_3H_6 inhibits this chemistry. In terms of evaluating the ability of the DL catalyst to oxidize NO, C_{12}, or C_3H_6, all three feeds lead to a sharp NO consumption peak and a concurrent N_2O formation peak. During this period the HCs are oxidized before the NO_2 appears. Besides the simple feed of NO only (Fig. 5.13a), the highest NO_2 formation is seen in the C_3H_6-only case, likely due to a lower light off temperature and resistance to diffusional limitations (Fig. 13c). In the experiments containing C_{12}, the catalyst is unable to reach 100% conversion, resulting in NO oxidation inhibition (Figs. B.8a,c). In the presence of C_3H_6, both the formation of NO_2 and the conversion of C_{12} are enhanced (Fig. 5.13d), most likely because of the increased exotherm caused by the facile oxidation of C_3H_6 (Fig. B.9). This effect results in slightly higher NO_2 formation than in the C_{12} only case.

5.4 Conclusions

The comparative effectiveness of a series of catalysts including single-layer catalysts, sequential, and dual-layer configurations containing two precious metals (Pt, Pd) and two zeolite frameworks (BEA, SSZ-13) was systematically investigated. Catalyst performance metrics were quantified, including the uptake of NO and C_{12} in the presence of O_2 and H_2O with performance features during uptake and desorption identified.

Pd/SSZ-13 excels for NO uptake even in the presence of C_{12}, and PtPdBEA is exceptional for C_{12} storage and oxidation. We find both the sequential and dual-

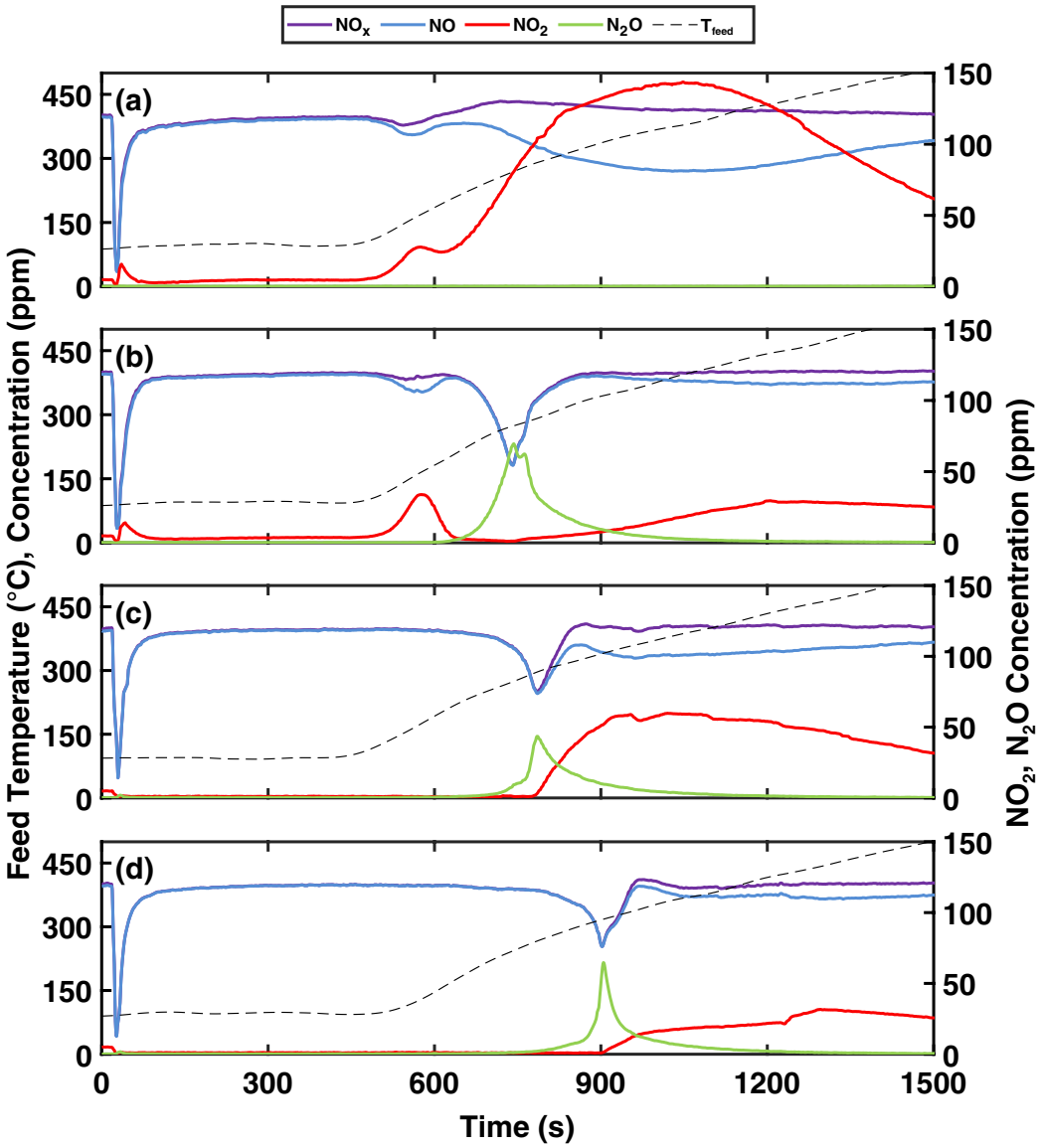

Figure 5.13: Type II NO_x profiles comparing feeds on DL catalyst. Feed: 2% O_2, 3% H_2O, and (a) 400ppm NO, (b) 400ppm NO + 200ppm C_{12}, (c) 400ppm NO + 800ppm C_3H_6, and (d) 400ppm NO + 800ppm C_3H_6 + 200ppm C_{12}.

layer systems to exhibit similar uptake features for NO and C_{12}, all of which perform significantly better than the individual systems. During sequential system experiments, the overall uptake of NO or C_{12} does not depend on the order of the sequence, but the order does affect NO_2 generation and exothermic effects.

The dual layer configuration consisting of 1 wt.% Pt-Pd/BEA on 1 wt.% Pd/SSZ-13 works particularly well because it traps HCs on the top layer and NO on the bottom

layer with little inhibition and with a smaller catalyst volume. We find that large and small hydrocarbons including C_{12} and C_3H_6 delay NO_x desorption for this dual layer system to temperatures between 300 and 400 °C, with 95-99 % of all NO_x desorption occurring above 200°C. The incorporation of Pt to the top layer can effectively oxidize C_{12} below 300°C and can oxidize NO to NO_2 as it desorbs from the bottom SSZ layer, a useful attribute for improving activity of the downstream SCR catalyst.

Several improvements of the dual-layer configuration were identified. Most importantly, a decrease in overall monolith volume is achieved without significantly compromising performance. However, we also find that C_{12} oxidation on the dual layer is diffusion-limited, although the addition of C_3H_6 leads to improved conversion at high temperatures. By performing two types of experiments (Type I and Type II), we were able to evaluate the desorption profiles at both a high level of accuracy and under practical feed conditions. Type I experiments show that too high of a NO_x release temperature may lead to a decrease in NO_2 formation. Since the dual layer catalyst releases NO_x at intermediate temperatures, it generates more NO_2. Type II experiments indicate an increase in NO uptake during a temperature ramp from 100 to 200 °C, likely due to thermal desorption of H_2O that drives the NO uptake mechanism forward. In conclusion, the results of these experiments are very useful in providing optimization strategies for LHCNT performance in the context of combining various trap materials under a variety of feed conditions.

Chapter 6: Conclusions

The research presented here focuses on gaining a deeper understanding of multi-functional catalysts that can be used as part of more complete engine aftertreatment system, and for determining optimization strategies for these materials. Through this work we provide a thorough investigation of the performance of both high and low temperature operating automotive catalysts that can store NO_x and release or convert it when the catalyst demands it. We also develop models that can predict the performance of these catalysts. The systematic results enable the development of improvements in automotive catalysts, particularly those focusing on low temperature sorption of NO_x and HCs.

6.1 Conclusions

Experiments performed on the TWNSC catalyst reveal that depending on the stoichiometric number of the feed, various performance metrics can be tuned. Steady state experiments reveal that CO and C_3H_6 conversion increase with temperature and stoichiometric number S_N, while NO_x conversion and NH_3 production decrease with increasing temperature and S_N. Under rich enough conditions, high amounts of NH_3 can be produced, which is useful for coupling with a downstream SCR.

For cycling performance, the TWNSC may be tuned to achieve a high NO_x conversion and N_2 selectivity. The concentrations of reductant and O_2, duration of the rich pulse (duty fraction), and cycle time may be tuned to achieve a desired NO_x conversion and/or NH_3 selectivity. If there is a large disparity in the lean/rich ratio over the cycle, the NO_x conversion exhibits a maximum value at an intermediate cycle time, as does the ANR. Optimization should be possible for a particular application that maximizes the NO_x conversion and reductant utilization. Modeling work con-

ducted on the TWNSC using experimental data was able to successfully predict most of the performance features of the TWNSC, which is useful for additional optimization studies.

Evaluation of 2wt.% Pd/BEA as a model LHCNT catalyst through both transient experiments and DRIFTS measurements reveal a combination of supportive and detrimental coupling effects. The desorption profiles indicate the presence of NO_x storage sites that lead to various release temperatures throughout the TPD. Adsorption of C_3H_6 is not trivial, resulting in higher hydrocarbons through coupling mechanisms based on the acidity and pore structure of the BEA zeolite. The co-uptake of NO and C_3H_6 indicates that C_3H_6 is the dominant adsorbing species on the BAS, inhibiting NO uptake. However, it was found that NO uptake on Pd is not affected and instead desorbs at elevated temperatures compared to the absence of C_3H_6. These results provide new insights into the chemical reaction pathways involved in the LHCNT, which are more complex than originally thought. Addition of water to the feed simplifies some of these interactions, however, as water blankets the entire surface of the zeolite, effectively eliminating uptake on BAS. The results are a useful stepping stone for developing a predictive model, which can ultimately be used to further refine and optimize the performance of the LHCNT.

Based on the experimental data obtained for co-adsorption of NO and C_3H_6 on Pd/BEA, a reactor model was developed. The model was able to predict NO and C_3H_6 uptake and release both individually and as a mixed feed. The model captures the inhibition effect of C_3H_6 on NO uptake on BAS, and illustrates the complexity of the reaction network when a mixed feed is involved. The model is an excellent tool for generating a crude preliminary assessment of various materials and operating conditions, including feed composition, temperature, and flow rate. Due to the complexity of the reaction scheme and the ongoing debate regarding the nature of the active sites of LHCNT-type materials, the model does not delve into molecular de-

tails, and instead serves as a macroscopic predictive tool. Further model refinement would address these challenges.

In order to achieve high uptake performance of both NO_x and HCs in the presence of water, additional catalysts and design strategies were employed. In an architectural study, small and large pore zeolites were combined with incorporated Pd or Pt in a variety of configurations to improve performance and provide insights for optimization. Individual catalysts were first tested, where Pd/SSZ-13 excelled at NO uptake, even in the presence of C_{12}, and Pt-Pd/BEA proved exceptional for C_{12} storage and oxidation. These catalysts were combined into a series of sequential and dual-layer configurations. Both types of configurations exhibited similar uptake features for NO and C_{12}, and all performed significantly better than the individual systems.

The dual layer configuration consisting of 1 wt.% Pt-Pd/BEA on 1 wt.% Pd/SSZ-13 works particularly well because it traps HCs on the top layer and NO on the bottom layer with little inhibition and with a smaller catalyst volume. We find that large and small hydrocarbons including C_{12} and C_3H_6 delay NO_x desorption for this dual layer system to temperatures between 300 and 400 °C, with 95–99 % of all NO_x desorption occurring above 200°C. The incorporation of Pt in the top layer can effectively oxidize C_{12} below 300°C and can oxidize NO to NO_2 as it desorbs from the bottom SSZ layer, a useful attribute for improving activity of the downstream SCR catalyst. The results of these experiments show promising results for improving the overall performance of the LHCNT.

6.2 Future work

Although this research describes well-organized studies that provide a detailed analysis of the phenomena that occur during operation of both the TWNSC and LHCNT, there are several opportunities for improvement. Some examples are provided in the following sections.

6.2.1 Spatiotemporal analysis of TWNSC

One of the interesting results of the TWNSC modeling work is the spatial resolution of reduction/oxidation products in the channels. To confirm these results, experiments can be done with a Spaci-MS system, which contains a moveable capillary that can analyze the products at various points along the length of a channel. It would be interesting to see which products form at the front of the TWNSC as opposed to only those measurable in the effluent. Work by Li et al. on a sequential LNT+SCR catalyst configuration showed that during a lean/rich cycle, large amounts of NO_x (up to 400ppm) were generated during the rich phase on the upstream LNT catalyst.[76] Because of the SCR downstream, however, virtually no NO was detected in the effluent. Therefore it is of interest to not only perform these spacial measurements on a standalone TWNSC, but to also equip it with a downstream SCR catalyst to see if the optimization strategies are upheld in practice.

6.2.2 Modeling of complex LHCNT systems

Our work on the LHCNT model thus far demonstrates the complexity of modeling a transient system in both the global and micro kinetic regimes. As the number of reactions increases, so does the computational effort for estimating parameters. Modeling the single catalyst is useful for confirming the proposed reaction schemes, and the model can be used to predict catalyst performance at different temperatures, feed conditions, or for zeolite frameworks, just by modifying specific parameters. After further refining the current model for a single LHCNT catalyst, it would be beneficial to model the dual-layer or sequential configurations described in Chapter 5. Predicting the behavior of a dual-layer system would be particularly useful in order to explore the diffusion limitations created by the top layer. It would allow further investigation into the conversion resistance experienced by C_{12}, and it would help us understand the delayed NO desorption temperature. Such a model would be

more complex however, not just because of the dual-layered architecture. A crystallite scale model would need to be developed, similar to that by the work of Shakya et al.,[88] in order to capture the effect of C_{12} pore blocking on NO diffusion. In that study, Pt crystallites were modeled for an LNT application to predict NO_x storage behavior during lean/rich cycles. A similar model would be very beneficial for predicting the diffusion of NO and C_{12} during desorption, enabling a deeper understanding of these mechanisms and generating a more accurate predictive model.

6.2.3 Investigation of LHCNT with more complex feeds

As mentioned previously, the PNA function of the LHCNT has only been extensively studied with simple feeds such as NO, O_2, H_2O, and smaller hydrocarbons. In our work we investigated the effect of both C_3H_6 and C_{12} on various LHCNT materials, including BEA and SSZ-13 zeolites. A systematic extension of this work investigating the effect of various hydrocarbons on NO uptake would be very useful for understanding the behavior of these catalysts with more practical feeds. Automotive exhaust contains a large number of hydrocarbons, including aromatics, and the high acidity of the zeolites used for LHCNT applications could lead to a number of reactions/coupling effects in the pores. These effects may cause a delay in NO desorption, as with C_{12}, or have an effect on the behavior of the other hydrocarbons in the feed. For example, recent work by Peng et al. discovered that propylene leads to a bimodal desorption behavior of hexane on BEA, resulting in a higher temperature peak than would occur without propylene. Such experiments on LHCNT materials would enable a more practical understanding of their behavior.

6.2.4 Stability and deactivation of multi-functional catalysts

Finally, although the multi-functional catalysts described herein are promising, our work focused solely on fresh catalysts. It would therefore be practical—and imperative—to evaluate these catalysts under harsh conditions that represent more

realistic driving conditions. Such conditions include higher temperatures, sulfur poisoning, highly reductive or oxidative environments, or attrition/ physical degradation forces on the catalyst. The LHCNT, for example, has been shown to irreversibly deactivate in the presence of CO. From the recent work by Gu et al. on the hydrothermal aging of Pd/BEA, even under highly oxidative conditions only some of the original activity of Pd could be recovered.[118] This is due to the presumed deactivation mechanism of the isolated Pd particles being reduced to Pd^0 and agglomerating on the external surface of the zeolite crystallites. Such studies are useful because stability results may contradict previous findings. Research shows that CO delays the desorption of NO to higher temperatures and increases NO uptake in the presence of water.[62,64] At the same time, continued exposure of CO on the catalyst will negate the benefits anticipated from the fresh catalyst observations. Knowledge of such deactivation effects would be useful in properly designing catalysts for implementation in engine after-treatment systems.

References

[1] Heck, R. M.; Farrauto, R. J. Automobile exhaust catalysts. *Applied Catalysis A: General* **2001**, *221*, 443–457.

[2] Twigg, M. V. Progress and future challenges in controlling automotive exhaust gas emissions. *Applied Catalysis B: Environmental* **2007**, *70*, 2–15.

[3] EPA: Light-Duty Vehicles and Trucks Emission Standards. 2016; https://www.epa.gov/emission-standards-reference-guide/light-duty-vehicles-and-trucks-emission-standards.

[4] Texas Emission Sources - A Graphical Representation. 2019; https://www.tceq.texas.gov/airquality/areasource/texas-emissions-graphical-representation.

[5] Emission Standards: USA: Cars and Light-Duty Trucks—Tier 3. 2016; https://www.dieselnet.com/standards/us/ld{_}t3.php{\#}supp.

[6] Murzin, D. *Engineering catalysis*; Walter de Gruyter GmbH, 2013; pp 364–365.

[7] Hayes, R.; Liu, B.; Moxom, R.; Votsmeier, M. The effect of washcoat geometry on mass transfer in monolith reactors. *Chemical Engineering Science* **2004**, *59*, 3169 – 3181.

[8] Amariei, D.; Amrousse, R.; Batonneau, Y.; Brahmi, R.; Kappenstein, C.; Cartoixa, B. In *Scientific Bases for the Preparation of Heterogeneous Catalysts*; Gaigneaux, E., Devillers, M., Hermans, S., Jacobs, P., Martens, J., Ruiz, P., Eds.; Studies in Surface Science and Catalysis; Elsevier, 2010; Vol. 175; pp 35 – 42.

[9] Metkar, P. S.; Balakotaiah, V.; Harold, M. P. Experimental study of mass transfer limitations in Fe- and Cu-zeolite-based NH_3-SCR monolithic catalysts. *Chemical Engineering Science* **2011**, *66*, 5192–5203.

[10] Wang, J.; Chen, H.; Hu, Z.; Yao, M.; Li, Y. A Review on the Pd-Based Three-Way Catalyst. *Catalysis Reviews* **2015**, *57*, 79–144.

[11] Graham, G. W.; Jen, H. W.; Chun, W.; Sun, H. P.; Pan, X. Q.; McCabe, R. W. Coarsening of Pt particles in a model NO_x trap. *Catalysis Letters* **2004**, *93*, 129–134.

[12] Rainer, D. R.; Koranne, M.; Vesecky, S. M.; Goodman, D. W. CO + O_2 and CO + NO Reactions over Pd/Al_2O_3 Catalysts . *The Journal of Physical Chemistry B* **1997**, *101*, 10769–10774.

[13] Barbier, J.; Duprez, D. Steam effects in three-way catalysis. *Applied Catalysis B: Environmental* **1994**, *4*, 105–140.

[14] Han, Z.; Wang, J.; Yan, H.; Shen, M.; Wang, J.; Wang, W.; Yang, M. Performance of dynamic oxygen storage capacity, water–gas shift and steam reforming reactions over Pd-only three-way catalysts. *Catalysis Today* **2010**, *158*, 481 – 489, Perspective on catalysis for sustainable energy and environmental technologies.

[15] Anderson, J. A.; Bachiller-Baeza, B.; Fernández-García, M. Role of Pt in Pt/Ba/Al_2O_3 NO_x storage and reduction traps. *Physical Chemistry Chemical Physics* **2003**, *5*, 4418–4427.

[16] Kabin, K. S.; Muncrief, R. L.; Harold, M. P. NO_x storage and reduction on a Pt/BaO/alumina monolithic storage catalyst. *Catalysis Today* **2004**, *96*, 79–89.

[17] Clayton, R. D.; Harold, M. P.; Balakotaiah, V. Performance Features of Pt/BaO lean NO_x trap with hydrogen as reductant. *AIChE Journal* **2009**, *55*, 687–700.

[18] Kumar, A.; Harold, M. P.; Balakotaiah, V. Isotopic studies of NO_x storage and reduction on $Pt/BaO/Al_2O_3$ catalyst using temporal analysis of products. *Journal of Catalysis* **2010**, *270*, 214–223.

[19] Li, M.; Easterling, V. G.; Harold, M. P. Towards optimal operation of sequential NO_x storage and reduction and selective catalytic reduction. *Applied Catalysis B: Environmental* **2016**, *184*, 364–380.

[20] Takahashi, N.; Shinjoh, H.; Iijima, T.; Suzuki, T.; Yamazaki, K.; Yokota, K.; Suzuki, H.; Miyoshi, N.; Matsumoto, S.-i.; Tanizawa, T.; Tanaka, T.; Tateishi, S.-s.; Kasahara, K. The new concept 3-way catalyst for automotive lean-burn engine: NO_x storage and reduction catalyst. *Catalysis Today* **1996**, *27*, 63–69.

[21] Harold, M. P. NOxstorage and reduction in lean burn vehicle emission control: A catalytic engineer's playground. *Current Opinion in Chemical Engineering* **2012**, *1*, 303–311.

[22] Pereda-Ayo, B.; R., J. *Diesel Engine - Combustion, Emissions and Condition Monitoring*; InTech, 2013.

[23] Kabin, K. S.; Khanna, P.; Muncrief, R. L.; Medhekar, V.; Harold, M. P. Monolith and TAP reactor studies of NO_x storage on $Pt/BaO/Al_2O_3$: Elucidating the mechanistic pathways and roles of Pt. *Catalysis Today* **2006**, *114*, 72–85.

[24] Epling, W. S.; Parks, J. E.; Campbell, G. C.; Yezerets, A.; Currier, N. W.; Campbell, L. E. Further evidence of multiple NO_x sorption sites on NO_x storage/reduction catalysts. *Catalysis Today* **2004**, *96*, 21–30.

[25] Liu, G.; Gao, P. X. A review of NO_x storage/reduction catalysts: Mechanism, materials and degradation studies. 2011.

[26] Jacobs, G.; Williams, L.; Graham, U.; Thomas, G. A.; Sparks, D. E.; Davis, B. H. Low temperature water-gas shift: In situ DRIFTS-reaction study of ceria surface area on the evolution of formates on Pt/CeO_2 fuel processing catalysts for fuel cell applications. *Applied Catalysis A: General* **2003**, *252*, 107–118.

[27] Kwak, J. H.; Kim, D. H.; Szanyi, J.; Peden, C. H. F. Excellent sulfur resistance of $Pt/BaO/CeO_2$ lean NO_x trap catalysts. *Applied Catalysis B: Environmental* **2008**, *84*, 545–551.

[28] Peralta, M. A.; Milt, V. G.; Cornaglia, L. M.; Querini, C. A. Stability of $Ba,K/CeO_2$ catalyst during diesel soot combustion: Effect of temperature, water, and sulfur dioxide. *Journal of Catalysis* **2006**, *242*, 118–130.

[29] Nova, I.; Castoldi, L.; Lietti, L.; Tronconi, E.; Forzatti, P. On the dynamic behavior of "NO_x-storage/reduction" $Pt-Ba/Al_2O_3$ catalyst. Catalysis Today. 2002; pp 431–437.

[30] Lietti, L.; Forzatti, P.; Nova, I.; Tronconi, E. NO_x storage reduction over $Pt-Ba/\gamma$ -Al_2O_3 catalyst. *Journal of Catalysis* **2001**, *204*, 175–191.

[31] Muncrief, R. L.; Khanna, P.; Kabin, K. S.; Harold, M. P. Mechanistic and kinetic studies of NO_x storage and reduction on $Pt/BaO/Al_2O_3$. Catalysis Today. 2004.

[32] Theis, J. R.; Dearth, M.; McCabe, R. LNT+SCR Catalyst Systems Optimized for NO_x Conversion on Diesel Applications. SAE Technical Paper. 2011.

[33] Metkar, P. S.; Salazar, N.; Muncrief, R.; Balakotaiah, V.; Harold, M. P. Selective catalytic reduction of NO with NH_3 on iron zeolite monolithic catalysts:

Steady-state and transient kinetics. *Applied Catalysis B: Environmental* **2011**, *104*, 110–126.

[34] Zheng, Y.; Harold, M. P.; Luss, D. Effects of CO, H_2 and C_3H_6 on Cu-SSZ-13 catalyzed NH_3-SCR. *Catalysis Today* **2016**, *264*, 44–54.

[35] Theis, J. R.; Kim, J.; Cavataio, G. Passive TWC+SCR Systems for Satisfying Tier 2, Bin 2 Emission Standards on Lean-Burn Gasoline Engines. 2015; `https://www.jstor.org/stable/26273100`.

[36] DiGiulio, C. D.; Pihl, J. A.; II, J. E. P.; Amiridis, M. D.; Toops, T. J. Passive-ammonia selective catalytic reduction (SCR): Understanding NH_3 formation over close-coupled three way catalysts (TWC). *Catalysis Today* **2014**, *231*, 33–45.

[37] Corma, A. Application of Zeolites in Fluid Catalytic Cracking and Related Processes. *Studies in Surface Science and Catalysis* **1989**, *49*, 49–67.

[38] Jolly, S.; Saussey, J.; Bettahar, M. M.; Lavalley, J. C.; Benazzi, E. Reaction mechanisms and kinetics in the n-hexane cracking over zeolites. *Applied Catalysis A: General* **1997**, *156*, 71–96.

[39] Cortright, R. D.; Dumesic, J. A.; Madon, R. J. Catalytic cycles for hydrocarbon cracking on zeolites. *Topics in Catalysis* **1997**, *4*, 15–26.

[40] Rahimi, N.; Karimzadeh, R. Catalytic cracking of hydrocarbons over modified ZSM-5 zeolites to produce light olefins: A review. *Applied Catalysis A: General* **2011**, *398*, 1–17.

[41] Weitkamp, J. Isomerization of Long-Chain n-Alkanes on a Pt/CaY Zeolite Catalyst. *Industrial and Engineering Chemistry Product Research and Development* **1982**, *21*, 550–558.

[42] Weitkamp, J.; Jacobs, P. A.; Martens, J. A. Isomerization and hydrocracking of C 9 through C 16 n-alkanes on Pt/HZSM-5 zeolite. *Applied Catalysis* **1983**, *8*, 123–141.

[43] Göltl, F.; Grüneis, A.; Bučko, T.; Hafner, J. Van der Waals interactions between hydrocarbon molecules and zeolites: Periodic calculations at different levels of theory, from density functional theory to the random phase approximation and Moller-Plesset perturbation theory. *Journal of Chemical Physics* **2012**, *137*, 114111.

[44] Townsend, R. P. Chapter 10 Ion Exchange in Zeolites. *Studies in Surface Science and Catalysis* **1991**, *58*, 359–390.

[45] Baerlocher, C.; McCusker, L. Database of zeolite structures. `www.iza-structure.org/databases/`.

[46] Higgins, J. B.; LaPierre, R. B.; Schlenker, J. L.; Rohrman, A. C.; Wood, J. D.; Kerr, G. T.; Rohrbaugh, W. J. The framework topology of zeolite beta. Preprints Symposia. 1988; p 642.

[47] van Koningsveld, H.; Jansen, J. C.; van Bekkum, H. The monoclinic framework structure of zeolite H-ZSM-5. Comparison with the orthorhombic framework of as-synthesized ZSM-5. *Zeolites* **1990**, *10*, 235–242.

[48] Wen, C.; Geng, L.; Han, L.; Wang, J.; Chang, L.; Feng, G.; Kong, D.; Liu, J. A comparative first principle study on trivalent ions incorporated SSZ-13 zeolites. *Phys. Chem. Chem. Phys.* **2015**, *17*.

[49] Dhillon, P. S.; Harold, M. P.; Wang, D.; Kumar, A.; Joshi, S. Hydrothermal aging of Pt/Al_2O_3 monolith: Washcoat morphology degradation effects studied using ammonia and propylene oxidation. *Catalysis Today* **2018**, *320*, 20–29.

[50] Gao, F.; Szanyi, J. On the hydrothermal stability of Cu/SSZ-13 SCR catalysts. *Applied Catalysis A: General* **2018**, *560*, 185–194.

[51] Shrestha, S.; Harold, M. P.; Kamasamudram, K. Experimental and modeling study of selective ammonia oxidation on multi-functional washcoated monolith catalysts. *Chemical Engineering Journal* **2015**, *278*, 24–35.

[52] Reşitoğlu, b. A.; Altinişik, K.; Keskin, A. The pollutant emissions from diesel-engine vehicles and exhaust aftertreatment systems. *Clean Technologies and Environmental Policy* **2015**, *17*, 15–27.

[53] Li, H.-X.; Donohue, J. M.; Chrmier, W.; Chu, Y. F.; Li A'*, H.-X.; Donohue, J. M.; Cormier, W. E.; Chu, Y. F. Application of zeolites as hydrocarbon traps in automotive emission controls. *Studies in Surface Science and Catalysis* **2005**, *158*, 1375–1382.

[54] López, J. M.; Navarro, M. V.; García, T.; Murillo, R.; Mastral, A. M.; Varela-Gandía, F. J.; Lozano-Castelló, D.; Bueno-López, A.; Cazorla-Amorós, D. Screening of different zeolites and silicoaluminophosphates for the retention of propene under cold start conditions. *Microporous and Mesoporous Materials* **2010**, *130*, 239–247.

[55] Migliardini, F.; Iucolano, F.; Caputo, D.; Corbo, P. MFI and FAU-type zeolites as trapping materials for light hydrocarbons emission control at low partial pressure and high temperature. *Journal of Chemistry* **2015**, *2015*.

[56] Otto, K.; Montreuil, C. N.; Todor, O.; McCabe, R. W.; Gandhi, H. S. Adsorption of Hydrocarbons and Other Exhaust Components on Silicalite. *Industrial and Engineering Chemistry Research* **1991**, *30*, 2333–2340.

[57] Burke, N. R.; Trimm, D. L.; Howe, R. F. The effect of silica:alumina ratio and

hydrothermal ageing on the adsorption characteristics of BEA zeolites for cold start emission control. *Applied Catalysis B: Environmental* **2003**, *46*, 97–104.

[58] Zelinsky, R.; Epling, W. Effects of Multicomponent Hydrocarbon Feed on Hydrocarbon Adsorption–Desorption and Oxidation Light-Off Behavior on a Pd/BEA Hydrocarbon Trap. *Catalysis Letters* **2019**, *149*, 3194–3202.

[59] Ambast, M.; Karinshak, K.; Harold, M. P. Passive NO_x Adsorption on Pd/H-ZSM-5: Experiments and Modeling. *Applied Catalysis B: Environmental*

[60] Chen, H.-Y.; Collier, J. E.; Liu, D.; Mantarosie, L.; Durán-Martín, D.; Novák, V.; Rajaram, R. R.; Thompsett, D. Low Temperature NO Storage of Zeolite Supported Pd for Low Temperature Diesel Engine Emission Control. *Catalysis Letters* **2016**, *146*, 1706–1711.

[61] Chen, H.-Y. Zeolite Supported Pd Catalysts for Low Temperature NO_x and HC storage. CLEERS. 2016.

[62] Zheng, Y.; Kovarik, L.; Engelhard, M. H.; Wang, Y.; Wang, Y.; Gao, F.; Szanyi, J. Low-Temperature Pd/Zeolite Passive NOx Adsorbers: Structure, Performance, and Adsorption Chemistry. *Journal of Physical Chemistry C* **2017**, *121*, 15793–15803.

[63] Descorme, C.; Gélin, P.; Primet, M.; Lécuyer, C. Infrared study of nitrogen monoxide adsorption on palladium ion-exchanged ZSM-5 catalysts. *Catalysis Letters* **1996**, *41*, 133–138.

[64] Khivantsev, K.; Jaegers, N. R.; Kovarik, L.; Prodinger, S.; Derewinski, M. A.; Wang, Y.; Gao, F.; Szanyi, J. Palladium/Beta zeolite passive NO_x adsorbers (PNA): Clarification of PNA chemistry and the effects of CO and zeolite crystallite size on PNA performance. *Applied Catalysis A: General* **2019**, *569*, 141–148.

[65] Theis, J. R.; Lambert, C. The Effects of CO, C_2H_4, and H_2O on the NO_x Storage Performance of Low Temperature NO_x Adsorbers for Diesel Applications. *SAE International Journal of Engines* **2017**, *10*, 2017–01–0942.

[66] Mei, D.; Gao, F.; Szanyi, J.; Wang, Y. Mechanistic insight into the passive NO_x adsorption in the highly dispersed Pd/HBEA zeolite. *Applied Catalysis A: General* **2019**, *569*, 181–189.

[67] Khivantsev, K.; Jaegers, N. R.; Kovarik, L.; Hanson, J. C.; Tao, F. F.; Tang, Y.; Zhang, X.; Koleva, I. Z.; Aleksandrov, H. A.; Vayssilov, G. N.; Wang, Y.; Gao, F.; Szanyi, J. Achieving Atomic Dispersion of Highly Loaded Transition Metals in Small-pore Zeolite SSZ-13: A New Class of High-capacity and High-efficiency Low Temperature CO and NO_x Adsorbers. *Angewandte Chemie* **2018**, *57*, 16672–16677.

[68] Aylor, A. W.; Lobree, L. J.; Reimer, J. A.; Bell, A. T. Investigations of the dispersion of Pd in H-ZSM-5. *Journal of Catalysis* **1997**, *172*, 453–462.

[69] U.S. Energy Information Administration: U.S. Job Market and Automotive Sales Trends Support Growth in Gasoline Use. 2015; `http://www.eia.gov/todayinenergy/detail.cfm?id=22932`.

[70] Packham, K. C. P. Lean-burn engine technology increases efficiency, reduces NO_x emissions. *Technical Information from Cummins Power Generation* **2007**, *7009*, 6–7.

[71] Shelef, M.; Otto, K.; Gandhi, H. The oxidation of CO by O2 and by NO on supported chromium oxide and other metal oxide catalysts. *Journal of Catalysis* **1968**, *12*, 361–375.

[72] Burch, R.; Millington, P. Selective reduction of nitrogen oxides by hydrocarbons

under lean-burn conditions using supported platinum group metal catalysts. *Catalysis Today* **1995**, *26*, 185–206.

[73] Luo, J. Y.; Epling, W. S. New insights into the promoting effect of H_2O on a model Pt/Ba/Al_2O_3 NSR catalyst. *Applied Catalysis B: Environmental* **2010**, *97*, 236–247.

[74] Colombo, M.; Tronconi, E. A comparative study of the NH_3-SCR reactions over a Cu-zeolite and a Fe-zeolite catalyst. *Catalysis Today* **2010**, *151*, 223–230.

[75] Zheng, Y.; Liu, Y.; Harold, M. P.; Luss, D. LNT-SCR dual-layer catalysts optimized for lean NO_x reduction by H_2 and CO. *Applied Catalysis B: Environmental* **2014**, *148-149*, 311–321.

[76] Li, M.; Easterling, V. G.; Harold, M. P. Spatio-temporal features of the sequential NO_x storage and reduction and selective catalytic reduction reactor system. *Catalysis Today* **2016**, *267*, 177–191.

[77] Ikeda, Y.; Sobue, K.; Tsuji, S.; Matsumoto, S. Development of NO_x Storage-Reduction Three-way Catalyst for D-4 Engines. *SAE* **1999**, 1999–01–12.

[78] Lietti, L.; Artioli, N.; Righini, L.; Castoldi, L.; Forzatti, P. Pathways for N 2 and N 2O formation during the reduction of NO x over Pt-Ba/Al 2O 3 LNT catalysts investigated by labeling isotopic experiments. *Industrial and Engineering Chemistry Research* **2012**, *51*, 7597–7605.

[79] Xu, J.; Clayton, R.; Balakotaiah, V.; Harold, M. P. Experimental and microkinetic modeling of steady-state NO reduction by H_2 on Pt/BaO/Al_2O_3 monolith catalysts. *Applied Catalysis B: Environmental* **2008**, *77*, 395–408.

[80] Voltz, S. E.; Morgan, C. R.; Liederman, D.; Jacob, S. M. Kinetic Study of Car-

bon Monoxide and Propylene Oxidation on Platinum Catalysts. *Industrial and Engineering Chemistry Product Research and Development* **1973**, *12*, 294–301.

[81] Burch, R.; Shestov, A. A.; Sullivan, J. A. A steady-state isotopic transient kinetic analysis of the $NO/O_2/H_2$ reaction over Pt/SiO_2 catalysts. *Journal of Catalysis* **1999**, *188*, 69–82.

[82] Dasch, J. M. Nitrous Oxide Emissions from Vehicles. *Journal of the Air and Waste Management Association* **1992**, *42*, 63–67.

[83] Nova, I.; Lietti, L.; Castoldi, L.; Tronconi, E.; Forzatti, P. New insights in the NO_x reduction mechanism with H_2 over Pt-Ba/γ-Al_2O_3 lean NO_x trap catalysts under near-isothermal conditions. *Journal of Catalysis* **2006**, *239*, 244–254.

[84] Bhatia, D.; Clayton, R. D.; Harold, M. P.; Balakotaiah, V. A global kinetic model for NO_x storage and reduction on $Pt/BaO/Al_2O_3$ monolithic catalysts. *Catalysis Today* **2009**, *S147*, S250–S256.

[85] Bhatia, D.; McCabe, R. W.; Harold, M. P.; Balakotaiah, V. Experimental and kinetic study of NO oxidation on model Pt catalysts. *Journal of Catalysis* **2009**, *266*, 106–119.

[86] Clayton, R. D.; Harold, M. P.; Balakotaiah, V. NO_x storage and reduction with H_2 on $Pt/BaO/Al_2O_3$ monolith: Spatio-temporal resolution of product distribution. *Applied Catalysis B: Environmental* **2008**, *84*, 616–630.

[87] Mráček, D.; Kočí, P.; Choi, J. S.; Partridge, W. P. New operation strategy for driving the selectivity of NO_x reduction to N_2, NH_3 or N_2O during lean/rich cycling of a lean NO_x trap catalyst. *Applied Catalysis B: Environmental* **2016**, *182*, 109–114.

[88] Shakya, B. M.; Harold, M. P.; Balakotaiah, V. Effect of cycle time on NH_3 generation on low Pt dispersion $Pt/BaO/Al_2O_3$ catalysts: Experiments and crystallite-scale modeling. *Chemical Engineering Journal* **2013**, *230*, 584–594.

[89] Solouk, A.; Shakiba-Herfeh, M.; Kannan, K.; Solmaz, H.; Dice, P.; Bidarvatan, M.; Kondipati, N. N. T.; Shahbakhti, M. Fuel Economy Benefits of Integrating a Multi-Mode Low Temperature Combustion (LTC) Engine in a Series Extended Range Electric Powertrain. *SAE Technical Papers* **2016**, *2016-Octob*.

[90] Murata, Y.; Morita, T.; Wada, K.; Ohno, H. NO_x Trap Three-Way Catalyst (N-TWC) Concept: TWC with NO_x Adsorption Properties at Low Temperatures for Cold-Start Emission Control. *SAE International Journal of Fuels and Lubricants* **2015**, *8*, 1–6.

[91] Adelman, B. J.; Sachtler, W. M. The effect of zeolitic protons on NO(x) reduction over Pd/ZSM-5 catalysts. *Applied Catalysis B: Environmental* **1997**, *14*, 1–11.

[92] Ogura, M.; Hayashi, M.; Kage, S.; Matsukata, M.; Kikuchi, E. Determination of active palladium species in ZSM-5 zeolite for selective reduction of nitric oxide with methane. *Applied Catalysis B: Environmental* **1999**, *23*, 247–257.

[93] Pommier, B.; Gelin, P. Infrared and volumetric study of NO adsorption on Pd-H-ZSM-5. *Physical Chemistry Chemical Physics* **2001**, *3*, 1138–1143.

[94] Perdana, I.; Creaser, D.; Öhrman, O.; Hedlund, J. NO_x adsorption over a wide temperature range on Na-ZSM-5 films. *Journal of Catalysis* **2005**, *234*, 219–229.

[95] Lee, J.; Ryou, Y. S.; Cho, S. J.; Lee, H.; Kim, C. H.; Kim, D. H. Investigation of the active sites and optimum Pd/Al of Pd/ZSM–5 passive NO adsorbers for the cold-start application: Evidence of isolated-Pd species obtained after

a high-temperature thermal treatment. *Applied Catalysis B: Environmental* **2018**, *226*, 71–82.

[96] Ryou, Y. S.; Lee, J.; Cho, S. J.; Lee, H.; Kim, C. H.; Kim, D. H. Activation of Pd/SSZ-13 catalyst by hydrothermal aging treatment in passive NO adsorption performance at low temperature for cold start application. *Applied Catalysis B: Environmental* **2017**, *212*, 140–149.

[97] Ballinger, T. H.; Manning, W. A.; Lafyatis, D. S. Hydrocarbon Trap Technology for the Reduction of Cold-Start Hydrocarbon Emissions. SAE Technical Paper Series. 1997.

[98] Chao, C. C.; Lunsford, J. H. Adsorption of Nitric Oxide on Y-Type Zeolites. A Low-Temperature Infrared Study. *Journal of the American Chemical Society* **1971**, *93*, 6794–6800.

[99] Kang, S. B.; Kalamaras, C.; Balakotaiah, V.; Epling, W. Hydrocarbon Trapping over Ag-Beta Zeolite for Cold-Start Emission Control. *Catalysis Letters* **2017**, *147*, 1355–1362.

[100] Serra, R. M.; Miró, E. E.; Bolcatto, P.; Boix, A. V. Experimental and theoretical studies about the adsorption of toluene on ZSM5 and mordenite zeolites modified with Cs. *Microporous and Mesoporous Materials* **2012**, *147*, 17–29.

[101] Loiland, J. A.; Lobo, R. F. Low temperature catalytic NO oxidation over microporous materials. *Journal of Catalysis* **2014**, *311*, 412–423.

[102] Loiland, J. A.; Lobo, R. F. Oxidation of zeolite acid sites in NO/O_2 mixtures and the catalytic properties of the new site in NO oxidation. *Journal of Catalysis* **2015**, *325*, 68–78.

[103] Hadjiivanov, K.; Saussey, J.; Freysz, J. L.; Lavalley, J. C. FT-IR study of NO + O_2 co-adsorption on H-ZSM-5: reassignment of the 2133 cm^{-1} band to NO^+ species. *Catalysis Letters* **1998**, *52*, 103–108.

[104] Szanyi, J.; Kwak, J. H.; Peden, C. H. F. The Effect of Water on the Adsorption of NO_2 in Na- and Ba-Y, FAU Zeolites: A combined FTIR and TPD Investigation. *Journal of Physical Chemistry B* **2004**, *108*, 3746–3753.

[105] Sedlmair, C.; Gil, B.; Seshan, K.; Jentys, A.; Lercher, J. A. An in situ IR study of the NO_x adsorption/reduction mechanism on modified Y zeolites. *Physical Chemistry Chemical Physics* **2003**, *5*, 1897–1905.

[106] Lobree, L. J.; Aylor, A. W.; Reimer, J. A.; Bell, A. T. NO Reduction by CH_4 in the Presence of O2over Pd-H-ZSM-5. *Journal of Catalysis* **1999**, *181*, 189–204.

[107] Van Den Berg, J. P.; Wolthuizen, J. P.; Clague, A. D. H.; Hays, G. R.; Hurs, R.; Van Hooff, J. H. C. Low-Temperature Oligomerization of Small Olefins on Zeolite H-ZSM-5. An Investigation with High-Resolution Solid-State 13C-NMR. *Journal of Catalysis* **1983**, *80*, 130–138.

[108] Wilshier, K. Propene Oligomerization Over H-ZSM-5 Zeolite. *Studies in Surface Science and Catalysis* **1988**, *36*, 621–625.

[109] Blomsma, E.; Martens, J.; Jacobs, P. Reaction Mechanisms of Isomerization and Cracking of Heptane on Pd/H-Beta Zeolite. *Journal of Catalysis* **1995**, *155*, 141–147.

[110] Hsia Chen, C. S.; Bridger, R. F. Shape-Selective Oligomerization of Alkenes to Near-Linear Hydrocarbons by Zeolite Catalysis. *JOURNAL OF CATALYSIS* **1996**, *161*, 687–693.

[111] Tkachenko, O.; Kucherov, A.; Kustov, L.; Virkkunen, V.; Leinonen, T.; Denifl, P. A Study of Ziegler–Natta Propylene Polymerization Catalysts by Spectroscopic Methods. *Materials* **2017**, *10*, 496.

[112] Li, G.; Larsen, S. C.; Grassian, V. H. Catalytic reduction of NO_2 in nanocrystalline NaY zeolite. *Journal of Molecular Catalysis A: Chemical* **2005**, *227*, 25–35.

[113] Burch, R.; Millington, P.; Walker, A. Mechanism of the selective reduction of nitrogen monoxide on platinum-based catalysts in the presence of excess oxygen. *Applied Catalysis B: Environmental* **1994**, *4*, 65–94.

[114] Khosravi, M.; Abedi, A.; Hayes, R. E.; Epling, W. S.; Votsmeier, M. Kinetic modelling of Pt and Pt: Pd diesel oxidation catalysts. *Applied Catalysis B: Environmental* **2014**, *154-155*, 16–26.

[115] Olson, D. H.; Haag, W. O.; Borghard, W. S. Use of water as a probe of zeolitic properties: interaction of water with HZSM-5. *Microporous and Mesoporous Materials* **2000**, *35-36*, 435–446.

[116] Brosius, R.; Habermacher, D.; Martens, J.; Vradman, L.; Herskowitz, M.; Čapek, L.; Sobalík, Z.; Dědeček, J.; Wichterlová, B.; Tokarová, V.; Gonsiorová, O. NO Oxidation Kinetics on Iron Zeolites: Influence of Framework Type and Iron Speciation. *Topics in Catalysis* **2004**, *30/31*, 333–339.

[117] Vu, A.; Luo, J.; Li, J.; Epling, W. S. Effects of CO on Pd/BEA Passive NO_x Adsorbers. *Catalysis Letters* **2017**, *147*, 745–750.

[118] Gu, Y.; Zelinsky, R. P.; Chen, Y.-R.; Epling, W. S. Investigation of an irreversible NO_x storage degradation Mode on a Pd/BEA passive NO_x adsorber. *Applied Catalysis B: Environmental* **2019**, *258*, 118032.

[119] Joshi, S. Y.; Harold, M. P.; Balakotaiah, V. Low-dimensional models for real time simulations of catalytic monoliths. *AIChE Journal* **2009**, *55*, 1771–1783.

[120] Joshi, S. Y.; Harold, M. P.; Balakotaiah, V. Overall mass transfer coefficients and controlling regimes in catalytic monoliths. *Chemical Engineering Science* **2010**, *65*, 1729–1747.

[121] Joshi, S. Y.; Ren, Y.; Harold, M. P.; Balakotaiah, V. Experimental and theoretical investigation of controlling regimes during lean oxidation of methane and propylene on Pt/Al 2O 3 monolithic reactors. *Industrial and Engineering Chemistry Research* **2012**, *51*, 7482–7492.

[122] Vjunov, A.; Fulton, J. L.; Huthwelker, T.; Pin, S.; Mei, D.; Schenter, G. K.; Govind, N.; Camaioni, D. M.; Hu, J. Z.; Lercher, J. A. Quantitatively probing the al distribution in zeolites. *Journal of the American Chemical Society* **2014**, *136*, 8296–8306.

[123] Loewenstein, W. The distribution of aluminum in the tetrahedra of silicates and aluminates. *American Mineralogist* **1954**, *39*, 92–96.

[124] Ramanathan, K.; Balakotaiah, V.; West, D. H. Light-off criterion and transient analysis of catalytic monoliths. *Chemical Engineering Science* **2003**, *58*, 1381–1405.

[125] Fuller, E. N.; Schettler, P. D.; Giddings, J. C. A new method for prediction of binary gas-phase diffusion coefficients. *Industrial and Engineering Chemistry* **1966**, *58*, 18–27.

[126] Balakotaiah, V.; West, D. H. Shape normalization and analysis of the mass transfer controlled regime in catalytic monoliths. *Chemical Engineering Science* **2002**, *57*, 1269–1286.

[127] Raj, R.; Harold, M. P.; Balakotaiah, V. Steady-state and dynamic hysteresis effects during lean co-oxidation of CO and C_3H_6 over Pt/Al_2O_3 monolithic catalyst. *Chemical Engineering Journal* **2015**, *281*, 322–333.

[128] Batalha, N.; Soualah, A.; Pinard, L.; Pouilloux, Y.; Lemos, F.; Belin, T. Impact of the BEA zeolite morphology on isobutane adsorption followed by Reversed-Flow Inverse Gas Chromatography. *Journal of Chromatography A* **2012**, *1260*, 206–214.

[129] Mowla, O.; Kennedy, E.; Stockenhuber, M. Mass transfer and kinetic study on BEA zeolite-catalysed oil hydroesterification. *Renewable Energy* **2019**, 417–425.

[130] Lang, W.; Laing, P.; Cheng, Y.; Hubbard, C.; Harold, M. P. Co-oxidation of CO and propylene on Pd/CeO_2-ZrO_2 and Pd/Al_2O_3 monolith catalysts: A light-off, kinetics, and mechanistic study. *Applied Catalysis B: Environmental* **2017**, *218*, 430–442.

[131] Li, M.; Malamis, S. A.; Epling, W.; Harold, M. P. Steady state and lean-rich cycling study of a three-way NO_x storage catalyst: Modeling. *Applied Catalysis B: Environmental* **2019**, *242*, 469–484.

[132] Divekar, S.; Nanoti, A.; Dasgupta, S.; Aarti,; Chauhan, R.; Gupta, P.; Garg, M. O.; Singh, S. P.; Mishra, I. M. Adsorption equilibria of propylene and propane on zeolites and prediction of their binary adsorption with the ideal adsorbed solution theory. *Journal of Chemical and Engineering Data* **2016**, *61*, 2629–2637.

[133] Pommier, B.; Ge, P. On the nature of Pd species formed upon exchange of H-ZSM-5 with Pd $(NH_3)_4^{2+}$ and calcination in O_2. **1999**, 1665–1672.

[134] Khivantsev, K.; Gao, F.; Kovarik, L.; Wang, Y.; Szanyi, J. Molecular Level Understanding of How Oxygen and Carbon Monoxide Improve NO_x Storage in Palladium/SSZ-13 Passive NO_x Adsorbers: The Role of NO^+ and Pd(II)(CO)(NO) Species. *The Journal of Physical Chemistry C* **2018**, *122*, 10820–10827.

[135] Azambre, B.; Westermann, A.; Finqueneisel, G.; Can, F.; Comparot, J. D.; Westermann, A.; Finqueneisel, G.; Can, F.; Comparot, J. D. Adsorption and Desorption of a Model Hydrocarbon Mixture Over HY Zeolite Under Dry and Wet Conditions. *The Journal of Physical Chemistry C* **2014**, *119*, 315–331.

[136] Malamis, S. A.; Harold, M. P.; Epling, W. S. Coupled NO and C_3H_6 Trapping, Release and Conversion on Pd-BEA: Evaluation of The Lean Hydrocarbon NO_x Trap (LHCNT). 2019.

[137] Hazlett, M. J.; Epling, W. S. Heterogeneous catalyst design: Zoned and layered catalysts in diesel vehicle aftertreatment monolith reactors. *The Canadian Journal of Chemical Engineering* **2019**, *97*, 188–206.

[138] Hazlett, M. J.; Moses-Debusk, M.; Parks, J. E.; Allard, L. F.; Epling, W. S. Kinetic and mechanistic study of bimetallic Pt-Pd/Al_2O_3 catalysts for CO and C_3H_6 oxidation. *Applied Catalysis B: Environmental* **2017**, *202*, 404–417.

[139] Avila, P.; Montes, M.; Miró, E. E. Monolithic reactors for environmental applications: A review on preparation technologies. *Chemical Engineering Journal* **2005**, *109*, 11–36.

[140] Olsson, L.; Persson, H.; Fridell, E.; Skoglundh, M.; Andersson, B. A kinetic study of NO oxidation and NO_x storage on Pt/$Al_2O_3$and Pt/BaO/Al_2O_3. *Journal of Physical Chemistry B* **2001**, *105*, 6895–6906.

[141] Weiss, B. M.; Iglesia, E. Mechanism and site requirements for NO oxidation on Pd catalysts. *Journal of Catalysis* **2010**, *272*, 74–81.

[142] Abedi, A.; Luo, J.-Y.; Epling, W. S. Improved CO, hydrocarbon and NO oxidation performance using zone-coated Pt-based catalysts. *Catalysis Today* **2013**, *207*, 220–226.

[143] Gupta, A.; Harold, M. P. NO_x Uptake and Release on Pd/SSZ-13: Impact of Feed Composition and Temperature. 2019.

Appendix A: Chapter 3 Supporting Information

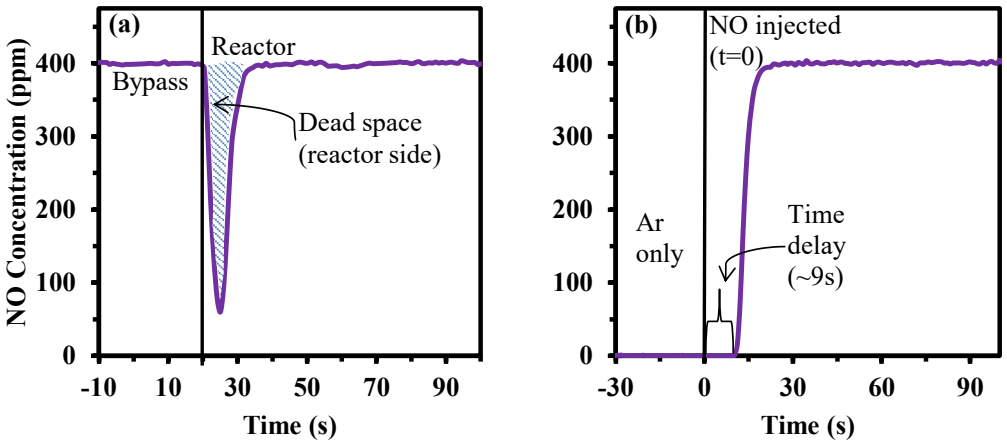

Figure A.1: Blank tube adsorption experiments using a feed of 400 ppm NO and 2% O_2.

Fig. A.1 (a) shows the blank tube adsorption experiment in which the gas mixture was fed through bypass until steady response was achieved, followed by a switch to the reactor, leading to a dip in concentration equivalent to volume of quartz tube and connected tubing. In case (b), Ar was fed until reference time t=0, after which the NO input was switched injected with a 4-way electronic switching valve and a response was observed, leading to a lag time of 9s. This lag time was taken into consideration for all experiments with similar flow rates and was reevaluated in the case of new conditions.

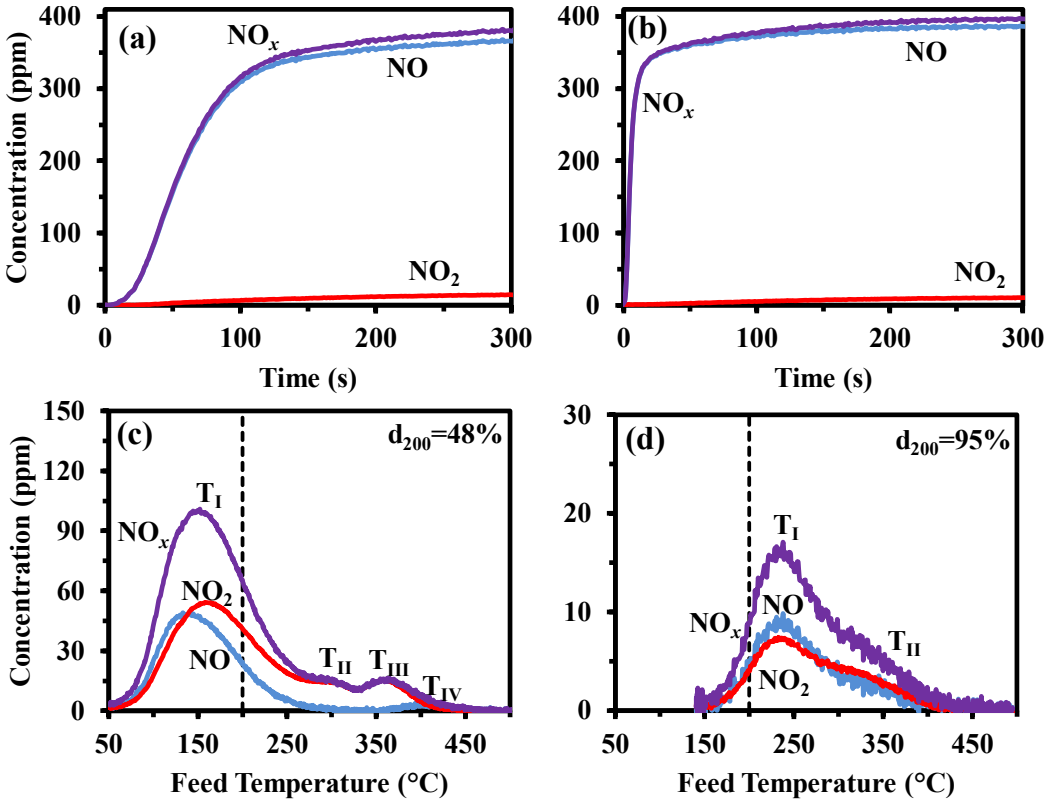

Figure A.2: (a,b) NO_x, NO, and NO_2 during adsorption for 300s at (a) 50°C and (b) 150°C for a feed of 400ppm NO, 2% O_2. (c,d) Corresponding TPD profiles at 20°C/min following adsorption at (c) 50°C and (d) 150°C in 2% O_2.

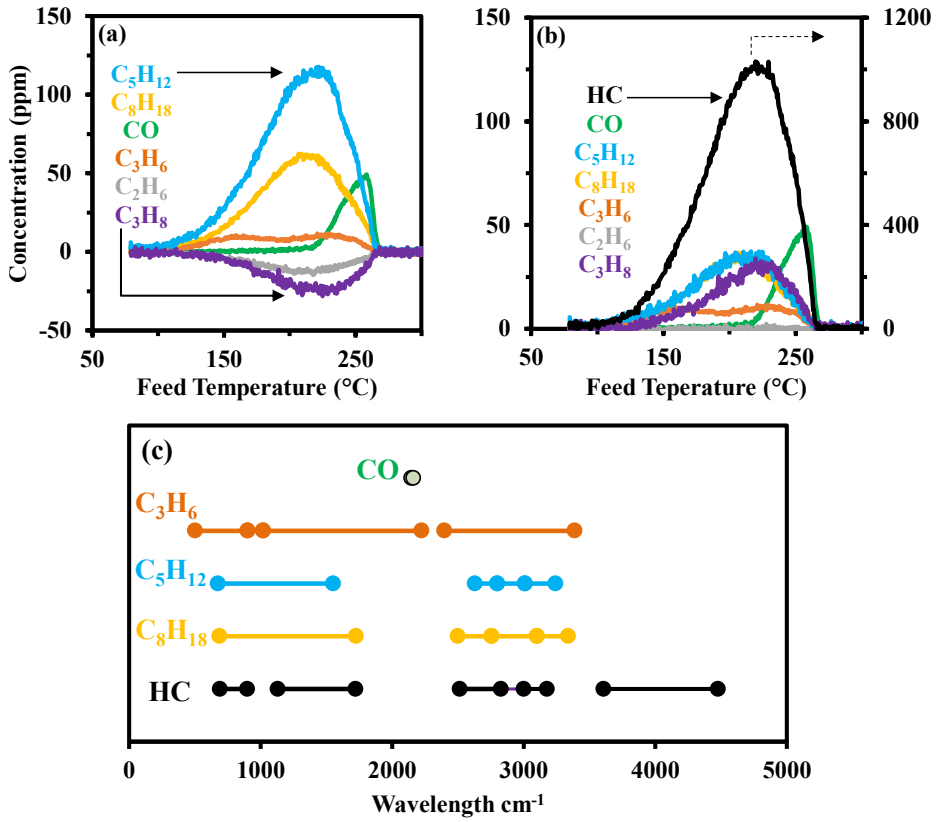

Figure A.3: FT-IR signal interference effects.

Fig. A.3 shows the FT-IR interference and overlap regions. Fig. A.3a shows the concentration of various hydrocarbons during desorption with 2%O_2, bal. Ar, at 20°C/min following adsorption at 80°C for 300s with a feed of 400ppm NO, 800ppm C_3H_6, 2% O_2 at a total flowrate of 2500sccm. Fig. A.3b shows the same data re-processed with total HC signal (C1 basis). Fig. A.3c shows spectral regions used in FT-IR calibration for selected hydrocarbons. Using the FT-IR data without the HC signal processing leads to negative peaks for some of the measurable species; we believe this is due to a calibration error in the system. Including the HC signal, however, normalizes all hydrocarbon species to zero and reduces the concentration of the larger alkanes (C5 and C8) based on the overlap (Figure S4.c). Therefore, we include the HC signal and any other measurable species in our analysis to provide a more accurate carbon balance.

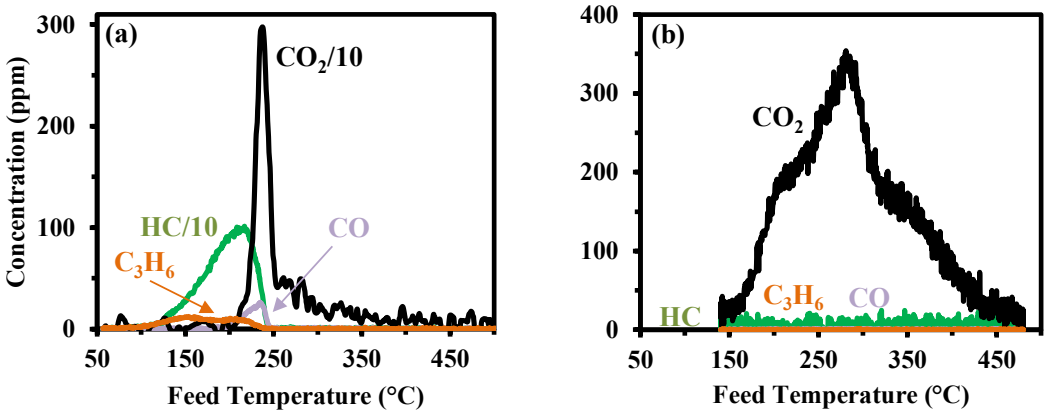

Figure A.4: Corresponding TPD profiles of C_3H_6, CO, HC, and CO_2 to data in Fig. 3.4. (a) 50°C adsorption; (b) 150°C adsorption. Ramp rate was 20°C/min with a feed of 2% O_2.

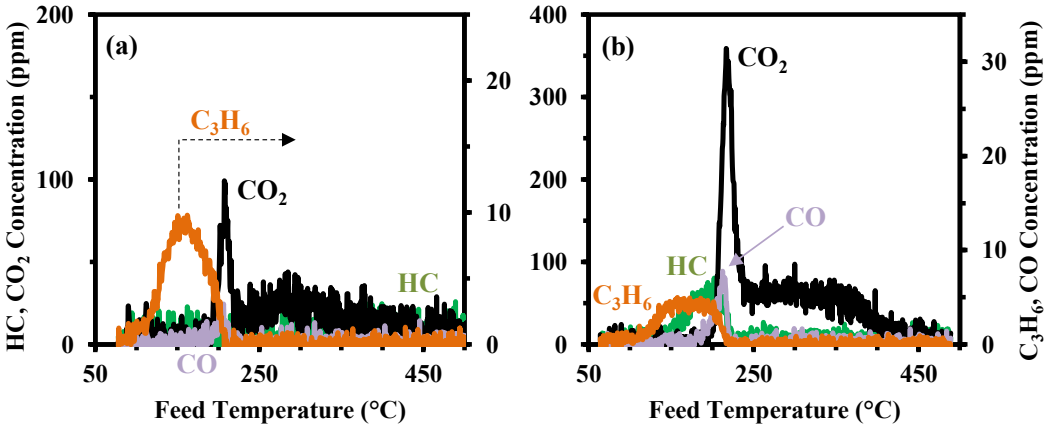

Figure A.5: Variable storage time experiments for a feed of 800ppm C_3H_6, 2% O_2, bal. Ar at 2500sccm. Corresponding desorption profiles are shown for (a) t=37s and (b) t=98s adsorption as a function of feed temperature.

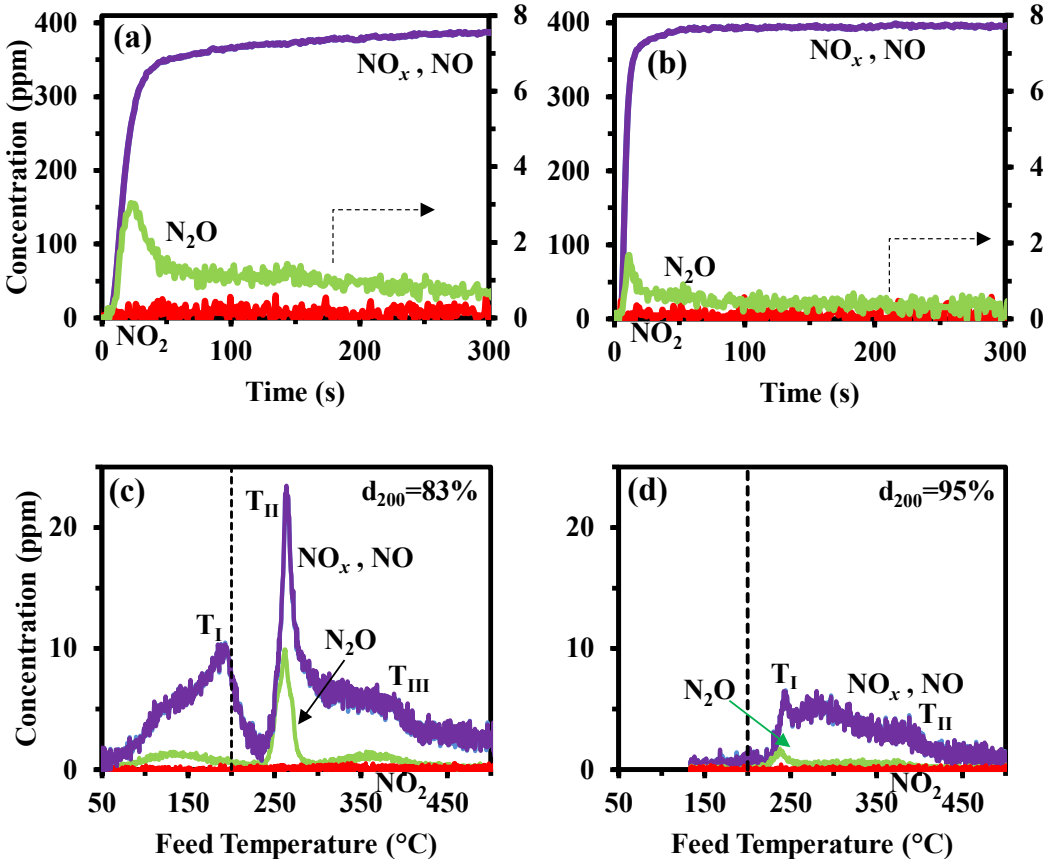

Figure A.6: (a,b) Effluent NO_x, NO, and N_2O adsorption at (a) 50°C and (b) 150°C for a feed of 400ppm NO, 800ppm C_3H_6, 2% O_2. (c,d) TPD profiles at 20°C/min following adsorption at (c) 50°C and (d) 150°C.

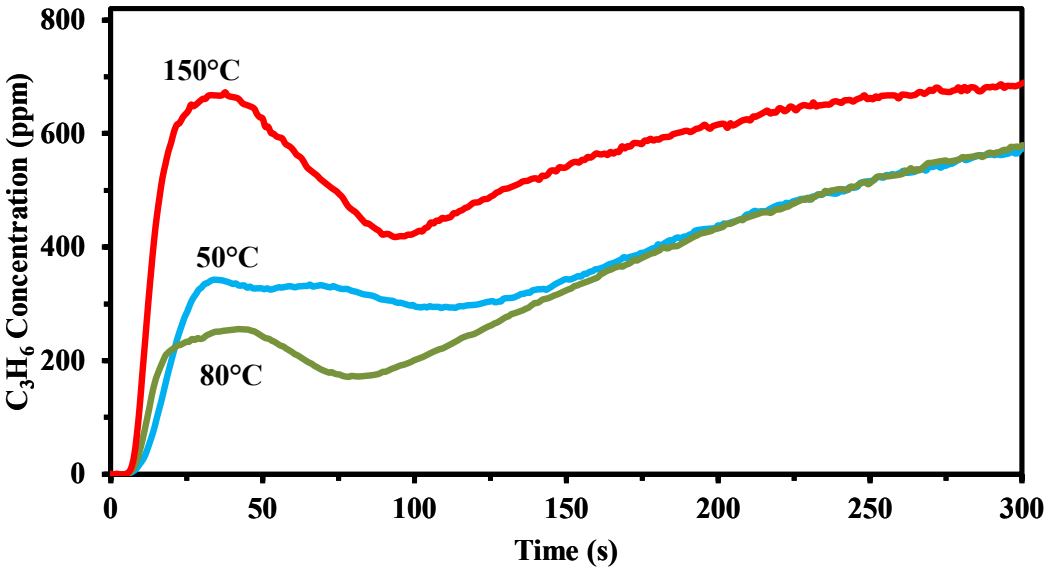

Figure A.7: Transient adsorption profiles of C_3H_6 during 300s adsorption at 50°C, 80°C, and 150°C for a feed of 400ppm NO, 800ppm C_3H_6, 2% O_2, bal. Ar.

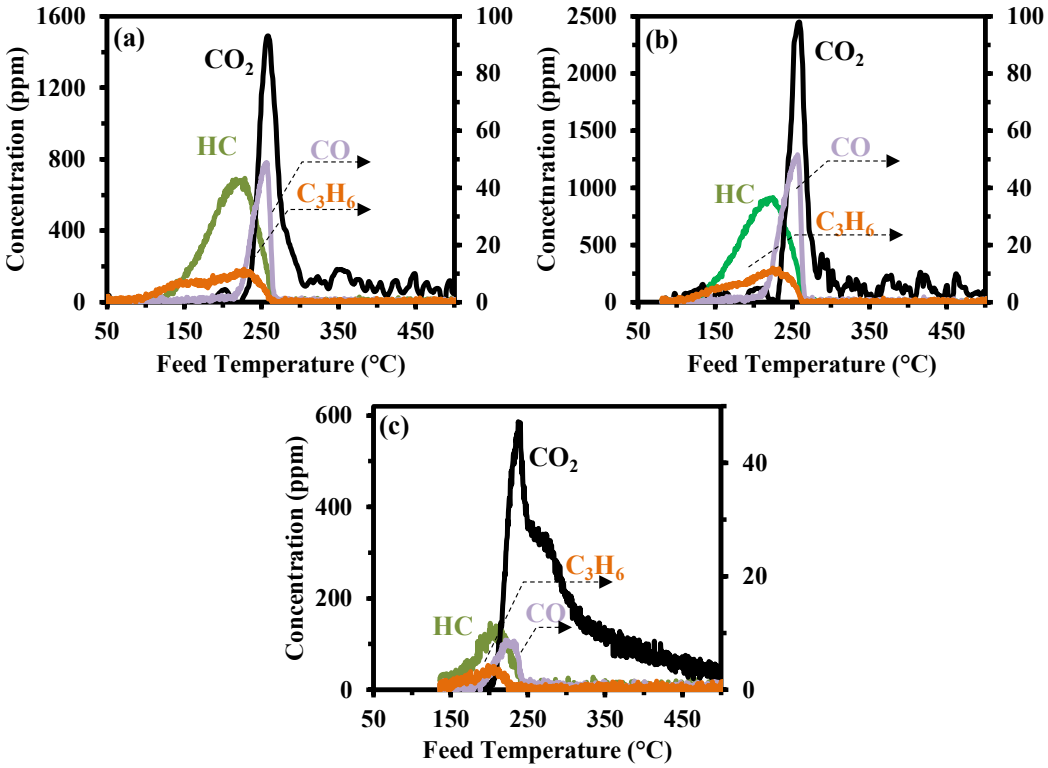

Figure A.8: TPD profiles of C_3H_6, CO, HC, and CO_2 for the adsorption profiles in Fig. A.7. (a) 50°C adsorption; (b) 80°C adsorption; (c) 150°C adsorption. 20°C/min ramp with a feed of 2% O_2, bal. Ar.

A.1 Sequential adsorption experiments

The sequential adsorption of NO and C_3H_6 adsorption is an effective method for assessing the extent of mutual inhibition. In these experiments, one species was pre-adsorbed before introducing the second (Figure A.9). Pre-adsorbing C_3H_6 leads to a reduction in NO adsorption from 5.3% to 1.4%, indicating that C_3H_6 is indeed blocking NO from adsorbing on most of the sites (Table A.1). It is also possible that due to the formation of larger hydrocarbons during C_3H_6 uptake, there are diffusional limitations preventing NO from accessing the binding sites in the pores. Additionally, we note the absence of NO_2 in this case, although it is unclear if its formation is suppressed by the presence of C_3H_6 on BAS or if it is being reduced. Despite the inhibition, NO, NO_2, and N_2O are detected during the subsequent temperature ramp, not shown here, indicating reaction between NO and C_3H_6. The adsorption profile of C_3H_6 is only marginally impacted by the pre-adsorption of NO, with the C_3H_6 trapping efficiency decreasing from 35% to 24%. The corresponding desorption profiles are very similar to the results in Fig. 3.9 since there is simultaneous desorption of NO and C_3H_6 from the surface. Additionally, during adsorption of the secondary species, there is no displacement of the pre-adsorbed species.

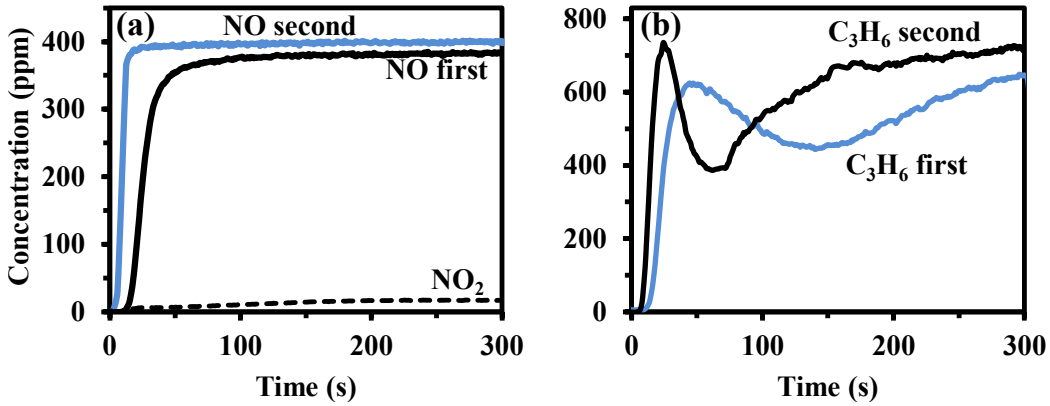

Figure A.9: (a) Adsorption profile of 400 ppm NO ("first") and pre-adsorption of 800 ppm C_3H_6 ("second"). (b) Adsorption profile of 800 ppm C_3H_6 ("first") and pre-adsorption of 400 ppm NO ("second"). T_{ads} =80°C.

Table A.1: Adsorption results for sequential experiments

First species	Second species	NO Ads. (μmol/g-cat)	NO Ads. (mol NO_x/mol Pd)	$\eta_{NO_{x(300)}}$	C_3H_6 Ads. (μmol/g-cat)	$\eta_{C_3H_6(300)}$
NO	C_3H_6	53.2	0.283	5.3%	246	24%
C_3H_6	NO	14.5	0.077	1.4%	355	35%

Appendix B: Chapter 5 Supporting Information

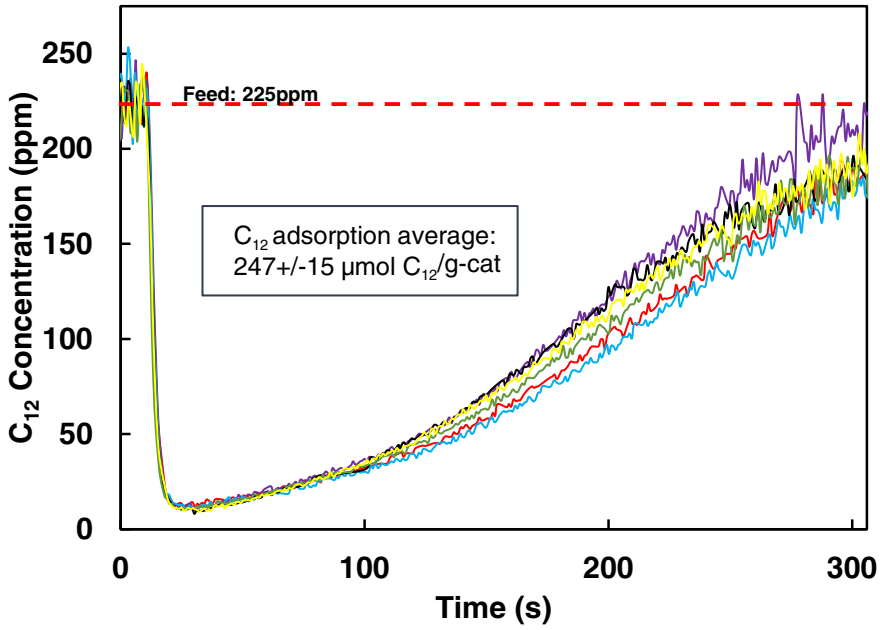

Figure B.1: C_{12} adsorption profiles from three dry experiments and three with 3% H_2O, two with 400ppm NO. Catalyst: 2wt.% Pd/BEA (2in., 1.5g/in^3) flowrate: 2500sccm (GHSV 35k hr^{-1}). Average adsorption was 247±15μmol/gcat.

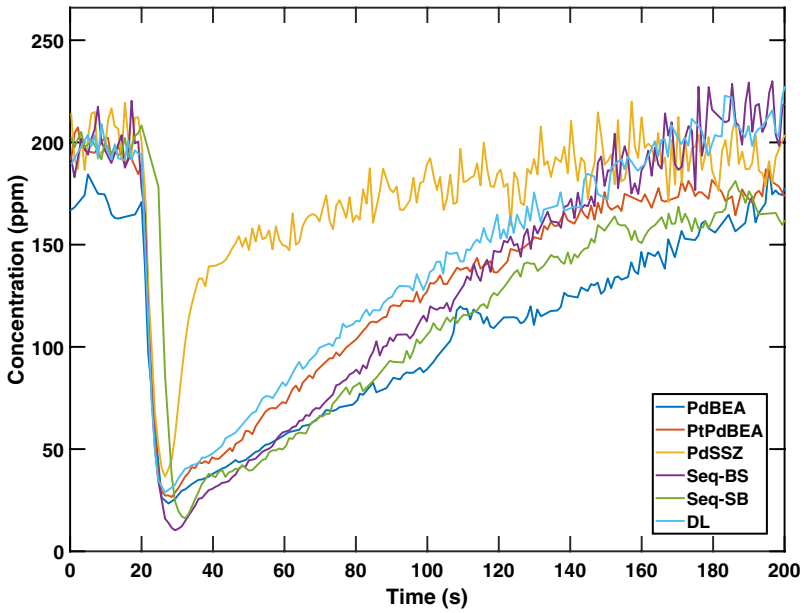

Figure B.2: C_{12} adsorption profiles for each catalyst tested (Table 5.2 for quantities), using a feed of 200ppm C_{12}, 400ppm NO, 2% O_2 and 3% H_2O.

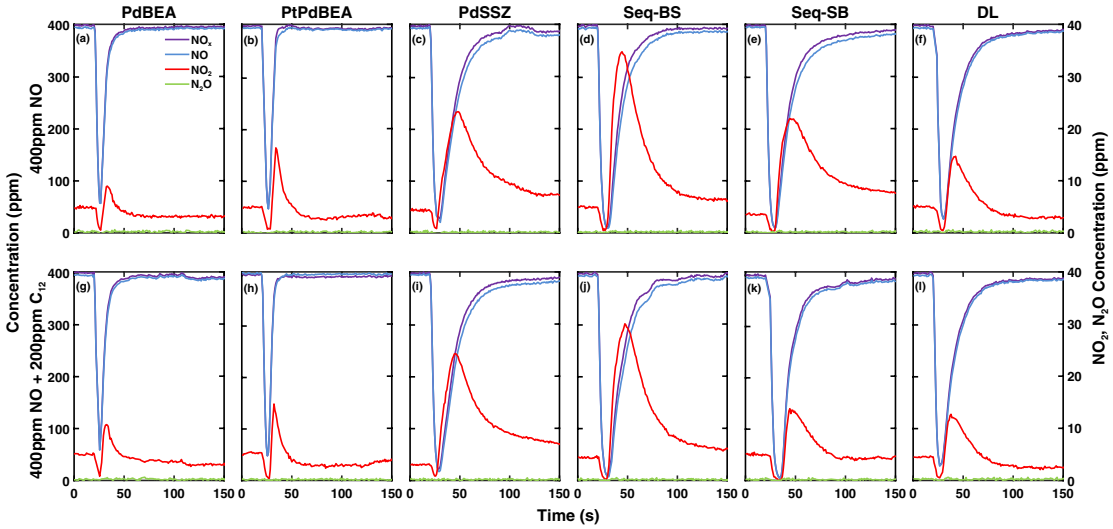

Figure B.3: Transient NO_x, NO, NO_2, and N_2O adsorption profiles for individual (a,b,c,g,h,i) and mixed (d,e,f,j,k,l) catalysts with NO only (Top) and with NO + C_{12} (Bottom). Adsorption was conducted at 100°C.

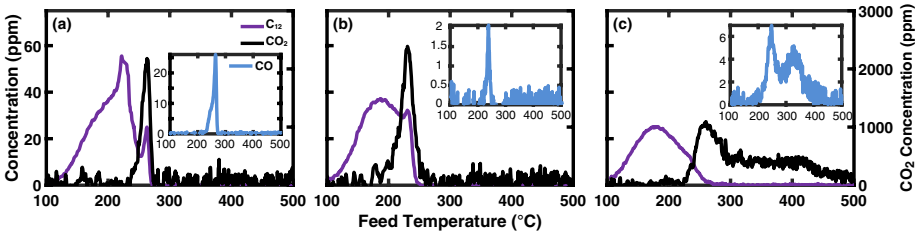

Figure B.4: Corresponding C_{12}, CO_2 and CO (inset) profiles for adsorption experiments in Fig. 3 (400ppm NO + 200ppm C_{12}, 2% O_2 and 3% H_2O, 100°C adsorption). (a) PdBEA, (b) PtPdBEA, (c) PdSSZ.

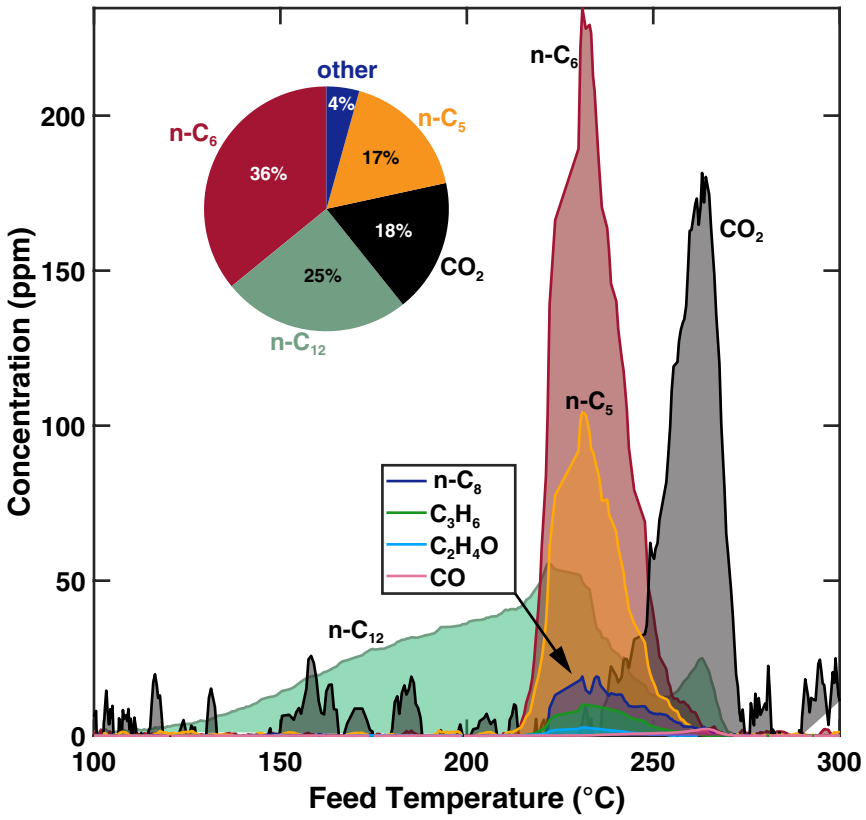

Figure B.5: Dodecane cracking product distribution on 2 wt.% Pd/BEA during TPD using a feed of 400ppm NO, 200pm C_{12}, 2% O_2, and 3% H_2O.

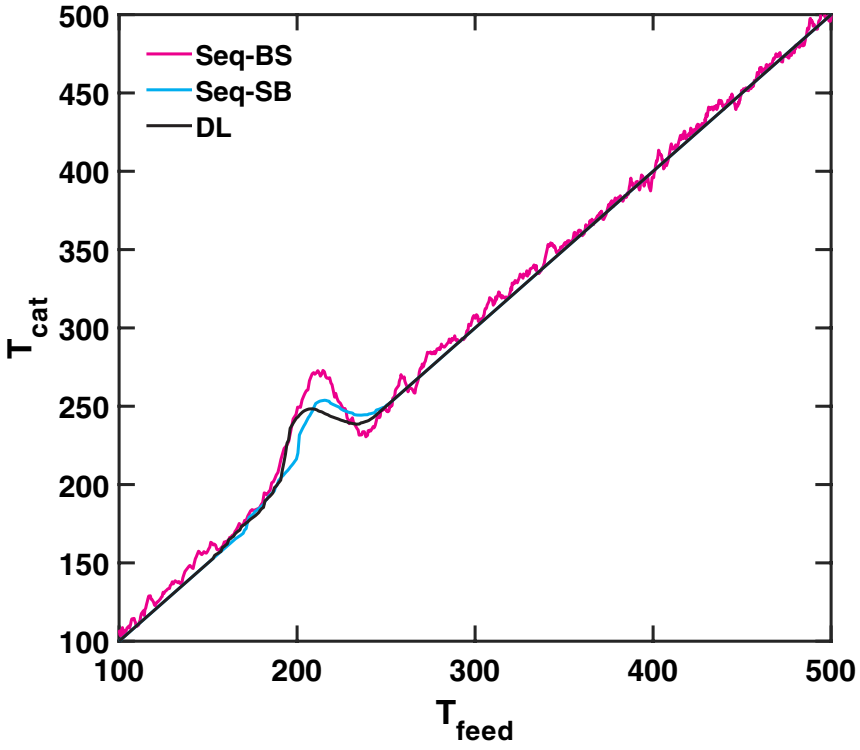

Figure B.6: Catalyst temperature vs. feed temperature during Type I TPD experiments for each sequential and layered catalyst using a feed of 400ppm NO, 200pm C_{12}, 2% O_2, and 3% H_2O.

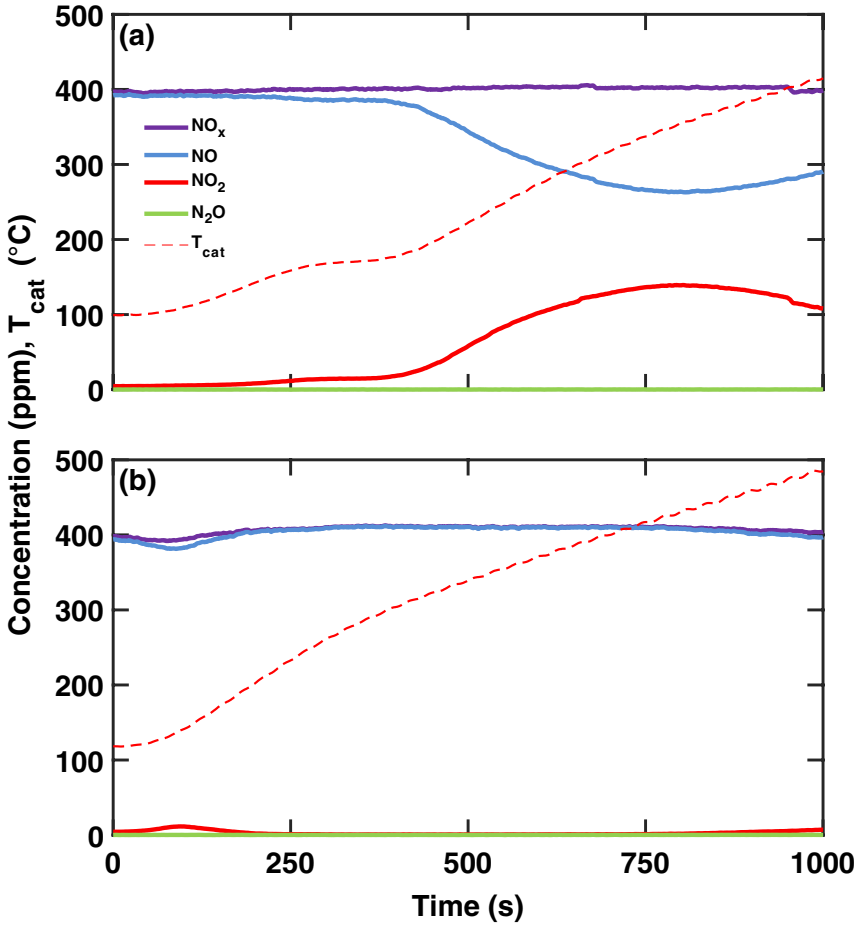

Figure B.7: Transient NO_x, NO, NO_2, N_2O, and T_{cat} profiles during Type II TPDs. Feed: 400ppm NO, 2% O_2, 3%H_2O for (a) PtPdBEA and (b) PdSSZ. Temperature ramp rate was 20°C/min.

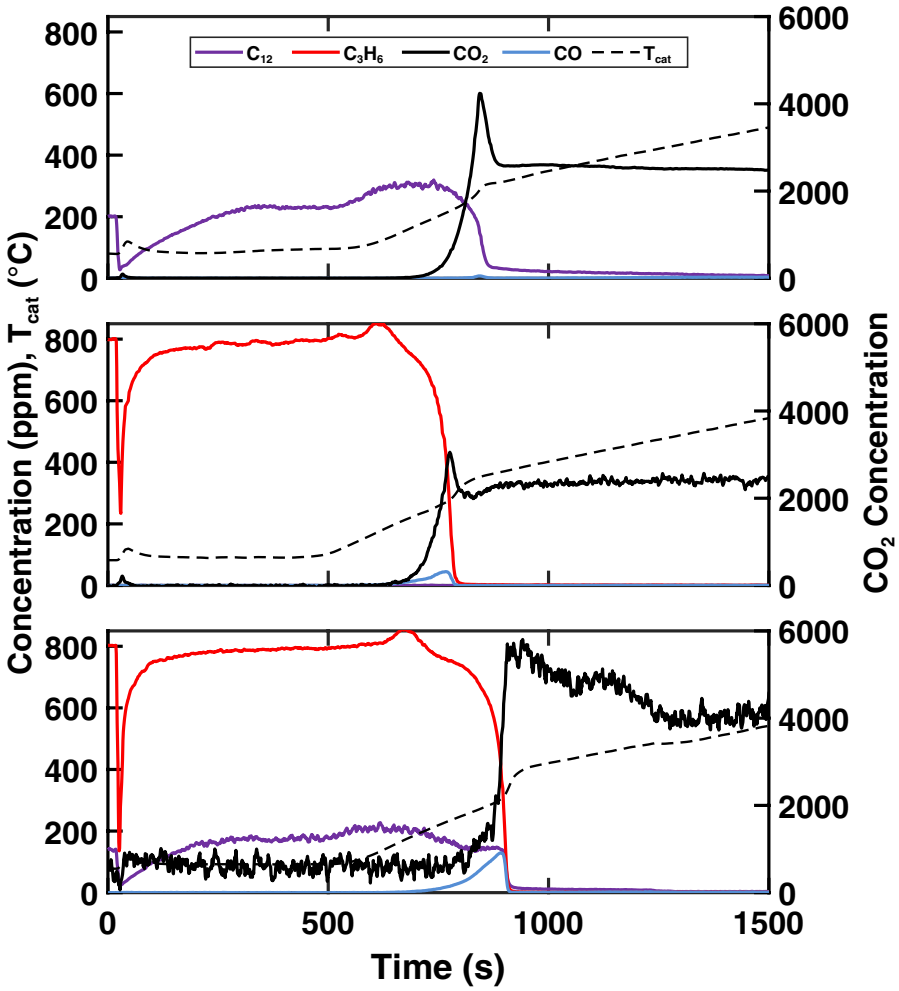

Figure B.8: Corresponding C_{12} and/or C_3H_6 adsorption and TPD profiles for experiments in Fig. 13 (b-d). (a) NO + C_{12}, (b) NO + C_3H_6, and (C), NO + C_3H_6 + C_{12}.

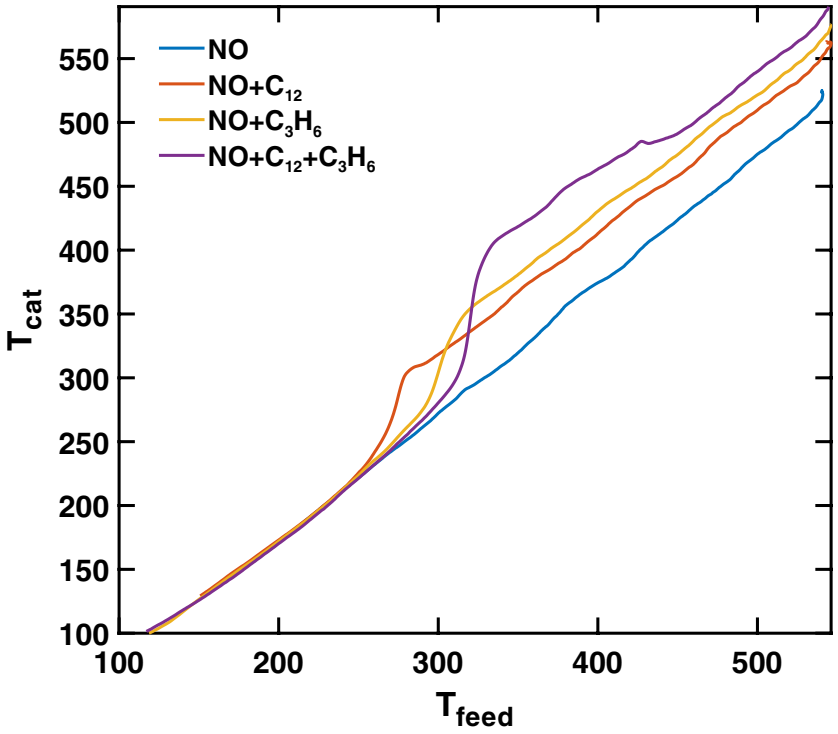

Figure B.9: Catalyst temperature exotherms vs. feed temperature for feeds containing NO only (blue), NO + C_{12} (red), NO + C_3H_6 (yellow), and NO + C_{12} + C_3H_6 (purple).